UNIVERSITÀ
DEGLI STUDI
DI PADOVA

Sede Amministrativa: Università degli Studi di Padova

Dipartimento di Ingegneria Industriale

CORSO DI DOTTORATO DI RICERCA IN INGEGNERIA INDUSTRIALE
CURRICOLO: INGEGNERIA MECCANICA
XXX CICLO

ANALYSIS AND DESIGN AGAINST PITTING OF GEARS IN POWER TRANSMISSIONS FOR OFF-HIGHWAY VEHICLES

Tesi redatta con il contributo finanziario di Carraro S.p.A.

Coordinatore: Ch.mo Prof. Paolo Colombo
Supervisore: Ch.mo Prof. Giovanni Meneghetti
Co-Supervisore: Ing. Fulvio Lo Conte (Carraro S.p.A.)

Dottorando: Andrea Terrin

"The most direct, and in a sense the most important, problem which our conscious knowledge of nature should enable us to solve is the anticipation of future events […]. As a basis for the solution of this problem we always make use of our knowledge of events which have already occurred, obtained by chance observation or by prearranged experiment. […] When from our accumulated previous experience we have once succeeded in deducing images of the desired nature, we can then in a short time develop, by means of them as by means of models, the consequences which in the external world arise only in a comparatively long time, or as the result of our own interposition. We are thus enabled to be in advance of the facts, and to decide as to present affairs in accordance with the insights so obtained."

Heinrich Hertz, *The Principles of Mechanics Presented in a New Form*
(published posthumously in 1899)

INDEX

Introduction

The work described in this thesis has been developed within the scope of a higher education apprenticeship program in cooperation with Carraro S.p.A., global player in the market of power drivelines for vehicles employed in industrial and agricultural applications, also addressed as off-highway vehicles. The study is part of a wider project initiated in 2012 by Carraro S.p.A. and the Department of Industrial Engineering of the university of Padova, and aimed to the study of the failure mechanisms of gears and the development of reliable and efficient methods to characterize the fatigue behaviour of gears materials.

The main failure mode of gears are fatigue fracture due to bending stress at the tooth root and surface fatigue due to contact stresses between the surfaces of mating teeth. The former mechanism is typically of greater concern, since it causes catastrophic failures with sudden unserviceability of the machine and possible serious consequences to other components, or even to the user. Hence a first Ph.D. project [1] developed between 2012 and 2015, was mainly focused on root bending fatigue failures of gears. The present work instead, started in 2014, deals with the second major issue in gears operation which is pitting. Pitting is the most hazardous among rolling contact fatigue phenomena, occurring in mechanical components subjected to repeated contacts between non-conformal surfaces. It manifests with the formation of craters on the surfaces leading to noise, vibration and loss of efficiency, and eventually may constitute the initiation cause for secondary damages such as tooth fractures.

The drivelines for off-higway vehicles are constituted by complicated transmission systems which may involve tens of gears, whose geometrical features must be accurately designed to ensure proper functioning and safety under the specific operating conditions to which each one will be subjected. Gears of the transmission, which are typically subjected to relatively small torques and high speeds are realized with helical teeth having small widths, bevel gear are implied in differential systems, while spur gears with large teeth are used in the final stages of reduction incorporated in the wheel hubs of axles, subjected to the highest torque levels. The operating regime of the whole vehicle as well as the peculiarities of the different stages of the driveline, determine the preferable failure mode of each gear. Particularly, bending failures are

more frequent in gears subjected to dynamic loads and repeated inversion of the rotating direction, or characterized by small web thickness. On the contrary, pitting occurs preferably on slow gears subjected to poor lubricating conditions, and particularly when the compliances of the shafts and supports lead to misalignment between mating teeth, resulting in an uneven distribution of the contact pressure. As an example, sun gears of the planetary gear sets, which constitute the final stage of reduction in off-highway drivelines, are particularly susceptible to pitting failures, being subjected to high torques under poor lubricating conditions determined by the low speed of rotation.

The pitting durability of gears is strongly influenced by the lubricating conditions, the relative velocity of the surfaces and their geometry, which in turn is affected by changes during the damaging process as a consequence of material removal. Moreover, the pressure distribution on gear teeth can be influenced by several factors such as modifications to the nominal involute profile of the tooth, gears and shaft deflections, bearings clearances and manufacturing inaccuracies. Hence, an accurate evaluation of the real load-time history experienced by the teeth is not straightforward and is affected by strong approximations even when advanced simulation software packages are used to create the theoretical model.

Due to the uncertainty of theoretical models, bench testing still constitute a fundamental step before the release of a new product. Durability tests on the complete off-highway transmissions however, involve a considerable investment leading to a significant impact in the final development costs. In the event of premature failure, moreover, redesign and further tests are required with serious consequences on the project's budget. It is therefore desirable to reduce at minimum the need of test and the eventuality of premature failures through a proper design of components and effective predictive models against the main causes of damages.

In the industrial practice the design methods against pitting and the prevision of the lifetime of gears are based on the comparison between a calculated value of contact pressure and a permissible limit determined by a fatigue curve derived by tests and strictly related to a specific material and operating condition. Accordingly, for the design and validation of gears, it is of fundamental importance to rely on solid calculation tools for a comprehensive estimation of the contact stresses acting on teeth, as well as on reliable data about the fatigue performances of the materials adopted for gears manufacturing. Moreover, fast and cost effective tests aimed to study the fatigue behaviour of the base materials and explore different solutions in terms of composition, heat treatment and surface finishing processes, already in the early phases of the

project, may be helpful to reduce the need of more expensive comparative tests on the finished product.

This thesis aims to address issues related to contact fatigue on gears, with particular reference to the geometries and materials of concern for Carraro S.p.A..

For an easier understanding of the following, chapter 1 is dedicated to the fundamentals of the calculation methods for the evaluation of the most influencing quantities with respect to the onset of contact fatigue damages on gears teeth, namely the applied pressures and the rolling and sliding speeds in gears teeth.

Chapter 2 reports an analysis of contact fatigue phenomena in sun gears of planetary gear sets, located in the wheel hubs of off-highway axles. These represent, among the products of the company, the components where pitting is most often observed.

Chapter 3 introduces the most common approaches proposed in the literature for the analysis of contact fatigue phenomena and the prevision of the lifetime of components.

Then the problem of the design against pitting of case hardened gears is faced in chapter 4 and 5 from two different perspectives: on the one hand the determination of reliable endurance limits for the materials used by the suppliers of Carraro S.p.A. in the manufacturing of case hardened gears, based on a reanalysis of the database of validation tests performed in the past on the whole axles; on the other hand an experimental analysis of the pressure distribution on gear teeth during operation is reported. This latter study was useful to assess the major discrepancies between theoretical models and actual systems, in order to improve the awareness in the use of calculation software packages dedicated to the prevision of the lifetimes of gears.

Finally, chapter 6 describes the development of a test rig for the contact fatigue characterization of gears materials by means of relatively fast tests on simple disc specimens. The first attempts to resemble the operating conditions of a particular gear pair with a dedicated design of specimens and to correlate the fatigue performances of gears and discs are discussed as well.

Chapter 1

FUNDAMENTALS OF CONTACT MECHANICS AND TRIBOLOGY

Surface fatigue damages originate by the propagation of cracks originated preferably in correspondence of weak points or stress concentration sites due to geometrical or microstructural defects, within a stress field generated by the contact between non-conformal surfaces. Although the fundamental process driving the formation of craters on the surface of the material will be treated in detail in the next section, it seems natural to assume that the damaging mechanism is related to the magnitude of the pressure developed in the contact between the surfaces, and that the tribological and functional characteristics of the components may influence dramatically their fatigue life.

This chapter is aimed to provide the basic information to understand and manage the equations which describe the physical quantities governing rolling contact fatigue phenomena in gears.

1.1 Calculation of contact stresses

The basis for the calculation of contact stresses between elastic bodies were settled by Heinrich Hertz apparently during the Christmas vacation in 1880 when he was 23 years old [2,3] and, despite the first discouraging review made to the Hertz's paper by Kirchhoff, the work immediately gained the attention of the scientific community after its presentation at the Physical Society. In that period, the German physicist was studying Newton's optical interference fringes at the Berlin Physics institute where he was research assistant of Hermann Von Helmholtz. Hertz's interest was moved by the conviction that elastic deformation of glass lenses in contact might be the cause of the elliptical interference patterns. His observations of the phenomena persuaded him that the contact area between continuous and non-conforming

surfaces is generally elliptical. To calculate the local deformations and the pressure distribution on the contact area, he based his theory on the subsequent hypothesis:

- The materials of the two bodies in contact are homogenous, smooth (the effect of roughness is not considered) and frictionless
- No plastic deformation occurs
- The elliptical contact area is much smaller than the dimensions of the bodies and the radii of curvature of the surfaces, therefore they can be treated as elastic half spaces loaded over a small elliptical area

In absence of load, the contact between two bodies having non-conformal surfaces occurs in a single point or over a line. Let us consider a reference system with origin in the point of first contact and where the z axis is oriented along the common normal direction. The surface of the two bodies can be represented by a function *z(x,y)* of the form:

$$z_{1,2} = A_{1,2}x^2 + B_{1,2}y^2 + C_{1,2}xy + \cdots \quad (1.1)$$

Neglecting higher order terms in x and y.

We now introduce two coordinate systems chosen as indicated in Figure 1.1, such that x_1 and x_2 are directed according to the plane containing the maximum curvature radii, R_{x1} and R_{x2} among all the possible cross sections of body 1 and 2 respectively, whilst y_1 and y_2 lay on the planes of minimum curvature radii of the two bodies R_{y1} and R_{y2}. By convention the curvature radii are assumed to be positive for convex surfaces and negative for concave surfaces. It can be proved [3,4] that the z coordinate of a generic point on the surfaces can be expressed through equations of the type:

$$z = \frac{1}{2R_{x1}}x_1^2 + \frac{1}{2R_{y1}}y_1^2 \quad (1.2)$$

For the first body, and

$$z = -\left(\frac{1}{2R_{x2}}x_2^2 + \frac{1}{2R_{y2}}y_2^2\right) \quad (1.3)$$

For the second body. It is to be note that if a symmetry plane exists for a body one of the principal radii lives in that plane.

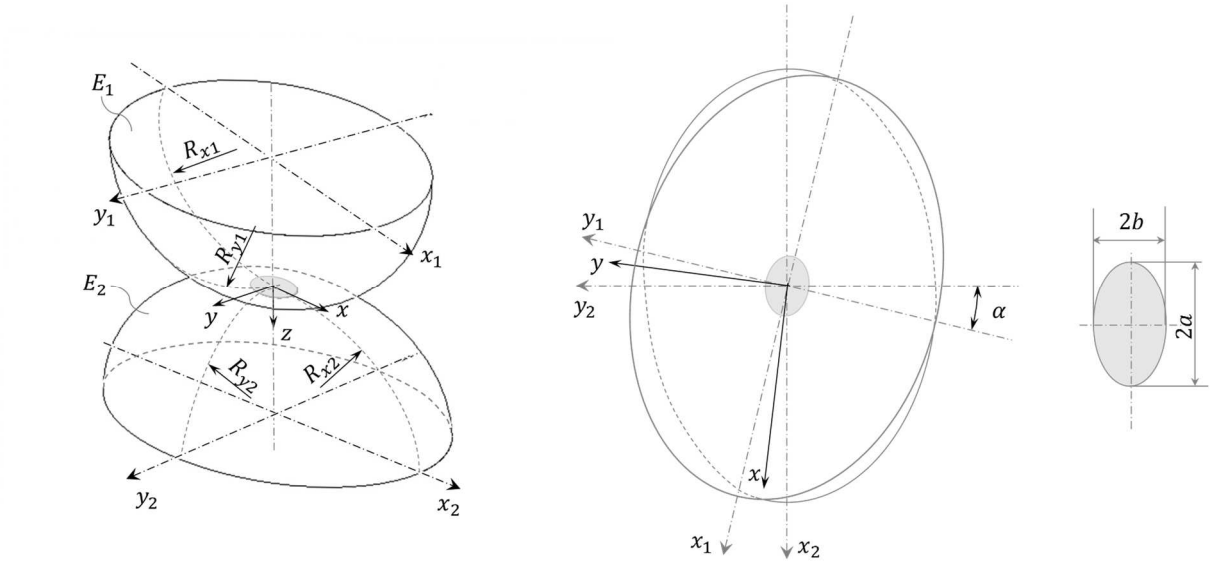

Figure 1.1 Bodies with general profile in contact

In the common reference system x, y, z, the distance of two points belonging to body 1 and 2 respectively, with the same x and y coordinate, can be defined as:

$$h = z_1 - z_2 = (A_1 - A_2)x^2 + (B_1 - B_2)y^2 + (C_1 - C_2)xy = Ax^2 + By^2 + Cxy \qquad (1.4)$$

by an appropriate choice of directions of the x and y axis, the term in *xy* vanishes and equation (1.4) becomes:

$$h = Ax^2 + By^2 = \frac{1}{2R'_x}x^2 + \frac{1}{2R'_y}y^2 \qquad (1.5)$$

Meaning that the coordinate of couples of points of the undeformed surfaces having constant gaps form in the plane xy ellipses whose semi-axes *a* and *b* are in the ratio $\frac{b}{a} = (A/B)^{\frac{1}{2}}$ where

$$A = \frac{1}{4}\left(\frac{1}{R_{x1}} + \frac{1}{R_{y1}} + \frac{1}{R_{x2}} + \frac{1}{R_{y2}}\right) - \frac{1}{4}\sqrt{\left[\left(\frac{1}{R_{y1}} - \frac{1}{R_{x1}}\right) + \left(\frac{1}{R_{y2}} - \frac{1}{R_{x2}}\right)\right]^2 - 4\left(\frac{1}{R_{y1}} - \frac{1}{R_{x1}}\right)\left(\frac{1}{R_{y2}} - \frac{1}{R_{x2}}\right)\sin^2\alpha} \qquad (1.6)$$

And

$$B = \frac{1}{4}\left(\frac{1}{R_{x1}} + \frac{1}{R_{y1}} + \frac{1}{R_{x2}} + \frac{1}{R_{y2}}\right) + \frac{1}{4}\sqrt{\left[\left(\frac{1}{R_{y1}} - \frac{1}{R_{x1}}\right) + \left(\frac{1}{R_{y2}} - \frac{1}{R_{x2}}\right)\right]^2 - 4\left(\frac{1}{R_{y1}} - \frac{1}{R_{x1}}\right)\left(\frac{1}{R_{y2}} - \frac{1}{R_{x2}}\right)\sin^2\alpha} \qquad (1.7)$$

The term α represents the angle between the planes containing the two maximum principal radii of curvature of the two bodies.

The doubled-sum of A and B defines the *reduced curvature radius* R', which is an important parameter in the determination of the contact pressure:

$$R' = 2(A+B) = \frac{1}{R_{x1}} + \frac{1}{R_{y1}} + \frac{1}{R_{x2}} + \frac{1}{R_{y2}} = \frac{1}{R_x'} + \frac{1}{R_y'} \qquad (1.8)$$

For increasing loads P the surface of the elastic bodies is deformed and the distance of the centers is reduced accordingly of a quantity

$$\delta = \delta_1 + \delta_2 \qquad (1.9)$$

In the contact between general profiles (point contacts), the contact area will approach an elliptical shape similar to that of the contours of constant separation. A particular case is represented by the contact between cylindrical bodies with parallel axes (line contacts), where the contours of constant separation are represented by straight lines and the contact area will be rectangular. The problem of determining the pressure distribution within the contact area can be afforded by evaluating the reaction opposed by the surfaces to their deformation. The displacements of each point in the contact area of the bodies can be expressed as difference between the rigid motion due to approaching of the centers δ and the original gap h (seeFigure 1.2):

$$\overline{u_{z1}} + \overline{u_{z2}} = \delta - h \qquad (1.10)$$

Or, by eq. (1.5)

$$\overline{u_{z1}} + \overline{u_{z2}} = \delta - Ax^2 - By^2 \qquad (1.11)$$

Outside the contact area on the other hand, it must be:

$$\overline{u_{z1}} + \overline{u_{z2}} + h < \delta - Ax^2 - By^2 \qquad (1.12)$$

The solution of the problem requires to find a pressure distribution which provides a parabolic function of displacements over the surface in order to close the gap defined by equation (1.5) and satisfy the conditions (1.11) and (1.12).

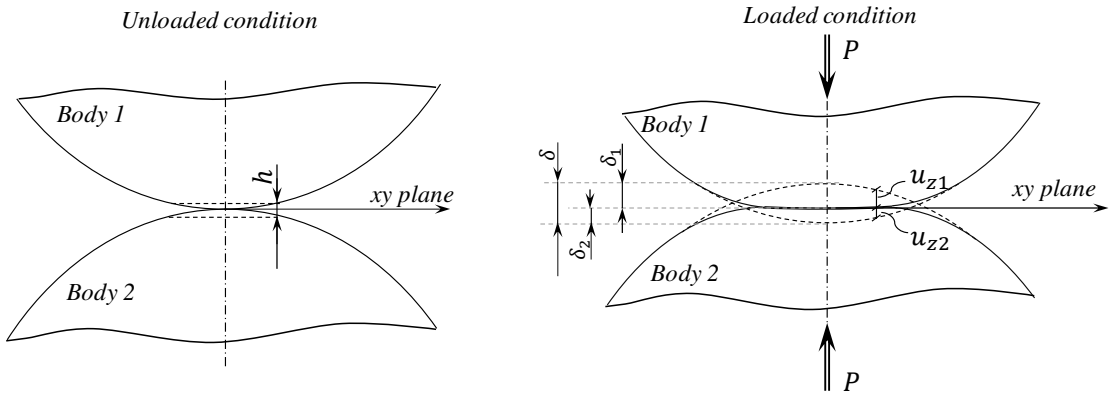

Figure 1.2 Deflection of two generic surfaces in contatct.

1.1.1 Contact between general profiles

Hertz noted that the problem of the deflections in contact between elastic bodies presented some analogies to the one of electrostatic potential. In fact, an ellipsoidal distribution of charge over the plane surface of a conductor, leads to a parabolic variation of the potential throughout that surface. Similarly, a semi-ellipsoidal pressure distribution given by

$$p = p_0 \left[1 - \left(\frac{x}{a}\right)^2 - \left(\frac{y}{b}\right)^2\right]^{1/2} \quad (1.13)$$

Where p_0 represents the maximum value of pressure occurring at the centre of the contact area, leads to parabolic displacements within the same area given by [3]:

$$\overline{u_z} = \frac{1-\nu^2}{\pi E}(L - Mx^2 - Ny^2) \quad (1.14)$$

Where:

$$M = p_0 \pi \left(\frac{b}{e^2 a^2}\right)[\boldsymbol{K}(e) - \boldsymbol{E}(e)] \quad (1.15)$$

$$N = p_0 \pi \left(\frac{b}{e^2 a^2}\right)\left[\left(\frac{a^2}{b^2}\right)\boldsymbol{E}(e) - \boldsymbol{K}(e)\right] \quad (1.16)$$

$$L = p_0 \pi b \boldsymbol{K}(e) \quad (1.17)$$

$\boldsymbol{K}(e)$ and $\boldsymbol{E}(e)$ are complete elliptic integrals of first and second species, respectively:

$$\boldsymbol{K}(e) = \int_0^{\frac{\pi}{2}} \frac{d\vartheta}{\sqrt{1 - e^2 \sin^2 \vartheta}} \qquad (1.18)$$

$$\boldsymbol{E}(e) = \int_0^{\frac{\pi}{2}} \sqrt{1 - e^2 \sin^2 \vartheta}\, d\vartheta \qquad (1.19)$$

The argument *e* of the elliptic integrals depends on the eccentricity $k = b/a$ of the contact ellipse:

$$e = (1 - k^2)^{\frac{1}{2}} = \left(1 - \frac{b^2}{a^2}\right)^{\frac{1}{2}}, \qquad b < a \qquad (1.20)$$

Therefore, introducing the reduced elasticity modulus *E'*, which is function of the elastic properties of the materials composing the two bodies,

$$E' = \left(\frac{1 - \nu_1^2}{E_1} + \frac{1 - \nu_2^2}{E_2}\right)^{-1} \qquad (1.21)$$

, equation (1.14) can be expressed as:

$$\overline{u_z} = \overline{u_{z1}} + \overline{u_{z2}} = \frac{L - Mx^2 - Ny^2}{\pi E'} \qquad (1.22)$$

By substituting the (1.22) into equation (1.11) appears that such pressure distribution satisfies the boundary conditions, provided that:

$$A = \frac{M}{\pi E'} = \frac{p_0}{E'}\left(\frac{b}{e^2 a^2}\right)[\boldsymbol{K}(e) - \boldsymbol{E}(e)] \qquad (1.23)$$

$$B = \frac{N}{\pi E'} = \frac{p_0}{E'}\left(\frac{b}{e^2 a^2}\right)\left[\left(\frac{1}{k^2}\right)\boldsymbol{E}(e) - \boldsymbol{K}(e)\right] \qquad (1.24)$$

$$\delta = \frac{L}{\pi E'} = \frac{p_0}{E'} b\boldsymbol{K}(e) \qquad (1.25)$$

Moreover, since the total load *P* must be equal to the integral of the semi-ellipsoidal distribution of pressure, it must be:

$$P = \left(\frac{2}{3}\right) p_0 \pi a b \qquad (1.26)$$

Hence

$$p_0 = \frac{3P}{2\pi a b} = \frac{3Pk}{2\pi b^2} \qquad (1.27)$$

Therefore, the contact pressure p_0 relevant to a load P is function of the dimensions of the elliptical contact area. Once the curvature radii of the surface are known, the value of the eccentricity, e can be derived numerically or by using tables of elliptic integrals solutions available in mathematical handbooks, by imposing the condition

$$\frac{B}{A} = \frac{R'_x}{R'_y} = \frac{\left(\frac{1}{1-e^2}\right)\boldsymbol{E}(e) - \boldsymbol{K}(e)}{\boldsymbol{K}(e) - \boldsymbol{E}(e)} \qquad (1.28)$$

Which is consequence of the equations (1.20), (1.23) and (1.24).
Then, to find the length of the semi-minor axis of the ellipse of contact b, we can consider the sum of equations (1.23) and (1.24) [5]:

$$A + B = \frac{1}{2}R' = \frac{p_0}{E'}\left(\frac{b}{e^2 a^2}\right)\left[\left(\frac{1}{k^2}\right) - 1\right]\boldsymbol{E}(e) \qquad (1.29)$$

Or, by simple operations:

$$R' = 2 \cdot \frac{p_0}{E'}\left[\frac{b}{(1-k^2)a^2}\right]\left[\frac{1-k^2}{k^2}\right]\boldsymbol{E}(e) = 2 \cdot \frac{p_0}{E^*}\frac{b}{a^2}\frac{a^2}{b^2}\boldsymbol{E}(e) = 2 \cdot \frac{p_0}{E'b}\boldsymbol{E}(e) \qquad (1.30)$$

Therefore

$$b = 2 \cdot p_0 \, \boldsymbol{E}(e)\frac{R'}{E'} \qquad (1.31)$$

And, in terms of the contact load P:

$$b = \sqrt[3]{\frac{3k\boldsymbol{E}(e)}{\pi}\left(\frac{PR'}{E'}\right)} = ka \qquad (1.32)$$

The principal stresses throughout the solids can be calculated for any point along the z-axiz by the following relations [5]:

$$\frac{\sigma_{xx}}{p_0} = \frac{2b}{e^2 a}(\Omega_x + \nu\Omega'_x) \quad (1.33)$$

$$\frac{\sigma_{yy}}{p_0} = \frac{2b}{e^2 a}(\Omega_y + \nu\Omega'_y) \quad (1.34)$$

$$\frac{\sigma_{zz}}{p_0} = -\frac{b}{e^2 a}\frac{1-T^2}{T} \quad (1.35)$$

Where:

$$T = \left(\frac{b^2+z^2}{a^2+z^2}\right)^{\frac{1}{2}} \quad (1.36)$$

$$\Omega_x = -\frac{1-T}{2} + \zeta[\boldsymbol{F}(\phi,e) - \boldsymbol{H}(\phi,e)] \quad (1.37)$$

$$\Omega'_x = 1 - \frac{T}{k^2} + \zeta\left[\frac{1}{k^2}\boldsymbol{H}(\phi,e) - \boldsymbol{F}(\phi,e)\right] \quad (1.38)$$

$$\Omega_y = \frac{1}{2} + \frac{1}{2T} - \frac{T}{k^2} + \zeta\left[\frac{1}{k^2}\boldsymbol{H}(\phi,e) - \boldsymbol{F}(\phi,e)\right] \quad (1.39)$$

$$\Omega'_y = -1 + T + \zeta[\boldsymbol{F}(\phi,e) - \boldsymbol{H}(\phi,e)] \quad (1.40)$$

With $\zeta = \frac{z}{a} = \cot\phi$. Unlike $\boldsymbol{E}(e)$ and $\boldsymbol{K}(e)$, the elliptic integrals $\boldsymbol{F}(\phi,e)$ and $\boldsymbol{H}(\phi,e)$ are indefinite and depend on the depth $\phi = \tan^{-1}\left(\frac{a}{z}\right)$ of the generic point where the stresses need to be calculated:

$$\boldsymbol{F}(\phi,e) = \int_0^{\phi} \frac{d\vartheta}{\sqrt{1-e^2\sin^2\vartheta}} \quad (1.41)$$

$$\boldsymbol{H}(\phi,e) = \int_0^{\phi} \sqrt{1-e^2\sin^2\vartheta}\, d\vartheta \quad (1.42)$$

Figure 1.3 shows the principal components of stress beneath the point of first contact normalized by the maximum contact pressure and plotted against the ratio between the depth z

and the semi-minor axis of the contact ellipse b. In absence of friction, beneath the centre of the ellipse of contact, the coordinate axes x,y and z coincide with the principal directions. The chart shows also the maximum principal shear stress τ_1 which magnitude correspond to the radius of the greater among the Mohr's circles and act in a plane inclined by 45° with respect to the x and z directions. This parameter is indeed the equivalent stress defined by the Tresca's criterion for yielding and has been often indicated as a useful index in the analysis of contact related damages which origins are generally driven by shear stresses [6].

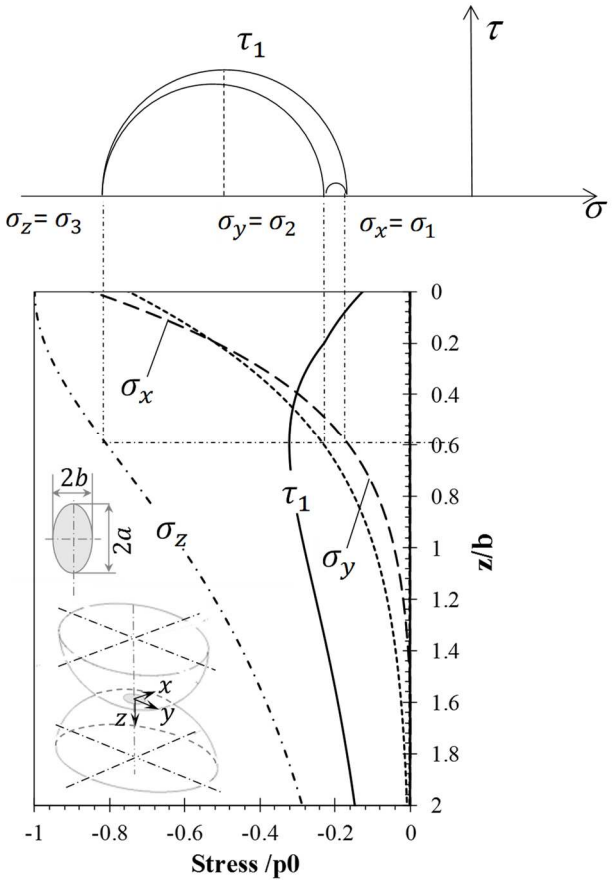

Figure 1.3 Principal shear stresses beneath the point of first contact of two bodies having curvature radii such that the ratio between the semi-axes of the contact ellipse is b/a=0.6.

The depth at which the principal shear stress τ_1 achieves the maximum value and its magnitude depend on the load and on the shape of the contact ellipse. The chart represented in Figure 1.3 is relevant to a couple bodies having curvature radii resulting in a contact ellipse with semi-axes in the ratio b/a=0.6. In this case the maximum value of τ_1 is about $0.32\ p_0$, occurring at a depth of $0.59\ b$.

For the sake of simplicity, various authors formulated approximate equations to estimate the values of the elliptic integrals. As an example, Hamrock and Dowson [7] proposed simplified formulas for the elliptical integrals obtained by linear regression with the least square methods. All the main contact parameters may be evaluated as functions of the simplified elliptical integral $\bar{\varepsilon}$ and of the simplified ellipticity coefficient $\bar{k}$ which represents the ratio of the major to minor semiaxis of the contact ellipse and can be calculated by the approximate formulas:

$$\bar{\varepsilon} = 1.0003 + 0.5968\frac{R'_y}{R'_x} \approx \boldsymbol{E}(e) \qquad (1.43)$$

$$\bar{k} = 1.0339\left(\frac{R'_x}{R'_y}\right)^{0.636} \approx \frac{1}{k} = a/b \qquad (1.44)$$

Hence, equation (1.32) becomes:

$$b = \left(\frac{3\bar{\varepsilon}PR'}{\bar{k}\pi E'}\right)^{\frac{1}{3}} \qquad (1.45)$$

Moreover, for the simpler particular cases where $k = 1$ (contact between solids of revolutions) or $k = 0$ (contact between parallel cylinders), the pressure and the dimensions of the contact area can be easily calculated by means of analytical formulas which will be presented in the next two paragraphs. A summary of the formulas presented in these sections is available in Table 1.1.

1.1.2 Contact between solids of revolution

For solids obtained by revolution around the *z* axis (such as spheres) the principal curvature radii are such as

$$R_{x1} = R_{y1} = R_1 \text{ and } R_{x2} = R_{y2} = R_2 \qquad (1.46)$$

Hence, the relative radius of curvature is given by:

$$\frac{1}{R'} = \left(\frac{1}{R_1} + \frac{1}{R_2}\right) \qquad (1.47)$$

The contact area will be circular, with radius *a,* as shown in Figure 1.4, where:

$$a = \pi p_0 R'/2E' \tag{1.48}$$

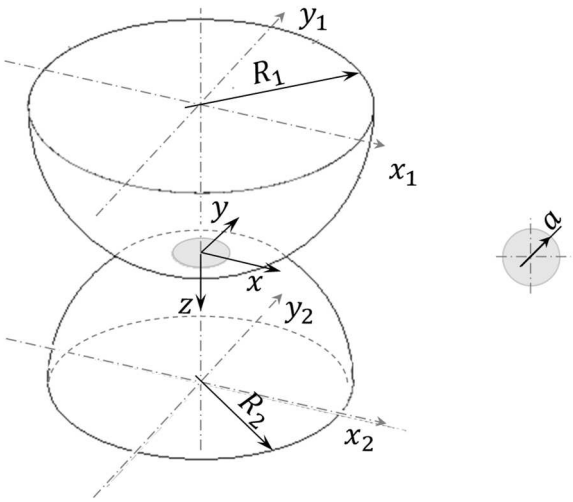

Figure 1.4 Contact between spherical surfaces

And the pressure distribution expressed in function of the polar coordinate r, within the contact area, is

$$p(r) = p_0 \sqrt{1 - \left(\frac{\mathrm{r}}{\mathrm{a}}\right)^2} \tag{1.49}$$

where p_0 is the maximum pressure at the center of the contact circle. The contact load is given by integration of pressure over the contact area:

$$P = \int_0^a p(r) 2\pi r \; dr = \frac{2}{3} p_0 \pi a^2 \tag{1.50}$$

The stresses along the *z* axis can be calculated by:

$$\frac{\sigma_x}{p_0} = \frac{\sigma_y}{p_0} = -(1+\nu)\left\{1 - \frac{z}{a}\tan^{-1}\left(\frac{a}{z}\right)\right\} + 1/2\left(1 + \frac{z^2}{a^2}\right)^{-1} \tag{1.51}$$

$$\frac{\sigma_z}{p_0} = -\left(1 + \frac{z^2}{a^2}\right)^{-1} \tag{1.52}$$

The principal shear stress is given by:

$$\tau_1 = \frac{1}{2}|\sigma_r - \sigma_\theta| \qquad (1.53)$$

And reaches a maximum value $\tau_1 = 0.31 p_0$ at a depth of *0.48a* below the surface.

Figure 1.5 shows the principal stress patterns beneath the point of first contact of two spheres. Due to the axis-symmetry of the problem the stresses in x and y directions are equal. The principal shear stress τ_1 achieves a maximum value of $\tau_1 = 0.31\ p_0$, at a depth of $0.48\ b$.

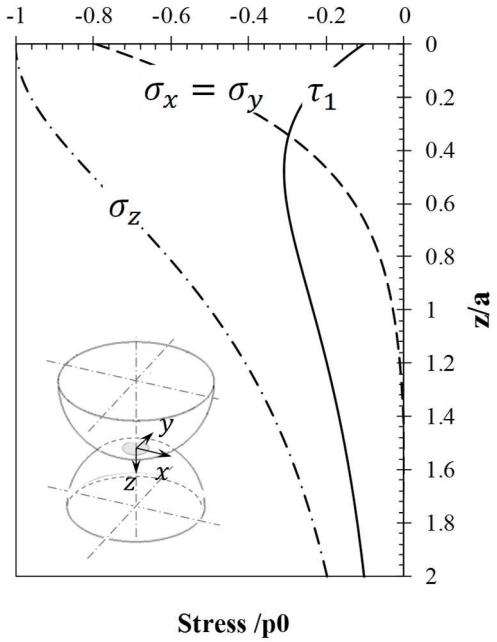

Figure 1.5 Principal shear stresses beneath the point of first contact of two spherical bodies.

1.1.2.1 Contact between cylinders

In the case of contact between cylinders, choosing the generatrix along which the first contact occurs as the *y*-axis of the coordinate system, the relative curvature is given by:

$$\frac{1}{R'} = \left(\frac{1}{R_{x1}} + \frac{1}{R_{x2}}\right) \qquad (1.54)$$

In this particular case the contact area assumes the shape of a strip with length l equal to the length of the cylinders and width *2a*, where

$$a = \sqrt{\frac{4PR'}{\pi l E'}} \tag{1.55}$$

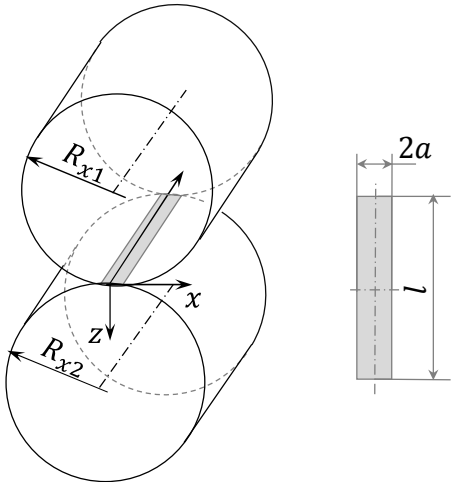

Figure 1.6 Contact between parallel cylinders

The pressure distribution is semi-elliptical throughout the width of the contact strip

$$p(x) = \frac{2P}{l\pi a}\sqrt{a^2 - x^2} \tag{1.56}$$

With a maximum value in correspondence of the origin *(x=0)*:

$$p_0 = \frac{2P}{l\pi a} = \sqrt{\frac{PE'}{\pi R'}} \tag{1.57}$$

The principal stresses along the z-axis, beneath the line of first contact, are given by:

$$\sigma_x = -\frac{p_0}{a}\left\{(a^2 + 2z^2)(a^2 + z^2)^{-\frac{1}{2}} - 2z\right\} \tag{1.58}$$

$$\sigma_z = -p_0 \cdot a\,(a^2 + z^2)^{-\frac{1}{2}} \tag{1.59}$$

$$\tau_1 = -\frac{p_0}{a}\left\{z - z^2(a^2 + z^2)^{-\frac{1}{2}}\right\} \tag{1.60}$$

Since typically the semi width of the contact area *a* is small compared with the length of the cylinders, the third component of stress can be found, recognizing the plain strain nature of the problem, as

$$\sigma_y = \nu(\sigma_x + \sigma_z) \qquad (1.61)$$

Figure 1.7 shows the principal stress patterns beneath the point of first contact of two cylinders. The principal shear stress τ_1 achieves a maximum value of $\tau_1 = 0.3\ p_0$, at a depth of $0.78\ a$.

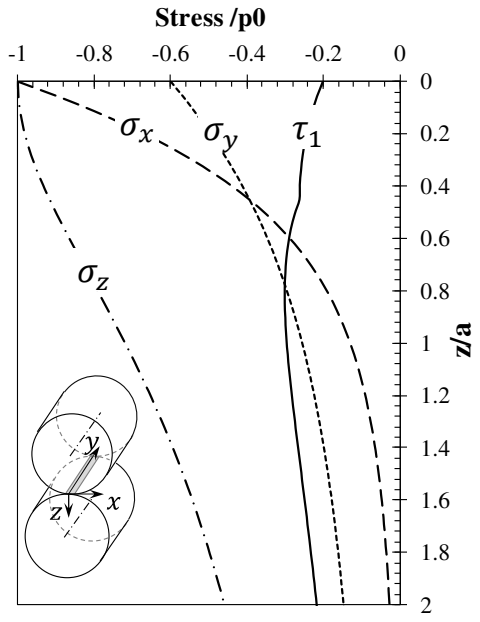

Figure 1.7 Principal shear stresses beneath the point of first contact of two cylindrical bodies.

Table 1.1 compendium of useful formulas for contact mechanics.

TYPE OF CONTACT	GEOMETRICAL AND MATERIAL PARAMETERS	CONTACT AREA DIMENSIONS	MAXIMUM PRESSURE	MAXIMUM SHEAR STRESS	PRINCIPAL STRESSES ALONG THE z-AXIS
Line contact between cylinders	$R' = \frac{R_{x1}R_{x2}}{R_{x1}+R_{x2}}$	$a = \sqrt{\frac{4FR'}{l\pi E'}}$ *a= half-width of the contact area*	$p_0 = \sqrt{\frac{E'F}{\pi R' l}}$	$\tau_{max} = 0.3\, p_0$ *Occurring at a depth:* $z = 0.78\, a$	$\frac{\sigma_x}{p_0} = -\frac{1}{a}\left\{(a^2+2z^2)(a^2+z^2)^{-\frac{1}{2}} - 2z\right\}$ $\frac{\sigma_z}{p_0} = -a\,(a^2+z^2)^{-\frac{1}{2}}$ $\frac{\sigma_y}{p_0} = \nu\left(\frac{\sigma_x}{p_0}+\frac{\sigma_z}{p_0}\right)$ $\frac{\tau_1}{p_0} = -\frac{1}{a}\left\{z - z^2(a^2+z^2)^{-\frac{1}{2}}\right\}$
Point contact between spheres	$R' = \frac{R_1R_2}{R_1+R_2}$	$a = \left(\frac{3FR'}{4E'}\right)^{\frac{1}{3}}$ *a= half-width of the contact area*	$p_0 = \left(\frac{6FE'^2}{\pi^3 R'^2}\right)^{\frac{1}{3}}$	$\tau_{max} = 0.31 p_0$ *Occurring at a depth:* $z = 0.48\, a$	$\frac{\sigma_x}{p_0} = \frac{\sigma_y}{p_0} = -(1+\nu)\left\{1 - \frac{z}{a}\tan^{-1}\left(\frac{a}{z}\right)\right\} + 1/2\left(1+\frac{z^2}{a^2}\right)^{-1}$ $\tau_1 = \frac{1}{2}\lvert\sigma_r - \sigma_\theta\rvert$
Point contact between general profiles*	$R^* = \left(\frac{1}{R_{x1}}+\frac{1}{R_{x2}}+\frac{1}{R_{y1}}+\frac{1}{R_{y2}}\right)^{-1}$ $\bar{\varepsilon} = 1.0003 + 0.5968\frac{R'_x}{R'_y}$ $\bar{\xi} = 1.5277 + 0.6023\ln\left(\frac{R'_x}{R'_y}\right)$ $\bar{k} = 1.0339\left(\frac{R'_x}{R'_y}\right)^{0.636}$ $R'_y > R'_x$	$a = \left(\frac{3\bar{k}^2\bar{\varepsilon}FR'}{\pi E'}\right)^{\frac{1}{3}}$ $b = \left(\frac{3\bar{\varepsilon}FR'}{\bar{k}\pi E'}\right)^{\frac{1}{3}}$ *a= major semi-axis of the contact ellipse* *b= minor semi-axis of the contact ellipse*	$p_0 = \frac{3F}{2\pi ab}$	$\tau_{max} \approx 0.3\, p_0$ *Occurring at a depth:* $z \approx \left(0.78 - \frac{0.3}{\bar{k}}\right)\cdot \mathrm{b}$	*See equations (**1.33**)-(**1.42**).* *The elliptic integrals can be solved numerically or found tabulated in mathematical handbooks.*

* For the case of general profiles the table reports the approximate formulas provided by [7]. For more accurate results refer to section 1.1.1.

The definition of $E' = \left(\frac{1-\nu_1^2}{E_1}+\frac{1-\nu_2^2}{E_2}\right)^{-1}$ holds for all cases.

1.1.3 Stress field within cylinders in contact in presence of frictions

The contact between cylinders with parallel axis is the most interesting from the viewpoint of gears investigations since, among the geometries for which analytical solutions are available, this case is the one which enables to resemble more closely the case of gears teeth in contact. Therefore, to understand the stress history to which a generic point in a cylinder is subjected during rolling contact, in this section is given an overlook of the stress field throughout the body. The solution is based on the formulas derived by Mc Ewen [8] which allow to account for the effect of friction. The equations for the determination of contact stresses presented in the above sections, in fact, have been derived for the case of absence of friction forces. However, in most cases, mechanical components are subjected to contacts with various degrees of relative rolling and sliding. Although friction forces affect the stress distribution in the components, if the elastic constants of the two bodies are the same, the tangential displacements are equal and opposite on the two surfaces and the distribution of normal pressure remains unaffected [9]. Therefore, in most practical cases the tangential stress distribution $q(x)$, estimated according to the Coulomb's law [3,9], is simply superimposed to the normal pressure $p(x)$.

$$|q(x)| = \mu|p(x)| \tag{1.62}$$

Or, in the case of two cylinders with parallel axis:

$$|q(x)| = \frac{2\mu P}{\pi l a}(a^2 - x^2)^{1/2} \tag{1.63}$$

Where μ is the coefficient of kinetic friction.

According to [8], the stresses at a generic point beneath the surface can be calculated as:

$$\sigma_x = -\frac{p_0}{a}\left\{m\left(1 + \frac{z^2 + n^2}{m^2 + n^2}\right) - 2z + \mu\left[2(x - n) + n\left(\frac{z^2 - m^2}{m^2 + n^2}\right)\right]\right\} \tag{1.64}$$

$$\sigma_y = \frac{2p_0\nu}{a}[m - z + \mu(x - n)] \tag{1.65}$$

$$\sigma_z = -\frac{p_0}{a}\left[m\left(1-\frac{z^2+n^2}{m^2+n^2}\right)-\mu n\left(\frac{z^2-m^2}{m^2+n^2}\right)\right] \quad (1.66)$$

$$\tau_{xz} = -\frac{p_0}{a}\left\{n\left(\frac{m^2-z^2}{m^2+n^2}\right)+\mu\left[m\left(1+\frac{z^2+n^2}{m^2+n^2}\right)-2z\right]\right\} \quad (1.67)$$

Where the parameters m and n are defined as functions of the coordinate of the point in the xz plane and of the semi-width of the contact strip a:

$$m = \frac{|z|}{z}\sqrt{\frac{1}{2}\{[(a^2-x^2+z^2)^2+4x^2z^2]^{1/2}+(a^2-x^2+z^2)\}} \quad (1.68)$$

$$n = \frac{|x|}{x}\cdot\sqrt{\frac{1}{2}\{[(a^2-x^2+z^2)^2+4x^2z^2]^{1/2}-(a^2-x^2+z^2)\}} \quad (1.69)$$

Let's consider first the contour plot of the stress field in absence of friction, generated in the contact between two parallel cylinders, which can be conveniently represented as the contact between a cylinder having radius equal to *R'* and a half plane (Figure 1.8). At the centre of the contact strip, in the symmetry plane, the principal directions coincide with the axes x, y, z of the reference system, therefore the shear stress τ_{xz} are null. Moving along the x axis, the principal directions rotate and a shear component appears. The variation of the stress components values along the x-axis at a given depth beneath the surfaces, represent the stress history to which each element of material at that depth is subjected during rolling contact. Note that the normal component of stresses are all compressive beneath the surface, therefore the alternating shear stresses τ_{xz} are deemed as responsible of the damaging mechanism in contact fatigue phenomena [6,10]. In frictionless contacts between cylinders the maximum value of τ_{xz} occurs at a depth of $0.5a$, where $\tau_{xz} = 0.25p_0$.

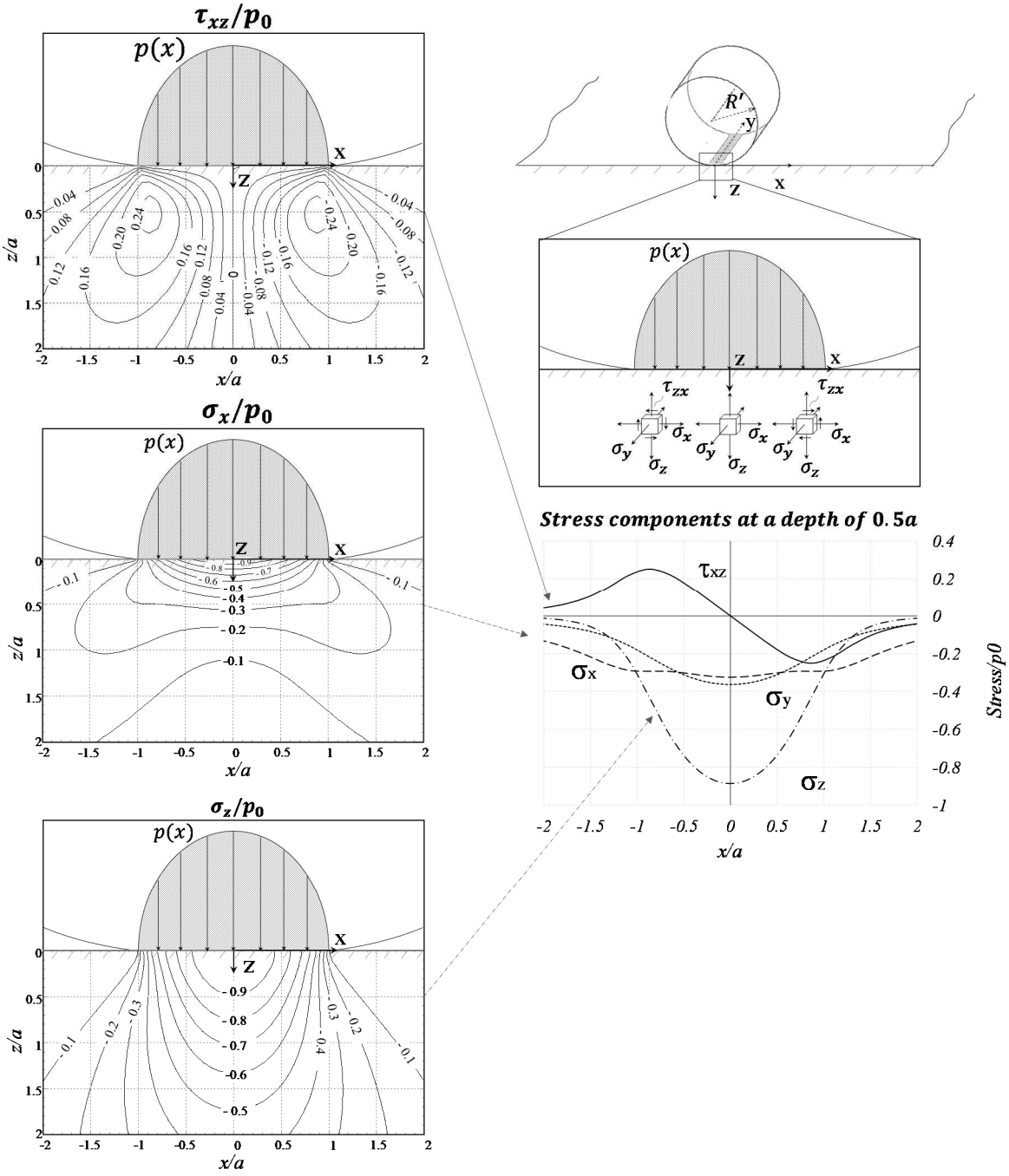

Figure 1.8 Stress field beneath the surface of a half plane in contact with a cylinder.

The contribution of friction is that of increasing the maximum value of the maximum principal shear stress and reduce the depth at which such value is achieved. Figure 1.9 shows a contour plot of the maximum principal shear stress τ_1 for different values of the friction coefficient.

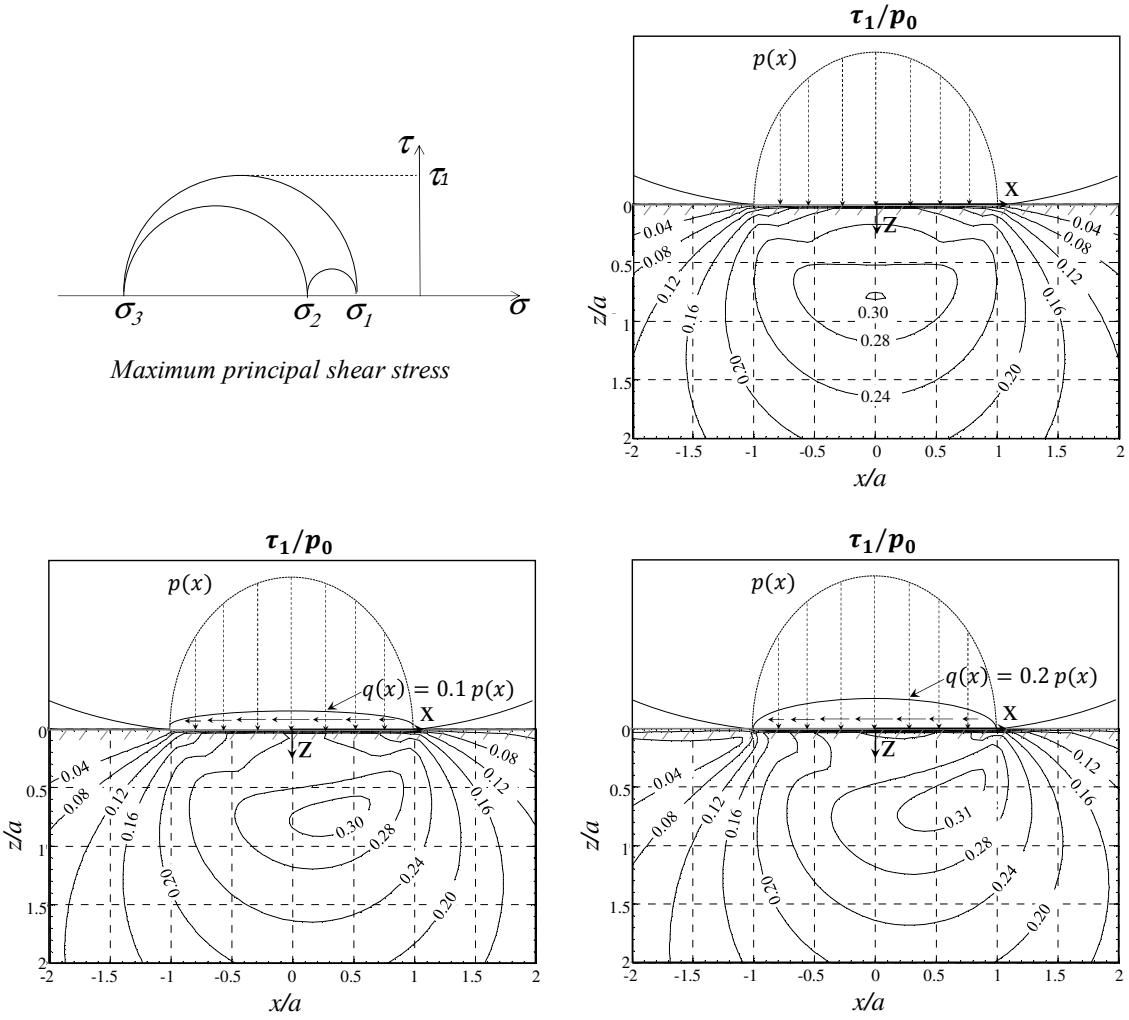

Figure 1.9 Contour plots of maximum principal shear stress beneath the surface of a half plane in contact with a cylinder considering friction coefficients μ=0, μ=0.1, μ=0.2.

1.1.4 Numeric calculation of contact stresses in case of complex geometries

In cases where the bodies are neither cylindrical nor solids of revolution, the calculation of contact stresses must be performed by means of a numeric algorithm. This paragraph describes a procedure that can be used in the case of a pair of surfaces which can be obtained by means of extrusion of a given profile. This is a case of practical relevance for gears since the working direction of the tool in hobbing processes is mainly directed along the gear axis. Therefore, any irregularity of the profile, due to defect or wear on the hob or to vibrations, generally reflects along the whole length of the tooth. This consideration holds also for the grinding operations and for the deviation of the profile due to wear occurring during regular operation of the gear.

On the contrary, other manufacturing or finishing operations such as skiving or shaving lead to furrows directed predominantly from the root toward the tip of the toot.

The following procedure leads to quite accurate results provide that the following hypothesis remain valid:

- absence of plastic deformations
- the bodies deform as elastic half spaces, or in other words the dimensions of the contact area smaller compared to the local curvature radii of the surface

In such conditions, the contact between the two bodies can be regarded as the contact between a rigid half plane and a body having reduced Young's modulus *E'* and which profile is given by the sum of the initial gaps between the original surfaces (Figure 1.10).

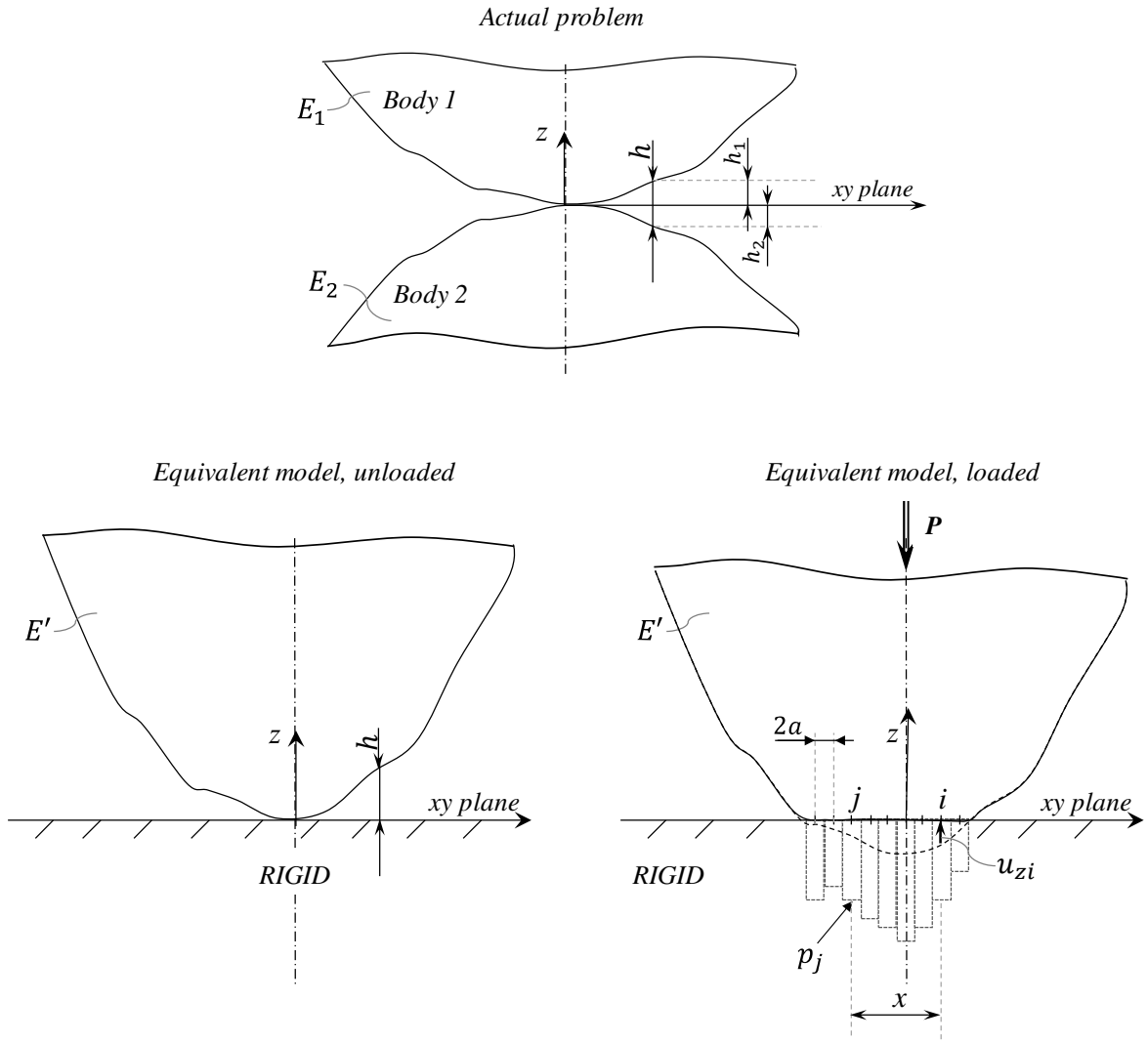

Figure 1.10 Schematic representation of the construction of the model for the numerical solution of a bidimensional contact problem.

The surface is discretized into a finite number of elements and an elementary pressure distribution is applied upon each element. Several different pressure elements are possible, such as concentrated forces, uniform pressure distributions or triangular pressure distribution. To simplify the implementation of the algorithm it is convenient to use equally spaced elements. The normal displacement u_z at any point of the surface caused by a single pressure element with any of the mentioned distribution can be calculated by means of analytical formulas available in contact mechanics textbook [3,11]. In the simplest case of uniform pressure elements, as an example, the normal displacement of node *i* caused by a load per unit length $\mathrm{P_j}$, applied to the node *j*, is given by :

$$(u_z)_i = -\frac{1}{E'}\mathrm{p_j}\left[(\mathrm{x}+\mathrm{a})\ln\left(\frac{\mathrm{x}+\mathrm{a}}{\mathrm{a}}\right)^2 - (\mathrm{x}-\mathrm{a})\ln\left(\frac{\mathrm{x}-\mathrm{a}}{\mathrm{a}}\right)^2\right] + \mathrm{const} \qquad (1.70)$$

Where the term *a* indicates the semi-distance between contiguous elements, while *x* is the distance which separates the nodes *i* and *j*.

Thus, being the superposition principle valid in the linear elastic field, the total displacement of the *i*-node caused by the sum of pressure elements *p* applied to the *j*-nodes can be expressed in the form

$$(u)_i = \sum_{j=1}^{n} C_{ij}p_j \qquad (1.71)$$

Where the elements of the matrix C_{ij} are defined as “influence coefficients” and depend on the choosen pressure distribution. As an example, for uniform pressure distributions loads:

$$C_{ij}(k) = \frac{u_{zi}}{p_j} = -\frac{\mathrm{a}}{\mathrm{E}'}[(\mathrm{k}+1)\ln(\mathrm{k}+1)^2 - (\mathrm{k}-1)\ln(\mathrm{k}-1)^2] + const \qquad (1.72)$$

Where $k = i - j$.

The constant can be vanished by referring displacements to an arbitrary datum, for instance by subtracting a row of the matrix C_{ij} (e.g. the one relevant to the node of first contact) to all the other rows. This operation introduces a singularity which prevents the matrix $\mathrm{C_{ij}}$ to be invertible. Therefore. the null row is eliminated and substituted in equation (1.71) the

equilibrion condition given by the equality between the external load and the sum of all the pressure elements. In the case of uniform pressure distributions:

$$\begin{pmatrix} u_0 \\ \vdots \\ P \\ \vdots \\ u_n \end{pmatrix} = \begin{bmatrix} C_{1,1} & \cdots & \cdots & \cdots & C_{1,n} \\ \vdots & & & & \vdots \\ a & \cdots & \cdots & \cdots & a \\ \vdots & & & & \vdots \\ C_{n,1} & \cdots & \cdots & \cdots & C_{n,n} \end{bmatrix} \begin{pmatrix} p_0 \\ \vdots \\ p_n \end{pmatrix} \quad (1.73)$$

Finally, the value of pressure elements p_j is determined by the following iterative procedure:

- A plausible value for the approaching of the two bodies after deformation is assumed
- From the condition of non-penetration of the surfaces a set of displacements is defined for the nodes of the surfaces
- The values of the pressure elements on each node are calculated from the corresponding displacements by inversion of the influence coefficients matrix C_{ij}:

$$p_j = C_{ij}^{-1} u_i \quad (1.74)$$

- If at the first iteration the assumed contact area is greater than the real one, some pressure element in the resulting vector $(p)_j$ will have negative value. Such element will be excluded by the contact area for the subsequent iteration. The convergence will be obtained when no negative elements are be found after an iteration.

The choice of pressure distribution may affect the convergence performance of the algorithm. As an example, Figure 1.11 shows that triangular (right) pressure elements allow to resemble a parabolic pressure distribution better than uniform (left) pressure elements, thus allowing the use of a coarser mesh. Once the value of pressures are note, the stress field inside the body can be easily calculated by superimposition of the known stress fields generated by each element, which are expressed by analytical formulas in function of the *xz* coordinates [3].

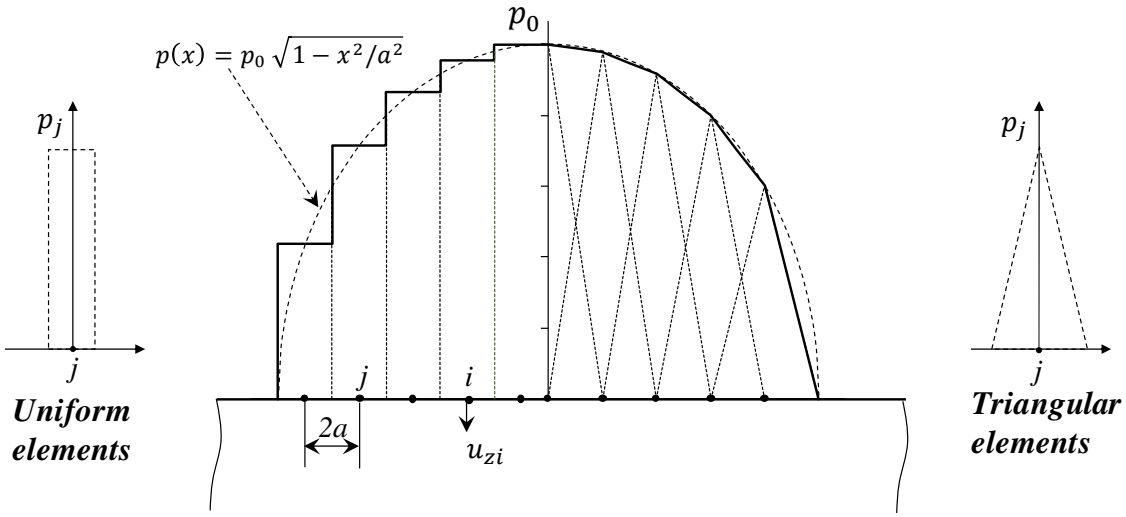

Figure 1.11 Example of representation of a parabolic pressure distribution (dashed line) with uniform (left) and triangular (right) pressure elements

The above method or similar approaches have been used by various authors to compute the contact stresses between rough surfaces [12–15]. Results of these calculation are necessarily qualitative since several aspects such as interlocking between asperities, plastic deformations and stick-slip effects are of course neglected. Moreover, the hypothesis of elastic half-space may be forced due to the small curvature radii of the asperity crests and the non-parallelism of the surface of contacts with the x-axis. However, despite the unavoidable approximations the outcomes provide a fundamental information, evidencing that the mutual interaction among asperities generate an intense perturbation of the nominal stress field that is however limited to a depth comparable to the roughness height, beyond which the stress components converge to the smooth solution defined by the nominal contact formulas. This result points out the fundamental importance of roughness and justify why, in well lubricated contact where the asperities are separated by the fluid, subsurface damages may precede surface originated ones, while in applications where the lubricant film is not capable to provide an adequate separation between the bodies, surface initiated cracks are almost always the root cause of contact fatigue.

1.2 Principles of elastohydrodynamic lubrication

The intense stress cycles generated by the interaction among the roughness asperities of rolling bodies are deleterious for the surface integrity and can be prevented or at least dampened only by means of an adequate lubrication. The analysis of the regime of lubrication in rolling components is usually dealt by the theory of elastohydrodynamic lubrication. In fact, in contacts between non-conformal surfaces, the elastic deformation of the bodies have a primary role in the formation of a lubricant film [16], which is influenced by hydrodynamic aspects and by the characteristic of the fluid as well. More in detail, in lubricated rolling contacts, the fluid is dragged in the contact area by the peripheral speed of the surfaces. Then, since oils are piezo-viscous fluids, the viscosity of the lubricant suddenly increase to extremely high values due to the pressure generated by the surface. The resulting lubricant film, under some circumstances, may be able to separate the bodies preventing contact among the crests of the roughness. A widely used parameter to predict the effectiveness of the lubrication regime in providing safe operation of the components, is the so-called λ-ratio, which is defined as the ratio between the film thickness, h_0 and the composite surface roughness:

$$\lambda = \frac{h_0}{0.5 \cdot (R_{a1} + R_{a2})} \qquad (1.75)$$

The problem of determining the thickness of the lubricant film is not straightforward, since the shape of the contact geometry, and the pressure and viscosity of the fluid, reciprocally affect each other. The issue is even harder in the case of point contacts where side squeezing of the lubricant outside the contact area inevitably occur. Details about the basics of the theory of elastohydrodynamics and the derivation of the fundamental equations are beyond the scope of this work and can be found elsewhere [11,16–18], however the structure of the formula for the calculation of the film thickness presents some interesting aspects which will be briefly commented in the next section.

1.2.1 Calculation of the specific film thickness

Consider the lubricated rolling contact between two parallel cylinders: when a highly viscous film of lubricant separates the surfaces, the effective contact area became slightly larger as

compared to the value predicted by equation (1.55) and the resulting pressure at the sides will be lower than the nominal Hertzian distribution. In the middle of the contact area the surfaces are substantially parallel, and the dimension of the gap, denoted by h_c in Figure 1.12 is defined as "central film thickness". The drop in the lubricant viscosity at the outlet of the contact area allows a partial elastic recovery of the surfaces with a consequent constriction of the gap to a dimension h_0 denoted as "minimum film thickness". To preserve the continuity of flow through the meatus, the lubricant pressure raises in the zone immediately preceding the necking and, when an equilibrium condition is achieved, the pressure distribution in the film approaches a shape which is qualitatively represented in Figure 1.12. Approximate analytical formula for the estimation of the position and magnitude of the pressure spike in the vicinity of the necking, called Petrusevich spike, can be found in [19].

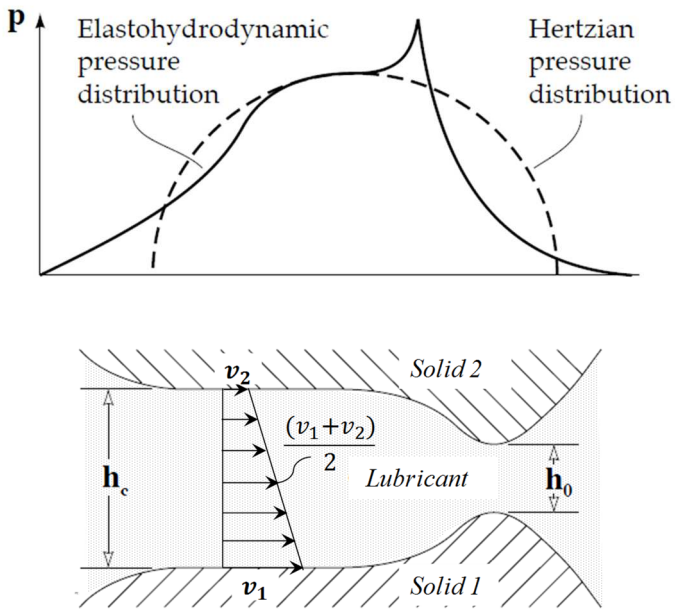

Figure 1.12 Qualitative sketch of the lubricant film and pressure distribution in the contact area. (adapted from [16])

Despite the high complexity of the problem, analytical formula for the calculation of the minimum film thickness, providing quite accurate solution, were developed by Dowson and Higginson [20] for line contact and by Hamrock and Dowson [21] for elliptical contact. The minimum film thickness is expressed as function of the ellipticity of the contact area and of three adimensional parameters related to load (W), speed (U) and material and lubricant properties (E) respectively. For line contacts:

$$\frac{h_0}{R'} = 1.6\, G^{0.6}\, U^{0.7}\, W^{-0.13} \qquad (1.76)$$

While, for elliptical contacts:

$$\frac{h_0}{R'} = 2.69\, G^{0.53}\, U^{0.67}\, W^{-0.067}\, (1 - 0.61\, e^{-0.73k}) \qquad (1.77)$$

Where the adimensional parameters are defined as follows:

- *Material parameter*: $G = \alpha E'$, where α is the viscosity-pressure coefficient $[Pa^{-1}]$ of the lubricant
- *Speed parameter*: $G = \frac{(v_1+v_2)}{2}\frac{\eta_0}{E'R'}$, where η_0 is the dynamic viscosity of the lubricant at atmospheric pressure $[Pas]$
- *Load parameter*: $W = \left(\frac{P}{lE'R'}\right)$, for line contact and $W = \left(\frac{P}{E'R'^2}\right)$, for elliptical contacts
- *Ellipticity parameter*: $k = \frac{a}{b}$, note that in this case *a* is the half width of the contact ellipse in the direction of motion and *b* is the half width in the transverse direction.

Looking at the exponents of equations (1.76) and (1.77), the first quite surprising consideration, is that the film thickness depends much more on the average peripheral speed of the surfaces and on the material and lubricant characteristic, rather than on the applied load. Moreover, high values of k in equation (1.77), denote large contact areas in the transversal direction with respect to the motion and therefore correspond to higher film thickness since the lateral squeezing of lubricant is limited. The formula is deemed to be valid for all the possible values of k in the range $0.1 \leq k \leq \infty$. Finally, it is to be noted that the dynamic viscosity of the lubricant η_0, as well as the viscosity-pressure coefficient α, are affected by the lubricant temperature in the contact area, which in turns, may depend on several properties of the mating bodies (such as geometry, elastic modulus, density and conductivity) and of the operating conditions (such as speeds, load and friction coefficient).

The approach discussed in this section is universally accepted to assess the condition of safe operation of the contact surfaces in rolling and sliding mechanical components, such as gears and bearings, and constitute the basis of the calculation method against micropitting in gears, proposed by the ISO technical report 15144 [22]. However, the formation of a fully developed

elastohydrodynamic film require sufficiently high surface speeds, which are practically never achieved in the gear problems analysed within the scope of this work.

1.3 Local operating conditions in gears teeth

A basic knowledge of some fundamental principles of gear functioning is essential to understand how contact fatigue phenomena manifest on teeth flanks and why craters are more prone to form in some areas of the tooth. Since the major influencing parameters affecting the onset and the type of Rolling Contact Fatigue (RCF) failure in mechanical components are the contact pressure and the rolling and sliding speed, the next sections report a brief explanation of how such quantities may be estimated for the simple case of involute spur gears.

1.3.1 Contact stress in involute spur gears

The contact pressure is the major parameter affecting macropitting phenomena. The main peculiarity of involute spur gears is that, if friction forces are neglected, during the whole contact path the load acts on a line directed along the common tangent line to the base circumferences of the meshing gears (the line of action), which is coincident with the involute generatrix and therefore normal to the teeth profiles. Therefore, to estimate the contact pressure, gears teeth are usually assimilated to a pair of cylinders in contact along a generatrix (Figure 1.13). The radius of each cylinder corresponds to the segment of line of action between the tangent point to the base circle and the contact point P.

When the load is carried by only one pair of teeth, such case can be treated according to the Hertz theory of contact between elastic solids. As the load increase, the surfaces of the cylinders flatten resulting in a rectangular contact area. The contact pressure, usually denoted with the symbol σ_H in the case of gears, assumes a semi-elliptical distribution with a maximum value given by:

$$\sigma_{H0} = \sqrt{\frac{E' F_n}{\pi \rho_{red} b}} \tag{1.78}$$

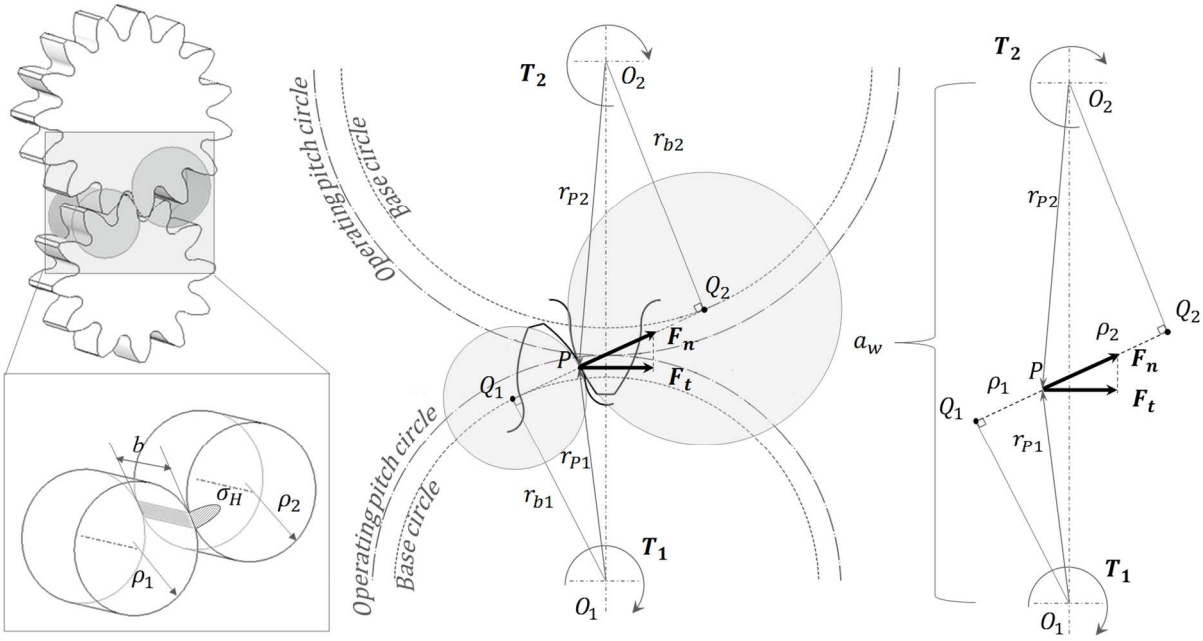

Figure 1.13: Modeling of gears teeth by means of cylinders in contact.

Where F_n is the normal force on the tooth flanks, b is the face width, E' is the reduced Young's modulus (E'≈113187 N/mm² when both gears are made of steel) and ρ_{red} is the reduced curvature radius, which is given by:

$$\rho_{red} = \frac{1}{\frac{1}{\rho_1} + \frac{1}{\rho_2}} \tag{1.79}$$

The local curvature radii of the involute profile ρ_1 and ρ_2 can be calculated for any point P given the base radius and the radius relevant to the considered point.

$$\rho_{1,2} = \sqrt{r_{P1,2}^2 - r_{b1,2}^2} \tag{1.80}$$

It is worth noting that during the first and last part of the meshing period part of the load is carried by the previous and subsequent pair of teeth respectively.

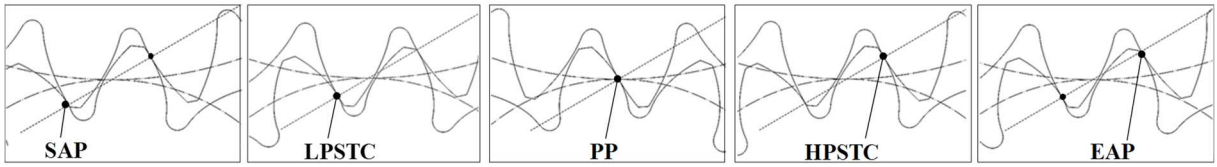

Figure 1.14: Sequence of meshing.

Referring to the sequence of meshing of Figure 1.14:

- The Start Active Profile (SAP) is the point (near the root circle) where the contact starts
- The Lowest Point of Single Tooth pair Contact (LPSTC) is the point where the force starts to be transmitted by only one pair of teeth
- The Pitch Point (PP) is the common tangent point of the two reference circles
- The Highest Point of Single Tooth pair Contact (HPSTC) is the last point where the force is transmitted by only one pair of teeth
- The End of Active Profile (EAP) is the point where the contact ends.

Although the normal force F_n is constant within the period where only a couple of teeth supports the whole load, the point corresponding to the LPSTC of the pinion gear usually experiences the highest value of pressure being the one with the lowest value of ρ_{red}.

1.3.2 Rolling and sliding speed in gears

Gears are a typical example of components operating in rolling-sliding contact conditions.

In rolling contacts, the speeds of the mating surfaces have a primary role in the tribological performances of the system, affecting aspects such as the thickness of the lubricant film, its temperature and the friction coefficient. To understand the influence of the kinematic of mating surfaces in wear and contact fatigue phenomena it is advisable to introduce the concept of Slide-to-Roll Ratio (SRR). As in the previous section, for the sake of simplicity, we can define the SRR taking advantage from the analogy between gears teeth and cylinders in contact. Referring to Figure 1.15, the rolling speed, v_R is defined as the mean peripheral speed of the surfaces. This quantity is often termed also as “entraining speed” because it represents the mean speed of the lubricant film dragged into the contact area by the rolling surfaces. Then, the relative

velocity of the counterface evaluated at the contact point for each cylinder is defined as sliding speed. The ratio between rolling and sliding speed is addressed as Slide-to-Roll Ratio (SRR).

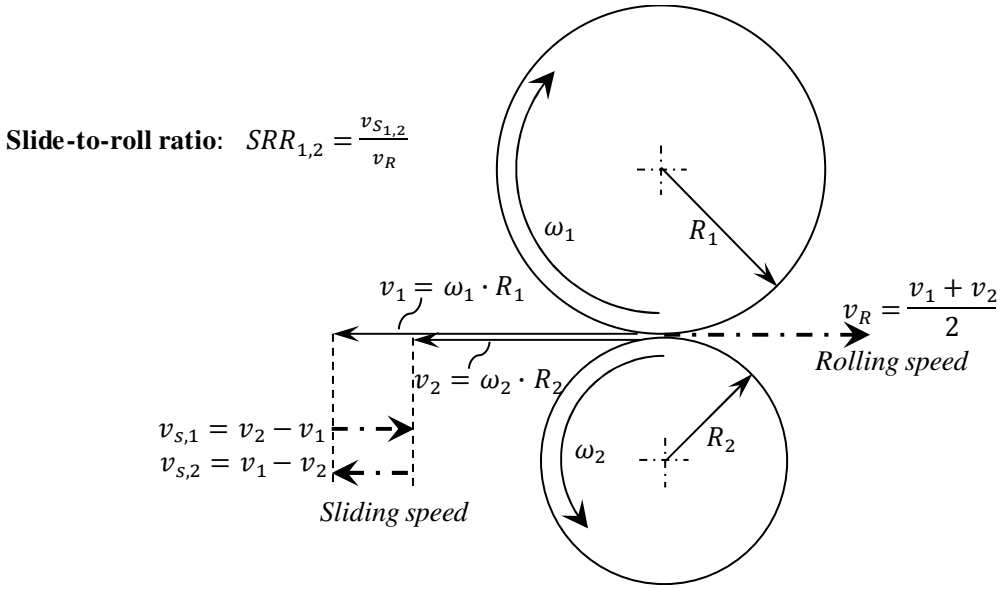

Figure 1.15: Definition of Slide-to-Roll Ratio.

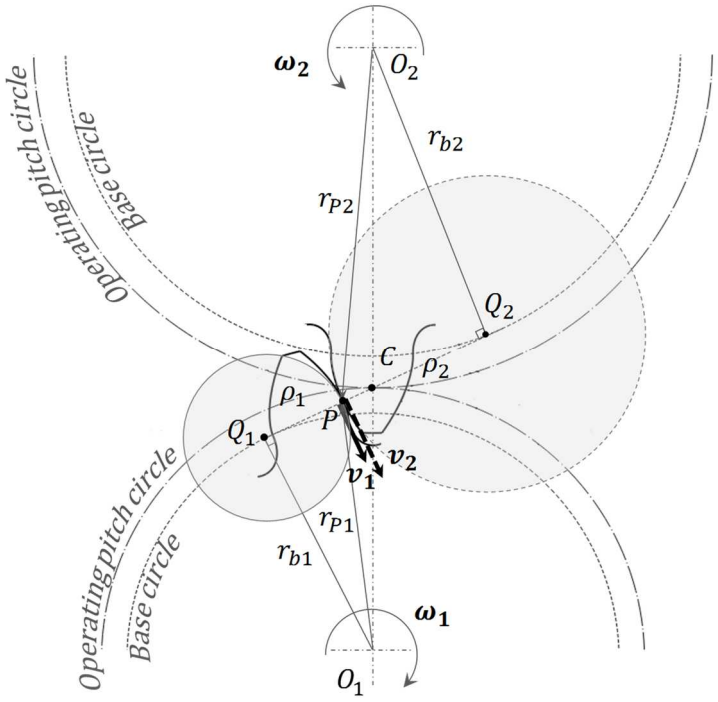

Figure 1.16: Peripheral speeds in gears teeth.

Figure 1.16 shows the peripheral speeds at the point of contact of a gears teeth pair. Considering the point P as belonging to the surface of gear 1:

$$v_1 = \omega_1 \cdot \rho_1 \tag{1.81}$$

Conversely, the speed at the surface of gear 2 is given by:

$$v_2 = \omega_2 \cdot \rho_2 = \omega_1 \cdot \frac{z_1}{z_2} \cdot \rho_2 \tag{1.82}$$

Therefore, the slide-to-roll ratio is given by:

$$SRR_{1,2} = \frac{\pm 2(v_1 - v_2)}{v_1 + v_2} = \frac{2\left(\rho_1 - \frac{z_1}{z_2}\rho_2\right)}{\left(\rho_1 + \frac{z_1}{z_2}\rho_2\right)} \tag{1.83}$$

Where the sign + and – refer to the SRR as calculated for gear 1 and 2 respectively. Note that equation (1.83) indicates that the slide-to-roll ratio in the tooth flank of gear 1 is negative for $\frac{\rho_1}{\rho_2} < \frac{z_1}{z_2}$. On the contrary, referring to gear 2 the SRR is negative for $\frac{\rho_1}{\rho_2} > \frac{z_1}{z_2}$. Since triangles O_1CQ_1 and O_2CQ_2 are similar, and segments O_1C and O_2C are in the ratio $\frac{z_1}{z_2}$ being the operating pitch diameters of the two gears, it may be easily demonstrated that the condition $\frac{\rho_1}{\rho_2} = \frac{z_1}{z_2}$, for which the SRR value vanishes, occurs when $P \equiv C$, in correspondence of the pitch point. Therefore, in the dedendum of both the driver and driven gears the direction of sliding of the counterface is opposite to the motion of the contact, as shown in Figure 1.17.

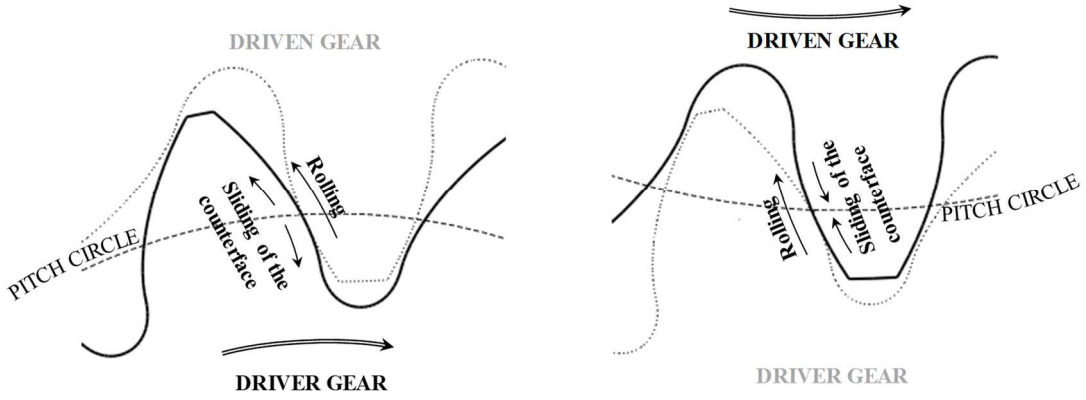

Figure 1.17: Sliding and rolling speed in gears teeth.

Chapter 2

PITTING IN GEARS TEETH

In power transmission systems for off-highway vehicles, the sun gears located in the planetary gear set in the wheel hub of axles are the most crucial components with respect to pitting failures (Figure 2.1). Being located in the final stage of the transmission, in fact, sun gears are subjected to high loads despite their small dimensions which implies small curvature radii of the flanks and consequently high contact pressure. Moreover, although the frequency of load cycles in sun gears is high due to the concurrent meshing with three or four planet gears, the speed of rotation is relatively low, therefore the capability of teeth surfaces to drag oil film in the contact area are limited resulting in a lubricant film inadequate to fully separate the mating surfaces.

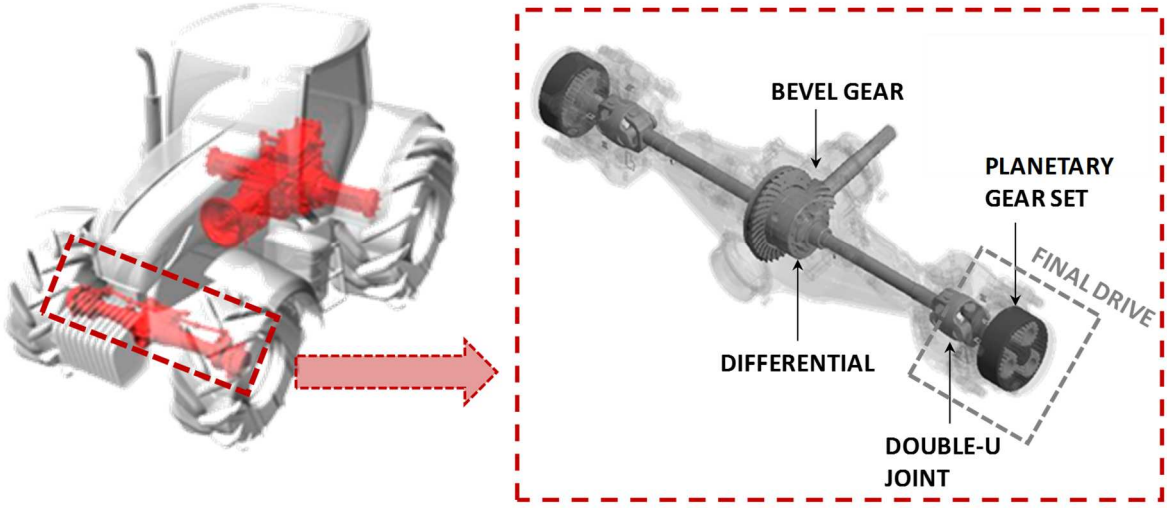

Figure 2.1 Scheme of a steering axle for agricultural applications

In this chapter contact fatigue phenomena will be treated in detail with reference to their manifestation in case hardened gears. Particularly, the damaging mechanisms related to pitting failures of sun gears during bench tests performed by Carraro S.p.a. on the complete axles, will be documented by pictures and commented in the light of a review of the existing literature.

2.1 Origin of rolling contact fatigue in gears

Referring to gears, pitting may be originated by subsurface cracks only in presence of high speeds, very smooth surfaces and optimal lubricating conditions [10,23,24]. In such cases, contact between asperities is prevented by the lubricant and the formation of subsurface cracks in correspondence of defects or inclusions may occur earlier than surface originated damages. However, in gears operation the thickness of the lubrication film is often not adequate to keep roughness asperities separated and most of the contact fatigue failures originate by the surface [25]. The damaging mechanism initiate with the plastic deformation of the surface layer, in the direction of sliding of the counterface. The crests of asperities are flattened giving to the surface a mirrorlike appearance (Figure 2.2).

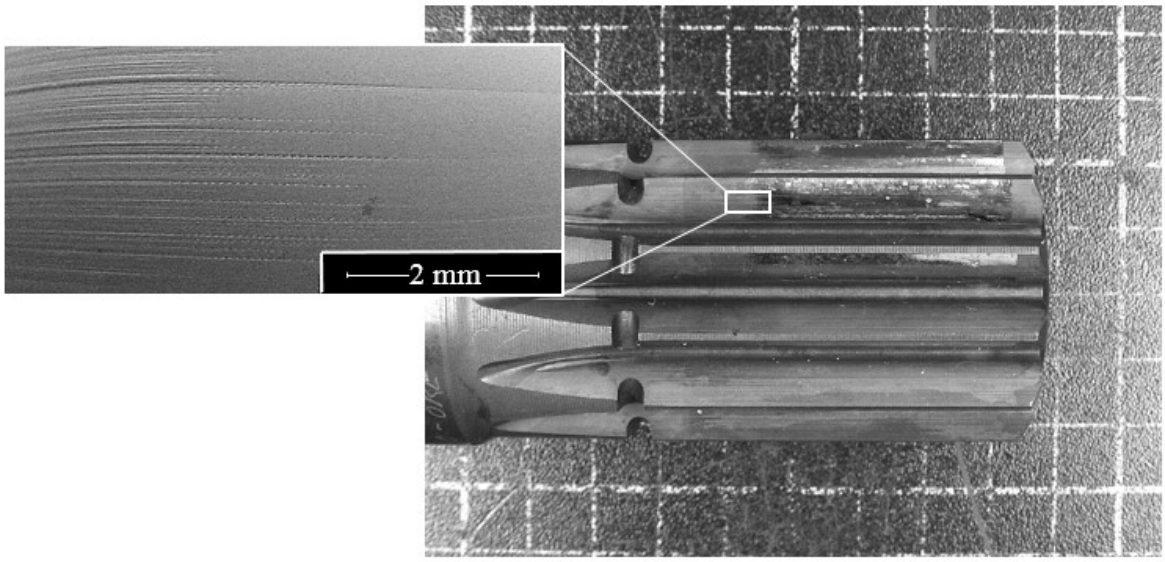

Figure 2.2 Polished area due to flattening of asperities. The detail shows the transition between the mirror-like surface and the part of the tooth that still shows grinding furrows.

Once the ductility of the material is exhausted cracks originate with shallow angles to the surface in the opposite direction with respect to friction forces, namely toward the pitch line in driver gears and toward the tip and root of the tooth in driven gears (Figure 2.3 and Figure 2.4).

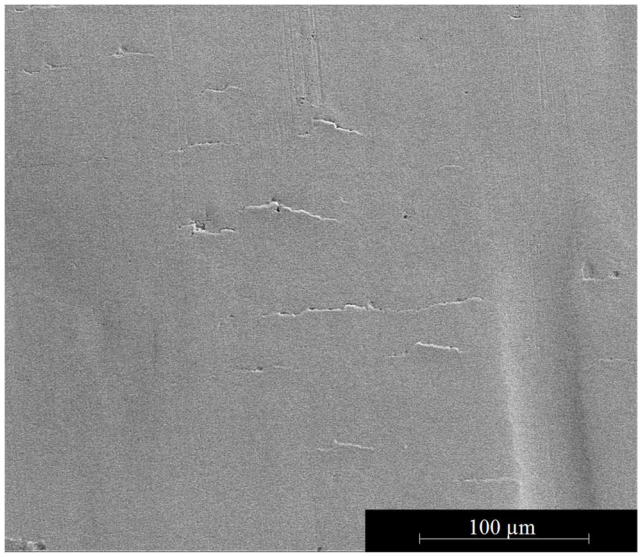

Figure 2.3 SEM image of surface distress cracks observed on the flank of the case hardened gear of Figure 2.2, in the area polished by running-in.

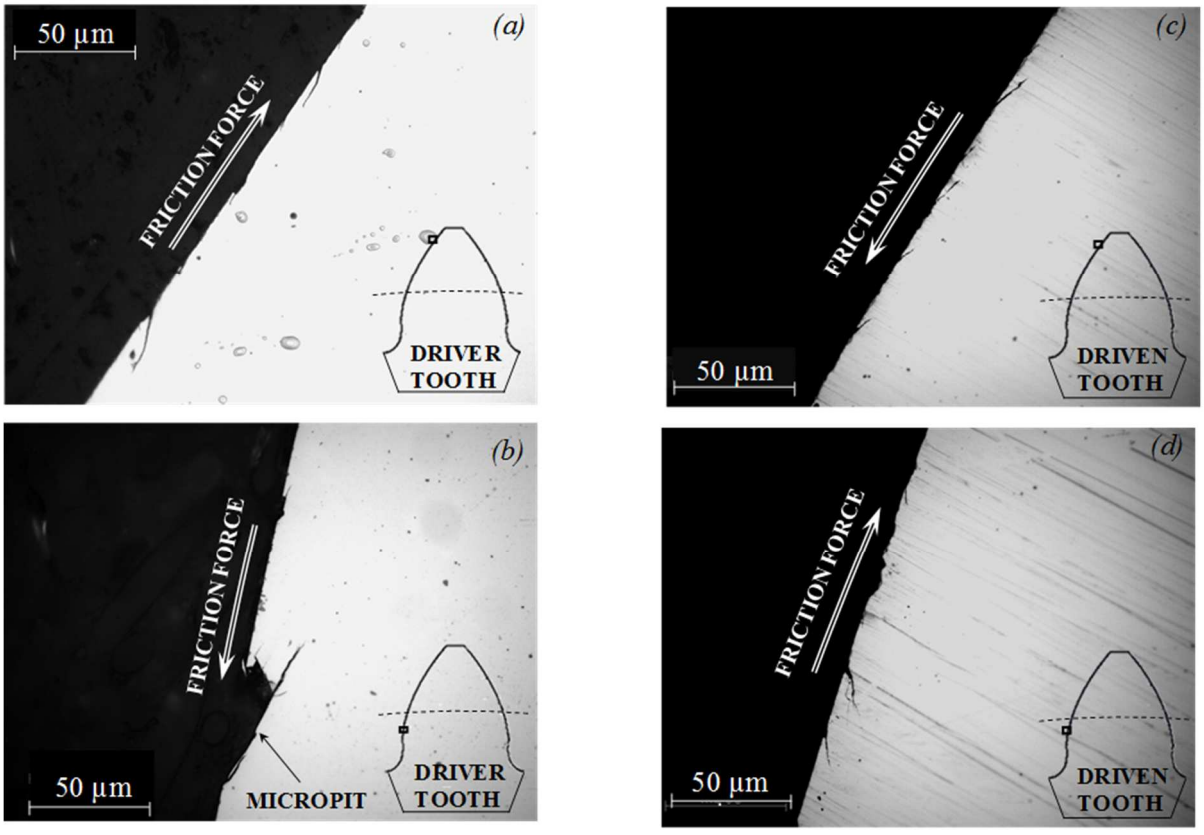

Figure 2.4: Surface cracks observed in: (a) the addendum of a driver gear, (b) the dedendum of a driver gear, (c) the addendum of a driven gear, (d) the dedendum of a driven gear.

The thickness of the deformed layer depends on the ductility of the material. Soft steels such as those adopted in railway rails, may be interested by plasticity up to a depth comparable with

the width of the contact area, while in case hardened steels usually adopted in gears manufacturing for power transmission systems, plastic deformations typically remain confined in the roughness scale [25,26].

Contact fatigue phenomena usually occur at first in the pinion gear, which is subjected to a higher number of contact cycles as compared to the wheel. Particularly, the dedendum of teeth represents the most favourable location for craters formation. It may be argued that this is due to the higher contact pressure to which the tooth is subjected in the dedendum, due to the lower values of ρ_{red}, as specified in section 1.3.1 and shown in Figure 2.5. However, the main reason of the greater likelihood of contact fatigue in gears dedendum is probably related to the presence of negative values of the SRR rather than to the value of contact pressure. The influence of SRR in contact fatigue phenomena is treated in detail in the next section.

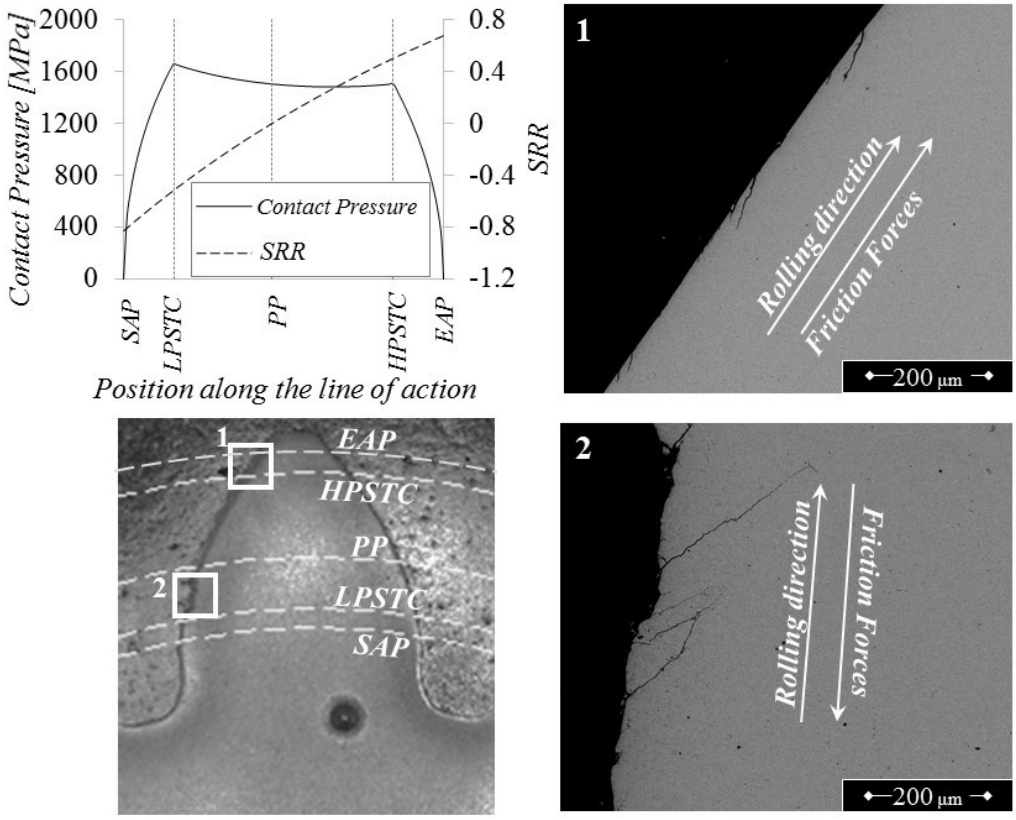

Figure 2.5: Contact pressure, Slide-to-Roll Ratio and crack morphology in a pinion gear tooth.

2.1.1 Effect of the slide to roll ratio

SRR is the major influencing factor in all contact fatigue failures related to direct contact with asperities crests, particularly surface distress, micropitting and scuffing. Nevertheless, since any surface defect, including scuffing scratches and micropits, can act as stress raiser, and promote the further propagation of cracks, the rolling and sliding behaviour of the surfaces is of primary importance also for pressure-related phenomena such as macropitting. Based on the current knowledge, it may be argued that SRR would affect both crack initiation and propagation phases. Referring to crack initiation, it has been already mentioned how the direction of sliding speed may affect the direction of crack's origin. The reasons behind the foremost importance in cracks initiation mechanisms attributed to SRR can be summarized as follows:

- The entraining speed is the main parameter relating to the thickness of the lubricant film. Higher entraining speeds correspond to greater thickness and therefore to a lower probability metal-to-metal contacts
- Higher sliding speed result in increasing surfaces and lubricant temperatures and consequently in a reduction of the fluid viscosity which in turn affects the capacity of the film to keep the surfaces separated
- Negative slide to roll ratios result in an increased number of asperity interaction

The last point of the list deserves a further insight. Consider the contact between two rough surfaces: the mutual interaction among crests and valleys of the asperities result in a very complex stress state interesting the surface layers up to a depth of few tens of microns, below which the stress field converges to the Hertzian solution [12]. If sliding occurs, each near-surface element is subjected to repetitive random stress cycles due to the contacts with the asperities of the counterface [15]. Extending this concept to the case of rolling contacts, clearly the slower surface (the one with negative SRR) is unfavoured because within the time interval required by an elementary sector of the surface to cross the contact area, the same area is traversed by a greater sector of the faster surface. Assuming that the linear density of roughness asperities is the same for both the surfaces a smaller number of asperities of the slower surface will interact with a higher number of asperities of the faster surface [15,27].

The problem of crack propagation is less straightforward. As shown in chapter 1, in fact, in rolling contact fatigue cracks develop in a stress field where all the principal components of stress are nominally compressive and therefore not prone to promote crack propagation. Based on this observation, for several years the alternating shear stresses were considered as the main

responsible for the entire damaging process. However, already in 1935 Way proposed that the pressure of the lubricant, forced inside the crack by the contact load, might promote crack propagation [28]. This mechanism, addressed as *hydraulic crack propagation*, would possibly explain why cracks propagate preferentially in surfaces characterized by a negative slide to roll ratio. If friction forces act in opposite direction with respect to the motion of the contact in fact, cracks mouth are opened before the passage of the counterface and lubricant is allowed to leak into the cracks (Figure 2.6), being subsequently pressurized by the contact with the mating surface and thus promoting mode I propagation. Such hypothesis was widely supported by various authors both with numerical models [29,30] and experiments [31,32], and still meet broad consensus in the literature [33–37]. Other authors, following the model of fluid *entrapment* and pressurization proposed by Bower [38], suggested that the greater likelihood of propagating cracks in negative SRR surfaces could lie in the fact that friction forces produce cracks oriented according to the motion of the contact. In such conditions, the lubricant could be entrapped into the crack during the passage of the contact and subsequently squeezed toward the crack tip as shown in figure Figure 2.6. The mechanisms of entrapment and pressurization, may occur only if the contact moves from the crack mouth toward the crack tip, conversely if the crack was generated in the opposite direction, the compression of the surface over the crack tip would cause the lubricant to leak out from the mouth before its closure. To further remark the role of lubricant as a crack propagation driver, it has been also postulated that it could also help in preventing crack closure and interlocking by keeping crack's faces separated and reducing the friction coefficient [39] and thus promoting propagation under shear mode. Bidimensional and three-dimensional fracture mechanics analysis of surface cracks performed since the 90's seem to converge to the hypothesis that cracks initially grow under shear mode until, once a critical length (usually comparable with the semi-width of the Herzian contact) is reached, the influence of lubricant pressure operate to enhance mode I stress intensity factors causing further propagation or branching [10,30,37,40].

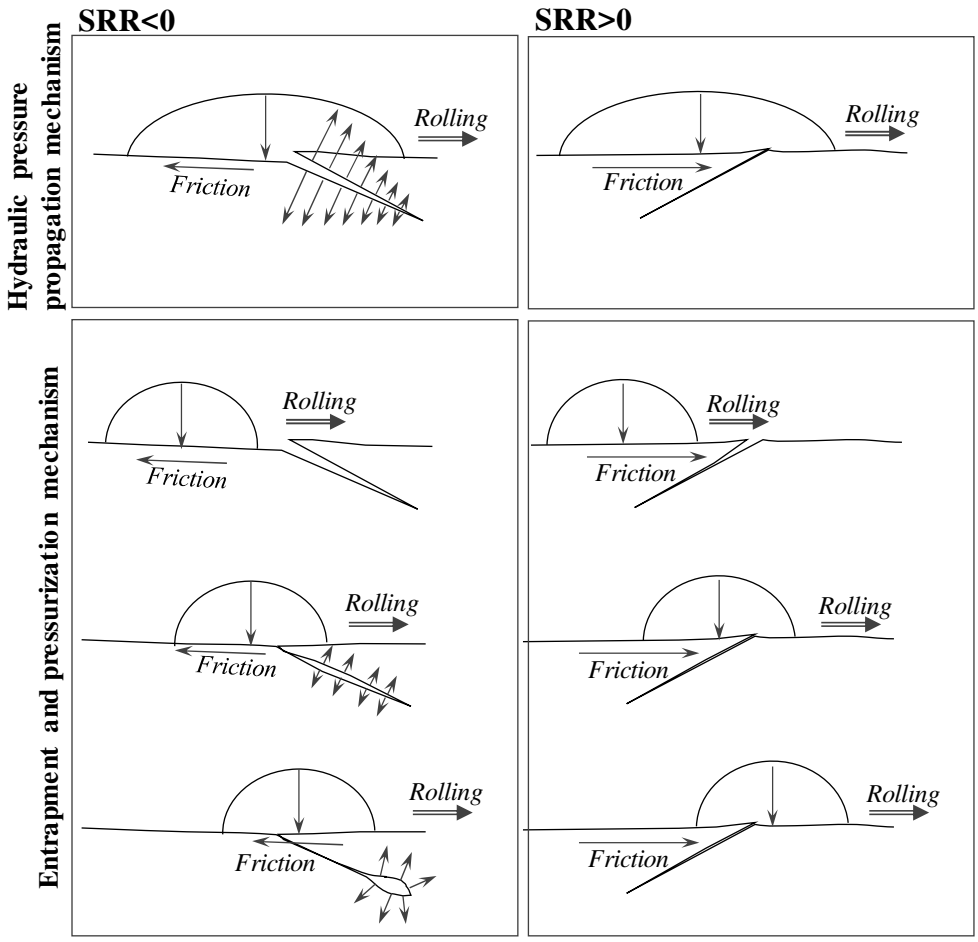

Figure 2.6 Scheme of the hydraulic propagation mechanism and of the entrapment mechanism proposed by Bower

From the viewpoint of fracture mechanics, theoretical models which do not account for the presence of lubricant cannot account for the influence of the SRR since they result in predicted cycles of stress intensity independent from the direction of the load motion as well as of surface traction [38]. On the other hand, someone argued that contact fatigue damages are commonly observed also in railways where a fluid is present at most in the form of rainwater [25]. Moreover, it is widely reported in the literature that worse endurance performances are obtained for increasing SRRs in a wide range. This observation is not compatible with a mechanism related solely to friction, since the friction coefficient increases with the SRR only for very low values of the latter [15]. In this work, macropits were experimentally observed (although rarely) also on surfaces with positive SRR (see section 2.2.2.1), suggesting that, at least in some circumstances, the main driving mechanisms for crack propagation may be other from hydraulic pressure or fluid entrapment.

2.1.2 Structural changes in rolling contact fatigue

The microstructure of case hardened gears is typically composed by a fine martensite structure near the tooth surface, with traces of retained austenite and upper bainite (plate form) and some lower bainite formations (acicular form) (Figure 2.7a). At the core, the microstructure presents low-carbon martensite with ferritic islands (Figure 2.7b)

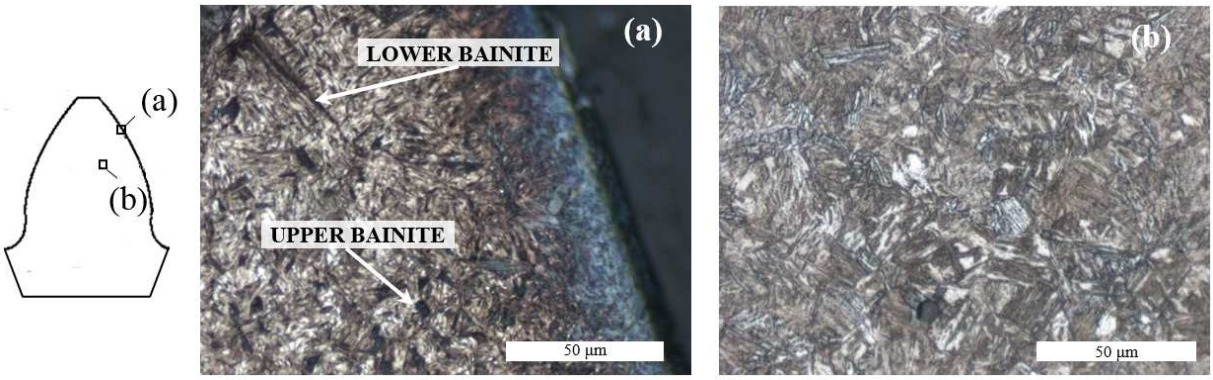

Figure 2.7: Typical microstructure of case carburized gears: (a) near-surface; (b) core.

The most common changes observed in the microstructure as a consequence of contact fatigue are White Etching Areas (WEAs). The name derives from the white appearance (see Figure 2.8) of the altered microstructure after attack with metallographic etching reagent such as Nital (nitric acid in ethanol). Although the structure of WEAs has been a debated in the past, evidences now exist that they are composed of equiaxed nanoferrite grains, with a fine distribution of carbide particles [41–45]. The resulting structure is 10-50% harder than the matrix [45].

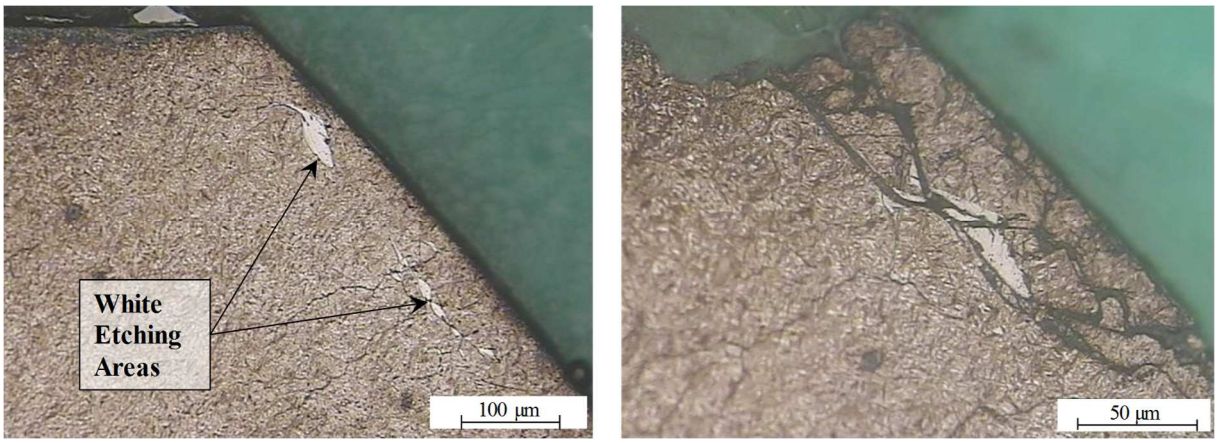

Figure 2.8 White etching areas observed in a case hardened sun gear.

WEAs are typically associated to the presence of cracks within the steel matrix, which may promote rolling contact fatigue failures. Whether cracks constitute a prerequisite for WEAs formation or develop as a consequence of the different hardness between the WEA and the matrix is still a controversial issue. Details on the competitive theories about the origin and driving mechanisms of WEA's can be found in the comprehensive review of the state of the art about the topic, published in 2016 by Evans [45] though currently the most accredited theory supports the hypothesis that microstructural changes forms after the cracks. During contact indeed, the compression stress field force the edges of cracks to close. The repeated inversion of shear stresses would cause an intense rubbing of crack faces associated to severe plastic deformation, which would possibly be the cause of carbide diffusion and dissolution.

Un-etched areas are often observed also around non-metallic inclusions. Such structures are addressed as butterflies due to the symmetric development of white "wings" around the inclusion. Butterflies are thought to originate by a decarburization mechanism similar to WEAs, caused by localized plastic deformation in the crack formed at the matrix-inclusion interface.

2.2 Different forms of pitting in case hardened gears

Pitting in case hardened gears usually manifests under one of the following forms:

- Diffused micro-craters over a relatively wide area (micropitting)
- Single isolated craters addressed as Point Surface Origin (PSO) macropits. origined in correspondence of localised stress raiser such as micropits, edges of tip relief, scuffing scratches, handling bruises or dents leaved by hard particles in the lubricant
- Coalesced macro craters in areas where contact pressure are particularly high, typically because of a Geometric Stress Concentration (GSC), namely a reduction in the curvature radius of the surfaces

Figure 2.9 shows a gear where the three mechanisms of damage described above occurred in different areas of the tooth flank. GSC macropitting manifested near the root of the tooth probably due to tip-to-root interference. Micropitting is spread in the dedendum, particularly at the centre of the tooth where the curvature due to crowning concentrates the contact pressure. Finally, PSO macropitting manifested in the addendum, possibly as a consequence of the presence of dents originated by the debris coming from the above damages.

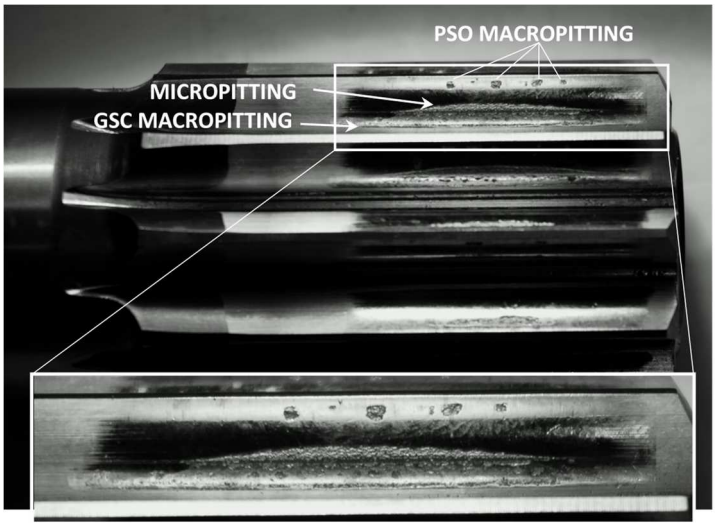

Figure 2.9: Different contact fatigue phenomena on the case hardend sun gear of a planetary gear set for off-highway axles.

2.2.1 Micropitting

Micropitting has been addressed in the past also with the name of gray-staining, because consists in the formation of a multitude of craters on the asperity scale which give to the surface a dull appearance (Figure 2.10).

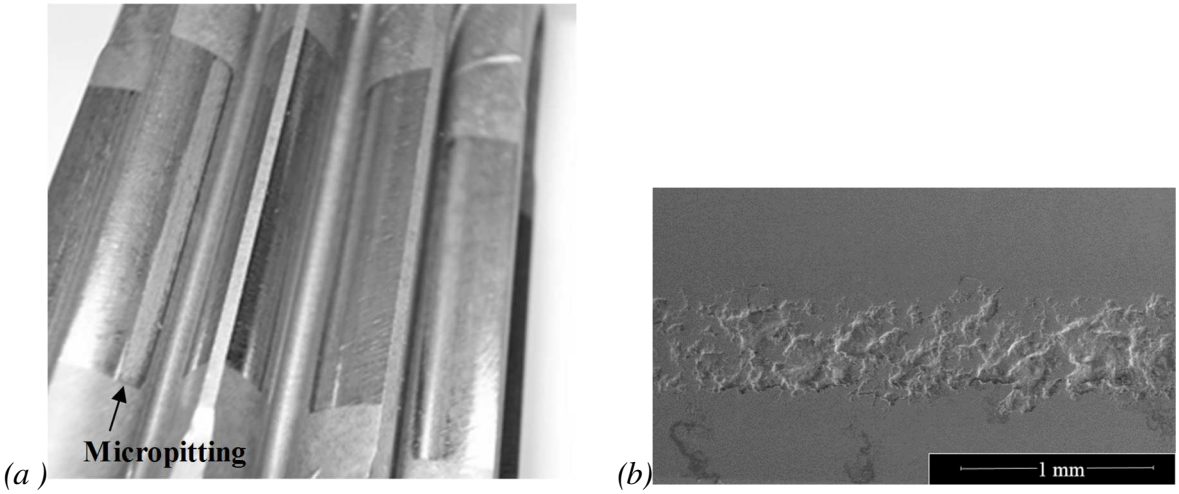

Figure 2.10: (a) Micropitting on the dedendum of a case hardened gear. (b) SEM image of micropitting craters on a case hardend gear.

It is particularly common in case hardened steels, where the low ductility prevent the surface layers to accommodate plastic strains and small cracks form after few load cycles. The damaging mechanism has been attributed to metal-to-metal contacts among asperities, because

experiments performed by different authors showed that micropitting does not occur in components finished to obtain a mirror-like surface [46]. Therefore, the dominant factor to prevent micropitting failures is the ratio between the lubricant film thickness and the roughness of the surface (also known as λ-ratio). It is worth noting that for a given viscosity of the lubricant, the film thickness is much more influenced by the rolling speed of the mating bodies than by the contact load: the higher is the entraining speed of the bodies, the thicker is the film. Craters originate by the detachment of small material debris from surface distress cracks (see Figure 2.4). In gears, micropitting generally interests the dedendum of the tooth and is not particularly hazardous by itself, but often results in subsequent macropitting formation as a consequence of further crack propagation. Moreover, the material removal in the dedendum, causes a reduction of the curvature radius in correspondence of the pitch line, at the upper edge of the micropitted area. The consequent increase in contact pressure promote the formation of macropits as shown in the next section.

2.2.2 Macropitting

Macropitting is the most detrimental form of contact fatigue. Craters can considerably affect the proper functioning of gears and may induce serious secondary damages such as tooth fracture (see Figure 2.11). It should be kept in mind indeed, that although gears teeth are assimilated to cylinders for the calculation of contact pressure, they are also subjected to bending stresses which tend to drive crack propagation inward the tooth. Moreover, the hard particles detached from the surface contaminate the lubricant causing further surface damages in other components of the transmission.

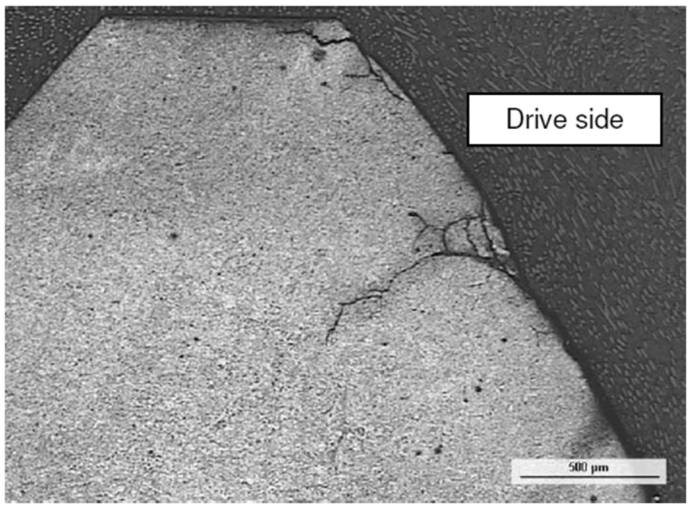

Figure 2.11: In-depth propagation of a crack originated by surface fatigue.

Macropitting damages can be divided into two major categories, based on the appearance of the damaged surface: Point Surface Origin (PSO) macropitting and Geometric Stress Concentration (GSC) macropitting [25,35,47,48]. The definitions relate to the root causes of the failure mechanism, as clarified in the following sections

2.2.2.1 PSO Macropitting

PSO macropits are characterized by a arrowhead appearance. It is widely accepted that such morphology is symptomatic of propagation from a surface originated crack [6,31,35,48,49] The craters originate by the tip of the arrowhead and develop toward the rolling direction regardless the direction of friction forces. The most common cause of PSO macropitting is the local stress concentation due to the edge of the micropitted area in the dedendum of a gear. A typical example of this phenomenon is reported in Figure 2.12. Craters probably originated from a previously formed crack nearby the pitch line, which further propagated in the addendum of the gear until it caused the detachment of a flake of material, perhaps facilitated by the presence in the addendum of smaller surface cracks oriented in the opposite direction. PSO macropits can also originate from surface defects such as nicks, dents, grinding furrows or debris bruises [35]. Some authors postulated that the spread angle of craters, which is typically in the range 70°÷140°, would be greater for higher values of the friction coefficient [30,49].

Although there is a body of research [35,38] indicating that PSO macropits can develop only by inclined surface cracks oriented according to the direction load movement (namely in surfaces with negative SRR), during this work arrowhead craters were eventually encountered in the addendum gears teeth (Figure 2.13). Even more surprisingly, the surface cracks observed in the addendum of a section of the driven gear reported in Figure 2.4 (c) were directed (as expected) toward the tip of the tooth, and therefore oppositely both to the rolling direction and to the direction of development of the crater (Figure 2.13). The causes of such phenomenon are yet to be clarified. Nevertheless, it seems to be overlooked in the literature that the same Littmann and Widner, authors of the work where the definition of Point Surface Origin macropitting was first introduced [47], recognised in their response to Mr Denning's discussion of the paper, that some of the V-shaped craters showed in the figures turned out to be originated in correspondence of oxide inclusions, thus admitting that, despite the morphology, the origin of such craters might be other than surface. According to the authors however, the shape of the

final crater was still to be attributed to the hydraulic pressure propagation mechanism which would have taken place as soon as the crack reached the surface.

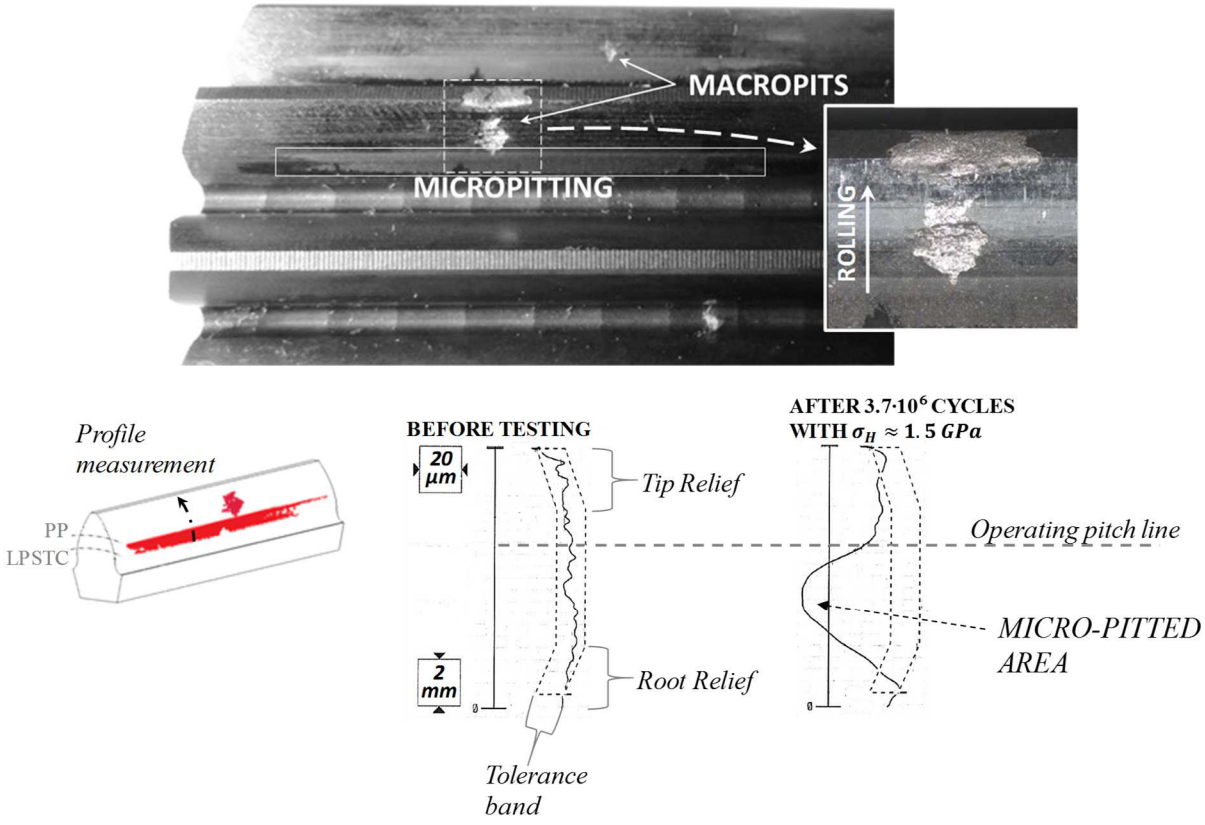

Figure 2.12: PSO macropitting generated at the pitch line of the sun gear of a planetary gear set in an off-highway axle. The profile diagrams show deviation from the nominal profile in the normal direction before and after the test. The upper edge of the micropitted area was the cause of the crater formation.

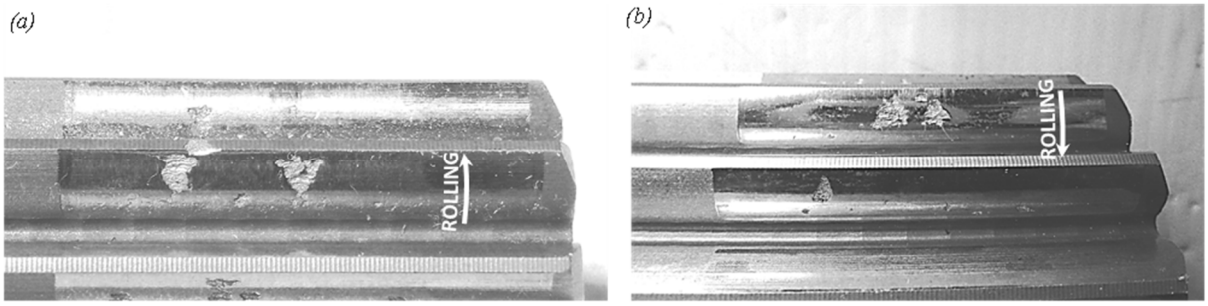

Figure 2.13: PSO macropitting observed on a driver (a) and driven (b) gear

In this work PSO craters were always observed in correspondence of localized geometric stress raisers such as bulges on the surface (e.g. edge of tip relief as shown in Figure 2.13b) or edges of dents or craters (micropitting or edge of previously formed macropits) in agreement

with other evidences reported in previous works [35,50]. The crack often continues to propagate in the subsurface even after the detachment of the first flake of material eventually linking with other surface cracks in a more forward location. Thus, if the arrowhead crater points toward the root of the tooth frequently subsurface cracks reach the upper extremity of the tooth causing tip fractures as shown in Figure 2.12 and Figure 2.13a and reported also in [25].

2.2.2.2 GSC macropitting

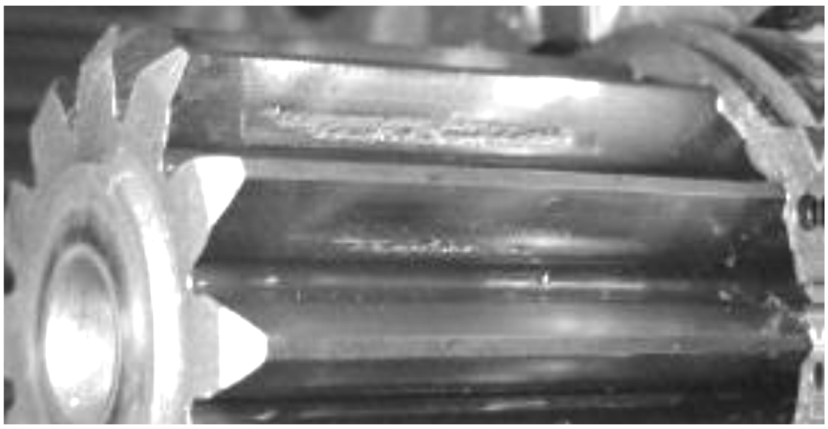

Figure 2.14: GSC macropitting on the sun gear of a planetary gear set in an off-highway axle.

GSC macropitting forms in areas where the non-conformity of the mating surfaces is particularly pronounced and therefore the load is carried by a small contact area resulting in extremely high pressures. In such cases several pits form in the overloaded areas, leading to a widespread damage as reported in Figure 2.14. Typical causes of GSC macropitting on gears are misalignments due to deflection of shafts and supports under load, corners of tip and root relieves, crowning, and tip-to-root interference.

2.3 Preventing contact fatigue in gears

In order to reduce the likelihood of contact fatigue failures it is necessary either to limit the stress to which the material is subjected or to enhance the material performances. The former approach focuses on the geometry of the gear as related to the particular operating condition it

is designed for. The latter, instead, relies on the quality of the material and to the thermal, thermochemical or mechanical processes used to treat the surface.

2.3.1 Gear design

Contact stresses should be regarded both in the macro-scale, by an accurate design of the tooth geometry to provide a good pressure distribution for the widest range of working conditions, and in the micro-scale, by preventing asperity contacts. As a matter of fact, it is commonly accepted that in the case-hardened steels usually adopted for power transmission gears in heavy duty applications, contact fatigue failures occurs primarily as a result of surface initiated damages. Therefore, all the expedients aimed to prevent direct contacts among asperities are considered to improve the durability of the surfaces. However, the major parameters influencing the lubrication regime, namely speed and roughness of the surfaces and lubricant viscosity, are often imposed by technological and application limits. From a macroscopic viewpoint instead, the manufacturing accuracy of the system and the modification to the nominal tooth geometry, introduced to improve the system behaviour for the specific design conditions, are perhaps the most important aspects affecting the pressure distribution over the tooth width and its variation along the path of contact. Deflections under load of gears teeth, gears bodies, shafts and supports, in fact, are unavoidable and contribute to deviate from the ideal case of contacts between parallel cylinders. In order to accommodate a certain degree of deflection without resulting into edge contact at the extremities of the teeth, gears for power transmission are typically manufactured with a variable tooth chordal thickness along the gear axis, aimed to avoid contacts at the extremities of the tooth. This feature takes the name of crowning or barrelling (Figure 2.15). In the typical applications treated in this work, characterized by gear modules in the range 2÷3 mm, an amount of crowning of few microns is enough to achieve the desired pressure distribution under the service load. Consequently, the contact between gears teeth is elliptical for low load levels, while at the high loads, when the mayor axis of the ellipse overcomes the tooth width, the contact area approaches a rectangular shape, while still preserving near-parabolic variability of pressure values along its length. It is to be noted that an excessive value of crowning is undesired because it would result in unnecessary contact stress concentration at the centre of the tooth face.

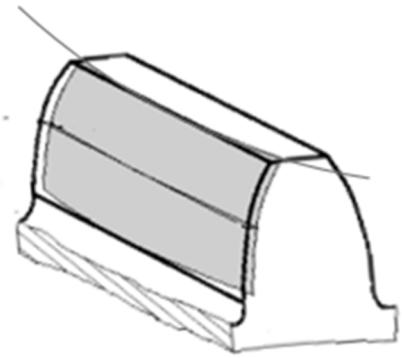

Figure 2.15: Crowning.

A second issue derived by teeth deflections under high loads is that the contact between two incoming teeth may start before the tips of driven gear intersect the line of action, and thus the tip corner tends to furrow the dedendum of driver gear causing a fast degradation of the surface (Figure 2.16a). To limit the risk of interferences under load, the tooth profile could be designed with tip and root relieves (Figure 2.16b).

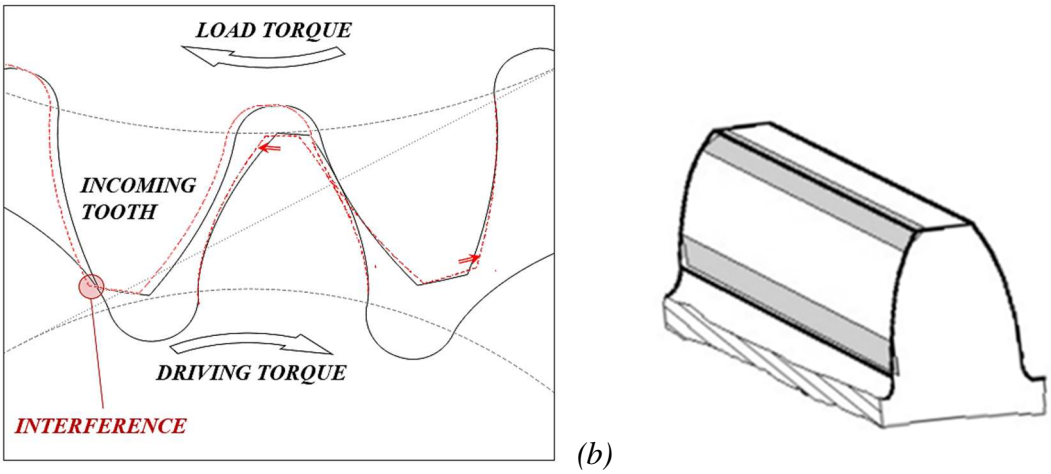

Figure 2.16: (a) Schematic representation of tip-to-root interference. Continuous line represents the theoretical position of gears, while dashed line represents the actual position of gears due to teeth deflections under load. (b) tip and root relieves on a gear tooth.

If the amount of relieves is appropriate (usually some tens of microns) for the service load of the transmission the contact force could be assumed to increase linearly between SAP and LPSTC and decrease linearly as well, between HPST and EAP [22]. Therefore, the contact pressure would change along the path of contact as shown in Figure 2.5.

2.3.2 Surface treatments

Enhancements in the contact fatigue resistance are often seeked focusing on the thermal or mechanical treatments of the surface. Generally, at least within certain limits, the harder is the material surface, the higher is its load carrying capacity with respect to contact fatigue failures. Accordingly, gears used in heavy duty power transmission systems are typically carburized to achieve high hardness values in the first tenths of a millimeter, while maintaining a good toughness at the core. However, the increase in surface hardness is not the only beneficial effect of case hardening. In fact, it is commonly accepted that crack propagation could be hindered by compressive residual stresses, which in case hardened steels are already introduced in the surface layers in consequence of the heat treatment. Some authors also claim that shoot-peening would provide a further beneficial effect in the pitting durability of gears [51–54]. Nevertheless, although concerning tooth root bending fatigue the improvement derived by shot peening is documented in the literature [55,56] and reported also in the international standards [57,58], regarding pitting the issue is controversial [59] and the ISO standard 6336 specifies that the effect of the increase in roughness caused by the treatment can be detrimental for the surface durability. It should be kept in mind that in rolling contact fatigue the principal components of the stress field generated by the contact are compressive as well, and thus tend to prevent crack propagation. An experimental measurement of residual stress by X-ray diffraction, performed on both shot-peened and un-peened case hardened gears within the present project, showed that residual stresses induced by rolling contact during normal operation can achieve values as high as the ones resulting by the shot peening treatment. The component of residual stress directed along the involute profile was measured at various depth in proximity of the pitch line of both the drive and non-driving flanks of the teeth, in order to investigate to which extent contact fatigue phenomena may alter the original residual stress state. Material was removed by electropolishing in a restricted area to minimize the effect on the measurement. Results are reported in Figure 2.17.

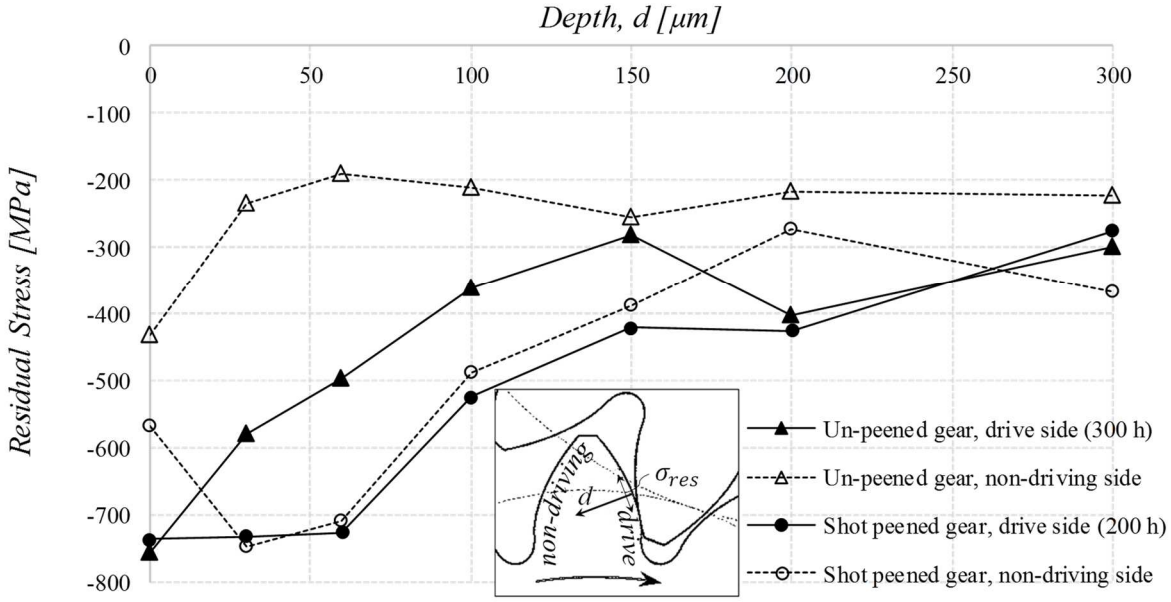

Figure 2.17 Residual stresses beneath the tooth surfaces of two case hardened gears [60]

At the surface of the non driving flank, the un-peened gear showed compressive residual stresses deriving from carburizing process up to -430 MPa. At depths greater than 50 μm the residual stress field stabilized at approximately -200 MPa. The shot peening treatment introduced higher compressive residual stresses, which achieved a maximum of -750 MPa at about 30 μm from the surface and then decreased with depth and resulted particularly effective up to a depth of 150 μm. In the driving flanks of the un peened gears, which was subjected to cyclic contact stresses, the residual stress at the surface reached the same value as the shot peened gear. The profile beneath the surface was affected only in the first tens of microns beneath the surface in the shot peened gear, probably due to plastic deformations in the asperity scale, while changed considerably up to a depth of 150 μm.in the un-peened gear. The effect of shot peening on the pitting durability of case hardened17NiCrMo6-4 case hardened steel has been also experimentally investigated by means of tests with disc specimens, which will be presented in Chapter 6.

Chapter 3

DESIGN METHODS AGAINST ROLLING CONTACT FATIGUE

A consistent body of research deals with the attempt to extend theories and methods developed for classical fatigue and fracture problems, to rolling contact fatigue phenomena. As pointed out by Olver in his comprehensive review on rolling contact fatigue phenomena [25] the issue is anything but straightforward. Contact fatigue damages in fact, develop right beneath the point of application of the load, where the material is characterized by a multiaxial, non-proportional stress field strongly influenced by the roughness of the surfaces and the lubrication regime. Being all the principal components of stress compressive, crack propagation is hindered not only in mode I, but also under mode II (driven by the alternating shear stresses) due to the friction between crack faces and the interlocking effect caused by the irregular crack path. Furthermore, diffused plasticity usually interests the top layers of material up to a depth which is typically comparable with the dimension of the contact area (in softer materials) or at least with the roughness height (for surface hardened materials). Finally, contact fatigue phenomena are usually the result of several modes of failure [47] that act at first independently, causing the formation of cracks at different locations (surface and subsurface), which can then interact with each other or modify the topography of the contact surfaces affecting the pressure distribution.

Calculation methods against contact fatigue can be divided into two categories [61]: engineering methods and research methods. The former methods rely on statistical approaches that correlate a physical quantity considered as significant in the failure process, to a probability of failure within a given number of stress cycles. These methods must be based upon extensive experimental evidences and therefore their applicability is usually restricted to the field of application to which the empirical data are referred. Research approaches instead, are usually developed to tentatively overcome such limit, providing a method based on the physical mechanisms that drive the damaging process of the material, and therefore being potentially valid for a wider range of different problems. Among these latter, we can distinguish between methods based on continuous mechanics and methods based on fracture mechanics [62]. Other works in the literature incorporate more than one of the above defined categories, usually mixing limits defined by multiaxial fatigue approaches or engineering relations to

assess whether and where a crack is likely to form, with fracture mechanics concepts to describe the propagation phase [12,23,61].

3.1 Engineering Methods

With the terms "Engineering methods" we embody such methods that have been used in engineering practice since 1940 and today form the background of life prediction models proposed by international standards and machine elements catalogues. Usually the calculation is based on a simplified physical model which accounts for the main variable affecting the component durability (e.g. contact load for pitting and lambda-ratio for micropitting) and several factors are used to correct the computed life to consider the effect of the most influencing parameters (material, geometry, speed, lubricant, etc.). Since most of such factors are derived by means of empirical relations based on extensive experimental data relevant to a specific type of components, the field of application may be limited. The first universally accepted engineering method, due to Lundberg and Palmgren, date back to 1947 [63] and still constitute the basis of most of the calculation methods for roller bearings. Behind the method is the concept that fatigue is the result of the growth of cracks originated in correspondence of weak points which can be treated as random defects. Therefore, the probability of failure of a component in a defined number of cycles should be related to an equivalent stress parameter, representative of the stress state, and to the volume of material subjected to the severest stress conditions. Based on this assumption, and on the statistical theory of the strength of materials developed by Weibull [64], Lundberg and Palmgren formulated the basic equation for the survival probability of two bodies in rolling contact [63].

$$-\ln(S) = \frac{\tau_0^k V N^\beta}{z_0^h} \tag{3.1}$$

Where:

- N is the life with probability of survival S
- τ_0 is the maximum value of subsurface orthogonal shear stress
- z_0 is the depth at which τ_0 occurs
- V is the volume of a crown of material of thickness z_0 and width equal to the semi-major axis of the contact ellipse
- β is the Weibull dispersion exponent
- $k \approx 10 \; and \; h \approx 1$ are experimental constant.

The Lundberg-Palmgren approach was extended first to spur and then to helical gears, beginning from 1975 by Coy, Townsend and Zaretsky [65,66]. The authors individuate as critical stressed

volume on the driving flank of the teeth, the band of material having thickness equal to the depth of maximum shear stress, height delimited by the lowest and highest point of single tooth contact, and width equal to ¾ the entire tooth face width (Figure 3.1). Moreover they consider that, by a statistical point of view, the survival probability of a gear is equal to the product of the survival probability of each of its teeth.

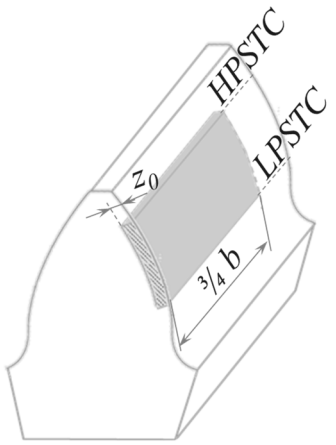

Figure 3.1 Critical stressed volume in a spur gear.

The method was calibrated by means of a test campaign on AISI 9310 spur gears obtaining a load-life power law with exponent k=4.3. Such result was considerably different compared with the fatigue curves reported by the AGMA standards 411.02 [67] and 210.02 [68], in force at that time. The authors argued that the reason could be found in the difference between the stressed volume of the tested gears with respect to the reference gears to which the AGMA fatigue curves were referred to. Anyway, also the pressure-life curves for case hardened steels suggested by the current ISO standard have an inverse slope of 13.22 [57]. Since the contact pressure between gears teeth is related to the square root of the load, this means a load-life law with exponent 6.61, clearly different from the results of Coy and Zaretsky.

Whilst in the field of bearings the Lundberg Palmgren approach is still adopted as a basis for all the calculation procedures defined in the standards, as well as in the manufacturer catalogues, regarding gears applications this method has been abandoned. Separated standards have been developed for pitting and micropitting of gears: pitting is prevented by limiting the contact pressure to a maximum value defined by means of experimental pressure-life fatigue curves, while design against micropitting is based on the λ-ratio. The evaluation of the load carrying capacity of gears with respect to pitting and micropitting according to the procedures defined in the relevant ISO standards will be treated in section 3.3.

3.2 Research methods

Although generally research methods are focused upon a limited part of the damaging mechanism, namely crack initiation or propagation [61], some attempts was made to find a model which covers the entire failure process [12,40,61,69]. Typically, methods based on continuous mechanics have been used to estimate the most favourable location for crack nucleation (surface or subsurface) and to assess whether or not a crack is likely to form in a component subjected to a given contact pressure. On the other hand, fracture mechanics approaches have been widely used to analyse the effect of various influencing parameters on the Stress Intensity Factors (SIFs) at the tip of an already formed crack, among others: friction coefficient, lubricant pressure inside the crack, direction of sliding and rolling and crack geometry. Thus, fracture mechanics models could be used to obtain valuable information on the driving mechanisms in crack propagation and to tentatively explain the morphology of the final craters.

3.2.1 Methods based on continuous mechanics

These methods try to describe the crack initiation phase of contact fatigue phenomena, which have in some cases deemed to involve a the dominant period in the entire failure process [6,26,70].

One of the first attempt to explain the basics of crack nucleation in rolling contacts relies on the theory of shakedown proposed bi Melan in 1938 [71].

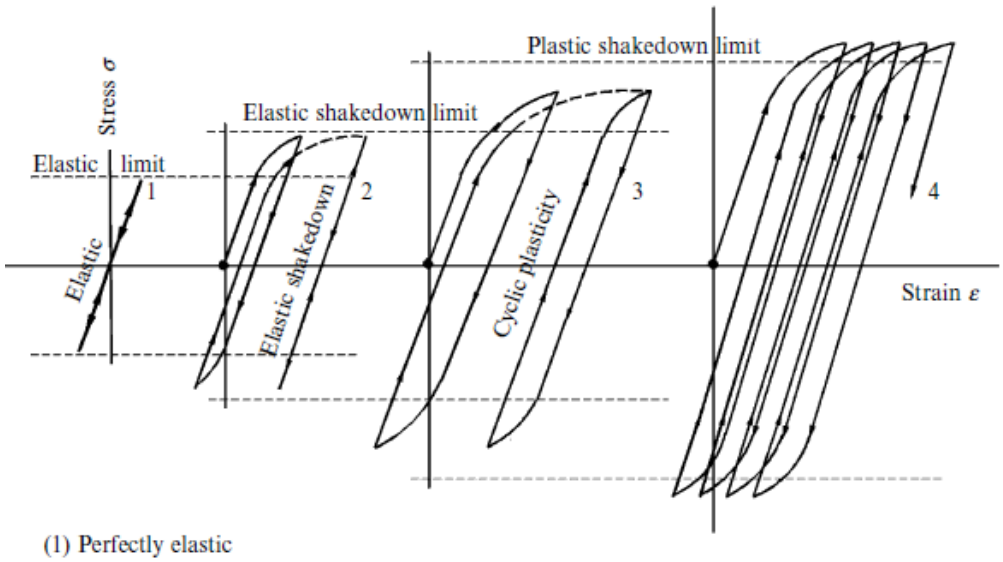

Figure 3.2 Material response under cyclic loading [6]**.**

In non-conformal surfaces in fact, contact stresses may easily exceed the yield stress of the material. However, the residual stress state introduced by plastic deformation as well as the effect of strain hardening can cause the material response after few load cycles, to be entirely elastic. According to the Melan's theorem if any self-equilibrating and time-invariant residual stress field exist, such that superimposed to the stresses due to loading, can prevent yield, then the material will shake down and the subsequent response will be elastic. The maximum load for which a residual stress field that meets the above conditions exist, is called shakedown limit. Loading beyond the shakedown limit will result in repeated plastic deformation in a closed (plastic shakedown) or open (ratchetting) loop (Figure 3.2). The problem of shakedown in rolling contact bodies was first analysed for the case of elastic-perfectly plastic materials by Johnson [72] using Hertz's theory and Melan's theorem. Nevertheless, since strain hardening may affect the material response as well, by raising the elastic limit, the shakedown concepts were extended by Ponter [73] for a kinematic hardening material behaviour. The work on shakedown of rolling contact bodies, has led to the definition of shakedown maps to predict the steady state material response and the position of probable damage initiation (surface or subsurface) for any given combination of the applied pressure p_0 (usually normalized by the yield stress of the material in pure shear k_e), and the friction coefficient f (Figure 3.3). Concerning line contacts, the construction of the map is facilitated by the hypothesis of plain strain conditions. All the components of the stress field can be calculated analytically and, chosen a yield criterion (e.g. the Tresca's criterion), it is possible to plot the limit curve below which the material response is elastic (dashed curve in figure Figure 3.3a). It is well known that increasing friction moves the location of maximum shear stress closer to the surface and at the same time increase its value, consequently for values of $f < 0.3$ yield occurs beneath the surface, while for $f > 0.3$ the surface layer yields first. Above the elastic limit the onset of residual stress intervenes making yield possible for gradually increasing stresses, according to the Melan's theorem. The principal shear stress in plain strain is given by:

$$\tau_1 = \sigma_1 - \sigma_3 = \left[\frac{1}{4}(\sigma_{xx} + \sigma_{zz})^2 + \tau_{zx}^2\right]^{\frac{1}{2}} \tag{3.2}$$

The importance of the role covered by friction in both the shackedown limit and the location of damage initiation is understandable remembering that all the principal components of stress beneath the contact surface are compressive. Hence, the only component in equation (3.2) that could not be compensated with a time-invariant residual stress field is the alternating shear stress in the plane of motion of the contact τ_{zx}^2, which is in fact addressed as responsible for the damage initiation in RCF.

Thus, the upper limit to contact pressure for which the yield can be prevented by contact induced residual stresses, according to the Tresca's criterion is given by:

$$\tau_1 \leq k_e \tag{3.3}$$

Or, in other terms:

$$\tau_{zx} \leq k_e \tag{3.4}$$

Since the maximum value of τ_{zx} in line contact in absence of friction is $\tau_{zx} = 0.25\, p_0$, the above condition can be also expressed, for f=0, as:

$$\frac{p_0}{k_e} \leq 4 \tag{3.5}$$

Such limit can be evaluated for all the possible values of *f,* obtaining the dashed-dotted line of figure Figure 3.3b, which delimits the elastic shakedown region for an elastic-perfectly plastic material. The presence of friction raises the maximum value of shear stresses and moves its location closer to the surface, thus promoting surface initiated cracks. In the region of sub-surface yield, the shakedown limit increases to the continuous line assuming a kinematic hardening material behaviour. If the shakedown limit is overcome the material undergoes to repeated plastic flow at each contact cycle (ratcheting) until fracture occurs.

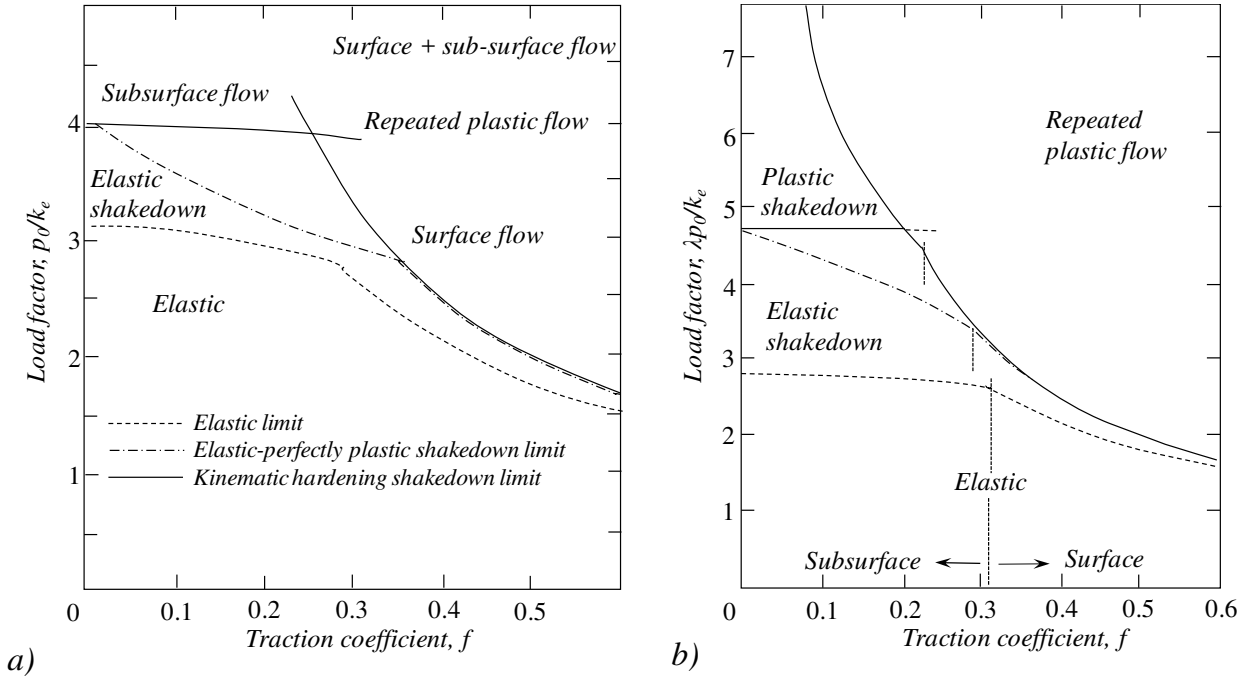

Figure 3.3 Shakedown maps for (a) line contacts [6] **and (b) point contacts** [74]**.**

The determination of shakedown maps for point contacts is complicated by the non-compliance with the plain strain hypothesis. However, an approximate solution was provided by Ponter et al., as shown in Figure 3.3. According to Ponter, in point contacts and especially for low friction, if p_0/k overcomes the elastic shakedown limit, the body experience closed loops of alternated plasticity confined in a subsurface restricted volume of material. However, since this region is entirely surrounded by undeforming material progressive strain growth is prevented at least in the region of the map denoted as "plastic shakedown".

The application of methods based on the theory of shakedown make sense especially when dealing with relatively ductile materials, which can accommodate a certain amount of plastic strain before crack initiation and where the friction coefficient may attain relatively high values as compared to the ones encountered in oil lubricated components. Moreover, in typical applications of the shakedown theory, such as railway's rails [75,76], the load is likely to induce stresses several times higher than the yield stress in pure shear of the material (often estimated as $\frac{\sigma_y}{\sqrt{3}}$ [75]) leading to failure in few load cycles. On the contrary, these methods typically do not found application in the analysis of case carburized steels for gear manufacturing, where the required service life is in the order of several millions cycles and therefore the design pressure should be fairly lower than the elastic shakedown limit. The validity of shakedown maps for case carburized steels is also questionable because of the strong gradient in residual stresses and mechanical properties in the first tens of microns of depth below the surface. Furthermore, it is worth noting that the charts of Figure 3.3 report no surface failures for the typical friction coefficients assumed for gears contacts ($f \approx 0.05$ as shown in Table 3.1), while rolling contact fatigue phenomena in gears are deemed to have preferentially origin from a plastically deformed layer in the scale of the roughness dimension.

Nevertheless, residual stresses and strain hardening are not the only responsible of shakedown: in point contacts, for instance, the initial plastic deformation, as well as the effect of wear in the long period, cause the formation of a groove with consequent increase in the conformity of the mating surfaces, reducing the level of contact pressure for a given load. This mechanism could not take place in line contacts because each point along the contact generatrix is subjected to the same stress history, and therefore wear and plastic deformation are homogeneous across the contact width. Hearle [77] observed that in point contacts loaded over the shakedown limit the shape of the contact area change from elliptical to near rectangular in the first few thousands of cycles. To explain the experimental results of Hearle, Kapoor and Johnson [78] developed a physical model based on the shakedown of elastic-perfectly plastic materials to predict the geometry modification, starting from the assumption that after a period of running in, the surfaces of the bodies would approach the shape which allow them to carry the maximum load without exceeding the elastic limit. The results of the theoretical

model were found to be in good agreement with the experimental measurement performed by Hearle and by the same authors. It is worth noting that both Hearle's and Kapoor and Johnson's experiments were performed with loads beyond the shakedown limits and endured for a maximum of 200000 cycles. After this limit, the plastic deformation and the residual stress field were thought to have reached a steady state condition and any further change in contact geometry would have been attributable only to wear, which was not considered in the proposed model. This particular aspect should be taken in great consideration instead when dealing with surface hardened materials, which are perhaps less sensitive to plastic deformations but may experience substantial changes in the contact geometry due to material removal as a consequence of wear and micropitting. The increase in load carrying capacity of a component due to geometry changes is sometimes addressed as "apparent shakedown" to distinguish it by the enhancement in strength induced by residual stresses.

In conclusion, some concepts developed within the framework of shakedown theory, such as the development of compressive residual stresses during rolling contacts and the increase in the conformity of the surfaces, remain valid and should be taken into account when considering gears problems. These aspects will be treated more in detail in chapter 6.

3.2.2 Multiaxial fatigue criteria

As already mentioned in the previous sections, rolling contact fatigue damages develop in a multiaxial and non-proportional stress field with the further unusual characteristic that the normal components of stress are all compressive, therefore the damaging mechanism is thought to be driven by the alternating shear stress in the plane of motion of the contact, at least in the first stages of crack nucleation. The extension of multiaxial fatigue criteria used for classic fatigue problems to such complicated conditions is not straightforward, mainly because such methods are usually supported by experimental data obtained with a positive mean stress value [79,80], in contrast with the compressive Hertzian stress field. One of the most common multiaxial fatigue methods, adopted for rolling contact fatigue problems, is the Dang Van criterion [81] which was initially applied in this context by Dang van himself, and his co-workers [82]. Several attempts were made to calibrate the constants of the method to fit rolling contacts data [80,83,84], nevertheless the validity of the model in the context of RCF is still object of discussion. The main problem is that Dang-Van criterion tends to overestimate the limit pressure for rolling contacts, providing values which would lead to cyclic plastic deformation of the bodies [75,83,84]. Ekberg et al. tried to overcome the limits of the method by proposing a modified form of the Dang Van criteria, which however was found to be accountable only for a limited range of application [83]. Moreover Ciavarella and Monno [79] found that the limit

pressure calculated with such method for point contacts, is less than 20% higher with respect to line contacts, and the trend may be even reversed for hard steels (having Dang-Van constant $\alpha_{DV} \approx 0.5$). Conversely, experimental findings suggest point contacts to have a RCF fatigue limit up to 75% higher with respect to line contacts [85]. The authors suggest that such difference could be explained with the occurrence of cyclic plastic deformation in point contacts loaded above the elastic shackedown limit, while according to the shakedown maps provided by Ponter et al. [86] in line contacts ratchetting would occur immediately when the shakedown limit is overcome. It should be also kept in mind that data from disc-on-disc tests with point contacts may be affected by an error due to apparent shakedown following the formation of the circumferential groove caused by wear and/or plasticity. Anyhow, the use of multiaxial fatigue criteria developed for high cycle fatigue problems seem to be inappropriate for contact fatigue of gears, where experimental evidences suggest that cracks have predominantly surface origin, occuring in an early stage of the damaging process under the complex action of the hardly predictable stresses developed in the mutual action among asperities.

3.2.3 Fracture mechanics approaches

Contrary to models based on continuous mechanics which assume that most of the component life is spent in crack initiation, these models are based on the assumption that the dominant phase is propagation [23,39,87]. The two different point of view are not necessarily in contradiction, the prevalence of the time spent in either crack initiation or crack propagation may be related to the location of damage initiation (crack propagation time is dominant in surface cracks, conversely to subsurface originated ones [61]), or to the material (relatively soft material may sustain cyclic plasticity before cracking [79]). Concerning gears applications, rolling contact fatigue cracks typically originate at the surface already during the running-in due to contact among the asperities, hence fracture mechanics approaches are much more diffused in the literature than continuous mechanics approaches. However, most of these models have been developed to provide a characterization of the phenomena in terms of damages morphology and to study the mechanisms that drive the crack propagation, rather than to obtain a quantitative prediction of the life of a component. Actually, one on the major advantages in using fracture mechanics approaches to analyse RCF problems is that it is possible to build the models to account for all the possible meaningful influencing parameters, such as fluid pressure, crack face friction, different shape, position and orientation of cracks and sliding and rolling directions, in order to verify if the predicted effect of each of them is consistent with experimental observations.

The study of the mechanisms driving RCF crack propagation has become a diffusely treated issue in the 1980s when the growing availability of computational resources allowed the application of fracture mechanics concepts to increasingly complex problems. The first works investigating contact fatigue crack propagation mechanism with fracture mechanics approaches were usually based upon bidimensional models where a moving Herzian distribution of pressure and friction was applied to a cracked half space (Figure 3.4).

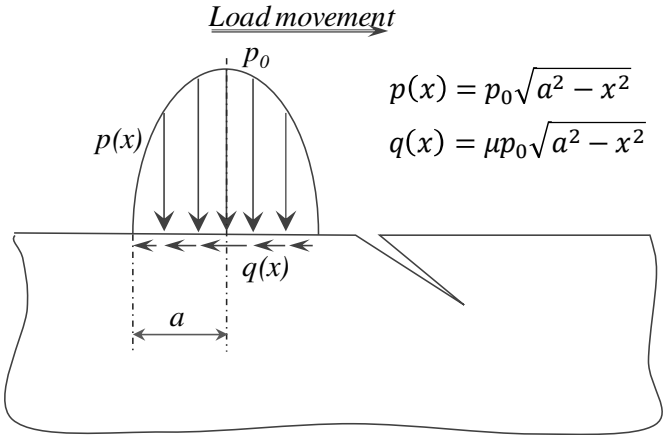

Figure 3.4 Bidimensional model of a cracked half-space.

Mainly, three different crack geometries were considered: a horizontal subsurface crack, a vertical surface crack and an inclined crack or a combination of the previous (see Table 3.1 for references). The inclined crack configuration is the commonest, especially in the more recent works, since it is the most frequent in experimental observation. Early methods were based on the multiplication of the nominal stress distribution in the uncracked body, by a kernel representing the solution of the problem of the cracked half space. Such approaches are based on the assumption that the stress field is entirely elastic and the external pressure distribution are not affected by the presence of the crack. They show the advantage of a limited computational effort together with a very good accuracy as compared to linear finite element calculations, feature that makes them still appealing [88]. The structure of the model allows to easily consider the effect on the stress intensity factors (SIFs) of various cracks geometry (in terms of both length and inclination angle) as well as of various influencing parameters, such as fluid pressure, friction and residual stresses, which can be accounted in the calculation by simple superimposition of the effects.

Stressing on the fact that the shape of macropits is intrinsically three dimensional, Murakami and co-workers proposed a 3D analysis of an arrow-headed surface crack [30] by applying the body force method developed by Nisitani [89] and extended to three-dimensional problems by Nisitani and Murakami [90]. The method is based on the closed form solution of a point load in an infinite elastic solid. A system of discrete point loads is distributed on the boundary of an imaginary crack surface

which is represented by a finite number of triangular elements. The known stresses generated by each point load, multiplied by a weight magnitude, are superimposed to the stress field of the uncracked body. The solution of the problem requires the determination of the system of unknown weight magnitudes which, multiplied to the elementary forces, define a load distribution that satisfies the boundary conditions. The computational effort required by the method is reduced as compared to a finite element model since the discretization is limited to the boundaries of the body.

Since then, fracture mechanics approaches have been extensively used to assess meaningful information about the damaging mechanisms in RCF and to analyse the effect of the tribological and operating parameter on the final crater morphology. Table 3.1 reports a list of investigations on RCF phenomena performed since the 1980s. The table point out the importance historically attributed to the presence of a fluid (whether in the form of lubricant or rain water according to the specific application) in the propagation mechanism of surface cracks. It is worth noting that most of the works rely on a negative SRR, expressed by the negative value of the friction coefficient, since only under this circumstance the fluid is enabled to leak into the crack. All the works dealing with an estimation of the crack path report a good correlation between the model prediction and experimental evidences. On the other hand, the estimation of the required number of cycles for the formation of a crater still remain a hard issue since the formation of craters in actual components is often the result of branching of a main three-dimensional crack and its interaction with various other surface or subsurface damages (such as micropitting or WEAs). Moreover, since the crack path develops mainly beneath the surface, an accurate experimental analysis of the growth rate is impossible for rolling contact fatigue phenomena. A recent experimental investigation on the propagation rate of V-shaped cracks, based on the extension of the edges visible on the surface during tests on bearing steel roller specimens, showed that the cracks growth could be represented by a Paris-type power law only in a later stage of the damaging process which covers a small fraction of the total life before pitting [87]. Finally, a further difficulty in life predictions is due to the fact that the pressure distribution itself, which is responsible of the damaging process can be in turn perturbated by the presence of microcraters and especially by the changes to which the contact geometry incurs due to wear and plastic deformation during operation, as will become evident in the chapters concerning the experimental results.

Table 3.1 List of studies on rolling contact fatigue by means of fracture mechanics approaches.

	DESCRIPTION		PARAMETERS					DETAILS OF LIFE PREDICTION		
Reference	**Crack geometry**	**Approach**	**Friction**	**Friction between crack faces**	**Hydraulic pressure**	**Entrapment**	**EHD**	**Failure criteria**	**Nucleation time**	**Experimental evidence**
Keer et al. (1982) [91]	Surface vertical and subsurface horizontal	Superimposition of Hertzian stress field and cracked half space	μ=0.1÷1.0	-	-	-	-	-	-	-
Keer & Bryant (1983) [39]	Surface inclined	Superimposition of Hertzian stress field and cracked half space	μ=-0.005÷0.005	μ'=0÷0.2	Yes	-	-	Crack length equal to contact width	-	Yes
Murakami et al. (1985) [29]	Surface vertical and surface inclined	Body Force Method	μ=±0.1	-	Yes	-	-	-	-	-
Bower (1988)[38]	Surface inclined	Superimposition of Hertzian stress field and cracked half space	μ=-0.05	$\mu' = 0.1$	Yes	Yes	-	-	-	-
Zhou et al. (1989) [12]	Surface inclined	Dissipated energy of hysteresis loop + Paris law	μ=-0.07	-	Yes	-	Yes	Critical crack length	Yes	Yes
Blake & Cheng (1991) [27]	Surface inclined	Nominal Hertzian stress corrected with factors	μ=-0.05÷0.1	-	-	-	-	Critical crack length	-	Yes but non-supporting
Hanson & Keer (1992) [92]	Surface inclined (3D)	Body Force Method	μ=-0.07	-	Yes	-	-	-	-	Yes
Murakami (1994) [30]	Surface inclined (3D)	Body Force Method	μ=-0.1÷-0.2	-	Yes	-	-	-	-	-

	DESCRIPTION		PARAMETERS					DETAILS OF LIFE PREDICTION		
Murakami (1997) [31]	Surface inclined	Body Force Method	μ=±0.045	$\mu' = 1$	Yes	-	-	-	-	Yes
Glodez et al. (1997) [23]	Subsurface	Virtual crack extension method and short crack growth	μ=-0.04	-	-	-	-	Crack reaching the contact surface	-	Yes
Flasker et al. (2001) [93]	Surface inclined	Virtual crack extension method	μ=-0.04	-	Yes	-	Yes	-	-	-
Frolish et Al (2002) [94]	Surface inclined	Green functions for surface inclined cracks	μ=-0.14	μ=0.04	Yes	-	-	-	-	Yes, good correlation in shape
Ringsberg & Bergkvist (2003) [95]	Surface inclined	Elasto-plastic finite element model with Chaboche kinematic hardening model	μ=-0. 1÷0.4	μ=0.1÷--0.5	Yes	-	-	-	-	-
Fajidiga et al. (Wear, 2007) [24]	Surface and subsurface	Virtual crack extension method	μ=-0.04	-	Yes	-	Yes	-	-	Yes, good correlation in shape
Bogdanski & Lewicki (2008)[96]	Surface inclined (3D)	FEM model with iterative calculaton of the trapped fluid pressure	μ=-0.1	μ=0.1	Yes	Yes	-	-	-	-
Fajidiga & Sraml (2009) [97]	Surface inclined	Strain-life + Virtual crack extension method and short crack growth	μ=-0.04	-	Yes	-	-	Crack reaching the contact surface	Yes	Yes, good correlation in shape
Beghini & Santus (2013) [88]	Surface inclined (2D)	Nominal stress field of the uncracked body multiplied by a weight function	μ=-0.01÷-0.2	-	Yes	-	-	-	-	-

	DESCRIPTION		PARAMETERS					DETAILS OF LIFE PREDICTION		
Panasyuk & Datsyshyn (2014) [98]	Surface inclined, surface vertical, subsurface horizontal (2D)	Singular integral equations method and Paris' law	μ=-0.1	μ=0.1	Yes	-	-	Critical crack length	-	-
Hannes & Alfredsson (2014) [49]	Surface inclined (3D)	Finite element model with asperity point load mechanism and crack closure	μ=-0 ÷--0.06	$\mu = 0.3$	-	-	-	-	-	-
Dallago et al. (2016) [37]	Surface inclined (2D)	Displacement extrapolation method implemented in a Finite Element Model of a cracked half space with Hertzian load	μ=0÷-0.2	-	Yes	Yes	-	-	-	Yes, good correlation in shape
Ancelotti et al. (2016) [36]	Surface inclined (2D)	Displacement extrapolation method implemented in a non-linear Finite Element Model of a contact	μ=0.1	-	Yes	Yes	-	-	-	-

3.3 Standard methods for pitting and micropitting

To date, the most reliable methods for design purposes are still the engineering ones, which are based on solid empirical bases and implemented in the technical standards in use in the industries all over the world. ISO 6336 (western Europe) [57], DIN3990 (Germany) [99] and AGMA 2101 (USA) [58] are the most common standard used for the calculation of the load carrying capacity of gears with respect to pitting and bending failures. ISO-TR15144 (Europe) [22] and AGMA 925-A03 (USA) [100] instead, deal with micropitting failures.

A brief description of the philosophy behind the calculation models of ISO 6336 and ISO-TR15144 is given in the next sections.

3.3.1 Calculation of pitting load carrying capacity according to ISO 6336

According to the ISO standard 6336, the validation of a gear design is based on the condition

$$\sigma_H \leq \sigma_{HP} \tag{3.6}$$

Where σ_H represent the maximum contact pressure acting on the tooth and σ_{HP} is a permissible value of pressure that the material could sustain for the required service life under given operating conditions. The value of σ_H in turn, is given by

$$\sigma_H = \sigma_{H0} Z_B \sqrt{(K_A \cdot K_V \cdot K_{H\beta} \cdot K_{H\alpha} \cdot K_\gamma)} \tag{3.7}$$

Where the product $\sigma_{H0} Z_B$ represents the nominal contact pressure calculated at the point within the path of contact where it reaches its maximum value, which usually correspond to the lowest point of single tooth pair contact of the pinion. Although expressed with different terms, the calculation procedure provided by the standard for spur gears takes advantage by the analogy with the contact between cylinders and is consistent with the method described in section 3.3. Then, K factors are introduced to increase the nominal contact force in order account for all the potential causes of overloads. More in detail:

- The *application factor* K_A accounts for possible dynamic overloads on the components of the transmission system due to the driver or driven machine.
- The *internal dynamic factor* K_V accounts for possible perturbations in the regular transmission of the force due to intrinsic wheel characteristics such as masses, inertia, meshing stiffness, micro-geometric deviations from the nominal profile, etc.
- The *face load factor for contacts* $K_{H\beta}$ accounts for contact pressure concentration caused by misalignments occurring between the meshing teeth due to:
  - manufacturing inaccuracies
  - assembly clearances
  - geometry modifications (e.g. crowning)
  - compliances under load of gears and shafts
- The *transverse load factor for contacts* $K_{H\alpha}$ accounts for the uneven distribution of load among various teeth simultaneusly in contact due mainly to their deflection under load, manufacturing inaccuracies and geometry changes as a consequence of running-in.
- The *load sharing factor* K_γ applies to gear stages which include power branching such as planetary gear sets. K_γ accounts for the possible uneven distribution of load among the various load paths (e.g. the various planets in a planetary gearing) due to positioning errors of the gear axes.

K factors are under the square root in equation (3.7) because the contact pressure developed in the contact between cylindrical bodies depends on the square root of the force.

The permissible stress is evaluated on the basis of experimental fatigue curves determined by tests on gears and provided by the standard for different materials. Accordingly, the permissible pressure is given by:

$$\sigma_{HP} = \frac{\sigma_{H\,lim} Z_{NT}}{S_{H\,min}} Z_L \cdot Z_R \cdot Z_V \cdot Z_W \tag{3.8}$$

The limit value $\sigma_{H\,lim}$ represents the endurance limit of the fatigue curve, or in other words, the maximum contact stress that a gear could withstand for at least 5×10^7 cycles with a survival probability of 99%. Values of $\sigma_{H\,lim}$ are provided in the part 5 of the standard for different class of material and, within each class, for three different material qualities addressed as follows:

- ML: modest demands on the material quality and on the material heat treatment process during gear manufacture;
- MQ: requirements that can be met by experienced manufacturer at moderate costs;
- ME: requirements that must be realized when a high degree of operationg reliability is required.

The relevant values of the endurance limit for case hardened steels are defined in Table 3.2

Table 3.2 Contact pressure endurance limits for case hardened steels with 99% of survival probability

	ML	MQ	ME
$\sigma_{Hlim}\ [MPa]$	1300	1500	1650

For each class of material moreover, the slope of the fatigue curve is defined by the coefficient Z_{NT}, which is a function of the required lifetime, as reported in Figure 3.5 for the particular case of case hardened steels.

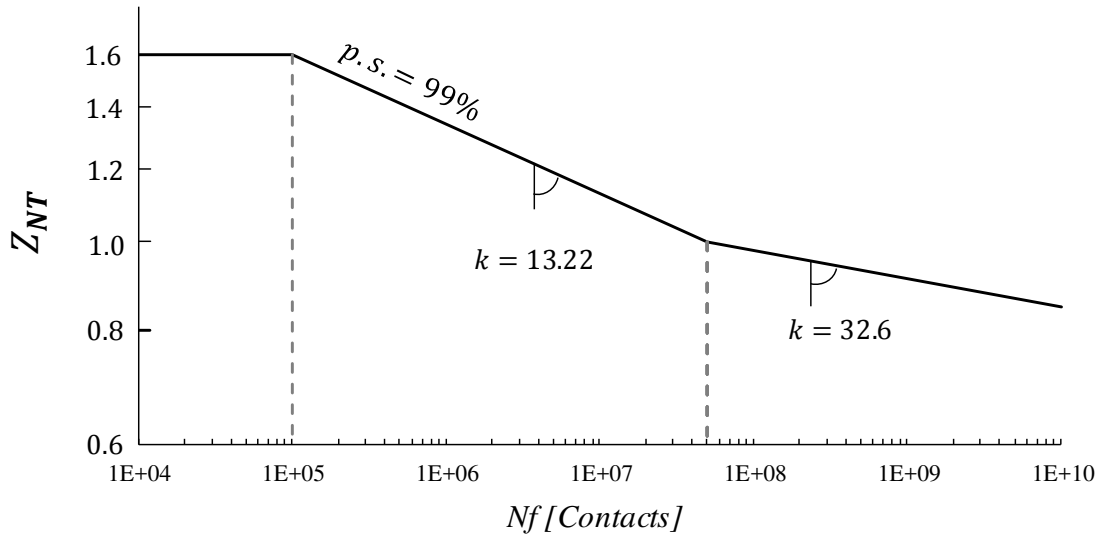

Figure 3.5 Life factor, Z_{NT} for case hardened steels.

Hence, the fatigue curve for a particular steel is given by the product of $\sigma_{H\ lim}$ for the Z_{NT}, as shown in Figure 3.6. The result is already accounting for a survival probability of 99%, however a further safety coefficient S_{Hlim} can be adopted at the discretion of the designer. Finally, the permissible value of contact pressure σ_{HP} relevant to the required lifetime should be corrected by factors Z_L, Z_R, Z_V and Z_W to take into account the difference between the

operating conditions of the actual application and the reference ones relevant to the tests from which the fatigue curves were determined. Specifically, Z_L accounts for the lubricant viscosity, Z_R for the roughness of the surfaces, Z_V for the speed, and Z_W for the hardness of the gears. It is to be noted that the influence of such influencing factors in the durability of gears decreases as the pressure increases. Thus, the ISO standard provides empirical formula and charts to compute their values with reference to the lower knee of the fatigue curve and suggest to assume a unitary value for the upper knee. For target lives between 1×10^5 and 5×10^7 cycles the result can be determined by interpolation in the double logarithmic scale. Figure 3.6 clarifies the procedure of validation of a gear pair according to the ISO standard.

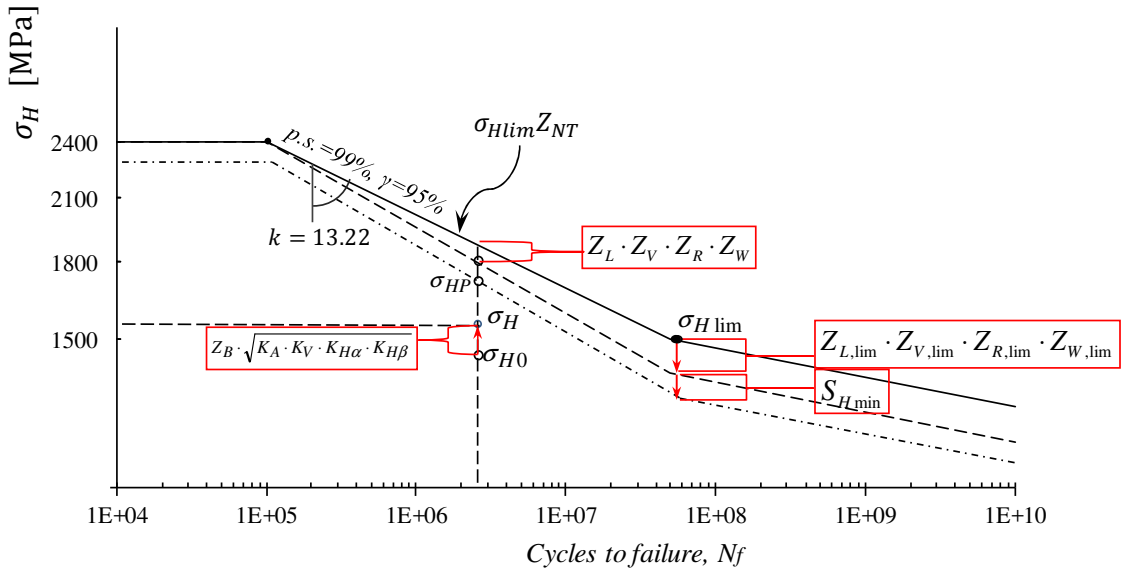

Figure 3.6 Scheme of the calculation procedure of ISO 6336 for a medium quality case hardened steel.

To better understand the role of the operating conditions in the durability of gears, a brief description of the factors introduced above is given in the following. Note that all the factors assume unitary values when the working conditions of the application to be rated correspond to the reference test conditions.

Lubricant Factor, Z_L

Within certain limits, an increase in lubricant viscosity may lead to an enhancement of the pitting durability, due to the improved capacity of the lubricant to form a film capable of separating the surfaces asperities. Figure 3.7 shows the curve of Z_L as a function of the nominal lubricant kinematic viscosity at 40°C, for materials having $\sigma_{H\,\mathrm{lim}}$>1200MPa.

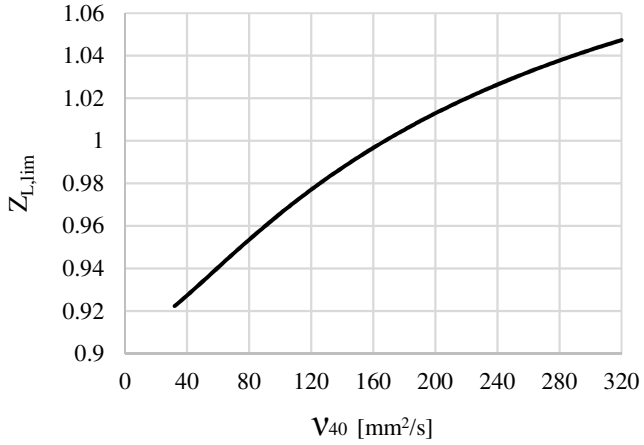

Figure 3.7 Lubricant factor, Z_L relevant to the lower knee of the fatigue curve, for steels with $\sigma_{H\,lim}$>1200MPa

Roughness factor, Z_R

Accounts for the fact that, especially in the contact between surfaces with small curvature radii, the dimensions of the actual contact area are reduced by the roughness. For case hardended steels, the value of Z_R relevant to the lower knee of the fatigue curve can be assessed by the chart in Figure 3.8, as a function of the parameter $R_{z\,10}$, which depend on the curvature radii and the roughness of the teeth flanks:

$$R_{z\,10} = \frac{R_{z1} + R_{z2}}{2} \sqrt[3]{\frac{10}{\rho_{red}}} = \frac{R_{z1} + R_{z2}}{2} \sqrt[3]{\frac{10}{\rho_{red}}} \tag{3.9}$$

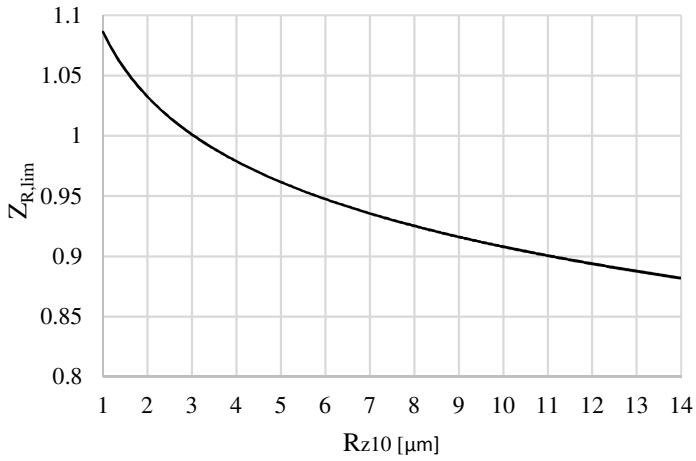

Figure 3.8 Roughness factor, Z_R relevant to the lower knee of the fatigue curve, for steels with $\sigma_{H\,lim}$>1200MPa

Velocity Factor, Z_V

Accounts for the beneficial influence of a greater entraining speed in the formation of an elastohydrodynamic film of lubricant. Z_V can be evaluated by the chart in Figure 3.9 given the value of the pitch line velocity of the gear v, expressed by the product of the reference radius r by the angular speed ω:

$$v = r\omega \tag{3.10}$$

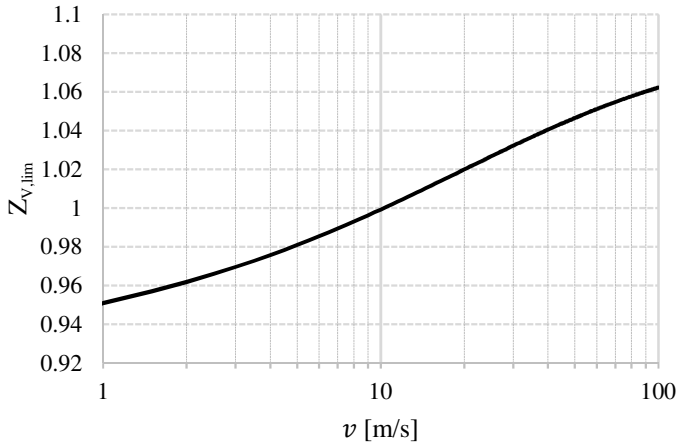

Figure 3.9 velocity factor, relevant to the lower knee of the fatigue curve, for steels with $\sigma_{H\,lim}$>1200MPa

Work Hardening Factor Z_W

Z_W is function of the hardness and roughness of the surfaces and can be introduced to consider that the durability of the gears can be improved by an greater pinion hardness with respect to the wheel. When both the pinion and the wheel are case hardened, Z_W is considered equal to unit.

3.3.2 Calculation of the micropitting load capacity according to ISO-TR 15144

The approach for the calculation of the micropitting load capacity of gears is substantially different as compared to the calculation method for pitting. First of all, micropitting, occurs preferably in materials characterized by a high surface hardness and is related to the contact among asperities. Therefore, the controlling parameter in this case is the lubricant film thickness which depends more on the entraining speed of the surfaces rather than on the applied load.

Then, the ISO technical report does not provide a direct method to assess the micropitting load capacity for a required lifetime, but rather suggest a procedure to evaluate whether, under specific operating conditions, the lubricant film thickness is thick enough to prevent metal to metal contacts. If not, in fact, micropitting would occur in a relatively short period.

The standard is based on the Dowson and Higginson formula, which is used to compute the minimum value assumed within the path of contact by the ratio between the lubricant film thickness at the generic point Y, h_Y and the mean composite roughness of the surfaces R_a, expressed in the form:

$$\lambda_{GF,min} = \min\left(\frac{h_Y}{R_a}\right) = 1600\ \rho_{rel,Y}\ G_M^{0.6} U_Y^{0.7} W_Y^{-0.13} S_Y^{0.22} \tag{3.11}$$

With the following meaning of the terms:

- $\rho_{rel,Y}$ is the normal radius of relative curvature of the surfaces
- G_M is a material-dependent parameter
- U_Y is function of the entraining speed of the surfaces
- W_Y depends on the applied load
- $S_{GF,Y}$ accounts for the effect of the sliding speed on the temperature of the lubricant and, in turn, on its viscosity.
- $R_a = 0.5(R_{a1} + R_{a2})$

Again, it is worth noting that that the exponent relevant to parameter G is much greater with respect to the exponent applied to parameter W, indicating the greater influence of the speed as compared to the load. The calculated λ-ratio is then compared with a limit value relevant to the specific oil used in the gearbox to be rated, which can be determined by means of the FVA-FZG micropitting test, performed according to FVA-Information Sheet 54/7 [101] by increasing stepwise the torque applied to a reference gear pair in a power-recirculating test rig until micropitting is observed on the surface. It may be noted that the (3.11) is equivalent to the equation reported in section 3.2.1 for line contacts, except for the sliding parameter S_Y, which is not included in the original theory of Dowson and Higginson and whose significance is debated [102].

Note that the range of applicability of Equation (3.11) is limited to cases where the pitch line velocity is $\geq 2\ m/s$, and that the ISO-TR 15144 procedure was developed on the basis of

experimental evidences relevant to gears with pitch line velocity in the range $8 \div 60\ m/s$. For values of pitch line velocity $< 2m/s$, the entraining speed is generally just too low to allow the formation of an elastohydrodynamic film of lubricant. Experimental works carried out within the present project, however, were aimed to investigate RCF failures on the slow sun gears of the final drive in axles for heavy duty vehicles, where the pitch line speeds are typically in the order of $0.5\ m/s$. In such applications a fully developed elastohydrodinamic lubricant film is not expected to form and surface distress could be only delayed by providing a good surface finish as well as an appropriate period of running-in at moderate loads. Therefore, the calculation method will not be treated here in further detail.

Chapter 4

ANALYSIS OF CARRARO'S DATABASE OF TESTS

As mentioned in the previous chapter, the ISO standard 6336 is structured to allow an easy evaluation of the nominal contact stresses acting on gears teeth, based on the main geometric features of the gear. Such value is then corrected with several factors to account for the influence of various aspects relevant to the operating conditions of the application, and the characteristics of the other components of the system. The calculated stress is finally compared to a permissible value based on empirical stress-life curves. The reliability in the prevision of the lifetime of a gear pair depends on the accuracy in the determination of the correcting factors, as well as of an appropriate permissible stress for the particular material and working conditions relevant to the application. For both these aspects, the standard suggests several different approaches, divided into classes denoted by the letters A, B and C, where:

- A is always relevant to results of full scale tests of the transmission system or at least to comprehensive theoretical model capable of accounting for all the possible influencing factors
- B indicates calculation methods developed to allow a relatively fast determination of the result with an acceptable degree of approximation
- C implies the use of simplified formulas or charts for a rough estimation of the unknown quantity

Obviously, the accuracy of the method, as well as the involved costs, decrease from A to C. The compromise method B, which usually provides a good accuracy at reasonable costs is implemented in several dedicated software packages. Despite their continuous progress however, the prevision of the actual pressure distribution on gears teeth still constitute a delicate issue. Particularly, as will be shown more in detail in Chapter 5, some aspects such as manufacturing inaccuracies are difficult to be predicted and their effect on the maximum value of pressure acting on the teeth may be hardly included in the model. Therefore, experimental

validation of the theoretical models is suggested at least in the development of new products for which a consolidated know how is not available.

Concerning the determination of reliable values for the permissible stress relevant to a particular material and required lifetime, the standard provides fatigue curves defined for classes of materials. Case hardened steels are all grouped in the same class regardless their composition and the eventual additional treatment they are subjected to (e.g. shot peening). A distinction can be made on the basis of the quality but in the industrial practice, the ranking of a particular material according to the prescription of the standard can be difficult due to partial or missing information from the suppliers, and may lead to serious misjudgements of the limits of the material. It is worth noting that, since the slope of the S-N curve for pitting in case hardened steel is approximatively 13.22, small deviations in the calculated pressure as well as in the permissible stress may result in very different values of predicted life. Therefore, it appears evident that, for the prevision of the lifetime of a transmission system, both the model and the fatigue data should be as representative as possible of the material and of the real working conditions of the gears object of rating.

This chapter resumed and carried forward an activity initiated by Dengo in the course of his Ph.D. project [1]. Dengo examined the database of bench tests performed by Carraro on the final products before the release to the market in order to determine the most common failure mode occurring in each test. Data relevant gear failures of gears were then used to derive valuable information about the fatigue performance of the materials used in gears manufacturing by the suppliers of the company. The work was mainly focused upon bending failures, nevertheless a section was dedicated to the analysis of pitting occurring in sun gears during tests performed on the complete axle. A model of the planetary gear set in the wheel hub was executed for a series of axle subjected to FSTs since the 2002 by means of the commercial software package KISSsoft. The models allowed the calculation of the maximum contact pressure acting at the Lowest Point of Single Tooth Contact (LPSTC) of the sun gear teeth within each test, and therefore the determination of a point in the stress-life plane, relevant to the first observation of pitting during the test. In this section, the work initiated by Dengo was reviewed by using the Tooth Contact Analysis (TCA) algorithm implemented in KISSsoft, for a more comprehensive evaluation of the contact pressure field over the whole flank area. Moreover, the analysis was extended including fourteen tests on different axles for a total number of 38 failed sun gears. The maximum contact pressure, calculated by means of the TCA, was then corrected by the coefficient suggested by ISO 6336 [57] to account for the real

operating conditions. Stress-life data were plotted in S-N charts and then used to define a design pitting curve considering the slopes recommended by ISO6336-5. The statistical scatter of the phenomenon was evaluated as well.

4.1 The Four-Square Test

The Four-Square Test (FST) bench is a power recirculating rig designed to investigate the structural durability of gears and bearings of axles (Figure 4.1). Two axles are positioned with their input shafts facing each other, and mechanically connected by means of a cardan shaft driven by an electric motor. On each side of the bench, a pair of sprockets connected by a chain is mounted on the wheel hubs of the axles. The cardan shaft is preloaded to impose a given applied torque to one of the two axles (hereafter referred to as the main axle), while the second (auxiliary) axle closes the kinematic chain recovering the power. Thus, operation under high wheel torques can be simulated with limited energy consumption. Torque, speed and lubricant temperature are measured during the test, lubricant cooling being provided by fans when the temperature set point is exceeded.

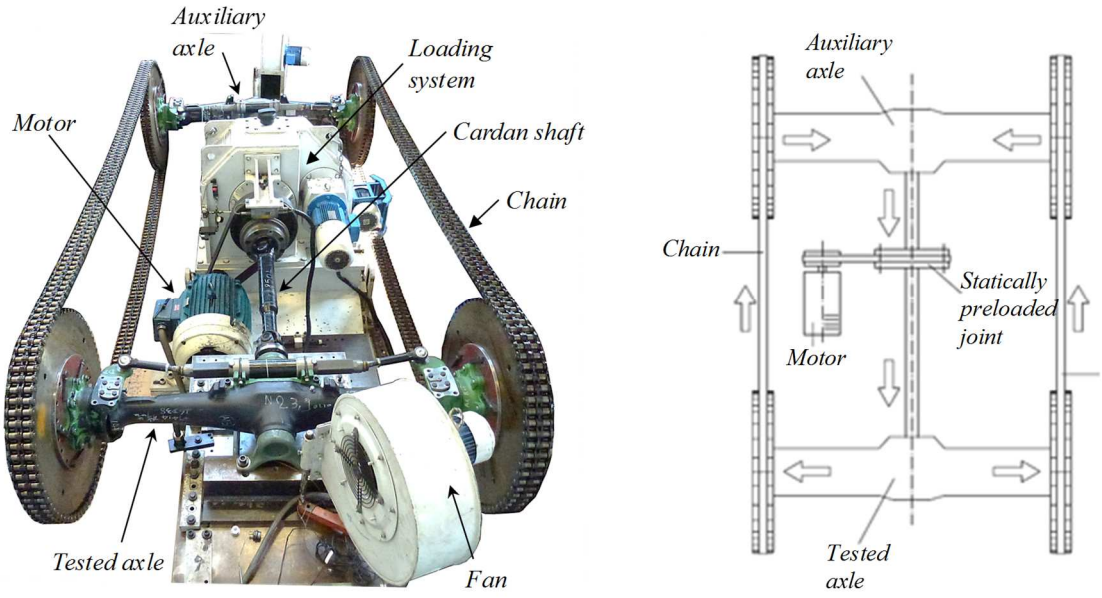

Figure 4.1 The four-square test set-up

Table 4.1- Duty cycle of the four-square test.

Load Case	Wheel Torque	Wheel Speed [rpm]	Duration [h]	Running Direction
1	Tc °	30	320	Forward
2	Tc °	30	80	Reverse
3	Tc °	30	80	Forward
4	Tp *	10	2	Forward

° Continuous torque: torque that produces a nominal contact stress around 1400-1650MPa on the tooth flanks of the sun gear of the planetary gear set. Tc is therefore dependent on the axle size. In the present analysis, Tc was in the range of 4320 ÷ 20640Nm.

** Peak torque:* $Tp = {}^{Tc}/_{0,48}$

The typical test program conducted on the axles is shown in (Table 4.1). Every 100 hours (or every time a failure is detected) the two axles are disassembled and each part is carefully inspected to ascertain possible damage. Depending on the percentage of worn surface observed, a pitting level is assigned to the component by visual inspection, according to Table 4.2.

The axles are assumed to have passed the test if at the end of the duty cycle of Table 4.1 they are still working and the pitting level of all the components is lower than 4.

Table 4.2 Pitting levels (determined by visual inspection).

Pitting Level	Percentage of Damaged Area
0	< 5%
1	5 %
2	10 %
3	25 %
4	50 %
5	100 %

4.2 Details of the tested products

The main features of the gears are summarized in Table 4.3, along with the number of pitting fatigue failures observed for each FST.

Table 4.3 – Geometry and test data of the sun gears

FST code	*Sun gear material*	*Normal Module* m_n	*Number of teeth* z	*Length of contact* b_{eff}	*Shot peening*	*Lubricant viscosity at 40°C*
		Mm		*mm*		*mm²/s*
3060	Ext. Supply	3	13	52	Yes	144
3098	Ext. Supply	3	13	44.6	Yes	66
3218	17NiCrMo6-4	2.9295	15	39	No	100
3268	17NiCrMo6-4	2.9295	15	44	No	55
3319	EN 353	2.9295	15	39	No	100
3353	Ext. Supply	3	12	39.6	Yes	66
3436	17NiCrMo6-4	3	13	44.6	Yes	66
3879	Ext. supply	2.75	12	31	No	56
3671	Ext. supply	3	12	39.6	Yes	66
2057	17NiCrMo6-4	3	12	29	No	59
2091	17NiCrMo6-4	3	12	29	Yes	59
3820	Ext. supply	2.9295	15	46.6	No	56
3568	17NiCrMo6-4	2.75	12	31	No	66
4286	Ext. supply	3	12	39	No	100

The tests were all made on case-hardened gears, twelve of which were subjected to shot peening. While no distinction was made for different compositions of the material, according to the ISO standard that groups all case hardened steel in a single class with uniform fatigue strength, results relevant to shot peened and un-peened gears were treated separately in order to investigate whether the compressive residual stresses introduced by shot peening could influence positively the pitting durability of the material.

4.3 Calculation method

The aims of the present analysis were to derive an endurable value of $\sigma_{H\,lim}$ based on the failure observed during the four-square tests, and to evaluate the statistical scatter of the pitting phenomenon. Each pitting failure occurred in a FST can be represented by a point in the $\sigma_{H\,lim}Z_{NT} - N_f$ chart. The value of $\sigma_{H\,lim}Z_{NT}$ is defined by computing all Z and K factors relevant to the specific application. It is assumed that a failure occurs when:

$$\sigma_H = \sigma_{HP} \tag{4.1}$$

Or, by equations 5.7 and 5.8:

$$Z_B \cdot \sigma_{H0} \cdot \sqrt{K_A \cdot K_V \cdot K_{H\beta} \cdot K_{H\alpha}} = \frac{\sigma_{H\,lim} Z_{NT}}{S_{H,min}} Z_L \cdot Z_R \cdot Z_V \cdot Z_W \tag{4.2}$$

Where the safety coefficient $S_{H,min}$ is set to unity. Equation (4.2) can be rearranged as follows:

$$(\sigma_{Hlim}Z_{NT})_{ISO} = \frac{Z_B \cdot \sigma_{H0}}{Z_L \cdot Z_R \cdot Z_V \cdot Z_W}\sqrt{K_A \cdot K_V \cdot K_{H\beta} \cdot K_{H\alpha}} \tag{4.3}$$

The term $(\sigma_{H\,lim}Z_{NT})_{ISO}$ represents the pitting fatigue strength for a given life (defined by the life factor Z_{NT}), computed according to the calculation algorithm proposed by the ISO standard 6336.

In this work the commercial software KISSsoft was used to create models of each planetary gear set considered in the analysis (Figure 4.2), in order to evaluate the maximum contact stress acting on the sun gear teeth during the FST. The kinematic chain was the same for all models but each one contained different information about the geometry of gears and shafts, the type and size of the supports, the lubricant, speeds and loads. The software implements the formulae of the standard ISO6336 to evaluate all the correction factors presented in chapter 3.

Figure 4.2 KISSsoft model of the planetary gear set located in the hub of an axle for agricultural vehicles.

Particular attention should be paid to the face load factor $K_{H\beta}$ of equation (4.3), which is defined as the ratio between the maximum force per unit width along the pitch line of a tooth and the nominal force per unit width. As already mentioned, it accounts for gaps between the contact surfaces, due to profile modifications, displacements, misalignments and manufacturing allowances, which may reduce the contact area causing substantial modifications to the Hertzian pressure distribution. The face load factor cannot be determined simply from the gear geometry, since also the compliance of shafts and housings as well as the bearing allowances

affect the teeth alignment. The Annex E of ISO6336-1 provides an iterative calculation method for the evaluation of the load distribution along the pitch line (Figure 4.3).

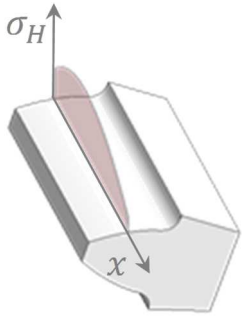

Figure 4.3 Distribution of the normal force along the pitch line.

The tooth face width is divided into slices, each one modelled as an independent spring representing the meshing stiffness calculated at the pitch line of the tooth. The displacements of gear body and shafts are calculated and summed to misalignments introduced by bearing clearance and teeth modifications (e.g. crowning). Such displacements create a gap between the mating surfaces, which causes some regions of the teeth flanks to come into contact before other ones. Therefore, for the subsequent iteration the load is redistributed among the slices in inverse proportion with the mutual distance between the slices composing the mating teeth, namely the slices with lower gap will carry a higher load. Such a load distribution is used to compute again the shaft and tooth deflections, defining new gaps, and thus a new load distribution. The procedure terminates when the gap distributions of subsequent iterations differ of less than a target admissible error.

It must be noted that according to ISO6336-2, the surface durability is based on the highest between the two contact stresses obtained at the pitch point and at lowest point of single tooth contact. For spur gears with transverse contact ratio $\varepsilon_\alpha \geq 1$ (corresponding to the cases here presented) the contact stress at the LPSTC is usually greater than that at the pitch point and therefore the former is used to assess the pitting strength. Since the procedure here presented allows to estimate the contact pressure only at the pitch point, the factor Z_B is introduced in equation (4.3) to consider the higher value at LPSTC.

The calculation method according to ISO6336-1 Annex E allows to evaluate with reasonable accuracy the distribution of normal force along the pitch line, but it gives no information about the contact stress on the other zones of the tooth flank which may be subjected to higher pressures, at least in some cases. As an example, tip and root relief are commonly performed in sun gears to avoid tip to root interference and to reduce the transmission error. These

modifications introduce a reduction of the local curvature radius along the tooth flank profile, at the point where the relief is introduced. This results in an increase of contact pressure in those areas, as shown in Figure 4.4.

Several software packages for gear Tooth Contact Analysis (TCA) have been developed over the years to allow a more comprehensive evaluation of the effect of misalignments and gear microgeometry on the whole tooth face. TCA could be made through FEM based approaches, but it would require a great effort to generate an appropriate mesh and run the calculation. Thus many software implement less time-consuming analytical methods based on recursive calculations [103].

KISSsoft provides a TCA algorithm, based on the theory of Weber and Banascheck [104], for the evaluation of the pressure field on the tooth face. The force distribution along the contact line is computed for a defined number of points along the path of contact, resulting in a 3D plot of the stress field.

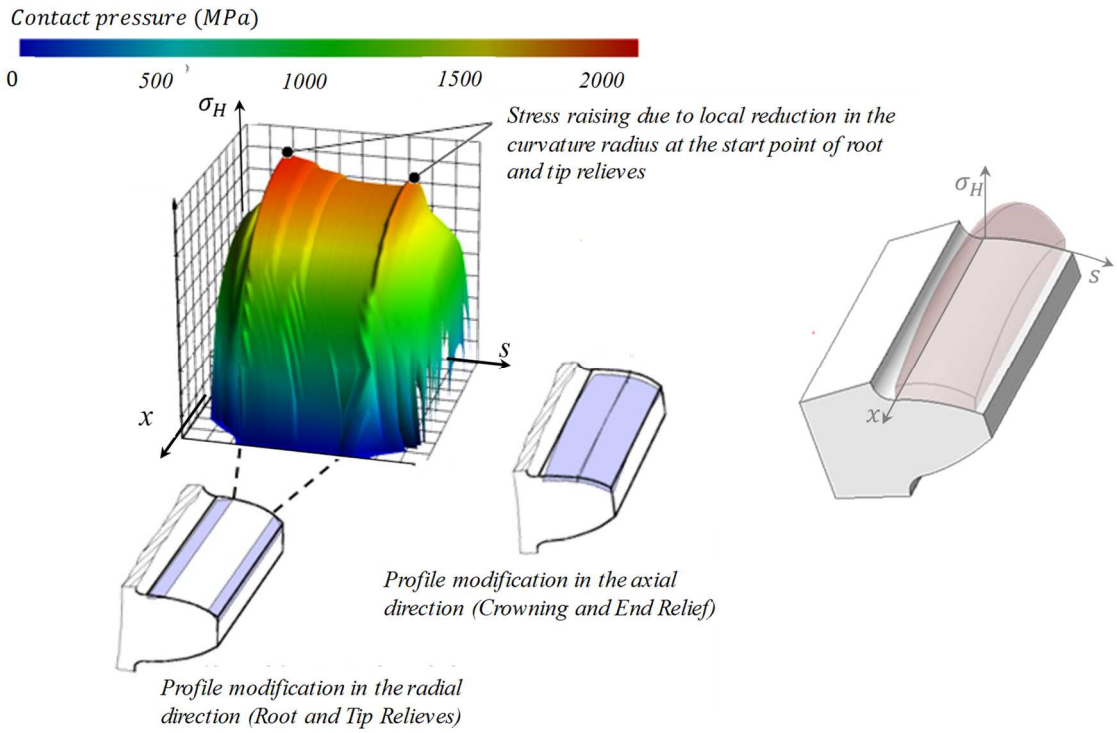

Figure 4.4 3D plot of contact pressure along the tooth flank of the sun gears in the axle tested in FST3879 ($T_c = 4320\ Nm$).

For each point the tooth is divided into slices, mutually coupled through a stiffness (C_c). Each slice is basically a spur tooth with infinitesimal thickness and is characterized by a series of three stiffnesses (variable over the path of contact) corresponding to the principal modes of deflection: bending, tilting of the gear body and Hertzian flattening, characterized by C_B, C_{RK}

and C_H stiffnesses respectively (Figure 4.5). One gear is twisted against the other, which is considered fixed by imposing an initial deformation of the mating teeth. The imposed deformation is split in three contributions according to the local stiffness relevant to each of the three deformation modes. The force acting on the slices is therefore determined by the imposed deformation by the corresponding stiffness.

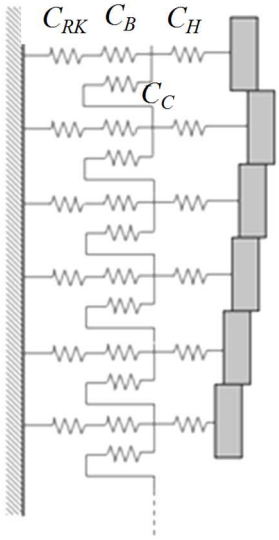

Figure 4.5 Scheme of the spring model for the tooth.

The amount of twisting is incremented step by step until the sum of the torques obtained by the force acting on each slice equals the nominal torque that must be transmitted by the entire gear. Finally, the force transmitted by the slices is used to evaluate the pressure field using the formulae of the Hertzian theory for contacts between cylinders. Therefore, the first term of Equation (4.2), representing the maximum contact stress at the LPSTC, can be substituted by the maximum contact stress $\sigma_{H\,TCA}$ evaluated on the whole flank area using the tooth contact analysis. In this case, the nominal pitting fatigue strength can be determined using the following expression:

$$(\sigma_{Hlim} Z_{NT})_{TCA} = \frac{\sigma_{H\,TCA}}{Z_L \cdot Z_R \cdot Z_V \cdot Z_W} \tag{4.4}$$

4.4 Discussion of the results

For each test, Table 4.4 summarises all pitting failures on the sun gears of the tested axles. In some cases, damaged sun gears have been substituted during the test due to premature failure, thus the actual number of data for each FST may be higher than two. Concerning the adopted failure criterion, sun gears are considered to be failed when a percentage of pitted area between 0 and 5% was found at least on one tooth (incipient pitting or pitting level 1), during periodical inspections. This criterion was chosen for consistency with the "no pitting allowed" curves of ISO6336, which were obtained considering a failure criterion corresponding to 4% of the working area of a single tooth damaged by pitting or 0.5% of the total working area of all the teeth.

The contact stresses acting on the tooth flanks during each test have been evaluated according to ISO6336-1 Annex E and through the TCA of KISSsoft. The values of $(\sigma_{H\,lim} Z_{NT})_{ISO}$ and $(\sigma_{H\,lim} Z_{NT})_{TCA}$, calculated with equations (4.3) and (4.4), respectively, are reported in Table 4.4, along with all the relevant calculation factors, evaluated by KISSsoft software according to ISO 6336. The face load factor $K_{H\beta}$, was calculated with the iterative method described into Annex E of ISO6336-1, without taking into account manufacturing allowances. It is important to note that the correction factors Z_L, Z_V and Z_R depend on the fatigue life of the considered gear, because of the procedure used in [105] to determine these factors, where they are evaluated for the low- and high-cycle knees of the pitting fatigue curve. Therefore, the correct value for a given number of cycles was obtained by means of a linear interpolation in a $\log \sigma_H - \log N_f$ chart (see figure 3.6).

As shown in Table 4.4, the TCA approach estimated contact pressures 2% to 23% higher than the standard calculation according to ISO 6336. Since the applied torque during FST test was chosen to produce a contact pressure in the range 1400÷1650 MPa, all available data gather around a limited range of fatigue life. Therefore, it was not possible to derive a sufficiently accurate estimation about the slope of the fatigue curve and the positions of high- and low-cycle fatigue knees. For this reason, the slope k=13.22 recommended by ISO 6336 was used to draw the fatigue curve, placing the low- and high-cycle fatigue knees according to the standard, i.e. at 1E05 and 5E07 cycles respectively. For number of cycles greater than 5E07, the standard suggests to use a horizontal line only in the case of optimum lubrication, material, manufacturing and experience. Otherwise a sloping line up to 1E10 cycles is suggested.

Table 4.4 – Summary of the results

FST #	*Sun Gear #*	*Pitting Level*	*Load Cycles [x10^6]*	*Elapsed Time* □ *[h]*	σ_{H0}* *[MPa]*	Z_B*	$K_{H\beta}$*	Z_L*	Z_V*	Z_R*	$(\sigma_{Hlim}\cdot Z_{NT})_{ISO}$* *[MPa]*	$(\sigma_{Hlim}\cdot Z_{NT})_{TCA}$° *[MPa]*	*Stress difference TCA-ISO %*
3060	1	0	3.2	100	1616	1.13	1.17	1.04	0.96	0.95	2248	2615	16
	2	1	3.2	100				1.04	0.96	0.95	2248	2615	
	3	1	3.2	100				1.04	0.96	0.95	2248	2615	
3098	1	0	5.39	169	1639	1.13	1.31	0.96	0.96	0.96	2381	2495	5
3268	1	1	3.65	100	1402	1.06	1.21	0.96	0.97	0.96	1829	2073	13
	2	0	8.33	228				0.95	0.96	0.95	1887	2139	
	3	0	7.31	200				0.96	0.96	0.95	1867	2117	
	4	0	9.94	272				0.95	0.96	0.95	1887	2139	
	5	1	16.5	452				0.95	0.96	0.94	1907	2162	
	6	0	8.04	220				0.96	0.96	0.95	1867	2117	
	7	0	11	300				0.95	0.96	0.94	1907	2162	
3218	1	1	5.83	200	1589	1.06	1.15	0.98	0.96	0.95	2038	2153	7
	2	1	2.92	100				0.98	0.97	0.96	1979	2108	
	3	0	2.92	100				0.98	0.97	0.96	1979	2108	
3319	1	1	8.75	300	1589	1.06	1.15	0.98	0.96	0.95	2021	2153	7
	2	0	11.7	400				0.97	0.96	0.94	2064	2198	
	3	0	2.33	80				0.97	0.96	0.94	2064	2198	
	4	0	2.33	80				0.97	0.96	0.94	2064	2198	
	5	0	2.92	100				0.98	0.97	0.96	1979	2108	
	6	0	5.83	200				0.98	0.96	0.95	2021	2153	
	7	0	8.16	280				0.98	0.96	0.95	2021	2153	
3353	1	0	7.2	200	1456	1.14	1.11	0.96	0.96	0.95	1997	2037	2
	2	0	14.4	400				0.96	0.96	0.95	1997	2037	
3436	1	0	6.39	200	1505	1.13	1.26	0.96	0.96	0.96	2158	2236	4
	2	0	6.39	200				0.96	0.96	0.96	2158	2236	
3879	1	1	8.64	400	1457	1.10	1.25	0.96	0.96	0.95	2121	2211	4
3671	1	0	7.2	200	1435	1.14	1.26	0.96	0.96	0.97	2054	2518	23
	2	0	7.2	200				0.96	0.96	0.97	2054	2518	
2057	1	0	6.30	250	1384	1.14	1.25	0.96	0.96	0.97	1973	2199	11
	2	1	9.37	372				0.96	0.96	0.96	1994	2222	
2091	1	0	6.63	263	1384	1.14	1.23	0.96	0.96	0.97	1957	2225	14
	2	0	6.63	263				0.96	0.96	0.97	1957	2225	
3820	1	0	5.83	200	1548	1.06	1.14	0.96	0.96	0.96	1980	2394	21
	2	0	5.83	200				0.96	0.96	0.96	1980	2394	
3568	1	0	2.16	100	1505	1.10	1.28	0.97	97.00	0.97	2052	2401	17
	2	0	4.32	200				0.97	97.00	0.97	2052	2401	
4268	1	1	10.8	300	1427	1.14	1.21	0.97	0.96	0.96	1998	2073	4
	2	1	10.8	300							1998	2073	

**Calculated by the software KISSsoft according to ISO 6336*

° Maximum stress acting on the tooth face, determined through KISSsoft TCA and subsequently corrected using Z_L,Z_V,Z_R

□ Corresponding to a maximum pitting level of 0 or 1 according to Table 4.2

The clouds of points obtained from the analyses were fitted using a least square regression, obtaining thus a curve at 50% of survival probability. Then, the scatter on the results was estimated using the approach presented in [106] based on the expression:

$$\log N_{p,\gamma} = \log \overline{N} - qs \tag{4.5}$$

where $N_{p,\gamma}$ is the anticipated life for a survival probability of $p\%$ and a confidence level of $\gamma\%$, $\overline{N}$ is the life at 50% of survival probability, s is the standard deviation of the number of cycles and

$$q = f(p, \gamma, \nu) \tag{4.6}$$

is the Lieberman factor assuming a log-normal distribution of the fatigue life data. The q factor is related to the desired survival probability and confidence level of estimations, and to the sample size n considered in the analysis (ISO 12107. Metallic materials - Fatigue testing - Statistical planning and analysis of data, 2003). The sample size is indeed used to define the number of degrees of freedom ν of the distribution, being $\nu = n - 2$ to account for the fact that analysis is performed considering different stress levels.

In order to verify whether the shot peening treatment of gears may improve the contact fatigue strength of case hardened steels, two different curves were determined for shot peened and un-peened sun gears. A 8% increment on the endurance limit has been observed for the shot peened sun gears as compared to un-peened ones (Figure 4.6). However, due to the small number of tested axles with shot-peened sun gears, the relevant scatter band is wider than for un-peened steels. More precisely, for shot peened steels 12 data were available against a number of 24 for un-peened steels. Considering p=99% and γ=95%, the scatter indexes are:

$$T_{\sigma,1-99,Un} = \frac{(\sigma_{H\,\mathrm{lim},Un,1\%})_{TCA}}{(\sigma_{H\,\mathrm{lim},Un,99\%})_{TCA}} = 1.43 \tag{4.7}$$

for un-peened steels (“Un” subscript), and

$$T_{\sigma,1-99,Sh} = \frac{(\sigma_{H\,\mathrm{lim},Sh,1\%})_{TCA}}{(\sigma_{H\,\mathrm{lim},Sh,99\%})_{TCA}} = 1.80 \tag{4.8}$$

for shot peened steels ("Sh" subscript). Therefore, further data relevant to shot peened gears are needed in order to better investigate the scatter and derive more reliable design curves at high survival probabilities.

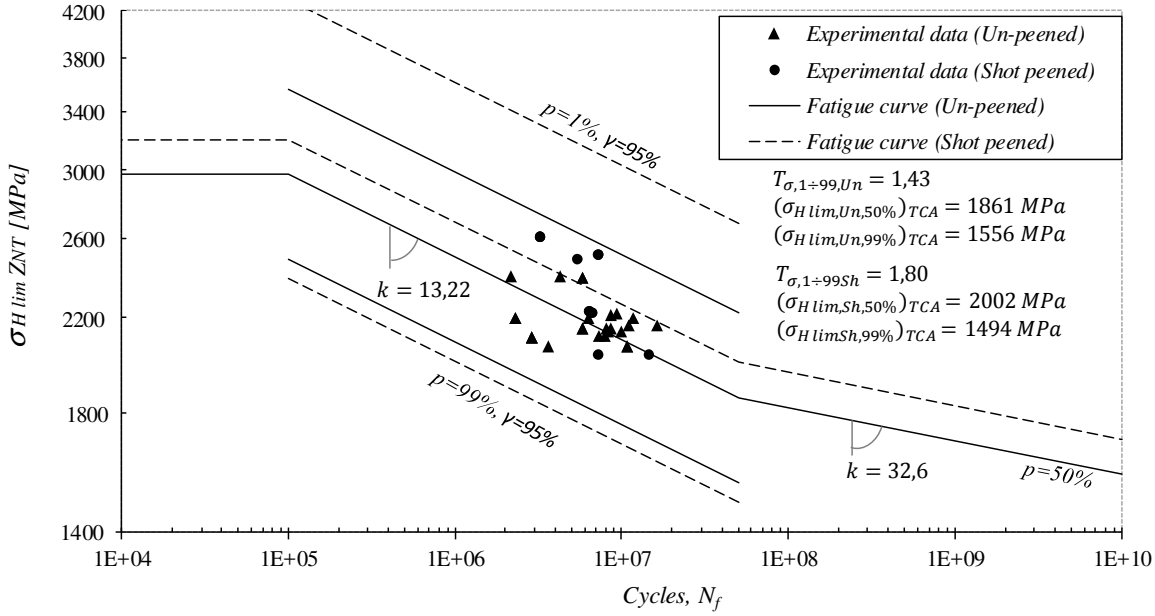

Figure 4.6 Comparison between pitting curves for shot peened and un-peened case-hardened steels.

The two endurance limits obtained with the best fitting curves at 50 million cycles on un-peened and shot-peened sun gears, have been used to normalize the data in order to evaluate the intrinsic scatter of the fatigue phenomenon. Thus, all the 38 data collected could be plotted in a chart reporting the life factor Z_{NT} versus the number of cycle at the pitting occurrence, being $Z_{NT} = \sigma_{HP}/\sigma_{Hlim}$. The normalized data are reported in Figure 4.7 along with the corresponding fatigue curve at p=50% and the scatter bands for p=1-99% considering γ=95%. The scatter index corresponding to such approach results:

$$T_{\sigma,1-99} = \frac{Z_{NT,1\%}}{Z_{NT,99\%}} = 1.52 \tag{4.9}$$

which is comparable with the values found in the literature. For instance a reliability factor $f_{99H} = 0.88 \div 0.92$ is suggested in [107] (Figure 4.8) to convert the permissible contact stress

at 50% survival probability into the value at 99% of survival probability, while for the present analysis the ratio between the two values is equal to

$$(1.52)^{-\frac{1}{2}} = 0.81 \tag{4.10}$$

Note that the corresponding life-based scatter index is

$$(1.52)^{13.22} = 254 \tag{4.11}$$

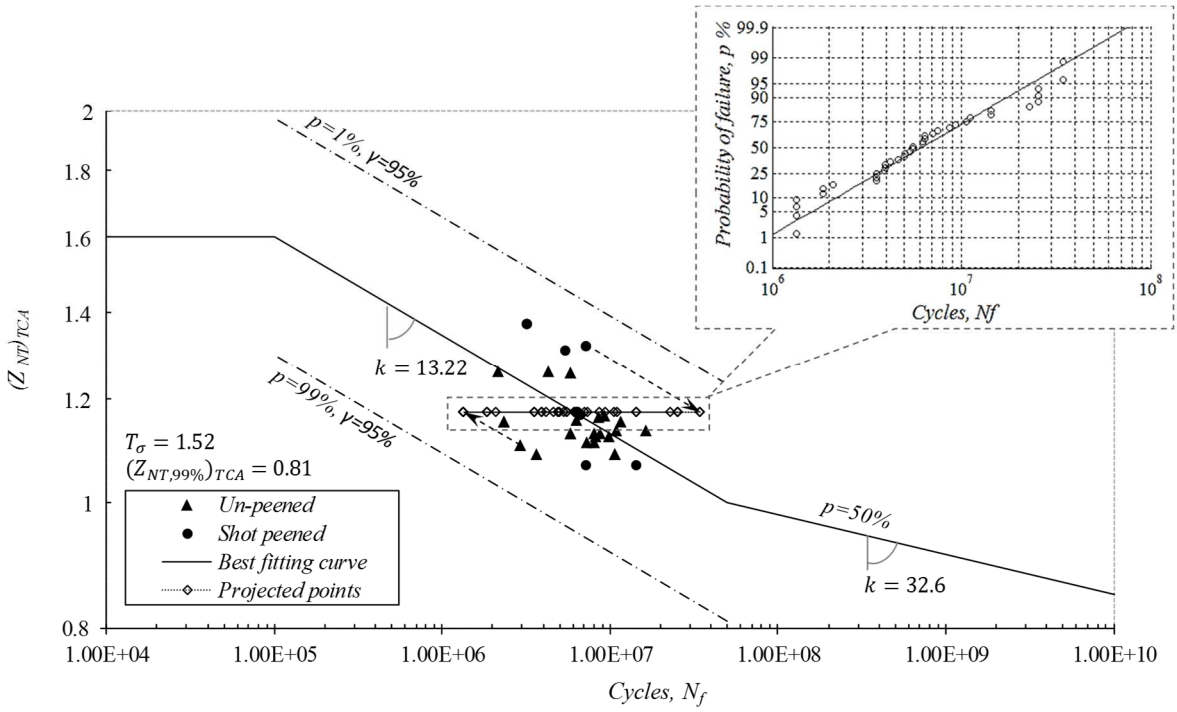

Figure 4.7 Pitting curves for case-hardened steels and plot of fatigue data on normality chart.

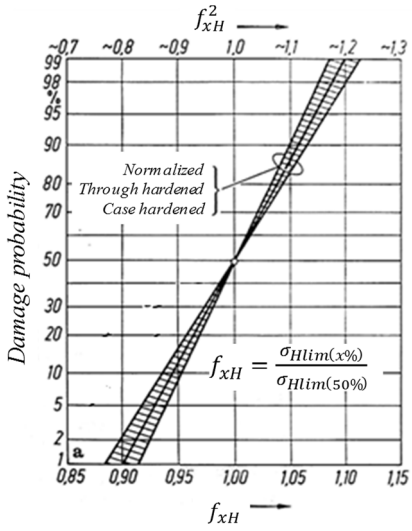

Figure 4.8 Reliability factor for pitting in normalized, through hardened and case hardened steel gears according to [107]**.**

In order to verify the hypothesis of log-normal distribution, data have been projected parallel to the curve to a single load level. Projected points have been then reported on a normality paper according to [106] showing that log-normal distribution line fits very well the experimental data.

Figure 4.9 shows the pitting curve for case-hardened steels of Figure 4.7 compared to the curves recommended by ISO 6336 for different steel qualities. It can be seen that the experimental curve is well represented by the pitting curve for medium quality case-hardened steels of ISO6336-5 (MQ, $\sigma_{H\,lim} = 1500$ MPa).

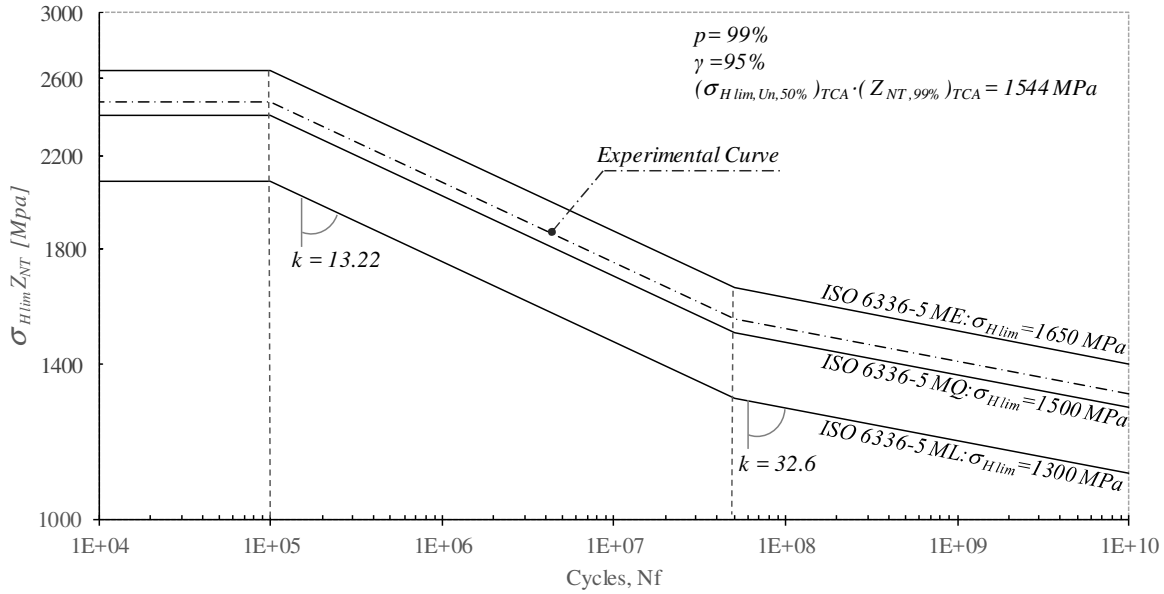

*- **ML** stands for modest demands on the material quality and on the material heat treatment process during gear manufacture.*
*- **MQ** stands for requirements that can be met by experienced manufacturers at moderate cost.*
*- **ME** represents requirements that must be realized when a high degree of operating reliability is required.*

Figure 4.9 Experimental curve for un-peened case-hardened steels as compared to the curves defined in the ISO standard 6336.

The fatigue curve obtained from experimental data and reported in Figure 4.9 is representative of case-hardened steels employed by Carraro S.p.A. and can be adopted for design of gears against pitting with 99% of survival probability. The difference between the values of $(\sigma_{Hlim}Z_{NT})_{ISO}$ and $(\sigma_{Hlim}Z_{NT})_{TCA}$ highlights the dependence of the results on the calculation method. Therefore, the proposed curve is reserved to analysis performed by means of a TCA, while if the contact stresses are calculated according to the Annex E of the ISO standard, more conservative limits are suggested, such as those proposed in [1]. Alternatively, a higher safety coefficient should be adopted.

4.5 Conclusions

Although the analysis of the database of tests performed by Carraro on the complete axles allowed to obtain valuable information about the materials used by the company's suppliers, the quality of the results is affected by some major limitations of these kind of tests: first of all inspections are performed only every 100 hours, therefore the determination of the number of cycles elapsed before the failure of the gear was necessarily approximative. Then, experimental investigation of the tooth root strain during bench testing of sun gears, which will be discussed in the next chapter, showed that manufacturing inaccuracies can considerably affect the load distribution on gears teeth contributing to widen the scatter of results. This is particularly likely for the prototypes of the new products subjected to endurance tests for the purpose of validation of a new design, since the manufacturing and assembly processes are typically less consolidated. Since a detailed report of quality controls is not available for all the cases examined in this chapter, it is not possible to determine whether the accuracies of components may have played an important role in the failures occurred during some tests. Hence the scatter of the results is representative of the specific application (as prescribed by the method A of Iso 6336), but the estimated curve at 99% of survival probability could be too conservative for systems where the manufacturing and assembly process are more easily controllable. Finally, FSTs require considerable investments in terms of time, employment of human resources, space dedicated to the bench, components involved in the tests and energy consumption, hence extensive tests campaigns dedicated to the characterizations of materials and the comparison of different treatments cannot be justified. Therefore, to cope with the needing to characterize materials in a fast and cost-effective way and under accurately controlled test conditions, for example to assess the convenience of a particular treatment (e.g. shot peening) or to compare the materials of various suppliers, a different test method is desirable. The first possibility is to use a bench appositely conceived to ensure accurately controlled and repeatable gear testing conditions, and where frequent inspections can be easily performed. In this regard, a brief description of the test rig diffused by the Gear Research Centre of the Technical University of Munich (FZG), that is the most widely used worldwide, is reported in Appendix B, along with some considerations on the possibility to develop a rig based on a planetary gear unit. Chapter 6 instead, will be entirely dedicated to a different solution, that is the one adopted within the scope of this project. The approach is based on the possibility, also mentioned by the ISO standard 6336, of investigating the pitting behaviour of material by means of tests on rolling discs in loaded contact.

Chapter 5

EXPERIMENTAL EVALUATION OF THE LOAD DISTRIBUTION ON SUN GEARS TEETH

Dedicated calculation software packages are widely used for fatigue assessments of gears application and for the determination of appropriate sets of geometry modification aimed to ensure the proper functioning of the gear set. Nevertheless, numerical results are based upon simplified models which cannot accurately account for all the possible causes of gears overloading. Moreover, lumped element models used to compute the meshing stiffness and the load distribution over the teeth faces are necessarily based on approximations whose reliability could be not equal with respect to all the possible applications. As an example, in the tooth contact analysis algorithm implemented in KISSsoft, empirical equations are adopted to compute the coupling stiffness C_c (see Figure 4.4), to improve the reliability of the Hertzian component of stiffness C_H and to reduce the stiffness at the sides of helical gears teeth avoiding unrealistic stress peaks near the edges. Therefore, despite the increasing reliability of computational tools for gear calculation, experimental validation of the numerical models may be still fundamental especially in the more complicated systems such as planetary gear sets.

The first experimental works on the dynamics of gear meshing date back to the 50s, when the advent of foil strain gauges and the rapid improvement of signal conditioning systems allowed the first on-line measurements of tooth root strains. Tests were typically conducted in gear boxes appositely developed, and bridge supply and strain signal were transmitted through slip rings [108–110]. The need for experimental data for the validation of calculation models was particularly felt in the aeronautic industry, where weight saving is of primary importance and the consequence of a failure would be catastrophic. Great attention has been drawn by researchers and engineers to planetary gear units, where any deviation by the nominal geometry of the system may lead to an uneven distribution of the load among the planet gears, the load sharing being usually worst for higher number of planets. This aspect was investigated

experimentally by Hidaka and Terauchi [111], Oswald [112], and Krantz [113], using strain gauges applied at the tooth root of the sun gear and, more recently, by Ligata et al. [114] by gluing strain gauges in the fixed internal gear. The latter approach is simpler because eliminates the need for current supply to the gauges and for transmitting the signal from a rotating shaft, but on the other hand does not allow to investigate the behaviour under load of the sun gear, which often represent the weakest component in the gear set especially regarding pitting failures. The distribution of the load over the width of a single tooth of the sun gear can be analysed by means of several strain gauges placed along the tooth root [111]. The same procedure was used also by Handschuh [115] and by Hotait et al. [116] for hypoid bevel gears and by Baud and Velex [117] for helical gears.

A crucial aspect in the dynamic measurements of tooth root strain is represented by noise, which may be introduced in the transmission of the un-conditioned signal through the slip rings. In the last years, the availability of multi-channel telemetry systems significantly contribute to improve the quality of measurements on rotating components such as gears Zhou et al. [118], by allowing the conditioning of the signal before its wireless transmission.

An experimental analysis aimed to assess the accuracy of calculation models of planetary gear sets, was performed on a low power axle for agricultural vehicles produced by Carraro, which was object of a series of recent unsuccessful validation tests where pitting occurred prematurely on the sun gear despite a relatively low level of applied torque. Three strain gauges were applied at different positions along the root of a sun gear tooth and the strain pattern was measured during a bench test of the complete axle by means of a telemetry system. Data were then used to estimate the load distribution on the tooth face under the design torque and speed of the axle.

5.1 Case study

Due to the complex structure of planetary systems, the estimation of the lifetime of sun gears is particularly complicated and may often lead to inaccurate results due to the approximations included in the theoretical model. The sun gear meshes with three or four planet gears mounted on needle bearings and supported by cantilever pins fixed at one end to the planet carrier. The construction quality of the planet carrier, in terms of design and manufacturing accuracy, is

perhaps the most important factor to guarantee the structural integrity of the drive. Deflections under load of the carrier and the pins, as well as positioning errors of the pins due to manufacturing or assembling defects may strongly influence the pressure distribution on gears teeth and bearings, and may lead to an uneven load sharing among the planet gears, considerably reducing the life of the components.

Concerning the planetary gear sets under analysis, the problem of determining the load distribution is complicated by the fact that pins are mounted by interference fit on the carrier and the assembly operation inevitably introduce some degree of perpendicularity errror among the planet pins and the carrier. Moreover, the width of planet gears is considerably lower as compared to the sun gear teeth, therefore the role of the coupling stiffness C_c (determined by an empirical equation in KISSsoft) is of primary importance since some slices of the sun gear model are unloaded but significantly contribute to support the neighbouring ones (buttressing effect).

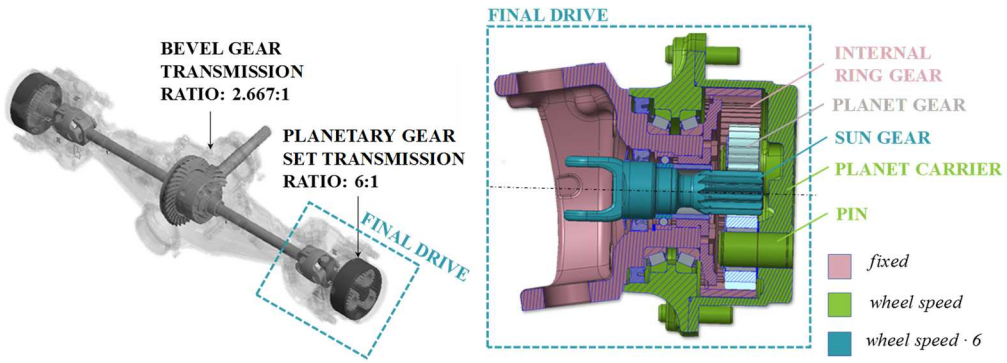

Figure 5.1 The planetary gear set under analysis.

The four planet carriers of the two axles involved in the four-square test were measured by a coordinate measuring machine. The position of the centres at the base (O") and at the top (O') of the planet pins was determined with reference to the y-z coordinate system defined in Figure 5.2. For an easier visualization of the errors the measures have been referred, by means of a simple transformation of coordinates, to the reference systems $(\xi\eta\zeta)_{1,2,3}$ centred in the nominal position of the pins and having axes oriented in the radial and tangential directions as shown in Figure 5.3. The perpendicularity error was defined as the distance between the two centres. The carrier A was chosen for the first test since it presents the lowest mean perpendicularity error among the measured ones.

Table 5.1 Perpendicularity errors of the pins in the planet carriers involved in the test.

			Centers location		*Perpendicularity error*			*Direction*
			η	*ζ*	*Tangential*	*Radial*	*Total*	(from bottom to top)
			[µm]	[µm]	[µm]	[µm]	[µm]	/
Carrier A	*Pin 1*	O_1'	-89	17	81	34	88	Counter clockwise
		O_1''	-8	-18				
	Pin 2	O_2'	6	73	40	37	54	Counter clockwise
		O_2''	46	36				
	Pin 3	O_3'	39	-32	37	18	41	Counter clockwise
		O_3''	76	-50				
Carrier B	*Pin 1*	O_1'	-165	-132	123	39	129	Counter clockwise
		O_1''	-42	-93				
	Pin 2	O_2'	-63	164	55	93	108	Counter clockwise
		O_2''	-8	71				
	Pin 3	O_3'	201	-36	56	2	56	Clockwise
		O_3''	145	-39				
Carrier C	*Pin 1*	O_1'	-211	2	132	29	135	Counter clockwise
		O_1''	-79	31				
	Pin 2	O_2'	34	148	31	126	130	Counter clockwise
		O_2''	65	22				
	Pin 3	O_3'	106	-162	79	39	88	Clockwise
		O_3''	27	-123				
Carrier D	*Pin 1*	O_1'	-117	-49	86	11	86	Counter clockwise
		O_1''	-31	-60				
	Pin 2	O_2'	-47	112	1	75	75	Counter clockwise
		O_2''	-46	37				
	Pin 3	O_3'	113	-39	33	15	36	Clockwise
		O_3''	80	-24				

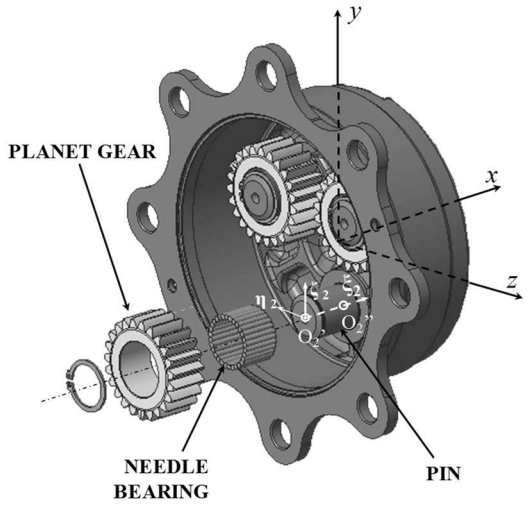

Figure 5.2 Planet carrier assembly.

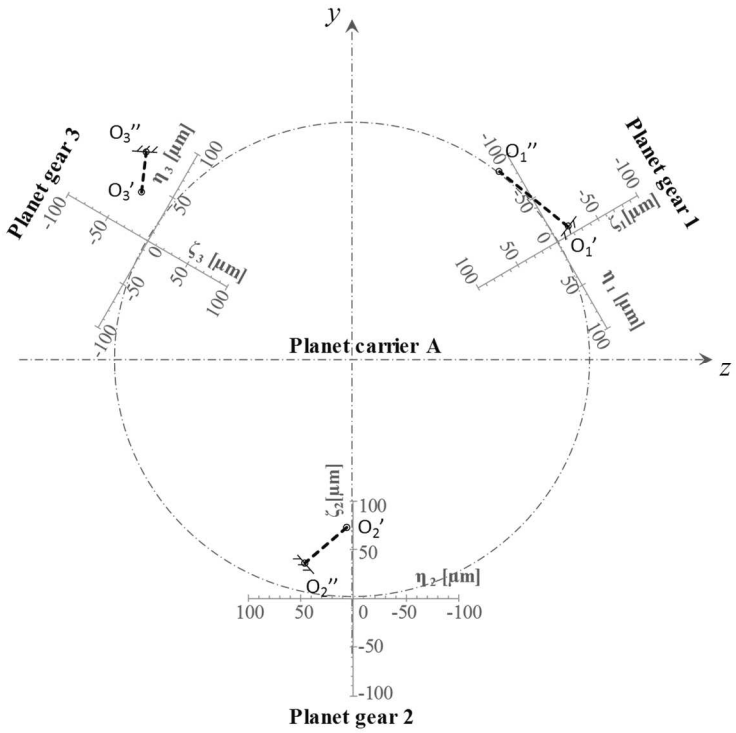

Figure 5.3 Misalignments of the pins of planet carrier A.

5.2 Calculation model

A model of the planetary gear set was created by the software KISSsoft, to compute the load distribution on the sun gear teeth. The calculation accounts for the compliances of gears and

shafts, the geometry modifications such as crowning, and the bearing clearances. Moreover, in this case a finite element model of the planet carrier was created to assess the influence of its compliances in the displacements of the planet pins. In the KISSsoft model, the pins are treated as cantilever beams sustained by two constraints connected to the carrier. The results of the finite element model allowed to determine an equivalent stiffness to be attributed to the central constraint of the pin in order to resemble the compliance of the carrier as shown in Figure 5.4.

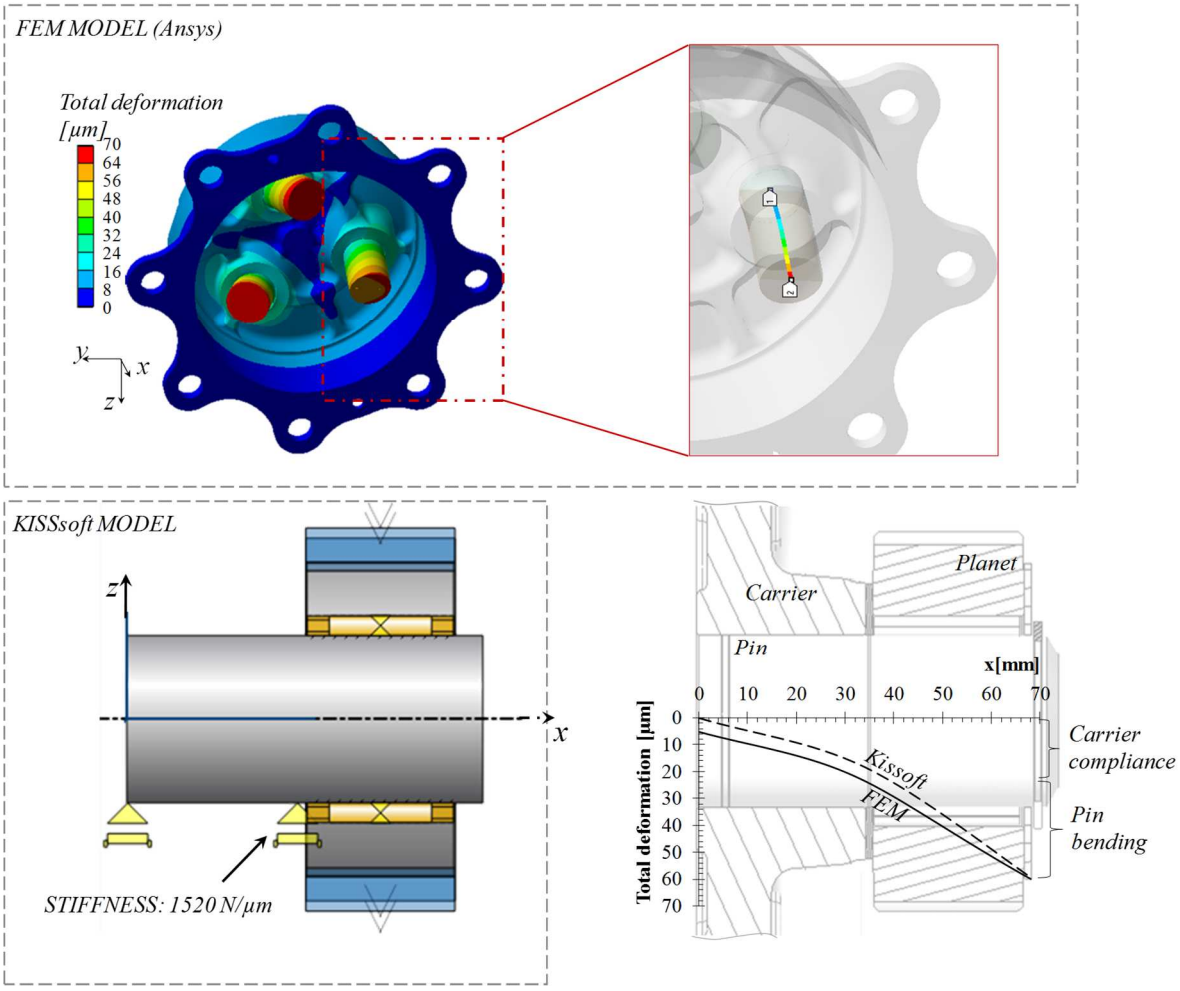

Figure 5.4 Finite element analysis of the planet carrier and determination of the equivalent stiffness for the pin support in the KISSsoft model.

On the other hand, the calculation model does not allow to consider individually the different perpendicularity errors of the three planet gears axes. Therefore, the tooth contact analysis tool implemented in the software package, allowed the calculation of the load distribution over the whole tooth face without considering the manufacturing errors.

Figure 5.5 shows the line load distribution along the tooth face, calculated in correspondence of the Highest Point of Single Tooth Pair Contact of the sun gear for the design input torque of

the final drive $T_s = 520\ Nm$. Such location was chosen for convenience in the comparison with the experimental data, as clarified in section 5.4.

Since sun and planet gears are crowned, the contact pressure between the teeth surfaces is maximum in correspondence of the centre of the elliptical contact area, whose position depend on the relative alignment between the gear axes, and decreases in both directions along the tooth width. Being tooth height much smaller with respect to its width, the load distribution affects the strain along the tooth root, therefore the measures of the three strain gauges can be used to assess, at least approximately the position of maximum pressure and hence verify the relative alignment of each planet gear and the reliability of the calculation model.

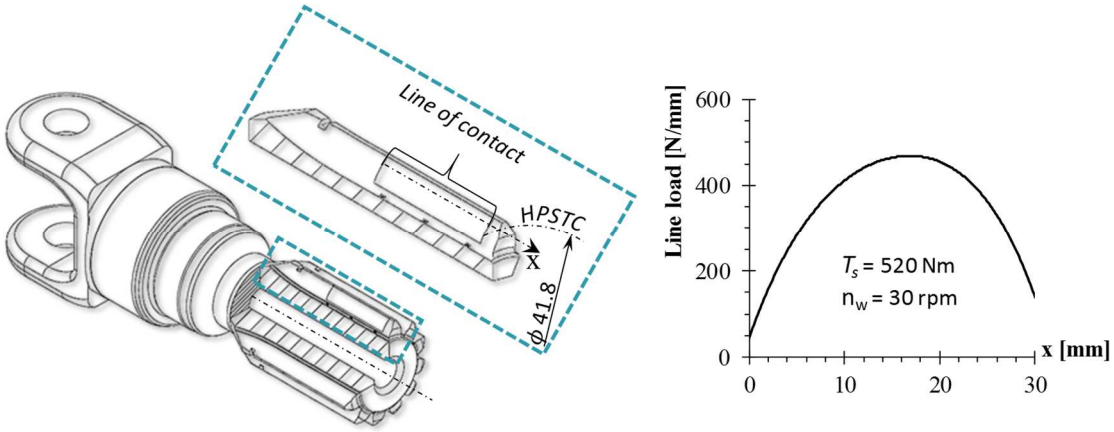

Figure 5.5 Line load distribution calculated by the KISSsoft model.

5.3 Description of the measurement system

Three strain gauges were applied along the tooth root of the left-side sun gear of the tested axle during the test (Figure 5.6). The sensors had a grid length of 0.2 mm and were glued within the 30 mm portion of the tooth width interested by the contact with the planet gear; the centre of the grid was shifted from the tooth root in the direction of the driving flank, as reported in Figure 5.7.

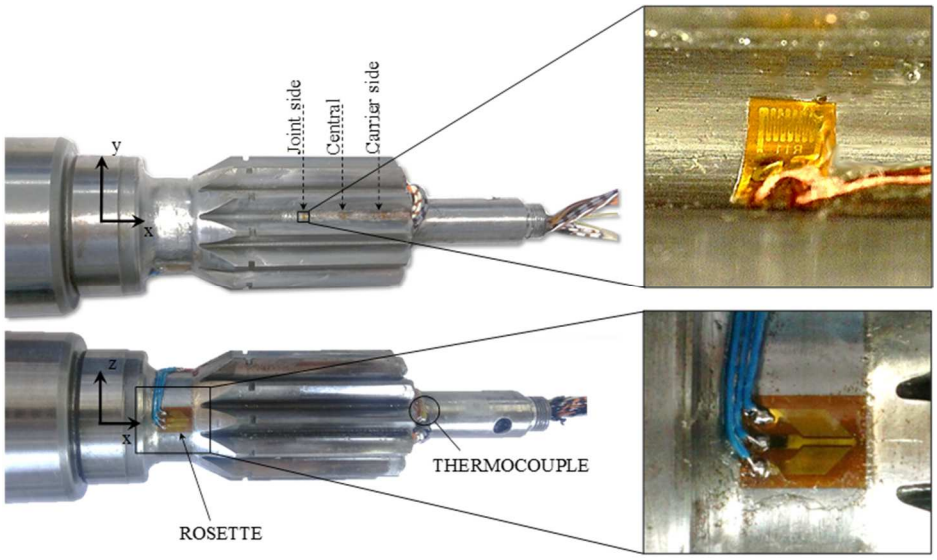

Figure 5.6. Strain gauges applied to the sun gear.

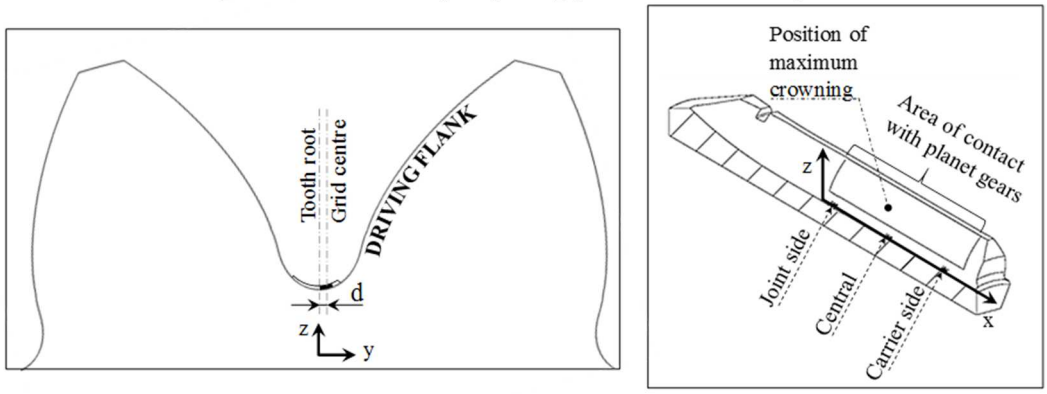

Figure 5.7 Nominal position of the strain gauges along the tooth root.

The actual position of the strain gauges after the application, with reference to Figure 5.7, was verified with an optical microscope and is reported in Table 5.2. Because of the high strain gradient along the fillet radius of the tooth root, the possible error in the strain measurement due to the ±0.1mm uncertainty in the strain gauge position was estimated by a finite element analysis of the sun gear and resulted to be as high as ±15%.

Table 5.2. Measured position of strain gauges along the tooth root (see Figure 5.7).

	Position along the x axis [mm]	Distance from the tooth root, d [mm]
Joint side	1.0 ± 0.2	0.1 ± 0.1
Central	13.0 ± 0.2	0.1 ± 0.1
Carrier side	26.0 ± 0.2	0.2 ± 0.1

Two combined ±45° rosette were applied between the gear and the double-U joint, to measure the input torque in the final drive. Strain gauges and cables were covered with a lacquer (DUE-CI Electronics, V-66) to provide insulation and protection from the lubricant. Finally, a T-type thermocouple was used to monitor the oil temperature inside the drive and in order to avoid overtemperature above 80°C.

Bridge signals and supply were transmitted by means of a KMT-MT32 multi-channel telemetry system to a IMC-CRONOS-PL2 acquisition unit. The system is composed by a battery and seven modules for signal conditioning (three modules for the tooth gauges, one for the torsion bridge and one for the thermocouple), the collection of data from the various channel (one module) and the transmission of the signal to the acquisition unit (one module). Strain gauges were connected to the cables coming from the telemetry modules by means of thin wires (0.14 mm diameter) fixed along the tooth root. Then a hollow shaft was mounted with interference fit in the sun gear to allow the passage of the cables out of the carrier (Figure 5.8).

The telemetry modules were disposed circumferentially on an aluminium plate coaxially screwed to the shaft (Figure 5.9). The battery was fixed in correspondence of the centre of the plate. A rubber tube connected a pin placed upon the battery support to the shaft of an incremental encoder. The stator was held by a support bracket fixed to the rig frame, therefore the encoder measured the absolute angle of rotation of the sun gear since the start of the test. In order to know the exact position of the sun gear with respect to each planet at any time during the test, the angular position of the gauged tooth was marked in the aluminium disc and its relative position with respect to the carrier was adjusted before each acquisition session.

The signal measured by the torque transducer mounted on the cardan shaft of the FST rig was also acquired. Table 5.3 reports a list of the sensors with the relevant product codes. It must be specified that, for the strain gauges channels, the sampling frequency of the acquisition unit was greater as compared to the maximum scanning rate allowed by the telemetry system which is 400 Hz with five connected conditioning modules.

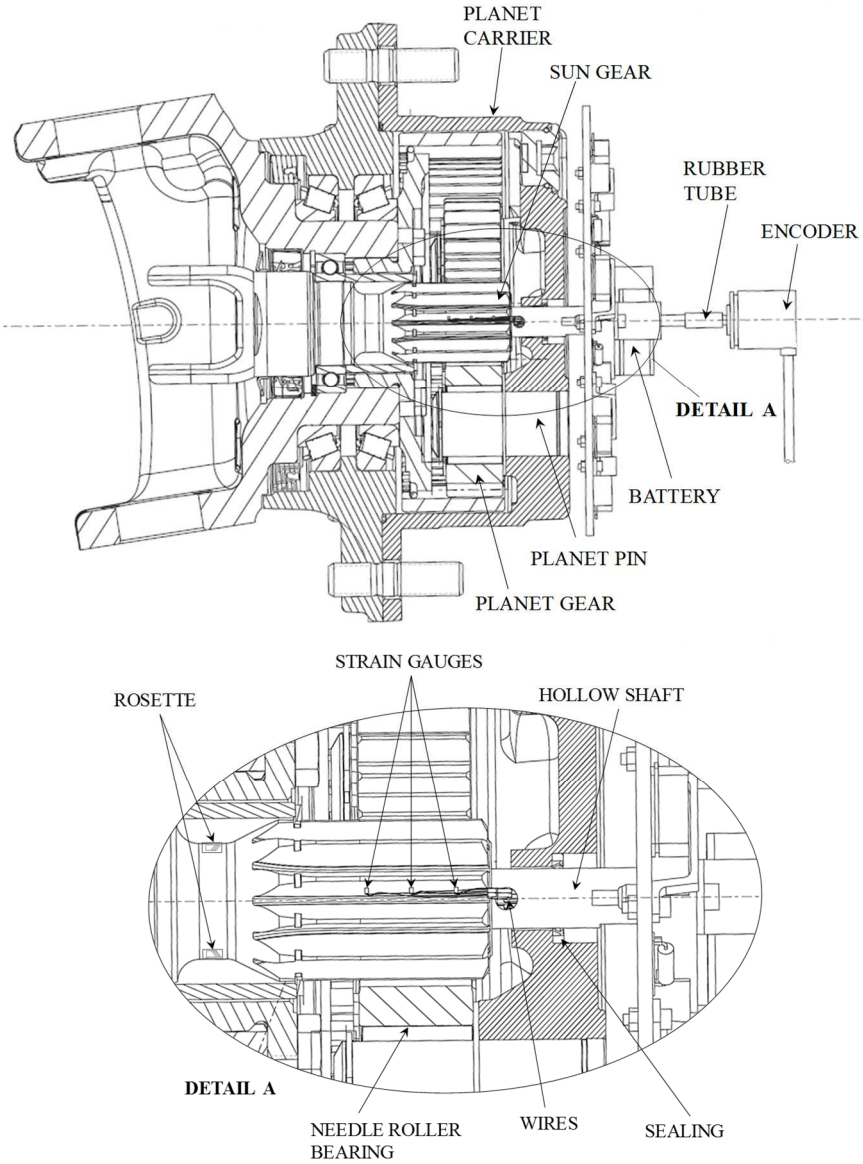

Figure 5.8. Scheme of the final drive and the measurement set-up.

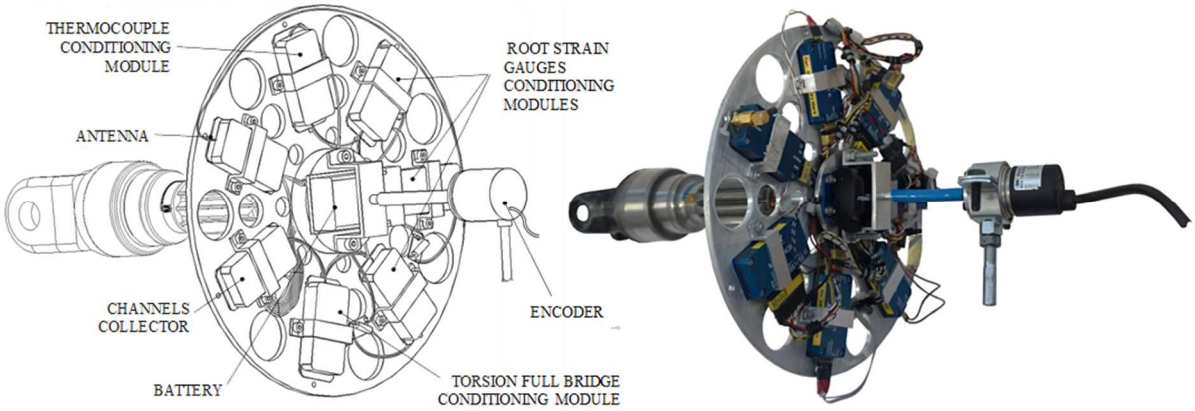

Figure 5.9. Assembly of the aluminium plate carrying the telemetry modules.

Table 5.3 List the measurement channels.

Channel	Sensor	Product code	Sampling frequency
#	-	-	[kHz]
1	Strain gauges rosette (two in full wheatstone bridge configuration)	HBM 1-XY41-3/350	1*
2, 3, 4	Root strain gauges □	KFR 02N-120-C1-11N10C2	1*
5	Thermocouple(Type T) ◊	RS Pro 363-0402	0.2
6	FST Torque transducer	HBM 71-124-046	0.2
7	Incremental Encoder	Baumer BDK 16.05A500-5-4	1

□*For each strain gauge a precision resistor UPW50B120RV fixed to the aluminium plate was used to arrange a half Wheatstone bridge.*
◊*Since the conditioning module of the telemetry system is specific for Type K thermocouple, an in-line elaboration of the measured signal was used to correct the temperature value.*
**The value is referred to the sampling frequency of the acquisition unit. The sampling frequency of the telemetry system with 5 connected channels is 400 Hz.*

5.4 Experimental measurements

The most influencing for the pitting durability of planetary gear sets in agricultural axles are the uneven distribution of load over the face width (quantified by the ISO standard with the factor $K_{H\beta}$) and among the three planet gears (quantified by the factor K_{γ}). As mentioned in the previous section, the non-uniform load distribution along the tooth produces differences among the strains measured by the three gauges, while the load sharing among the planet gears would result in a different strain pattern when the tooth meshes with the three planets. Concerning the other possible causes of non-uniform strain patterns, for accurately manufactured gears with appropriate profile modifications and high specific loading, usually $K_{H\alpha}$ is less significant and therefore will not be analysed in the following. Also factors K_A and K_V are typically negligible for this kind of application, since during the four-square test the axle is driven by a constant torque at relatively low speeds.

Figure 5.10 shows the typical strain pattern measured by the gauge placed in the central position, versus the angle of relative rotation of the sun gear with respect to the carrier. The measure was performed with an input torque to the final drive of $T_s = 520\ Nm$ and a wheel speed $n_W = 30\ rpm$. For easiness of comprehension the zero of the x-axis in the chart was

placed in correspondence of the start of meshing of the gauged tooth with a planet gear (see Figure 5.11). Then, since the encoder measures the absolute angle of rotation of the sun gear γ, while the carrier rotates at 1/τ the sun speed in its same direction, the relative angle γ_r is computed as:

$$\gamma_R = \gamma \cdot \frac{\tau + 1}{\tau} \tag{5.1}$$

Where τ is the transmission ratio of the final drive. Thus, in the relative reference system, the period between two consecutive meshing of the considered sun tooth is equal to the angular spacing of the three planets, namely 120°

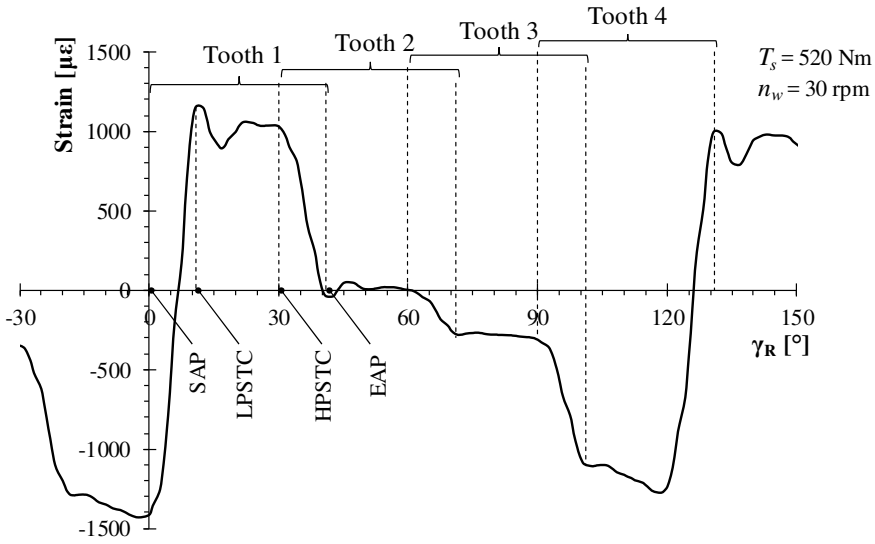

Figure 5.10. Strain pattern (central gauge).

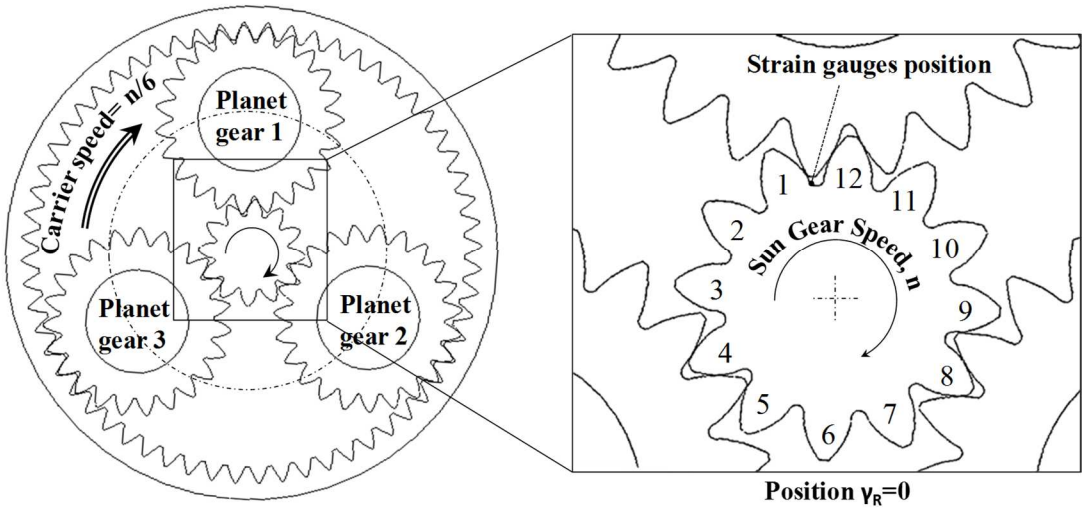

Figure 5.11. Scheme of the planetary gear set.

With reference to the configuration defined in Figure 5.11 and Figure 5.12, the strain-time history can be interpreted as follows:

- The gear covers an angle of about 41° during the period of meshing of a tooth pair, between the Start of Active Profile (SAP) and the End of Active Profile (EAP)
- Considering the gauged tooth (tooth 1), the strain rapidly increases during the first 11° of rotation, until the Lowest Point of Single Tooth pair Contact (LPSTC), while tooth 12 is gradually unloaded.
- Between the lowest and the Highest Point of Single Tooth pair Contact (HPSTC) the curve is altered because the direction of mutual sliding between the mating teeth (and therefore the direction of friction forces) reverses in correspondence of the pitch point.
- In correspondence of the HPSTC the strain drops because tooth 2 engages and therefore tooth 1 is gradually unloaded within the following 11°.
- In the coordinate system relative to the carrier, the sun gear covers 120° before tooth 1 encounter a new planet gear. The strain reaches very high compressive values when tooth 12 is loaded.

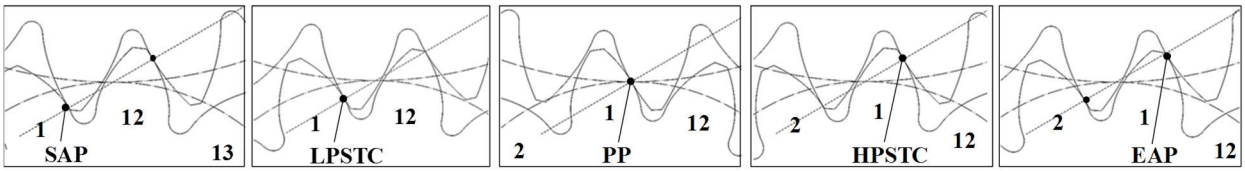

Figure 5.12. Sequence of meshing between sun and planet gear.

The signal of the three gauges are shown in Figure 5.13 for a complete revolution of the planet relatively to the carrier. Considering the strain gauges in the joint and carrier sides, the strain pattern measured during the meshing with planet gear 1 is considerably different with respect to the one observed during the meshing with planet gears 2 and 3. The strain measured by the three gauges in correspondence of the contacts with the three planets at the HPSTC of the sun gear are reported in Table 5.4. Such location is considered as reference because it is easily recognizable in the chart and is relatively far from the pitch line, where the change in the direction of friction forces causes a perturbation in the strain pattern. It can be noted that the values measured by the strain gauge in the central position are quite repeatable, with a difference among the values measured in correspondence of the contact with the three planet gears lower than 8%. However, the two lateral gauges measure very different strain values

during the contact with the first planet as opposed to those registered in the contact with the second and third planet gears. It could be verified that this behaviour is repeatable in the subsequent revolutions.

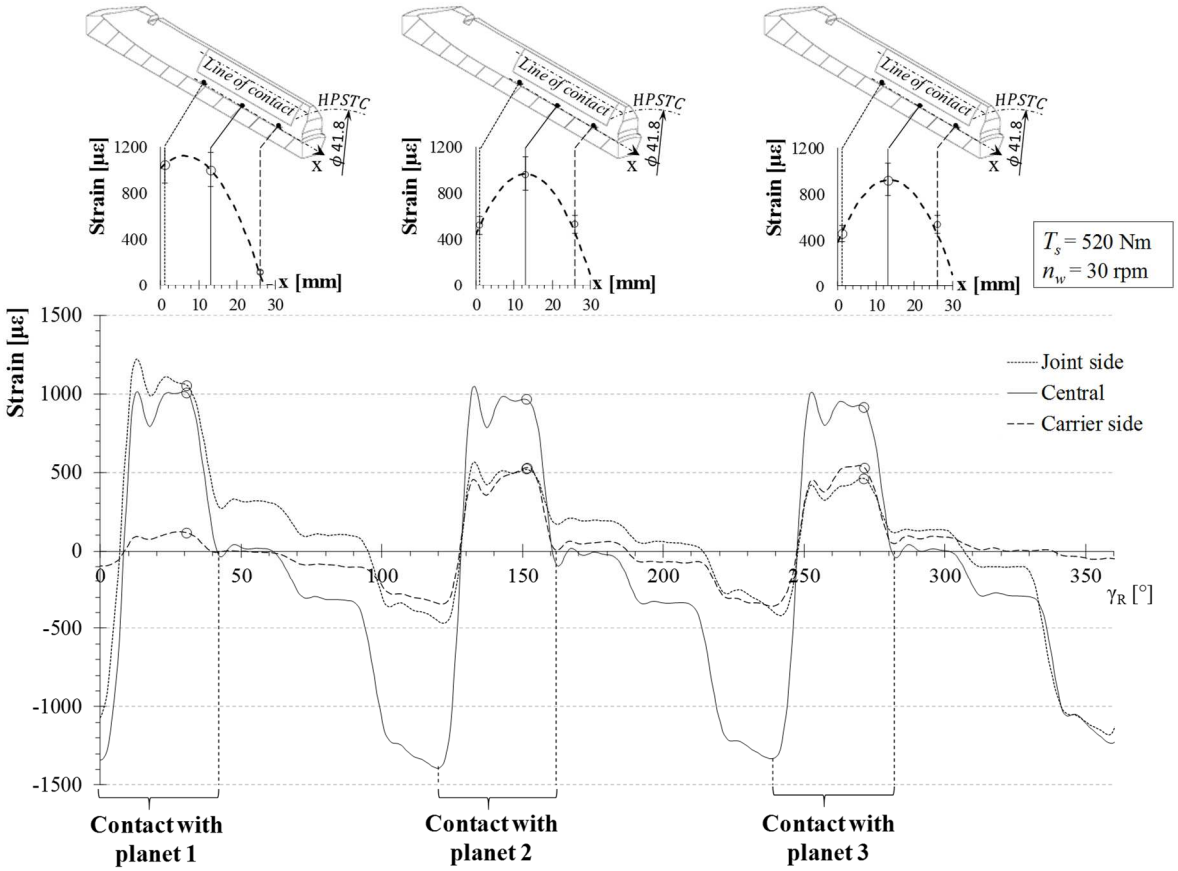

Figure 5.13. Strain patterns at three different position along the face width. The upper charts report the values of strain relevant to the meshing with the three planet gears, when the contact occurs at the HPSTC of the sun gear.

Table 5.4. Strain values relevant to contacts with the three planet gears, in correspondence of the HPSTC of the gauged tooth.

		Contact with planet gear 1	Contact with planet gear 2	Contact with planet gear 3
STRAIN [με]	Joint side	1048	518	461
	Central	1004	967	927
	Carrier side	113	528	537

In the upper part of Figure 5.13, the strain values reported in Table 5.4, are shown in correspondence of the contact with each planet gear. The parabolic interpolation of the strain values highlights the different load distribution in the three cases: it is reasonable to suppose that the strain observed in the contact with planet gears 2 and 3 could be originated by a line

load distribution with a maximum value near to the position of the central gauge as predicted by the calculation model. On the contrary in the contact with planet gear 1 the maximum load is probably shifted between the position of the central and the joint side strain gauges. This condition was not surprising since, as shown in Figure 5.3, the pin around which planet gear 1 rotates in planet carrier A, presents the greatest amount of perpendicularity error, and its misalignment in the tangential direction is such that the load tends to concentrate on the joint side of the sun gear. Although the magnitude of the error is lower, the pins of planet gears 2 and 3 are inclined counter clockwise in the tangential direction as well. As reported in Figure 5.4, during rotation in the forward direction, displacements of the planets due to bending of the pin and compliances of the carrier occur in the clockwise direction and therefore tend to reduce the initial amount of tangential misalignment and the maximum value of the strain distribution at the tooth root moves toward the carrier side of the sun gear. Figure 5.14 as an example, compares the strain patterns measured for different loads, with a wheel speed of 2.4 rpm during the contact with planet gear 2. The maximum of the best fitting parabolas relevant to the strain measures in correspondence of the HPSTC of the sun gear moves rightward for increasing loads. The same phenomenon was observed for planet gears 1 and 3 (Figure 5.15) Moreover, it is evident from the comparison of the strain patterns at 300 and 750Nm, that at higher loads the meshing period of the strain gauged tooth increases. It is well known in fact, that the overlap ratio of gear pairs increases under load due to the same mechanism of teeth bending which can eventually lead to tip-to-root interference as described in section 2.3.1. Particularly, the periods of double tooth contact between SAP and LPSTC and between LPSTC and EAP became longer.

Based on the measurements of strain at the tooth root an approach for the determination of the load distribution is proposed in the next section.

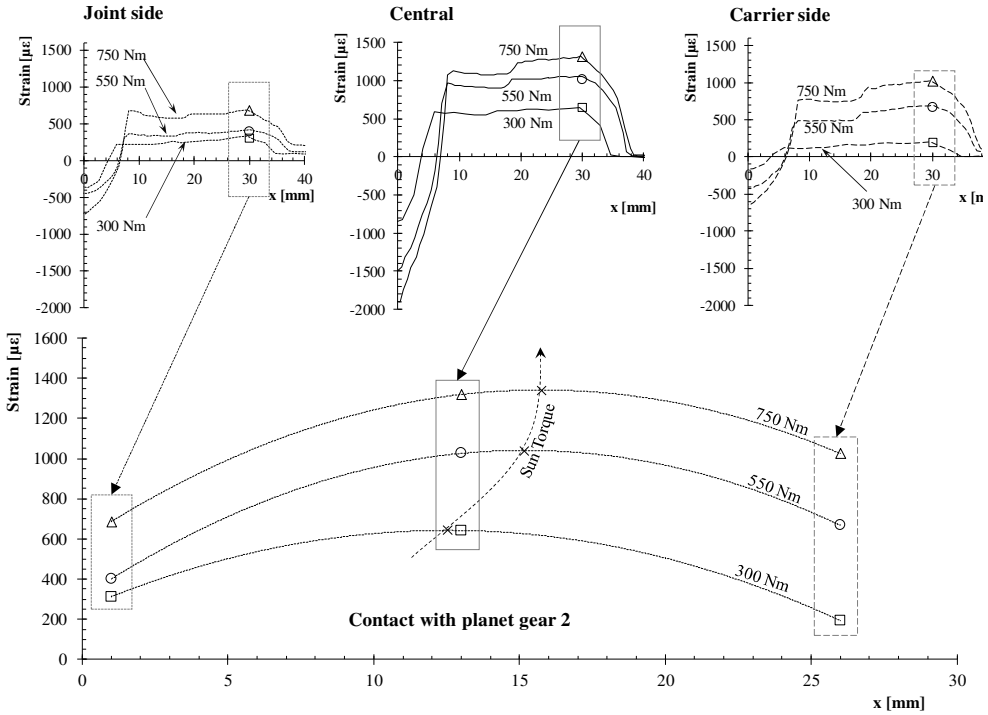

Figure 5.14 Strain patterns measured at different torque levels in correspondence of the contact of planet gear 2 with the HPSTC of the strain gauged tooth.

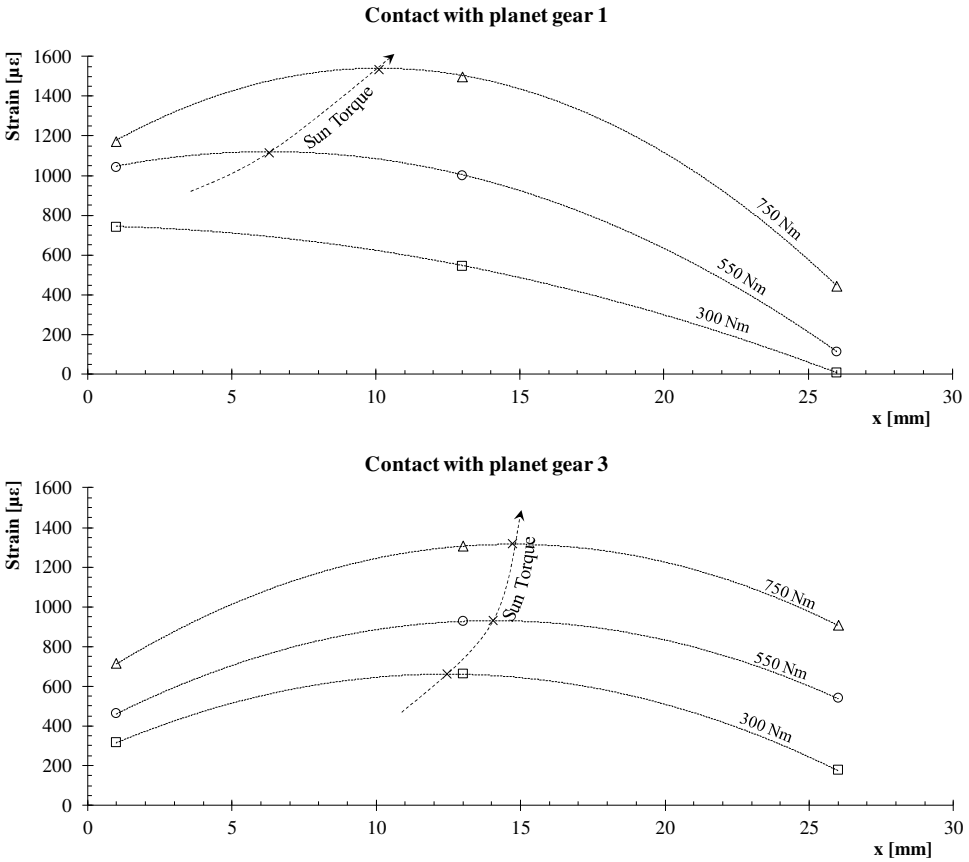

Figure 5.15 Strain patterns measured at different torque levels in correspondence of the contact of planet gear 1 and 3 with the HPSTC of the strain gauged tooth.

5.5 Determination of the load distribution

The relatively good repeatability of the strain pattern measured by the central gauge in the acquisition performed at the design load of the axle (Figure 5.13) suggests that the differences in strain during the contact with the three planet gears would be caused more by differences among the alignments of the pins, rather than to an uneven sharing of the load among the three planets. This is in agreement with Oswald et al. [112] and Krantz [113] who observed that for gear sets with three planets and number of teeth of the sun gear multiple of three, the load is typically shared quite evenly among the planet gears. The relatively large clearance of the sun gear bearing (clearance class C4) contributes to provide an even load sharing by allowing a certain degree of freedom to the sun gear axis which has a self-centring tendency in three planets gear sets [119]. Therefore, the following analysis focused on the problem of the gear axis misalignments. An attempt was made to estimate the line load distribution along the tooth face compatible with the signal of the strain gauges. The procedure followed to assess the face load distribution is the following:

- a parabolic distribution for both the strain along the tooth root and the line load on the tooth face was assumed:

$$\varepsilon_{root} = ax^2 + bx + c \tag{5.2}$$

$$L = ux^2 + vx + z \tag{5.3}$$

- the equations of the root strain parabolas relevant to the contact with each planet were determined from the three strain values measured in correspondence of a contact at the HPSTC. From the equation of each strain parabola the position of the maximum strain along the tooth root was determined as:

$$x_{max} = -\frac{b}{2a} \tag{5.4}$$

- Note that this position corresponds to the point of maximum strain provided that the strain values used for the determination of the equation are all measured along the same line parallel to the sun gear axis. Therefore, in this phase, the values measured by the strain gauge in the carrier side were scaled by a factor 0.85 to account for the

different position of the centre of its grid with respect to the others, as reported in Table 5.2. The scale factor was estimated from the results of a FE analysis.

- the maximum line load was assumed to occur approximately at the same coordinate x_{max}, as the maximum strain, therefore:

$$-\frac{v}{2u} = x_{max} \tag{5.5}$$

Or

$$v = -2ux_{max} \tag{5.6}$$

- Assuming that the load is evenly distributed among the planet gears ($K_\gamma \approx 1$), the integral over x of the line load, within the face width b of the planet gear must equal the normal load F_n:

$$F_n = \int_{x_{L1}}^{x_{L2}} (ux^2 + vx + z)dx \tag{5.7}$$

Where x_{L1} and x_{L2} are defined as follows:

$$x_{L1} = \max\left[0, \quad \frac{-v + (v^2 - 4uz)^{0.5}}{2u}\right] \tag{5.8}$$

$$x_{L2} = \min\left[30, \quad \frac{-v - (v^2 - 4uz)^{0.5}}{2u}\right] \tag{5.9}$$

In other words, since the load cannot assume negative values, the integral is evaluated only between the roots of the parabola if they are included within the interval $0 \leq x \leq 30\ mm$. Therefore:

$$\frac{1}{3}u({x_{L2}}^3 - x_{L1}^3) + \frac{1}{2}v({x_{L2}}^2 - x_{L1}^2) + z(x_{L2} - x_{L1}) = F_n \tag{5.10}$$

Or, combining eq (5.6) and (5.10):

$$z = \frac{\left[F_n - \frac{1}{3}u({x_{L2}}^3 - x_{L1}^3) + ux_{max}({x_{L2}}^2 - x_{L1}^2)\right]}{(x_{L2} - x_{L1})} \tag{5.11}$$

The normal force generated at the HPSTC of the sun gear tooth can be calculated according to appendix A. Note that the sun gear torque should be divided by three to account for the load sharing among the three planet gears.

- The values of the coefficient v and z are given by equations (5.6) and (5.11). Moreover, the experimental data clearly shown that the entity of the crowning is such that the line load parabola has a downward concavity (u is negative). Thus, various parabolic load distribution may be derived changing the value of the first coefficient u as shown in Figure 5.16. Note that, for a chosen value of u, z may depend on x_{L1} and x_{L2}, which in turn depend on z. However, the problem may be solved iteratively using $x_{L1} = 0$ and $x_{L2} = 30$ as seeding values to compute z, then x_{L1} and x_{L2} may be calculated and used to derive a new value of z. Usually the calculation converges in few iterations.

- Finally, a finite element model of the sun gear was built to find the value of *u* relevant to the load distribution that, applied to the model in correspondence of the diameter of HPSTC along with the relevant friction force (see appendix A), produces the least square error between the measured root strain and the results of the analysis. A friction coefficient of 0.05 was assumed, which is a typical value adopted for gear calculations [38].

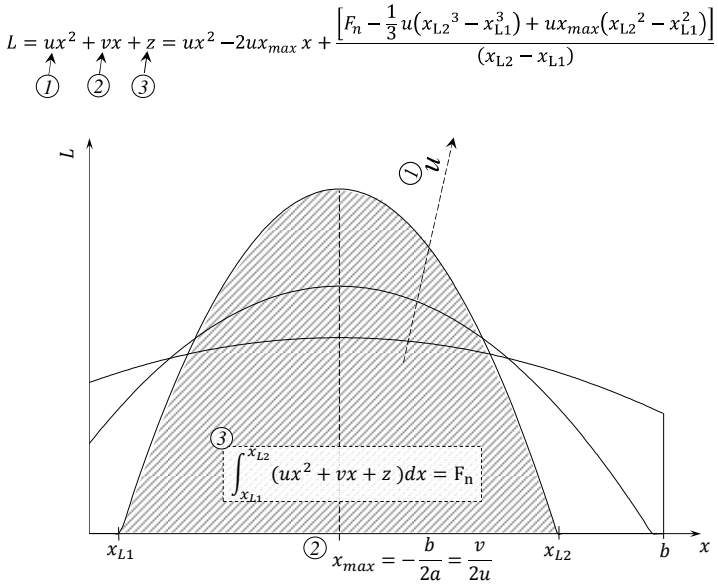

Figure 5.16 Schematic representation of the procedure of determination of the load distribution.

Figure 5.17 shows the finite element model of the gear. The load is applied on the three teeth in contact by means of pressure distribution *p(x)* applied on a narrow strip in correspondence of the HPSTC and defined as functions along the coordinate x. Since the load distribution is

resembled only by the portion of function comprised between the root of the parabola, the pressure is defined in the software as

$$p(x) = \frac{L(x) + \sqrt{L(x)^2}}{2t} = \frac{ux^2 + vx + z + \sqrt{(ux^2 + vx + z)^2}}{2t} \tag{5.12}$$

Where the term $\sqrt{L(x)^2}$ is used instead of the module to vanish the negative part of the curve since the latter is not implemented in the function editor, and t is the height of the strip, used to transform the parabolic line load into a pressure distribution. Then, the friction load is applied in the portion of strip delimited by the root of the parabola by means of an uniform pressure tangential distribution $q(x)$:

$$q(x) = 0.05 \cdot \frac{F_n}{t(x_{L2} - x_{L1})} \tag{5.13}$$

, since the definition of tangential pressure by a parabolic function of the coordinate axis is not allowed by the software.

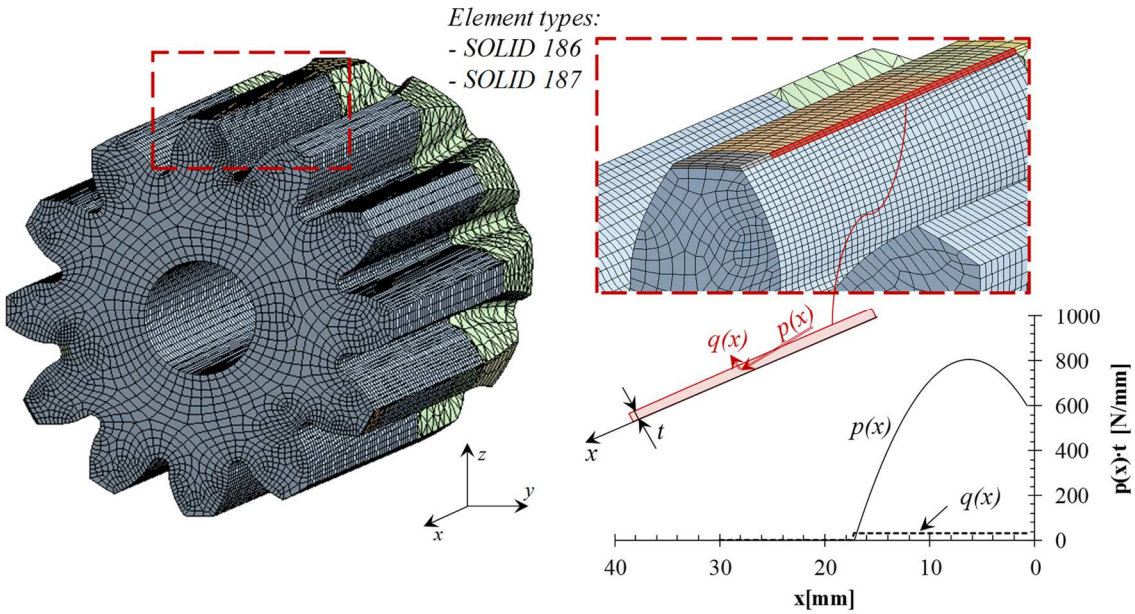

Figure 5.17 Example of finite element model of the sun gear

Figure 5.18 shows the line load distribution for the contact with the three planet gears computed with the above procedure, and the comparison among the tooth root strain resulted

by the finite element model and the experimental data, represented along with the relevant error bands as defined in section 5.3.

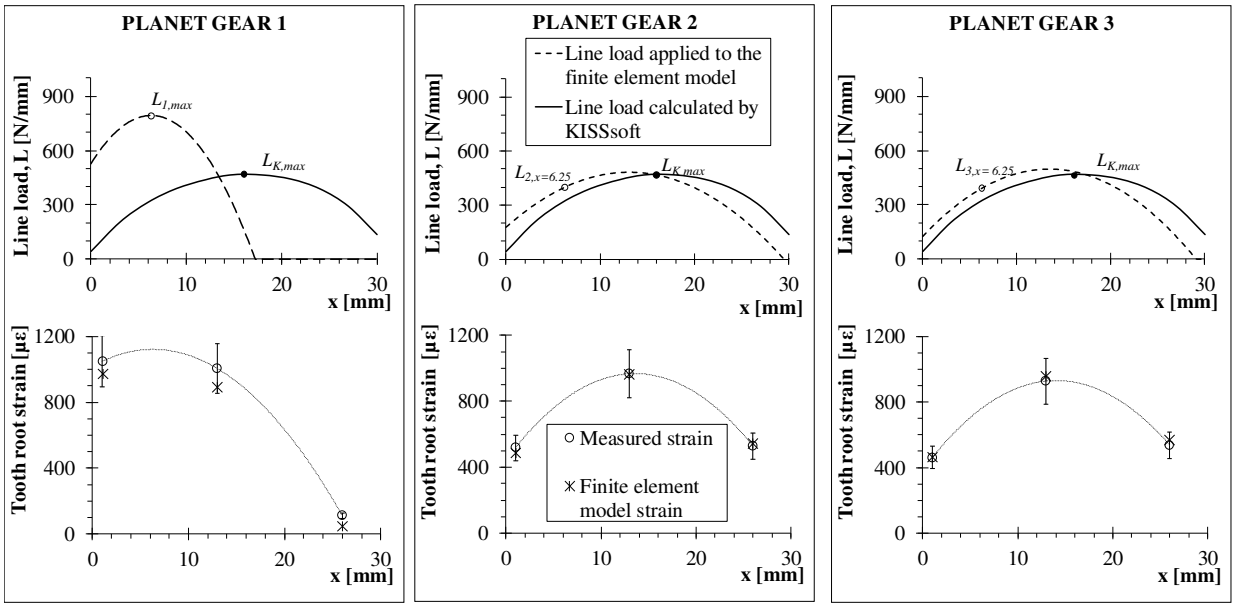

Figure 5.18. Comparison between the line load distribution calculated by the software KISSsoft, and the parabolic line load distribution which produces the least square error among the measured values of strain and the results of the finite element model.

Note that the very good agreement between output of the finite element calculation and measured strain values supports the hypothesis that the load sharing factor K_γ is almost unitary. The calculated line load distributions for planet gear 2 and 3 are similar and reach a maximum value close to the one calculated by the KISSsoft model, $L_{K,max}$. On the contrary, the contact with the first planet results in a maximum value of line load $L_{1,max}$ 69% higher than $L_{K,max}$. It is worth remembering that the fatigue curve suggested by the ISO standard 6336 for the evaluation of the pitting durability of case hardened gears are based on a relation of the type:

$$\sigma_H{}^{13.22} N = c \tag{5.14}$$

Where c is a constant that depends on the material quality and N represent the expected pitting life (in terms of number of contact cycles) of a gear subjected to the maximum contact pressure σ_H which is proportional to $L^{0.5}$. The damage calculated by KISSsoft for a given number n of contact cycles sustained by a sun gear tooth can be expressed in the form n/N_K , where N_K represents the life relevant to the contact load $L_{K,max}$. However, based on the experimental results, seems more appropriate to compute the damage in correspondence of the coordinate $x = 6.25\ mm$ where the pressure generated by the contact with the first planet gear

is maximum. At this location, the sun gear tooth is subjected to a line load 69% higher than $L_{K,max}$ during the contact with the first planet gear and 15% and 18% lower than $L_{K,max}$ in the contact with planet gear 2 and 3, respectively. Thus, considering a linear damage sum according to the Palmgren-Miner rule, as suggested by the ISO standard for life calculations under variable amplitude loading conditions, the damages accumulated by the tooth in *n* contact cycles is given by

$$\frac{\frac{1}{3}n}{N_K\left(\frac{L_{1,max}}{L_{Kmax}}\right)^{-\frac{13.22}{2}}}+\frac{\frac{1}{3}n}{N_K\left(\frac{L_{2,x=6.25}}{L_{K\,max}}\right)^{-\frac{13.22}{2}}}+\frac{\frac{1}{3}n}{N_K\left(\frac{L_{3,x=6.25}}{L_{K\,max}}\right)^{-\frac{13.22}{2}}}=\frac{n}{3N_K}(1.69^{6.61}+0.85^{6.61}+0.82^{6.61})=10.9\frac{n}{N_k} \tag{5.15}$$

Therefore, the service life of the sun gear, is expected to be more than 10 times lower than that predicted assuming the line load distribution resulted by the theoretical model for all the three planets.

An endurance test with the analysed parts was not performed to date. Currently further tests are ongoing using different combinations of the planet carriers involved in the test with the strain gauged sun gear, in order to investigate the influence of different amounts of manufacturing errors.

5.6 Conclusions and limits of the proposed approach

To assess the accuracy of a typical theoretical model, adopted within the R&D department of Carraro S.p.A. to compute the expected life of planetary gear sets, experimental measurements of tooth root strain were performed on a sun gear during a bench test of the complete axle. A procedure was then proposed to evaluate the load distribution on the tooth face, based on the strain measured at three different position along the root. The analysis showed that manufacturing error of the entity which can be typically encountered in prototypes of new axles, can lead to high discrepancies between the results of the model and the actual load distribution, highlighting the need of separating tests for product validation, from tests performed with the aim to characterize gears material. Regarding the former kind of tests, in fact, it is essential that the statistical scatter include also the effect of inaccuracies that can normally derive by the manufacturing process. On the contrary, information relevant to the

fatigue strength of material should be derived by tests under accurately controlled operating conditions.

It must be specified that the proposed method for the determination of the load distribution based on the root strain measurement can be adopted only when at least one of the gears is crowned, otherwise the hypothesis of parabolic load distribution along the tooth width is not satisfied. Moreover, if the applied torque is too low, or the line load is excessively concentrated toward one side of the tooth, the signal of one or two strain gauges may vanish and the determination of the position of maximum root strain is no more possible. Finally, it should be remarked that in cases where the load is distributed in a restricted portion of the tooth width, the root strain distribution will have a parabolic trend in the vicinity of its maximum and presents two gradually degrading side tails as shown in Figure 5.19. Normally this is not a problem since the equation of the parabola interpolating the measured strains is used only to determine the axial position of the maximum strain. However, in cases where the strain measured by one of the strain gauges is very low, it is possible that the determination of the position of maximum will be imprecise and could require some adjustment to improve the correlation with the results

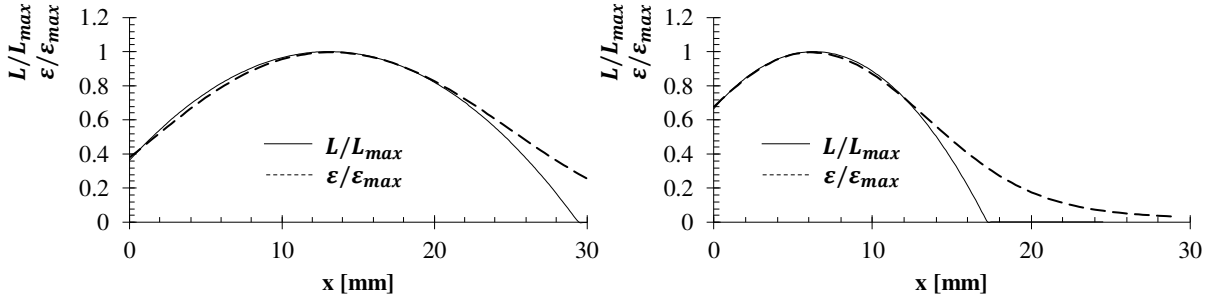

Figure 5.19 Distributions of line load at the HPSTC and relevant strain along the root of the sun gear normalised by their maximum values. Strain values are computed by a FE analysis for the cases of: (a) line load distributed over the entire portion of tooth delimited by the strain gauges position; (b) line load distributed over a restricted area

Figure 5.19 also indicates that the strain along the tooth root naturally tends to be distributed more evenly than the load. Therefore, in the procedure defined in the previous section a first attempt value for the parameter *u* could be the one which produces a normalized shape of the load distribution similar to the parabolic interpolation of the strain values. Then the value of *u* should be increased in the subsequent iterations obtain a more slender load parabola and find the best approximation.

Chapter 6

CONTACT FATIGUE TESTS ON DISC SPECIMENS

The similarities between gears teeth and cylinders in contact have been already discussed in the previous chapters. Based on this concept, pairs of disc specimens have been developed to resemble the operating conditions of gears on apposite test benches aimed to study rolling contact fatigue phenomena and to investigate the performances of materials and lubricants. Such tests are usually referred to in the literature as *two-disc, disc-on-disc, twin disc* or *roller tests*. Specimens consist of two discs loaded one against the other to obtain the desired contact pressure. The rolling speeds and diameters may be chosen in order to generate a relative motion with different degrees of rolling and sliding between the specimens surface. Among the factors affecting the pitting durability, the material, lubricant and roughness can be easily transferred from actual gear to disc tests. The task is not that simple concerning with speed and geometry. In a gear mesh the curvature radii of teeth changes continuously along the involute profile and the sliding speeds, which are null at the pitch point, increase in module moving toward the tip and root of the tooth. On the contrary being their curvature radius unique, discs allow to resemble only a specific instant in the path of contact of gears. Nevertheless, since it is much cheaper to use metal discs instead of actual gears and since the analysis and interpretation of surface damages is easier on discs specimens due to the simple geometry and the stationary operating conditions, disc test rigs have been widely used to investigate on the contact fatigue behaviour of different materials [85,120–123], or to investigate on the influences of various parameter affecting contact fatigue such as case carburizing depth [124,125], residual stresses [126] and slide to roll ratio [122,127,128]. It is worth noting that the presently withdrawn standard BS436 [129] based the determination of the pitting durability of gears upon the results of disc tests. The currently used standard ISO 6336 [105], still mentions the possibility to use twin discs tests to characterize gears materials, although advising, in the last review of the part 5 [130], that “contact stress numbers derived from rolling contact fatigue testing have to be

used with caution since they tend to overestimate allowable contact stress numbers for gear teeth".

6.1 Brief history of disc tests

The first documented work where discs are used to resemble the contact conditions of gears date back to 1935, when Way [28] conducted his pioneering study on pitting and proposed the hydraulic pressure propagation mechanism.

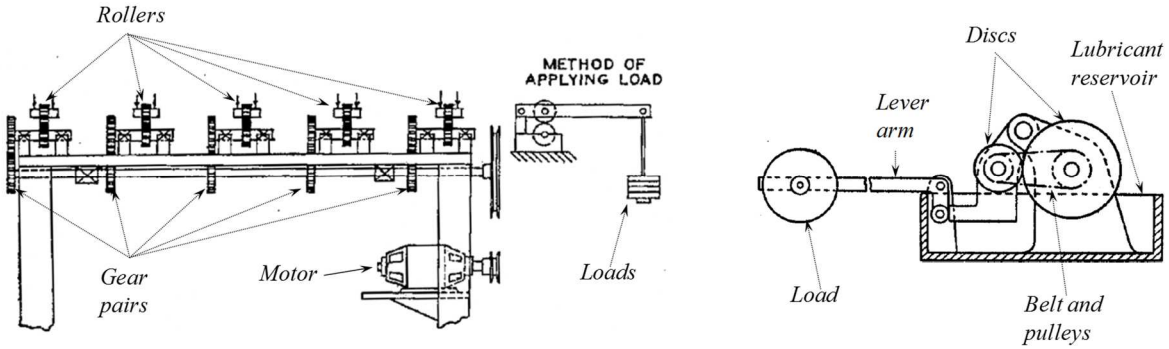

Figure 6.1 Schematic diagram of the test rigs used by Way (a) and Merrit (b).

The test bench used by Way allowed to test five couple of rollers simultaneously (Figure 6.1 a), each one composed by two discs with different diameters to ensure that points on the surface of one specimen do not came in contact at each revolution with the same point on the surface of the other specimen. The lower discs were all driven by the same line shaft, while upper discs were moved by friction in the contact surface, therefore no macroscopic sliding occurred. In the same year, Merrit published a study on the characterization of worm gears [131] where a two-disc test rig was used to investigate the friction performances of lubricated line contact. Merrit's machine used specimens with different diameters mounted on shafts connected by belt and pulleys with non-unitary transmission ratio in order to provide a defined amount of sliding between the rolling surfaces. Actually, most of the disc test rig developed in the last century are designed to allow a fixed or adjustable degree of sliding which may be chosen in order to resemble the operation conditions of specific mechanical components. Facilities similar to the ones adopted by Way and Merrit are still in use for tribological and contact fatigue analyses. The main differences with respect to the original design can be found on the method adopted to applythe load that, to date, is typically provided by spring mechanisms rather than weights,

and in the jet lubrication which often substitute dip lubrication in modern designs. As an example, Figure 6.2 shows a schematic diagram of the twin-disc test rig developed at the Gear Research Centre (FZG) of the Technical University of Munich (TUM).

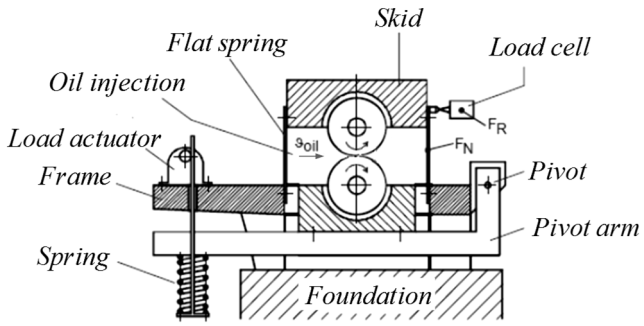

Figure 6.2 Scheme of the FZG twin-disc test rig [132]**.**

The four-disc test rig configuration shown in Figure 6.3 deserves a particular mention. A central self-centring test roller is in contact with three larger discs. One of the discs is loaded by means of a ball screw and a strain-gauged pivot arm. The arrangement of the discs 120° apart one from each other, ensures that equal loads develop in the three contacts. This apparatus is used for both micro- and macropitting investigations [87,122,127] and presents some advantages: first of all he central roller is subjected to three contacts per revolution allowing a considerable reduction in the test duration. Then, the self-equilibrating radial loads on the test specimens eliminate the need to be carried by a robust shaft allowing a small diameter. Hence high contact pressure can be obtained with relatively small loads.

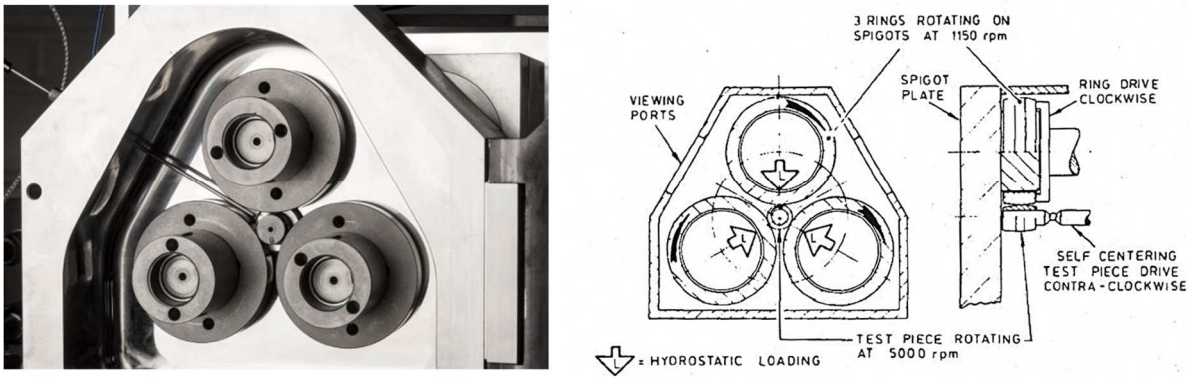

Figure 6.3 Four three disc test rig, picture [133] **and scheme** [127]

On the other hand, the costs related to specimens manufacturing would be higher as compared to traditional two-disc tests, since the larger discs should be substituted for each test. Nevertheless, some authors suggest that they can be re-used since they appear substantially

undamaged at the end of a test, being the slide to roll ratio positive on their surface and because of the lower number of contact cycles with respect to the central roller.

Finally, it is worth noting that two kinds of specimens can be adopted in disc tests, namely cylindrical discs, usually with chamfered edges, aimed to obtain a line contact between the surfaces, or alternatively couples of discs where at least one is crowned resulting in a point contact. The selection of the more appropriate design is not trivial, since both the geometries have been reported to present advantages and disadvantages in the literature. Particularly, tests performed on chamfered discs often lead to the formation of craters in correspondence of the sides of the contact area due to stress concentration caused by edge loading [123,134]. Specimens designed for point contacts, instead avoid such problem. Moreover, given the external diameters of the specimens, crowning of one of the discs allows to considerably reduce the force required to achieve a desired value of contact pressure. On the other hand, in point contacts, the pressure gradient in the transverse direction with respect to the motion causes an uneven damaging of the surface and, if micropitting or wear occur, a groove may form on the slower surface. Modifications on the contact geometry during the test are undesired since they cause unpredictable variations of the contact pressure for a given applied load. To cope with the above mentioned issues, Li and Kahraman [134] recently proposed the use of a cylindrical disc coupled with a disc which profile approaches the cylindrical shape at the centre of the contact and curves exponentially at the sides. Such correction is commonly used to avoid edge loading in roller bearings.

6.1.1 Survey of data available in the literature

Although within this project preliminary tests were performed also on a through hardened C45 steel, the review presented in this section deals mainly with works performed on case hardened steels which are of greatest interest for high power applications drivelines.

Concerning case hardened steels, the existing literature about discs tests shows how the pitting durability of the specimens can be very different depending on the specimens features and the test parameters. Particularly, contact fatigue phenomena can be affected by: curvature radii of the surfaces, sliding conditions, lubricant viscosity and temperature, roughness, case depth, and residual stresses induced by the heat treatment or by shot peening. Also the damaging mode can be different: in many cases tests on case hardened discs led to micropitting on the surface [34,123,134–136] which can arrest after the redistribution of load due to the

modification in surface topography or degenerate to macropitting [121,127]. Pressure-life data relevant to macropitting failures from various publication are reported in Figure 6.4, where results relevant to case hardened steels have been grouped in a single chart regardless of material composition according to the classification proposed by the ISO standard 6336.

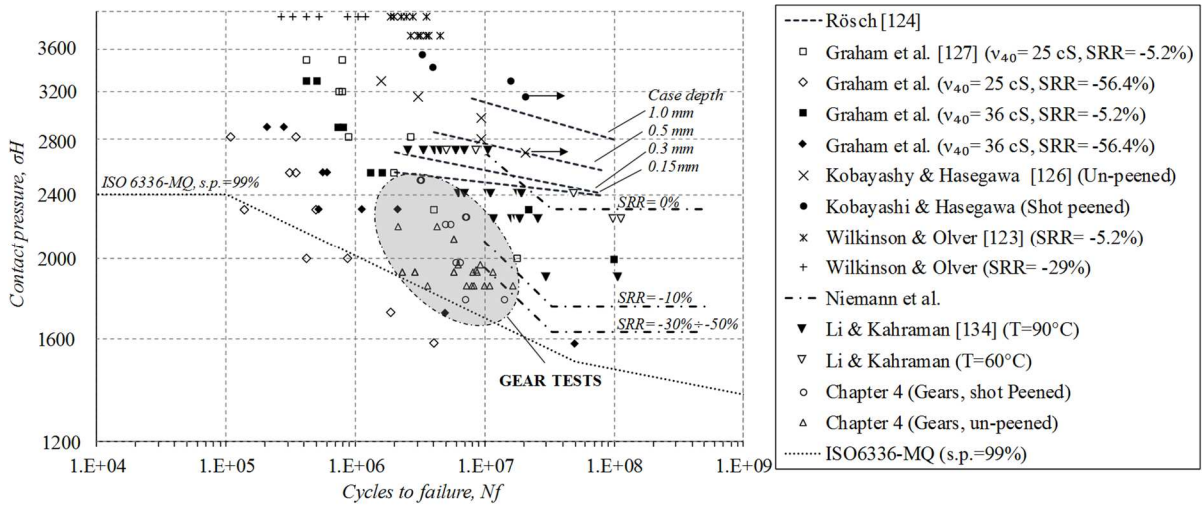

Figure 6.4 Survey of literature data about disc tests, compared to data relevant to pitting in sun gears from the analysis presented in Chapter 4.

Disc test are compared with the data relevant to sun gears failures presented in chapter 4. Note that the S-N values reported in Figure 6.4 are different with respect to the ones reported in figures 4.6 and 4.7 because, since in this case gears data are directly compared with disc tests performed in various conditions in terms of lubricant, surface finish and speeds, the correction applied in chapter 4 to make data coherent with the curve of ISO 6336 was not applied here. Even at first glance, the chart reports the wide variety of results obtainable by means of disc tests on case hardened steels, which in most cases showed much higher fatigue performances as compared to gears. The variety in damaging modes and durability of discs revealed by the literature review emphasizes that, to obtain representative data from this kind of tests, manufacturing process and heat treatment of the specimens, as well as the test parameters, need to be chosen in order to recreate as close as possible the stress state, material properties and working conditions of the gear pair that are intended to be resembled. Based on the existing literature about disc tests, some considerations may be drawn:

- The slide-to-roll ratio plays a fundamental role in the durability of specimens, leading to a considerable reduction of lifetime for increasing percentage of sliding. When the SRR is high, scuffing may occur earlier than pitting on the discs surface as reported by Wilkinson and Olver after tests on discs ran with a SRR of 56.4% [122].

- Specimens with crowned surfaces (point contacts) typically show a higher durability with respect to cylindrical specimens (line contacts), as shown in Figure 6.5. Edge loads at the axial edges of cylinders, as well as the increase in the conformity of the surfaces due to wear in points contacts, are thought to be the main reasons of such difference.
- Higher temperature and lower lubricant viscosities generally correspond to shorter lifetimes, because the capacity of the elastohydrodinamic film of lubricant is reduced.

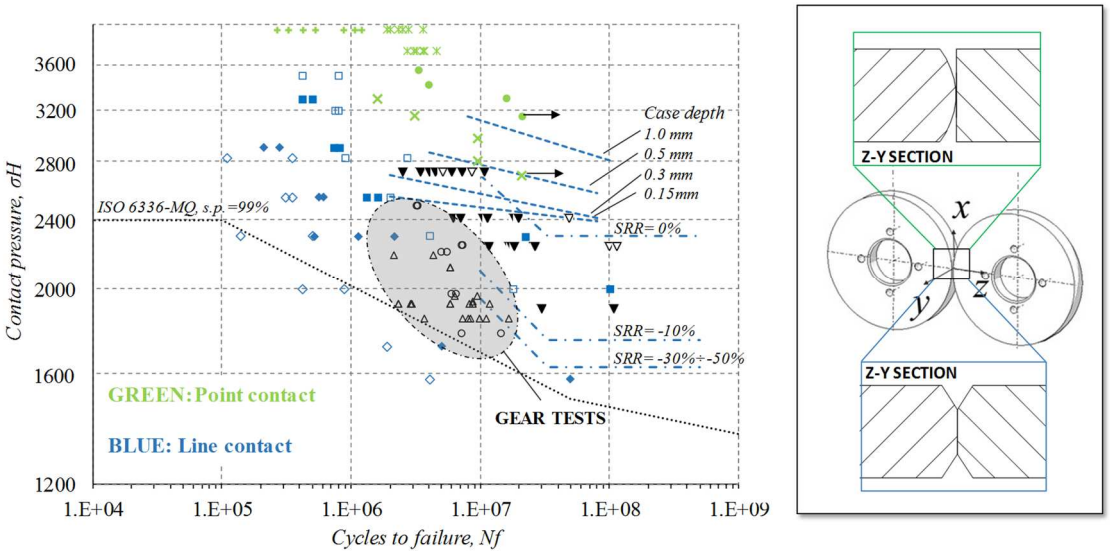

Figure 6.5 Disc data divided according to the type of specimens (point or line contact)

While the chance to use twin-disc tests to compare the surface fatigue performances of different materials relative to one another is universally accepted, the possibility to correlate results of disc tests and gears durability is debated [121,123,137]. Many authors [121,122,126,138–140] claim a higher durability of disc specimens with respect to gears, nevertheless, even if the transfer of absolute values of endurable contact stresses from disc tests to actual gear applications is questionable, a good relative correlation was proven by several works [126,127,139].

Table 6.1 Summary of works available in the literature about twin disc tests

Reference	Type of test	SRR	End of test criteria	Contact	Material	Kinematic viscosity of lubricant at 40°C	Temperature	Eht
Rosh (1976) [124]	ND	-24%	ND	Line contact R'=10.5 mm	16MnCr5	100 cS	50°C	0.15 mm 0.3-0.5 mm 1 mm
Graham et al. (1980) [127]	4 discs	-5.2% -56.4%	Torque measurement (lower treshold)	Line contact R'=15.4 mm	EN39b	25 cS and 36.2 cS	ND	0.65 mm
Kobayashi & Hasegawa (1990) [126]	2 discs	-40%	Change on reflectivity mesured by optical fiber and accelerometrs	Point contact R'=18.9 mm	Case hardened Cr-Mo steel (shot peened and un-peened)	87 cS	80°C	0.7 mm
Wilkinson & Olver (1999) [123]	4 discs	-5.2% -29% -56.4%	RMS of vibration signal	Point contact R'=5.56 mm	BS156	92 cS		1.5 mm
Niemann et al. (2005) [85]	ND	0 -10% -30…-50%	ND	Line contact	16MnCr5	ND	ND	0.75 mm
Li & Kahraman (2011) [134]	2 discs	-25%	First Macropit greater than 1 mm²	Esponential correction of profile	SAE 4620M	Defined for different temperatures: 6.61 cS at 90°C 15.39 cS at 60°C	90°C and 60°C	ND

6.2 Development of a two-discs test rig

A twin disc test rig was designed and initially developed starting from the master thesis of the author [141], in cooperation with OZ S.p.A., and is currently applied for a European patent [142].

A schematic representation of the bench is given in Figure 6.6. The discs are mounted on a couple of spindles and rotate with the same angular velocity ω. With reference to Figure 6.7, the desired sliding speed v_s is obtained by using two discs with different radii R_{x1} and R_{x2}:

$$v_s = \omega \cdot (R_{x1} - R_{x2}) \tag{6.1}$$

And the slide-to-roll ratio is given by

$$SRR_{1,2} = \frac{2(R_{x1} \mp R_{x2})}{R_{x1} + R_{x2}} \tag{6.2}$$

The centre distance of the two discs is equal to 70 mm (R_{x1}+R_{x2}=70 mm). One of the spindle is fixed, while the other is capable of small rotations around a pin and is loaded by means of a screw-spring system equipped with a load cell. The number of contacts elapsed by the start of the test is measured by a cycle counter.

The whole system is suspended by means of anti-vibration mounts. A lubrication unit serves the gear box, the spindles bearings and a nozzle aimed to keep the contact area of the specimens wet. A second work of thesis [143], concluded before the beginning of the present Ph.D. project, was dedicated to settle the basis for the development of a vision system aimed to automatically perform periodical inspections of the damagin condition of the surfaces and to stop the test when a defined end of test criteria is attained. Details about the improved version of system, completed whithin the scope of this work, will be given in section 6.2.1.3.

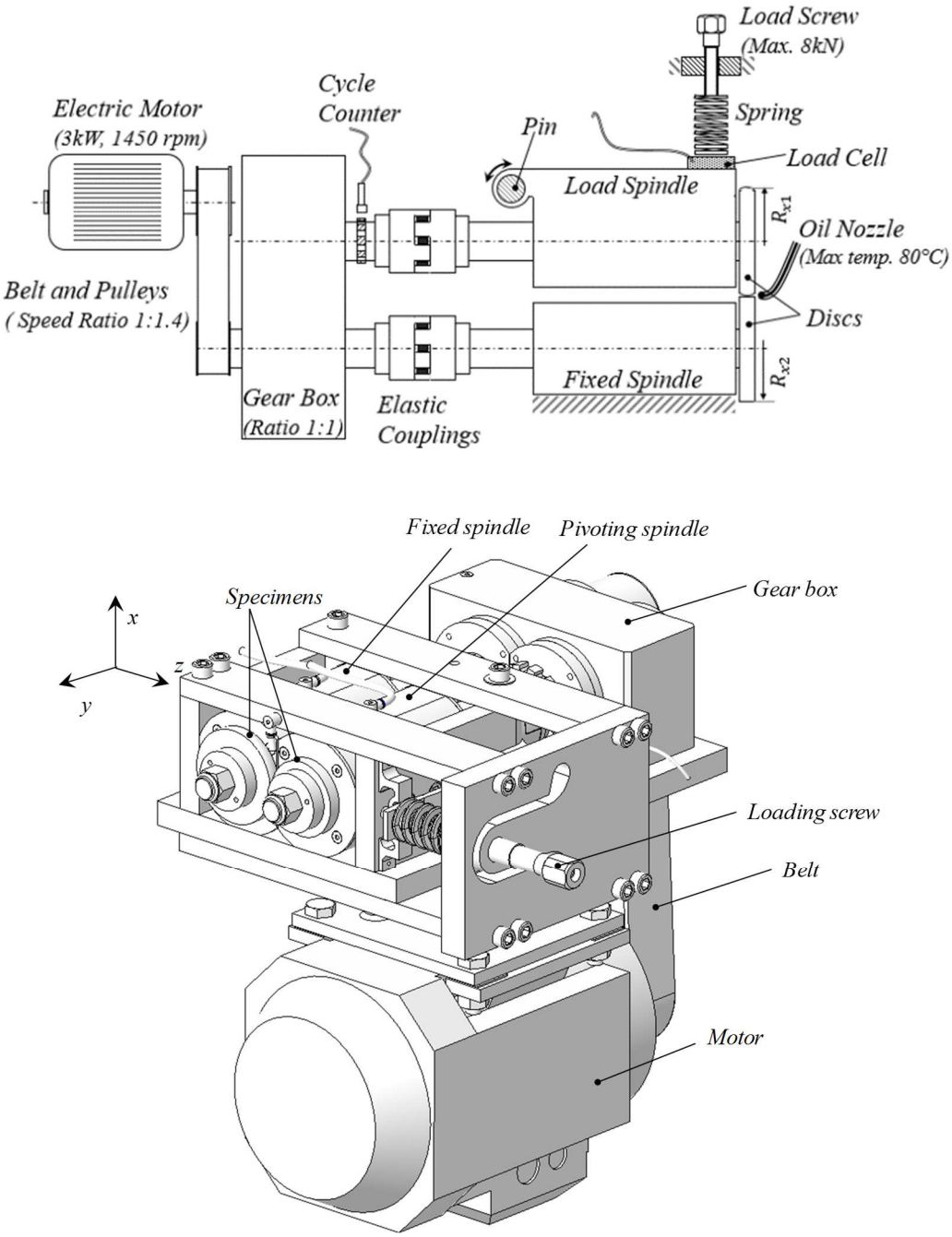

Figure 6.6 Scheme of the two-disc test rig and isometric view of the set-up.

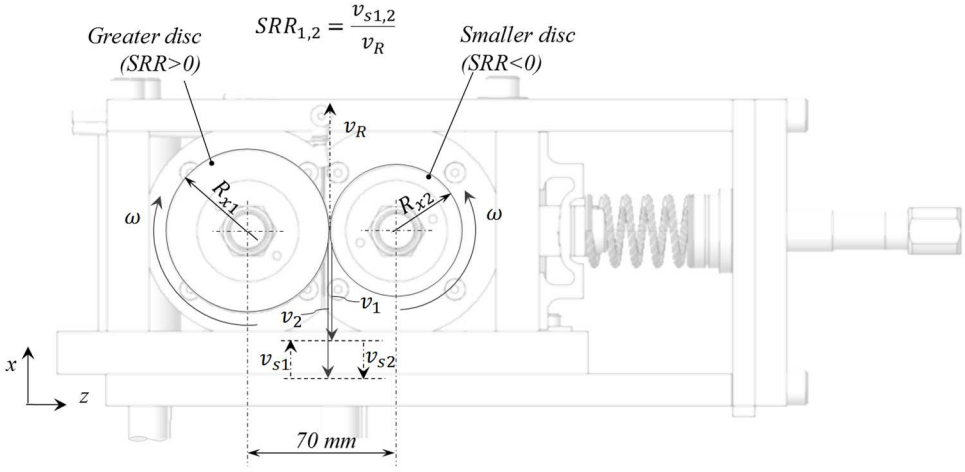

Figure 6.7 Rolling and sliding speeds on the surface of the specimens.

6.2.1 Improvement of the test rig

At the beginning of the present project, the test bench was already functioning but still failed to meet some important requirements to allow the execution of fast tests with uniform and objective failure criteria. Particularly:

- The oil stream on the contact region was supplied at the tank temperature which was fairly lower than the typical operating temperature of gear boxes.
- The load cell measured the applied force indirectly (before the spring) and was calibrated off-line.
- The automatic vision system was in the initial stages of development, therefore to monitor the damaging of the discs, the test was periodically stopped by the operator and the level of damage of the surface was determined by visual inspection.

To overcome these problems, the rig underwent substantial modifications in the early phases of the present project. Particularly:

- The bench was provided with a heating device to control the temperature of the lubricant in the contact area.
- The system for the load application and measurement was completely re-designed, in order to measure the force directly on the spindle and to allow the in-line calibration of the load cell.
- The rig control and the vision system were completed and currently allow periodical inspections of the specimens surface and measurement of the percent of damaged area.

The modifications listed above are discussed in the next sections.

6.2.1.1 Heater

It is well known how the temperature affects the viscosity of the lubricants and, therefore, its capability to form a film capable of separating the contact surfaces [16,144]. In the planetary gear boxes of axles for off-highway vehicles, gears operate with splash lubrication and the oil achieves temperature around 80°C. However, during twin disc tests with relatively low values of the slide-to-roll ratio, the temperature of the lubricant in the contact area is typically below 50° C if no heating is provided. Therefore, the rig was provided with an electric heater to increase the temperature of the oil stream which lubricates the contact region.

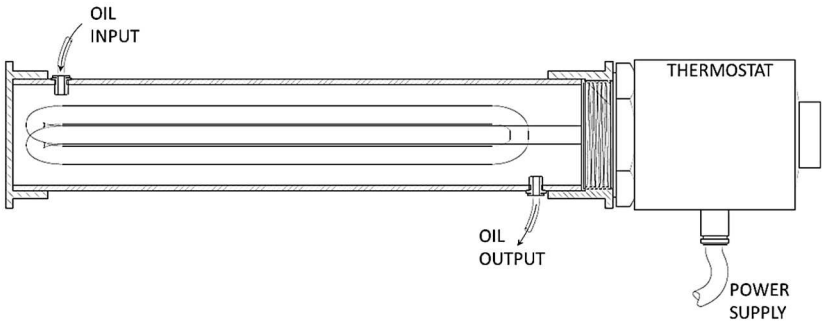

Figure 6.8 Scheme of the heater of the test rig.

The heater is composed by a commercial heating resistance Masterwatt 72V101032000325, inserted in a steel tube with an external insulation (Figure 6.8). A rough estimation of the required size of the heater was made considering the volumetric flow rate $\dot{V}$ of the oil from the nozzle placed over the specimen, approximatively equal to $0.125\ l/min$. Assuming for the oil a density of $\rho = 0.88\ kg/l$ and a specific heat of $c = 2.1 \frac{kJ}{Kg\ K}$, and considering an inlet temperature of $14°C$, the ideal thermal power needed to heat the oil up to a temperature of 80°C is given by:

$$P = V \cdot \rho \cdot c \cdot \Delta T = \frac{0.125}{60} \cdot 0.88 \cdot 2.1 \cdot 1000 \cdot (80 - 14) = 254\ W \qquad (6.3)$$

The chosen product has a nominal power of 330 W. To prevent deterioration of the oil as a consequence of overheating at the interface with the heater, a coil with specific power $< 1 W/cm^2$ was selected. As shown in Figure 6.9, only the oil flow sent to the specimens passes through the heater, unlike the lubricant for the gear box and the bearings which is kept at the

temperature of the reservoir. Nevertheless, all the flows are in the end collected in a common tank, whose temperature inevitably raises when the heater is functioning.

The heater is activated and switched-off by the controller Pixsys ATR121 whenever the oil temperature exceeds defined set-points. A further threshold can be set to stop the test if the temperature overcomes a maximum value. Moreover, a safety thermostat on the heater, set at 95°C, prevents excessive overheating of the lubricant.

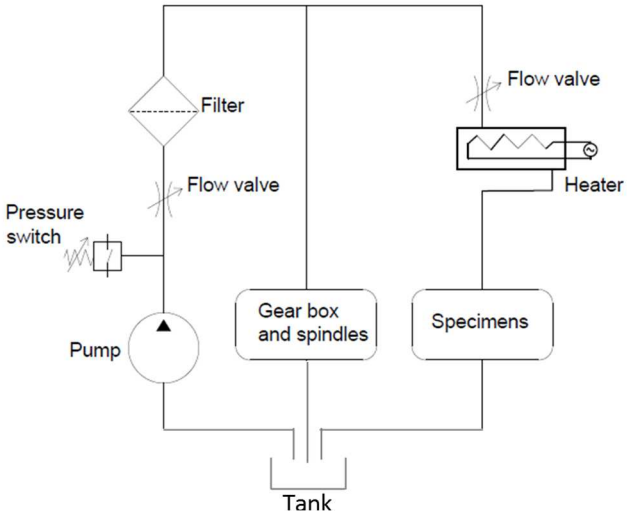

Figure 6.9 Hydraulic circuit of the two-disc test rig

6.2.1.2 Load Cell

The first improvement in the loading system, was the development of a dynamometric specimen aimed to test the proper functioning of the load cell mounted on the rig and to allow periodical in-line static calibrations. The disc was designed to be mounted on the rig coupled with one of the specimens used for the regular tests and was realized in medium-carbon steel C45. The particular geometry was studied to allow the measurement of the radial load with a proper sensitivity by means of strain gauges, and at the same time to ensure at any point of the device an adequate safety margin against yield, up to a load of 6.25 kN. The outer profile of the disc is recessed in correspondence of the point of contact with the coupled specimen to allow some self-alignment capability. The 40 mm radius of curvature was chosen to ensure that the elliptical contact area between the discs be entirely included in the recess for all the possible applied loads, thus avoiding edge contacts which possibly would have caused non linearities or unsymmetrical loading of the cell. A full Wheatstone bridge was arranged on the disc as shown in Figure 6.10.

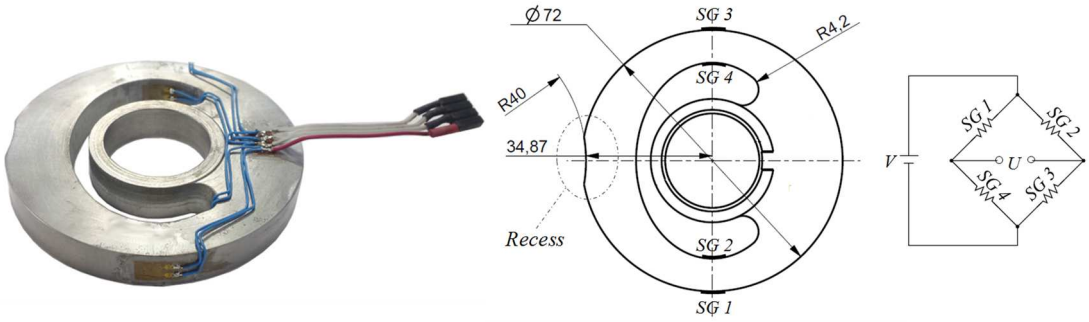

Figure 6.10 Dynamometric specimen for the in-line calibration of the rig's load cell.

Figure 6.11 shows the results of the finite element analysis performed in the design stage of the disc. With an applied load of 6250 N the strain in the grids positions of strain gauges 1 and 2 are equal to 404 $\mu\varepsilon$ and 962 $\mu\varepsilon$ respectively. Therefore, the resulting sensitivity of the Wheatstrone bridge would be equal to:

$$\frac{U}{V} = \frac{K}{4}(\varepsilon_1 - \varepsilon_2 + \varepsilon_3 - \varepsilon_4) = \frac{1}{2}(2 \cdot 4{,}0395 + 2 \cdot 9{,}6226) \cdot 10^{-4} = 1{,}3662 \cdot 10^{-3}\frac{mV}{V} \quad (6.4)$$

corresponding to a calibration constant of $4.574\frac{kN}{mV/V}$.

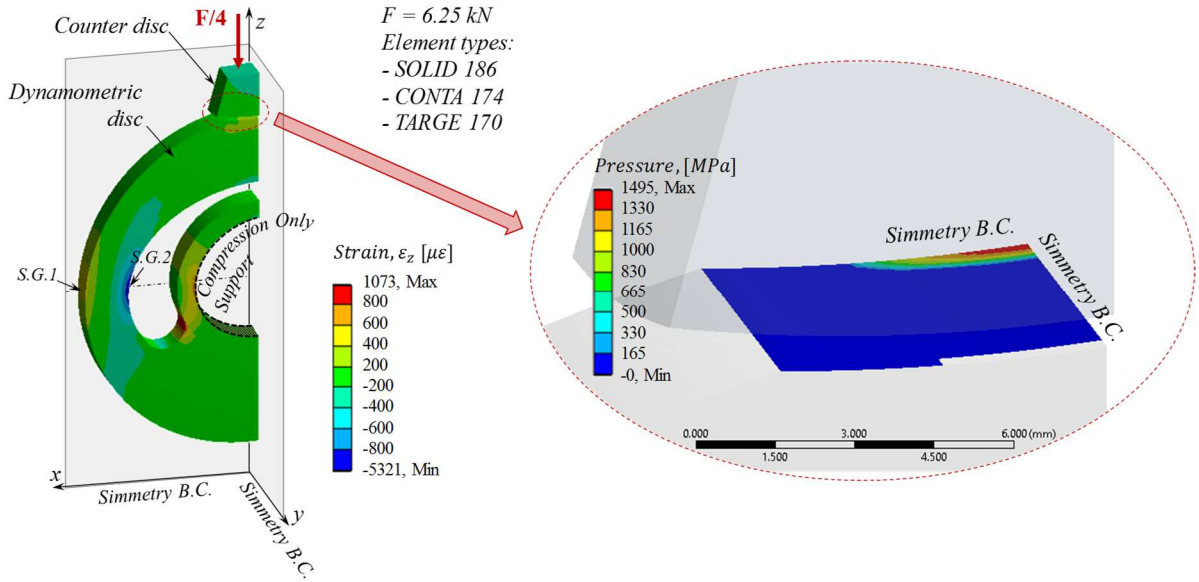

Figure 6.11 Results of the FEM analysis of the dynamometric specimen with an applied load F = 6250 N.

The dynamometric specimen was calibrated by applying constant load ramps by means of a servo-hydraulic testing machine with a 15 kN load cell (see Figure 6.12)

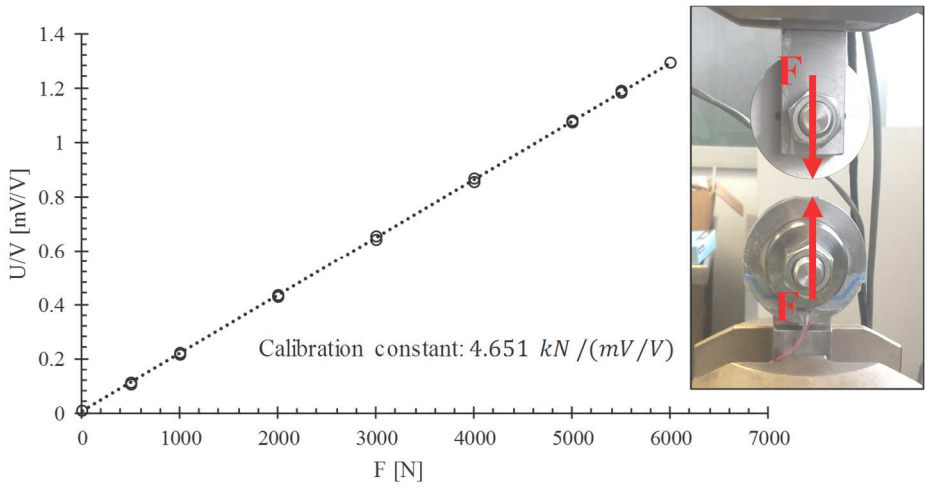

Figure 6.12 Calibration of the dynamometric specimen.

The derived calibration constant was in good accordance with the results of the preliminary finite element analysis.

Subsequently, the strain gauged disc was used to verify the proper functioning of the loading device of the rig. In the early configuration of the rig, the load was applied by means of a series of disc spring which were compressed by a screw sustained by a cantilever support (Figure 6.13). The load was measured by strain gauges applied to the screw support. A comparison between the signals of the dynamometric specimen and of the load cell of the rig showed that the clearances between the screw and the thread caused a misalignment between the axis of the screw and of the spring package leading to unacceptable oscillation between the measured and applied load [145]. Moreover, internal friction in the disc spring package caused a difference between the curves measured in the loading and unloading phases. Therefore, to improve the quality of the load measurement, the loading system was modified as follows:

- A new load cell was designed to be mounted directly on the spindle in order to measure the load in a position as close as possible to the specimens.
- The disc springs were replaced with a helical spring
- A steel pivot arm was introduced to ensure that the load is applied to the cell in a fixed direction regardless the movement allowed to the screw by the clearance in the thread

A schematic representation of the system is given in Figure 6.14.

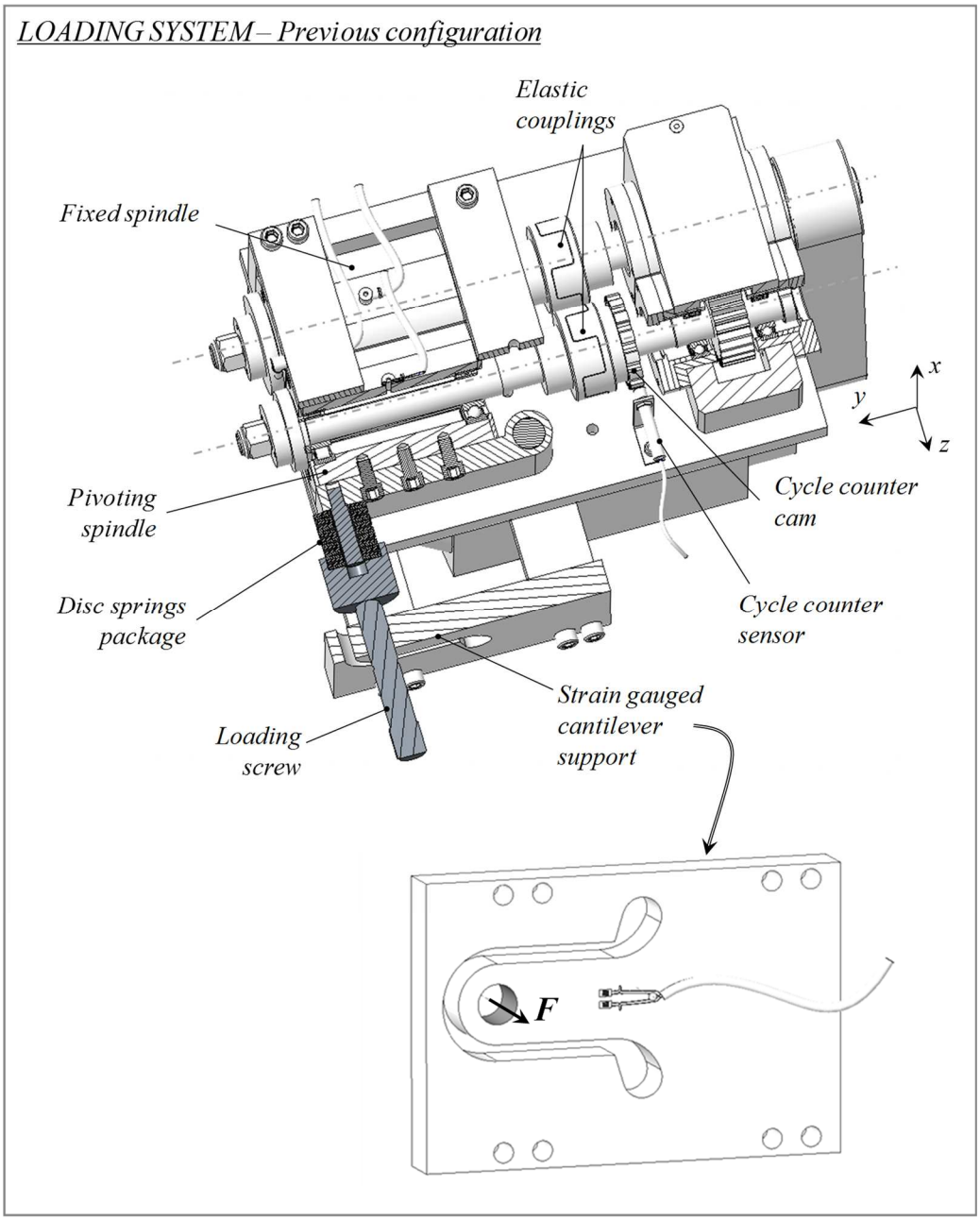

Figure 6.13 The two-disc test rig with the loading system in the early configuration.

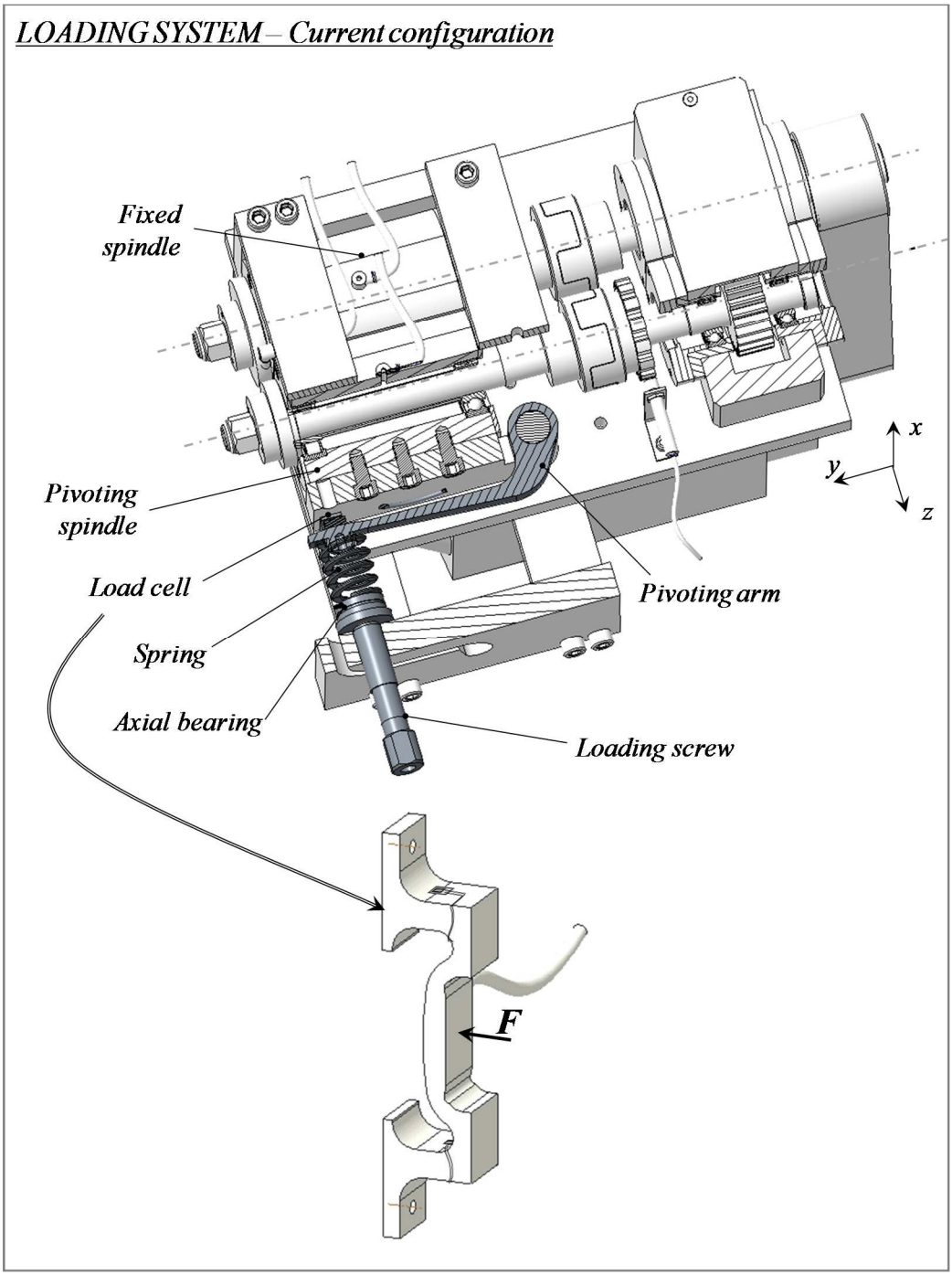

Figure 6.14 The two-disc test rig with the loading system in the current configuration.

The unusual bridge-shape of the load cell was determined by the limitation in size due to the need to fit the new system in the volume dedicated to the previous solution, with minimum modifications to the existing components. To allow an adequate safety coefficient against yield, while still maintaining a good sensitivity the load cell was realized in Aluminium EN 7075 ($R_{p\ 0.2,\min} = 495\ MPa, \mathrm{E} = 72500$ MPa). To maintain the load concentrated at the center of

the load cell even when the span of the cell is bended by elevate loads, both the terminal part of the pivot arm and the span are crowned.

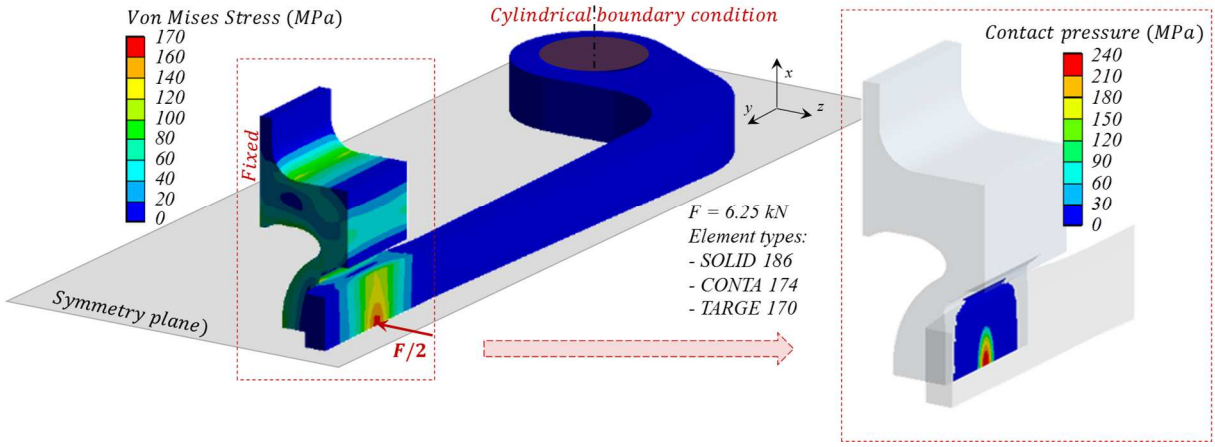

Figure 6.15 Finite element model of the current loading system.

Since the curvature of the two parts lies in orthogonal direction one respect to the other, the contact area between the parts is elliptical as shown in Figure 6.15. The criteria for the choice of the crown radii was similar to the one used for the dynamometric specimens: for the entire load range of the cell the contact ellipse had to be included between the edges of the pivot arm. The calibration of the new system by means of the dynamometric specimen showed a much better reliability as compared with the previous solution.

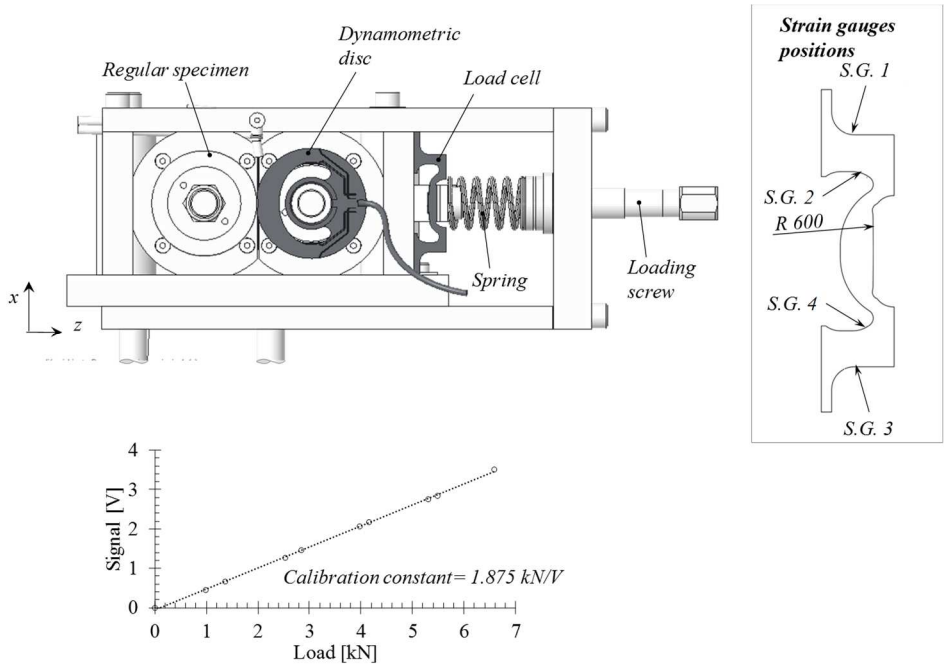

Figure 6.16 Calibration of the load cell by means of the dynamometric specimen

Figure 6.16 illustrates the process of in-line calibration of the rig's load cell. The load is applied through the loading screw and controlled by the measurement of the dynamometric specimen. The output voltage of the load cell conditioner is registered for a number of load steps and plotted against the applied force. The calibration constant is relevant to the whole measurement chain and is expressed in kN/V.

6.2.1.3 Control system

When it was initially conceived [143], the control system of the machine was structured to operate as follows: during periodical stops of the test a pneumatic motor was moved by a cylinder in order to engage the bevel gear mounted on the shaft of the electric motor (Figure 6.17). Specimens were thus rotated at moderate speed while a webcam, mounted on an arm controlled by a second pneumatic cylinder, was positioned over either of the two discs and recorded a video of the surface (Figure 6.18). The image processing was performed by a LabVIEW virtual instrument.

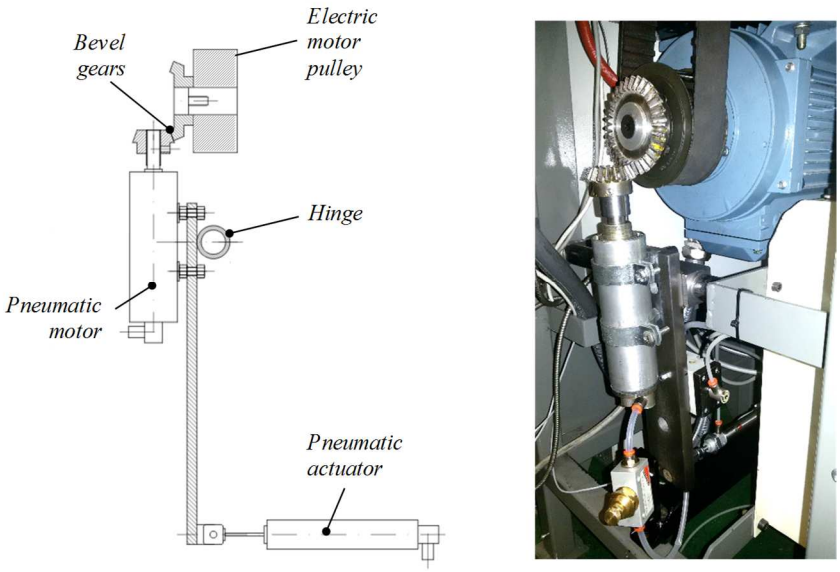

Figure 6.17 Scheme and picture of the System used in [143] **and to move the specimens during the inspection phase.**

Figure 6.18 First concept of the vision system for the automatic inspection of the specimen's surface [143]**.**

Although the original design provided a good background for the subsequent development, it presented some issues:

- the quality of the image of the webcam was not adequate to allow the identification of small craters
- although the pneumatic motor enabled a slow speed of rotation of the specimens, the frame rate of the webcam was not enough to allow an analysis of the specimens surface during motion
- the algorithm for the pit recognition was based only on a threshold on the grey level of the pixels, therefore it was sensitive to the ambient light variation and to the non-uniform light reflection condition of the curved surface of the specimens
- The system was controlled by the PLC and lacked of a user interface. Hence, the setting of the number of cycles for the periodic inspections was tricky and required the modification of the program code of the PLC.

Therefore, in cooperation with a master thesis project [145], some improvements were developed to ensure the proper operation and the versatility of the system. First of all, the Labview interface created for the analysis of the photograms grabbed by the webcam was modified to allow the complete control of the rig, including start and stop of the test, load monitoring and settings for the periodical automatic inspections. The communication between the PC and the rig is provided by an Arduino board which is directly manageable by Labview. The controller allows the reading of the analog signal coming from the load conditioner and the sending of signals to the PLC by means of relays. A signal is periodically sent to the PLC, thus if for any reason the connection with the control computer is interrupted, the test is automatically stopped. Thanks to the above described arrangements, the rig became

manageable from any place, provide that a web connection is available to allow the remote control of the computer dedicated to the rig. An e-mail alert system was also developed to inform the user in cases of stops of the test. This is a very useful feature since it allows to identify by remote the cause of stops and, if appropriate, to restart the test avoiding downtimes. The webcam was substituted with a USB microscope Dino-Lite AM4115ZTL to improve the resolution of the acquired images. The microscope provides a magnification up to 150x and allow to work at a relatively great distance from the workpiece (105 mm with a magnification of 20x). On the other hand, it requires the specimen to be perfectly stationary and the focus is manual, therefore the position of the microscope need to be adjusted when moving from one specimen to the other to keep the focus distance constant despite the difference in the diameters. Hence the microscope is fixed to the pneumatic arm by means of a vertical sliding support which position is set by means of a stepper motor controlled by the Arduino board. To overcome the problem related to the specimen's rotation during the image acquisition, a cam with 14 teeth was mounted on one of the shaft in correspondence of the sensor of the cycle counter. During the periodical stops of the machine, the counter sends an impulse to the PLC at the passage of each tooth, thus allowing to rotate the specimens by small sectors. Initially the rotation was provided by the pneumatic motor as in the first design of the vision system. Nevertheless, since the pneumatic motor incurred in frequent jams, in a later configuration it was dismissed in favour of the use of the main electric motor. In fact, since the inverter which controls the electric motor allows soft starting, the specimens rotate at first very slowly and, provided that the time interval between the signal of start and stop is relatively small, the positioning is accurate enough to allow the scanning of the surface. To avoid an excessive frequency of starts and stops, and reduce the positioning error, the vision systems grabs 14 images of 26° sectors of the surfaces, but at each step rotates the discs of an angle equivalent to three sectors (78°). Thus, after three complete revolutions of the discs all the sectors of the surface will have been acquired. To ensure cleanliness of the discs the residual lubricant is removed from the surface by compressed air, taken from the pneumatic arm handling circuit, and sent to two nozzles located over the specimens (see Figure 6.19). The microscope and the specimens area are obscured from ambient light by means of a cover; a number of LEDs provides repeatable light conditions. However, the surface geometry originate undesired shadows on the image, which can make troublesome the automatic recognition of pits. In order to minimize the effect of different light conditions, the images are processed as follows:

1. A region of interest (ROI) is defined in the image and the gray level of each pixel is evaluated;
2. For each pixels row in the ROI, a moving average over the gray levels of 100 pixels is calculated;
3. The averaged frame is subtracted to the original image obtaining a new photogram where local defects such as pits are evidenced;
4. All pixels having a grey level greater than a predefined threshold are considered to belong to a damaged area;
5. The damages may be filtered by shape and dimensions in order to discard all candidate defects which cannot be attributed to pitting damage;

Finally the total extension of damaged area is compared with a target defined by the user and adopted as failure criterion to stop the test.

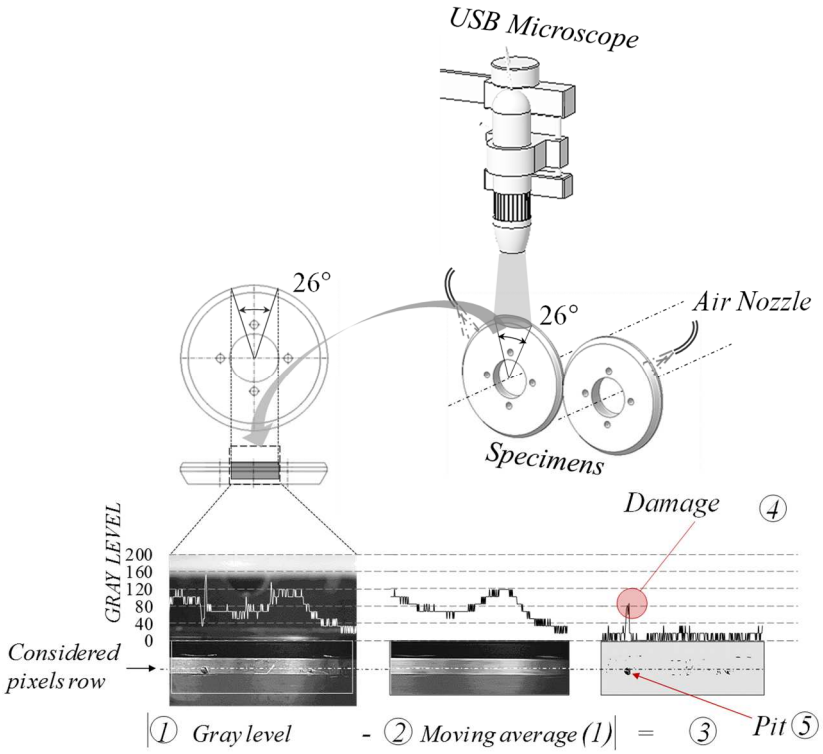

Figure 6.19 Schematic representation of the image processing algorithm.

When the control software is started, a working directory is created to record all the images and information relevant to the test, including a report containing a summary of date, time, number of cycles and percent of damaged area relevant to the automatic analyses. For each inspection moreover, a dedicated folder is created in the main directory with both the original images and the results of the elaboration, and a text file reporting the number of craters and the

damaged area measured for each image. Figure 6.20 shows the front panel of the Labview program, which constitutes the user interface of the control system.

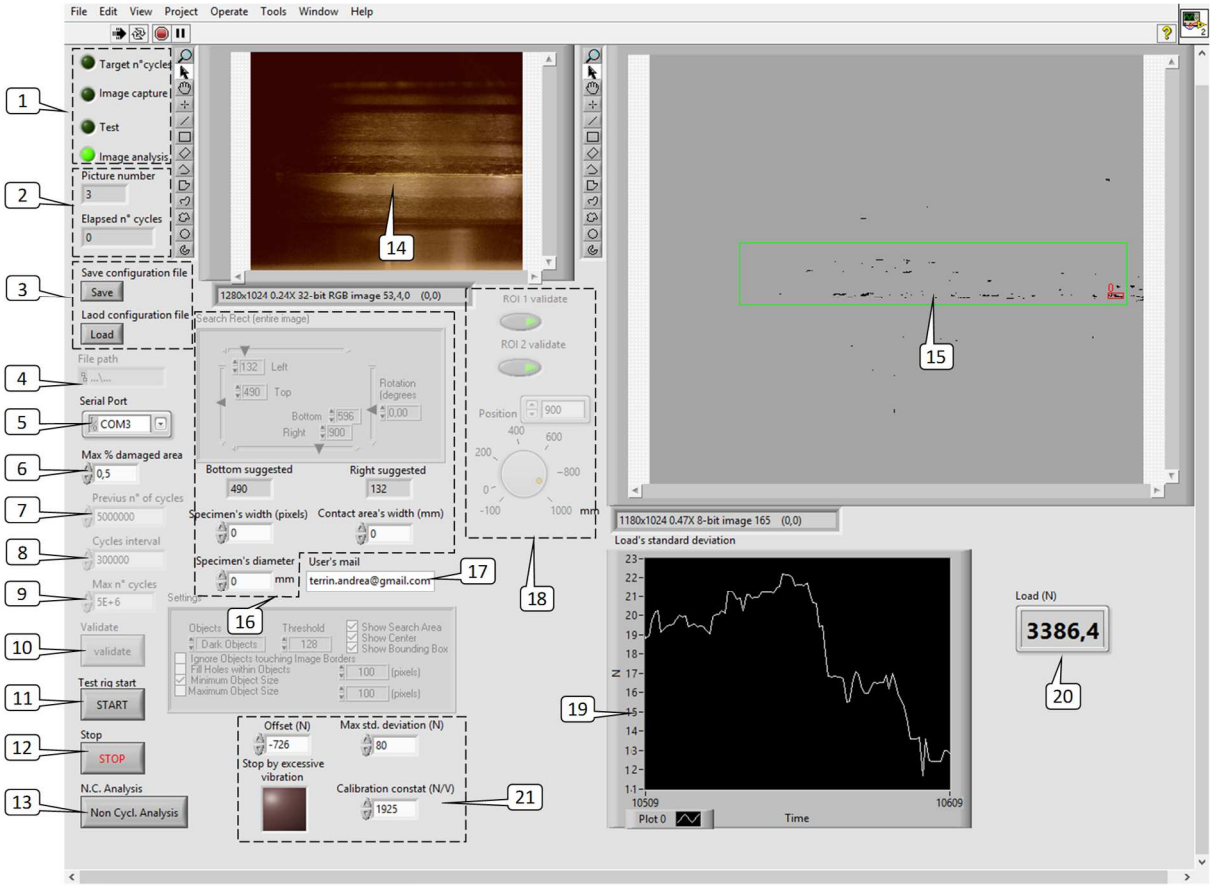

1. *Indicators of the mode of functioning (Test, analysis,…)*
2. *Counters (number of cycles/number of picture)*
3. *Save / Load a configuration settings*
4. *Saving directory path*
5. *Arduino serial port selection*
6. *Maximum percentage of damaged area allowed*
7. *Number of cycles already elapsed during previous tests*
8. *Number of cycles among each inspection*
9. *Maximum number of cycles allowed*
10. *Confirm settings*
11. *Start button*
12. *Stop button*
13. *Request of a non programmed inspection*
14. *Non elaborated image*
15. *Elaborated image*
16. *Definition of the region of interest*
17. *User e-mail for notifications*
18. *Positioning of the microscope*
19. *Standard deviation of the load signal*
20. *Load*
21. *Load settings (tare, calibration…)*

Figure 6.20 User interface of the control system.

For the sake of safety, the rig is automatically stopped when either of the following conditions manifests:

- The access window to the specimens is opened
- The pressure of oil in the supply duct drops to ambient pressure
- The lubricant temperature in the specimens area overcomes a defined set-point
- The standard deviation of the force signal repeatedly overcomes a defined set-point

- The failure criteria or the maximum allowed number of cycles is fulfilled
- The connection with the control computer is missing

6.2.1.4 Torque transducer

In its actual configuration, the test rig lacks of a transducer capable of measuring the friction force generated in the contact. Such information could be interesting to compare the friction coefficients resulting by different lubricants or slide to roll ratios, and to investigate the evolution of friction characteristics during the test. Moreover, the measure of torque on discs spindles have been deemed to be a reliable indicator for the onset of damages, at least in the case of line contact [127]. A feasibility study was performed to assess whether it could be possible to introduce a torque measuring system in one of the spindles, with simple modifications of the components and without changing the size and the global structure of the bench. Since as far as the author's knowledge, the dimension of torsiometers available in the market is not compatible with the actual design of the rig, the proposed solution uses a strain gauge torsion bridge applied directly to one of the shafts, whose signal is handled by a telemetry module for rotating shaft TEL1-PCM, produced by KMT (Figure 6.21).

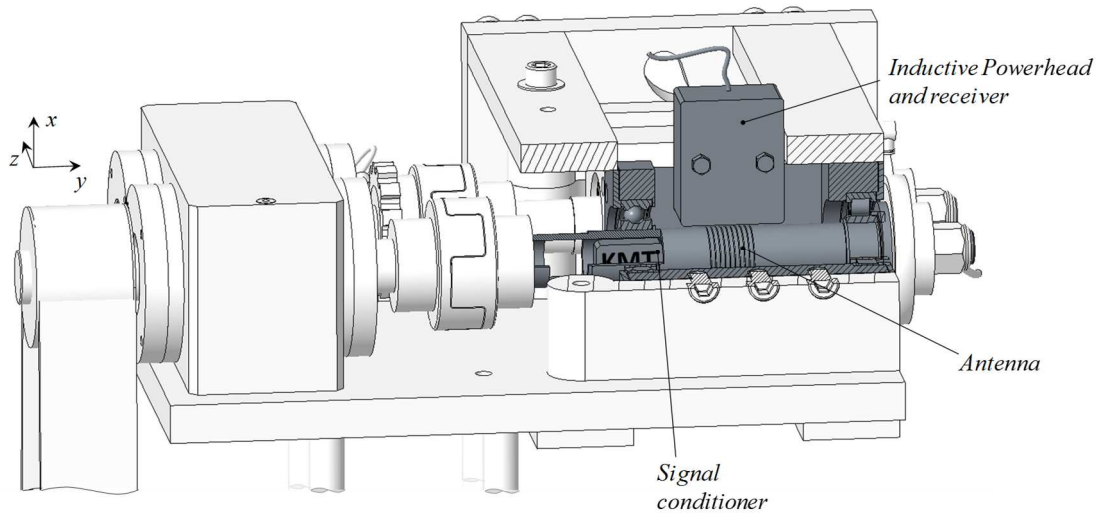

Figure 6.21 Proposed solution for a torqe measuring system aimed to asssess the friction coefficient during disc tests.

Power supply to the conditioning module and the strain gauge is provided by an inductive device by Hall effect. The same system is used to receive the measured signal as well, and transmit the information to the acquisition unit.

The conditioning module has dimensions $12 \cdot 18 \cdot 35\ mm$, thus is sufficiently small to be enclosed in a cavity appositely realized in the shaft beneath the ball bearing, where the stresses due to bending are the lowest. Being limited to a section of the shaft where the stresses are low, the above described modification would not affect the integrity of the part during normal operation. A small hole allows the wire of the antenna to pass through the cavity wall in order to be wound externally around the shaft. The receiver can be easily fitted into a seat milled on the spindle support, with the precaution of maintaining a sufficient clearance between the inductive power head and the shaft support, as recommended by the guidelines of the device, to avoid power dispersion in the surrounding metal. The hollow part of the shaft is weakened by two rectangular slots dimensioned to allow a sensitivity of the bridge of at least 0.4 mV/V when a load of 6 kN is applied to the specimens and assuming a friction coefficient approximatively equal to 0.05 and a diameter of the greater specimen equal to 78.4 mm. Under such conditions the torque induced by friction would be:

$$T = 6000 \cdot 0.05 \cdot \frac{78.4}{2} = 11760\ Nmm \tag{6.5}$$

Figure 6.22 shows the design of the modified shaft and the results of the finite element analysis dedicated to the sensitivity analysis of the wheatstone bridge.

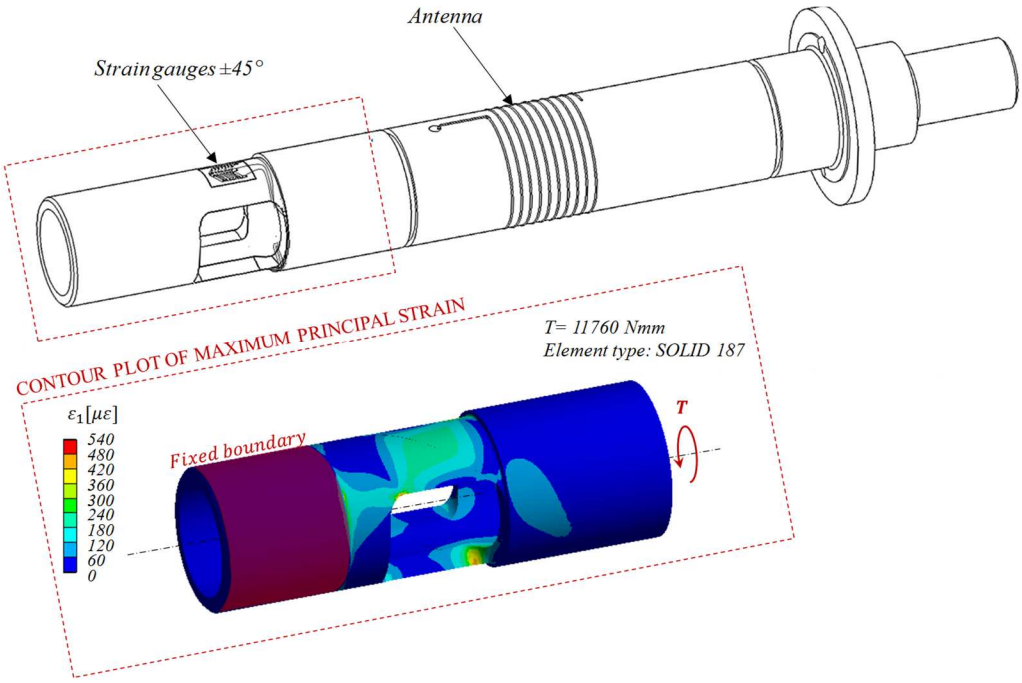

Figure 6.22 Scheme of the strain gauged shaft and finite element sensitivity analysis.

6.3 Tests on C45 through hardened steel discs

Preliminary tests were conducted on 4 pairs of chamfered discs made of C45 through hardened wrought steel, with a surface hardness of 270 HV [146]. The tests were aimed to verify the correct functioning of the rig and of the vision system. The geometry of the specimens is represented in Figure 6.23. The cylindrical surface is reduced to a width of 2 mm by the chamfers in order to allow to achieve relatively high contact pressure with moderate loads.

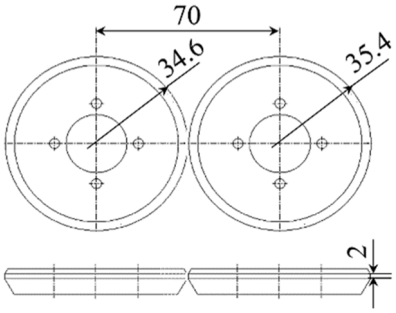

Lubricant properties	
Viscosity at 100°C	10.1 mm²/s
Viscosity at 40°C	65.6 mm²/s
Density	0.885 kg/l

Figure 6.23 Specimens geometry and lubricant properties.

The tests were run with different pressure levels and a speed of the spindles of 1600 Rpm, corresponding to a sliding speed at the specimens surface of 0.134 m/s. The lubricant was specific for agricultural drivelines (see Figure 6.23 for the main properties). The lubricant temperature, measured at the outlet of the contact area stabilized in the range 42÷48 °C during all the tests without providing any form of heating or cooling. The applied force F to obtain the desired contact pressure σ_{H0} was calculated by the Hertz's formulas for contact between parallel cylinders, reported in chapter 1. The specimens were deemed to be failed when the first pit was observed on the surface. One of the test was then continued until a second crater was formed.

6.3.1 Damage analysis

After the tests the craters produced by pitting were observed both with optical microscope and SEM. The mechanism of pitting formation can be explained as follows: during running in, in mixed rolling/sliding contacts, friction between the mating components causes the flattening of the asperities accompained by a severe plastic deformation of the top layers in the direction of sliding of the counter surface (Figure 6.24).

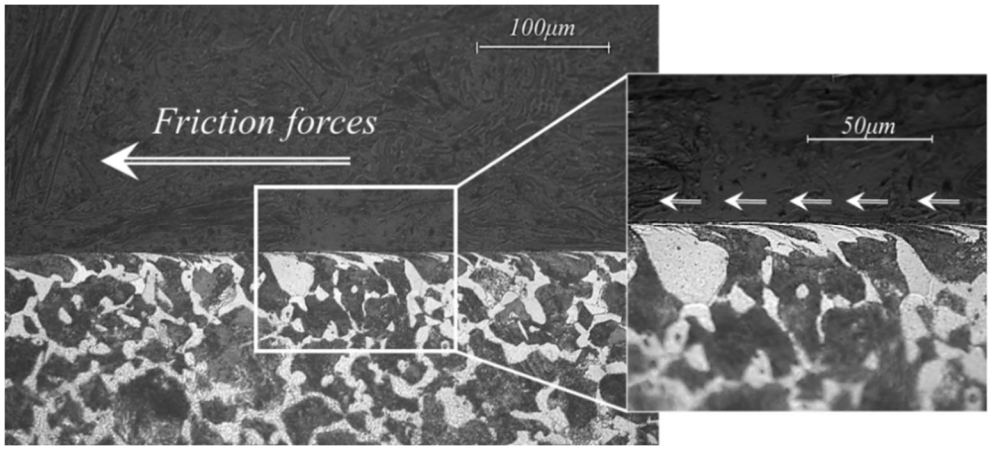

Figure 6.24 Plastic deformation on the surface layer of a disc tested at 1120MPa for 520000 cycles. The sample was subjected to chemical attack with Nital 2%.

After several load cycles cracks forms due to cumulative plastic strain. The alternating shear stress due to repetitive contacts and the pressure of the lubricant inside the cracks cause the propagation with angles typically below 30° with respect to the surface [24,32,147] (Figure 6.25). Eventually cracks curve up (see Figure 6.25, specimen a) or a brittle fracture causes the detachment of a debris of material (see Figure 6.25, specimen b) leaving a crater [24]. From a top view it may be noted that all the craters present the caracteristical arrowhead shape of Point Surface Origin (PSO) macropitting [30,35,47]. Pits origin from the arrow point in correspondence of surface cracks and then spread with an angle α typically ranging between 70° and 140° [30].

Due to the stress raising originated by the passage of the contact over the crater and because of the lacking of support previously provided by the removed material, cracks originated by surface distress during running-in rapidly grow in front of the pit giving rise to optimal initiation spots for further craters formation. In specimen *a*, as an example, a second pit was observed in front of the first after 600000 contact cycles.

Pits were always observed in the smaller disc, supporting the hypotesis of hydraulic crack propagation mechanism presented in Chapter 2.

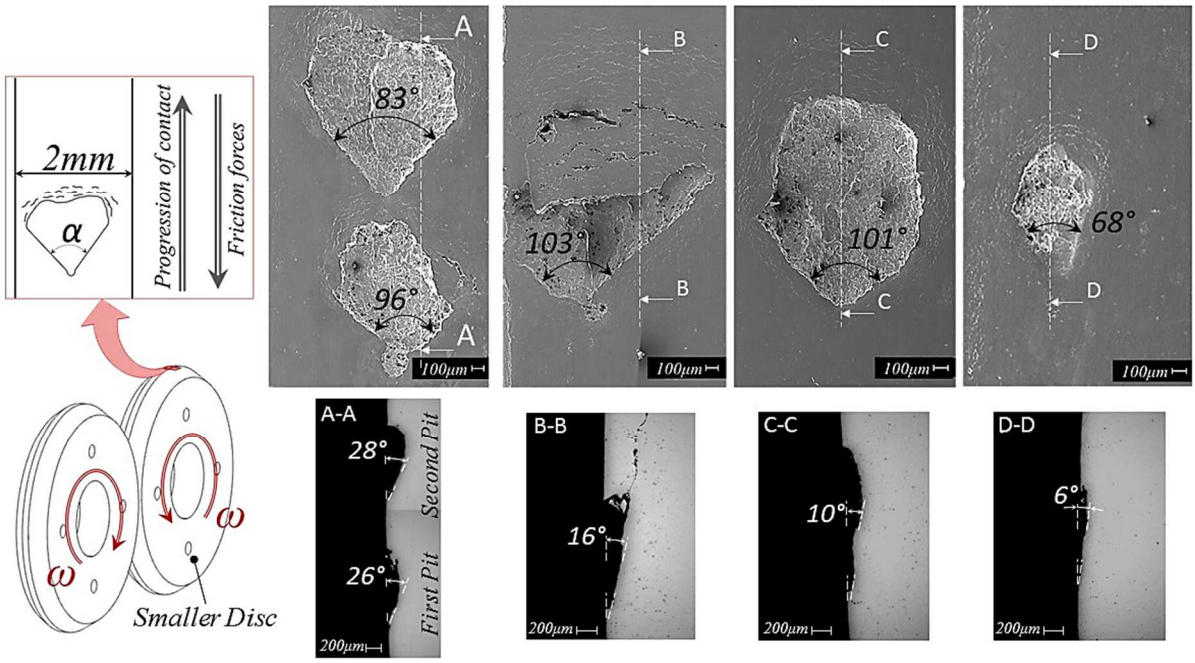

Specimen	*a*	*b*	*c*	*d*
Contact Pressure *[MPa]*	*940*	*1050*	*1120*	*1200*
Number of cycles $[\times 10^5]$	155	*61.2*	5.2	1

Figure 6.25 SEM image of the top view of pits on the surface of the specimens after the tests and optical microscope image of the section.

Figure 6.26 shows the disc test results compared with the fatigue curve suggested by ISO standard 6336 for through hardened steels. It is to be noted that the standard provides the fatigue curve for a survival probability (s.p.) of 99% but there is a lack of information regarding the statistical scatter of the phenomena. Due to the small numbers of data available, a statistical analysis of the results was not possible. However, the analysis of data relevant to pitting failures of case hardened sun gears during tests performed on the whole axles by Carraro S.p.A., and reported in chapter 4, leaded to a scatter index $T_{\sigma\ 1\div 99\%} = 1.52$. Therefore, assuming that a similar statistical dispersion affects the pitting phoenomenon in case hardened and through hardened steels, according to [107], Figure 6.26 shows the fatigue curve for 50% of survival probability extimated starting from the curve for high quality through hardened whrought steel provided by the ISO 6336. It is worth noting thath, according to the standard, the value of σ_{Hlim} depends on the surface hardness x according to the following relation [130]:

$$\sigma_{Hlim} = A \cdot x + B \tag{6.6}$$

where A and B depend on the quality of the material and the surface hardness of gears x is limited to a value of 210 HV, although the hardness of disc specimens was of 270 HV. The chart shows that the experimental points are located above the estimated fatigue curve for x=210 HV, 50% of survival probability and the highest steel quality (dash-dot line). However, a better correlation was found using the value x=270 HV in Equation (6.6) (dot line).

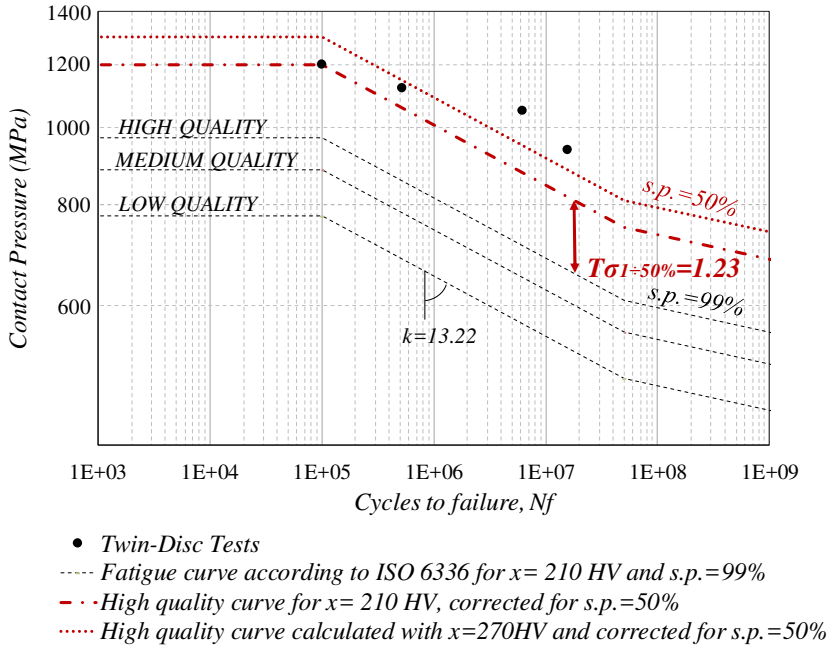

Figure 6.26: Comparison between twin-disc tests and fatigue curves according to ISO 6336 for through hardened wrought steel.

The higher durability of discs with respect to gears has been already discussed in section 6.1.1 and may be related to:

- dynamic loads: additional dynamic loads are generated during the meshing of gears;
- deflection of gears teeth and supports can cause misalignments and engagement interferences with consequent raising of contact stresses at some location on the tooth face;
- the condition of lubrication of discs cannot be fully representative of that of gears where a stationary regime of lubrication cannot be established because each pair of teeth engages for a short period during which the major influence factors such as contact pressure, curvature radii and sliding speed change continuously;

- debris dent: when a crater forms in gear teeth hard particles of material are trapped in the meshing and can dent the surface forming initiation spots for surface cracks. The filtered stream of oil and the lack of recessed geometry prevent such a mechanism in twin disc tests;
- size effect: the likelihood that a material defect or a surface furrow caused by manufacturing or handling affects the contact area is higher with increasing dimension. The sum of gear teeth surface is much larger than the contact strip of discs.
- the manufacturing process of gears is more complicated and less controllable; thus surface irregularities are more common than in discs;

Moreover, as observed in chapter 2, the lubricating conditions, as well as the effect of speeds and roughness mainly affects the components life at low loads, therefore a higher difference between gears and discs tests is to be expected for the long life part of the fatigue curve.

Based on the above considerations, the obtained data encouraged further test campaigns with the 17NiCrMo6-4 case hardened steel adopted to date by Carraro's suppliers, for the manufacturing of sun gears of off highway axles. Since these tests were intended to recreate the failure mechanism of a particular application, much more attention was paid in the specimens design in order to resemble as close as possible the working consitions of the actual gears, as reported in the next section.

6.4 Tests on 17NiCrMo6-4 case hardened steel discs

To further investigate on the possible correlation between disc tests and gear durability a new specimens geometry was proposed, which was aimed to recreate the working conditions experienced by sun gears of planetary gear sets mounted in a medium power axle for agricultural vehicles manufactured by Carraro S.p.A. [148]. The main features of the planetery gear set are summarized in Table 6.2.

It is to worth remembering that, in the case of gears, the radii of curvature and the ratio between sliding and rolling speeds (slide-to-roll ratio or SRR) vary continuously during the path of contact. The former factor influences the contact pressure and the stress gradients beneath the surface, while the latter affects friction forces and temperature.

Table 6.2:Main features of the considered planetary gear set.

	Sun	Planet	Ring
Pressure Angle, α [deg]	20		
Module, m [mm]	2.9295		
Number of Teeth, z	15	31	81
Centre distance [mm]	72.05		
Case Hardening Depth [mm]	0.6÷1.1	0.6÷0.8	0.22÷0.45
Surface Hardness H.R.C.	58÷62	58÷62	62÷66
Core Hardness H.R.C.	36÷42	36÷42	22÷27
Residual Austenite (% max)	20		
Material	17NiCrMo6-4	17NiCrMo6-4	20MnCr5

The specimens geometry must be chosen in order to recreate the gears working condition at the most critical point along the path of contact. In the meshing between sun and planet gears, the highest pressures are attained at the LPSTC of the sun gear, where pitting is also favoured by the condition of negative SRR (see Figure 2.5).

6.4.1 Design of the specimens and test parameters

Two series of specimens were manufactured with external diameters chosen to obtain respectively the same absolute sliding speed and the same SRR of gears teeth at the considered point along the line of action. In typical working conditions the absolute sliding speed at the LPSTC of sun gears is 0.05m/s and the SRR is equal to -24%. To reduce the time required for tests the discs were designed to attain the required speeds when the rig is ran at the highest spindle speed allowed by the test rig, which is $\omega = 2000 rpm$. Hence, given the 70 mm of center distance, which imposes the condition:

$$R_{x1} + R_{x2} = 70\ mm \tag{6.7}$$

, the diameter of the discs could be calculated using either the (6.1) or the (6.2) in order to obtain a sliding speed of 0.05 m/s or a SRR of 24%, respectively. In the following, we will refer to the former type of specimens as “low SRR’’ and to the latter as “high SRR”. The main features of the two designs are reported in Table 6.2.

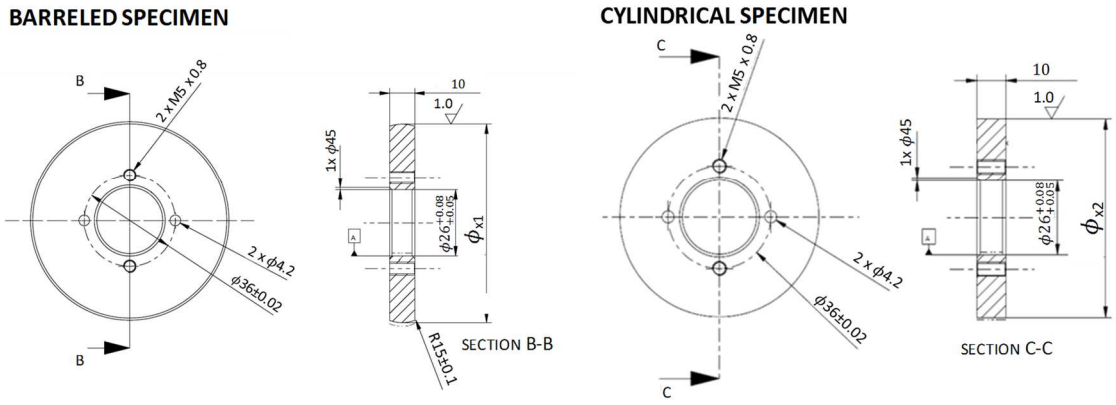

Figure 6.27 Design of the case hardened discs (refer to Table 6.2 for the external diameters).

Table 6.3 Main features of the case hardened discs

		Low SRR	High SRR
Diameter of the barreled disc, ϕ_{x1}	*mm*	70.26	78.40
Diameter of the cylindrical disc, ϕ_{x2}	*mm*	69.74	61.60
Crown radius	*mm*	15	
Surface hardness	*HRC*	58÷62	
Core hardness	*HRC*	36÷42	
Residual austenite	*%*	20	

One of the discs was crowned to avoid the risk of border effects which can lead to stress concentration close to the edges. Moreover, crowning reduces the amount of force needed to obtain the required contact pressure. The crown radius was chosen in order to obtain a stress field beneath the surface close to the one experienced by gears teeth. Figure 6.28b shows the subsurface stresses for the low SRR geometry but the differences for the case of high SRR specimens are so small that they would not be appreciable in the chart. The pressure generated by a given contact force was calculated analytically according to the Hertz theory for contact between elastic bodies (Johnson [3]). The internal stresses were evaluated according to Thomas and Hoersch [3,4], neglecting the effect of friction (see chapter 1 for details). The integrals necessary for the calculation of the stress components in the elliptical contact [3] between the

crowned and the cylindrical specimens were calculated numerically by implementing the Simpson's rule in a MS Excel worksheet. Since the eccentricity of the contact ellypse is not known a-priori, the parameter *e* was evaluated by means of the MS Excel Solver by searching the value of *e* in the range 0÷1 which satisfies the condition of equation 1.28.

Figure 6.28a shows that the use of cylindrical specimens would have lead to a stress field beneath the contact point very different with respect to the one experienced by gears. This is due to the higher radii of the discs with respect to the curvature radii of sun and planets teeth at the selected contact point, which were equal to 9.3mm and 25.24mm respectively. Note that for a given contact pressure the stresses beneath the surface are independent from the thickness of the specimens. Therefore the use of chamfers (like in the through hardened specimens) would affect the entity of force required to obtain the desired pressure, but not the stress gradient throughout the disc. The effect of crowning of one disc is shown in Figure 6.28b. The modification in the shape and dimension of the contact area due to the crowning leads to a stress field much closer to the one of gear teeth.

Finally, the point contact solution was preferable in order to allow the application a wider range of pressures. Figure 6.29, in fact, shows a comparison between the forces required to obtain given values of contact pressure with the proposed geometry and with specimens having a cylindrical surface of 2mm width similar to the one used for the through hardened C45 steel. The test rig was designed to work with a maximum load of 6.8kN corresponding in the case of line contact to a pressure of 2870 MPa. By using the crowned geometry, on the contrary, pressure up to 3600 MPa can be obtained with loads lower than 5 kN.

The decision of crowning only one of the discs was aimed to facilitate the manufacturing of specimens. Since pitting is expected to manifest at first in the smaller disc due to the negative SRR, the lower diameter was assigned to the cylindrical disc because the single curvature surface allow better light conditions during the frame capture and therefore less difficulties in the image processing.

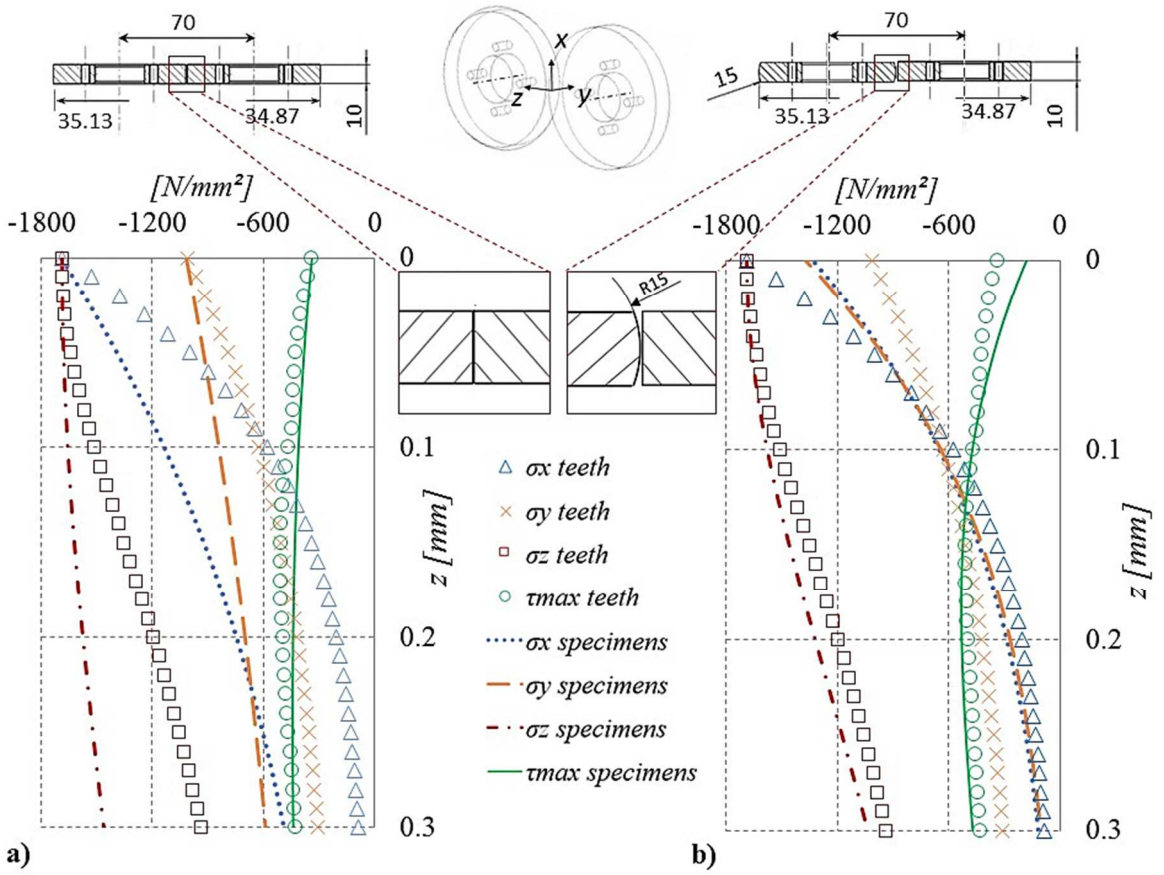

Figure 6.28: Comparison between the stress components beneath the point of contact of gears and discs in the case of: (a) cylindrical specimens and (b) a cylindrical and a crowned specimen.

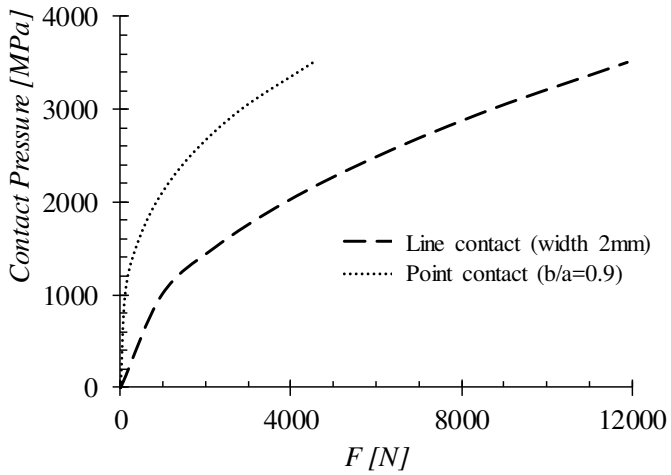

Figure 6.29 Comparison between the load-pressure relation in the case of chamfered specimens with contact width of 2 mm and crowned specimens with ratio between minimum and maximum semi-axes of the contact ellipse equal to 0.9.

As mentioned in the previous section, due to the low operating speed of sun gears, a film of lubricant capable of separating the surfaces is not likely to form. The classic methods for the calculation of the elastohydrodynamic film thickness are not applicable to the present case; as an example both the AGMA 925-A03 [3] and the ISO/TR 15144-1:2014 [22] standards extend the validity of their formulae down to pitch line veocity of 2 m/s, while the typical pitch line velocity of the considered sun gears is below 0.5 m/s. Compared to gear teeth, the entraining speed of discs is much higher, but the formation of an elastohydrodynamic film of lubricant is prevented as well because of the low crown radius. In fact, if the Hamrock and Dowson formula for the calculation of the film thickness in contacts between elliptic bodies [16,21] was applied to the case of the specimens, the result would be 0.15µm, which is lower than the mean roughness recommended for the discs surface Ra=1.0 µm.

The specimens were made with the 17NICrMo6-4 case hardened steel typically used by Carraro's suppliers for sun gears manufacturing. Discs were case carburized, quenched and tempered in order to obtain a hardness profile similar to the one encountered in gears (Figure 6.30).

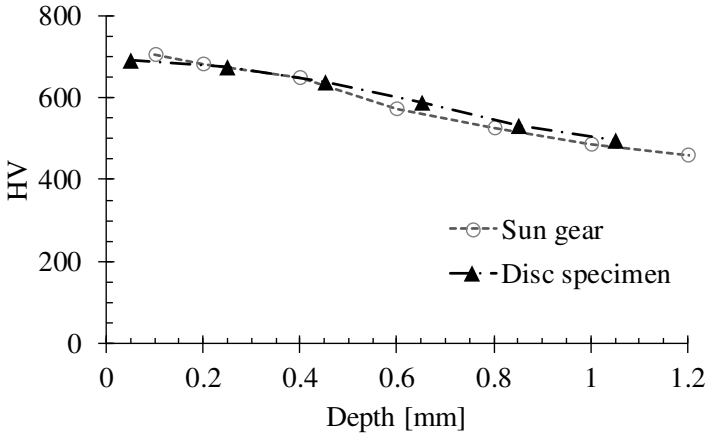

Figure 6.30 Micro-hardness profiles of a disc specimen and of a sun gear.

Then grinding of the surfaces allowed to obtain the desired geometry and to eliminate the surface layer where Inter-Granular Oxidation (IGO) can be induced by the carburizing process, with deleterious effects on the surface fatigue strength. Part of the high slide-to-roll ratio specimens were finally shot peened to evaluate the possible beneficial effect of compressive residual stresses introduced by the treatment.

The lubricant used for the tests is a API GL-4 oil with kinematic viscosity v_{100}= 9.3 mm^2/s at 100° C and v_{40}= 56 mm^2/s at 40° C. The oil temperature was measured at the outlet of the

contact area and kept constant by means of a heater and a flow adjuster. For the -0.7% SRR specimens a temperature of 80±2°C was used, while for the -24% SRR test the temperature raised up to 90°C even without the use of the heater. The rig was set to automatically stop the test if the temperature exceeded 90°C.

6.4.2 Results of the tests

The first tests on case hardened discs were performed on the low SRR discs. Two tests were ran with applied loads of 1125 N and 1460 N corresponding to contact pressures of 2200 MPa and 2400 MPa, and endured for $28 \cdot 10^6$ and $20.7 \cdot 10^6$ cicles respectively, with the only formation of mild micropitting on the surfaces. Therefore the specimens tested at 2200 MPa were further subjected to a test were the load was increased stepwise with the following order:

- $4 \cdot 10^6$ cycles at 3300 N, ideally corresponding to a contact pressure of 3150 MPa
- $4.3 \cdot 10^6$ cycles at 4930 N, ideally corresponding to a contact pressure of 3600 MPa
- $15.5 \cdot 10^6$ cycles at 6270 N, ideally corresponding to a contact pressure of 3900 MPa

Even at the maximum load the specimens did not show any macro crater, although micropitting was already diffuse on the surface as shown in Figure 6.31.

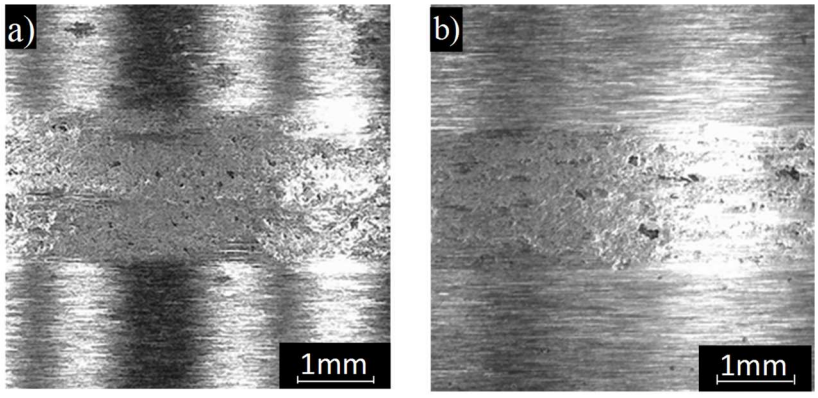

Figure 6.31 Surface of the smaller specimen: a) 0.7% SRR specimen after $20.7 \cdot 10^6$ cycles at 2400 MPa. b) 0.7% SRR specimen after $5 \cdot 10^5$ cycles at 3900 MPa

The subsequent tests were therefore performed with the high SRR specimens. A first series of test with a load of 2815 N, corresponding to a thoretical contact pressure of 3000 MPa, led to the formation macropitting craters on the surface of the smaller discs, which is the one subjected to the negative SRR.

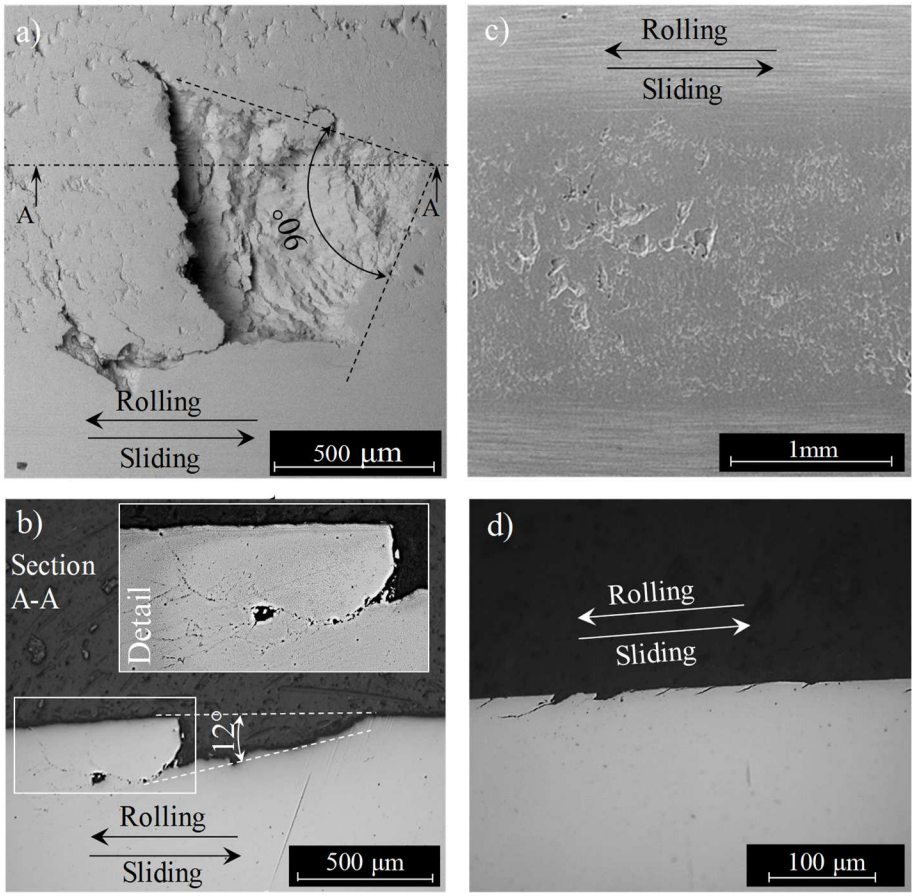

Figure 6.32 Top view (a) and section (b) of a macropit and top view (c) and section (d) of micropitting craters in the smaller disc (SRR= -24%) of test #1 after $4.6 \cdot 10^6$ cycles at 3000 MPa.

The craters had the typical seashell shape with relatively straight edges branching from the origin toward the rolling direction (Figure 6.32). A cross section of the specimens showed micropitting cracks extending up to a depth of 20 µm while the macropit was generated by a crack which propagated up to 200 µm and then branched and curved up toward the surface. As observed in gears (see chapter 2), the crack path often propagate below the surface even after the formation of the first crater, branching and interacting with several other surface cracks in a more advanced location. Surface distress cracks and micro-craters were observed also in the greater discs as shown in Figure 6.33.

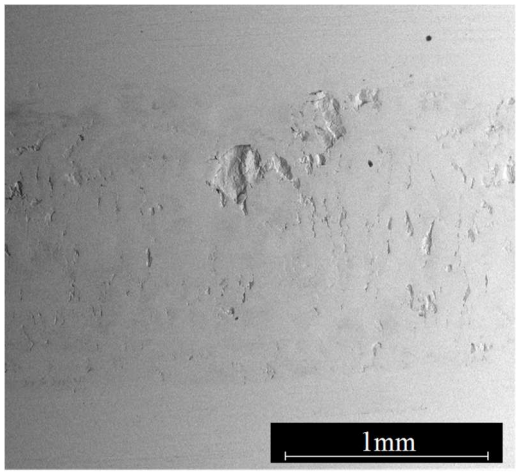

Figure 6.33 SEM image of surface cracks and micro-craters in the greater disc (SRR= 24%) of test #1, after $4.6 \cdot 10^6$ cycles at 3000 MPa.

Further high SRR tests were then conducted at contact pressures of 2650 MPa, 2850 Mpa, 3150 MPa and 3380 MPa, as reported in Table 6.4. During high SRR tests the temperature of the oil increased considerably therefore, during the summer period, the speed of rotation of the spindles had to be reduced in order to prevent excessive overheating of the lubricant from 2000 rpm to 1250rpm during tests number 8 and 9 and 13 and to 1000 rpm during tests number during tests number 6 and 11. It is important to note that the slide-to-roll ratio is not affected by changes in the speed of rotation of the specimens, which result in a equal modification of the absolute rolling and sliding speeds.

Test #2 performed with the highest load of 4025 N, corresponding to a contact pressure of 3380 MPa, leaded to a failure mode attributable to plastic deformation rather than to pitting, suggesting that this limit should not be overcome with high SRR spcimens. The specimen was irregularly deformed along the contact strip (Figure 6.34) and the test was stopped due to the excessive vibrations of the rig.

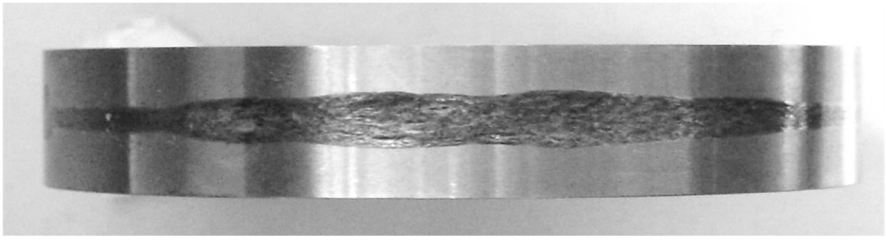

Figure 6.34 Surface of the smaller disc after test #2 ($7.1 \cdot 10^5$ cycles at 3380 MPa).

Table 6.4 Summary of disc tests on case hardened specimens.

Test number	Shot peening	Load	Nominal pressure	Cycles to first crater formation	Cycles to failure*	Total test duration	Speed of rotation	Surface at the end of the test**
#	.	$[N]$	$[MPa]$	$[\times 10^6\ cycles]$	$[\times 10^6\ cycles]$	$[\times 10^6\ cycles]$	$[rpm]$	
3	no	1940	2650	/	ran-out	50.0	2000	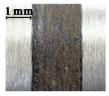
10	no	2410	2850	9.64	9.64	9.93	2000	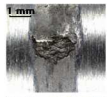
1	no	2815	3000	4.05	4.05	4.60	2000	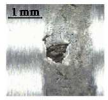
4	no	2815	3000	11.36	11.36	11.36	2000	
5	no	2815	3000	4.69	4.69	4.69	2000	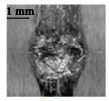
6	no	3255	3150	10.28	10.28	10.28	1000	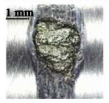
13	no	3255	3150	10.1	10.10	12.10	1250	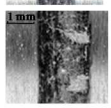
2	no	4025	3380	/	0.71	0.71	2000	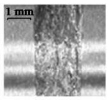
12	yes	2410	2850	19.3	ran-out	50.0	2000	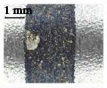
7	yes	2815	3000	5.88	5.88	7.00	1600	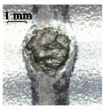
8	yes	2815	3000	5.26	5.26	5.26	1250	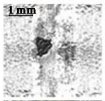
9	yes	2815	3000	8.9	8.90	9.20	1250	
11	yes	3255	3150	6.90	6.90	6.90	1000	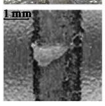

* Failure criteria: first pit with dimension greater than 1mm

** For test # 5 a picture of the surface of the greater disc is reported since it was exceptionally the first to manifest pitting. In the other cases the image is relevant to the smaller disc.

Two ran-out were obtained in tests with high SRR specimens: one with shot peened discs at 2850 MPa and one with un-peened discs at 2650 MPa respectively. It is to be noted that in the tests on shot peened discs at 2850 MPa, a small crater formed after $19.3 \cdot 10^6$cycles, however, due to the small dimensions it did not fulfilled the failure criteria of crater dimension greater than 1mm. The tests were then continued up to $50 \cdot 10^6$cycles without further propagation.

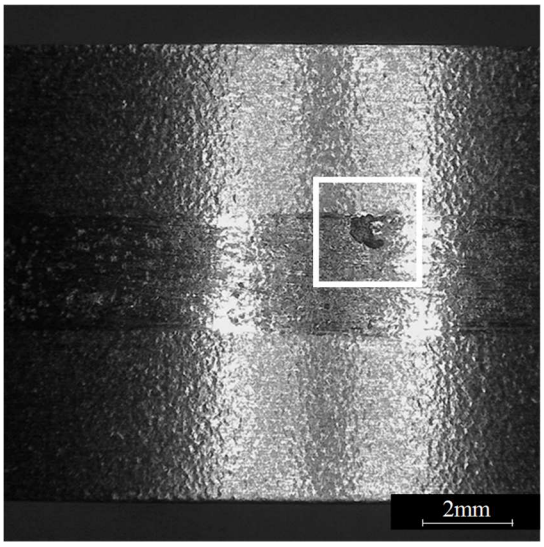

Figure 6.35 Crater on the surface of the smaller disc in test #12, after $1.93 \cdot 10^7$ cycles at 2850 MPa.

Only in one case, during test #5, performed with a nominal contact pressure of 3000 MPa, the first crater manifested on the surface of the greater disc, as shown in Figure 6.36. As specified in chapter 2, the formation of macropits in surfaces characterized by a positive SRR is unlikely. Murakami and co-workers [31] reported that surface cracks developed under negative slide to roll ratio conditions during disc tests, stopped growing when the direction of rolling was changed. Similar results were observed by Fujita and Yoshida [149] and by Tyfour and Beynon [150], although the formers specified that the improvement in contact fatigue life due to the reversal in rolling direction occurred with through hardened but not with case hardened steels. However, the formation of pitting craters on the positive SRR specimen during disc tests, although rarely, was reported also in [31]. The authors noticed that such craters showed a different morphology as compared with the arrowhead shaped pits observed in the negative SRR discs and suggested that the origin could have been located in the subsurface. A section of the crowned disc of test #5 (Figure 6.36) did not shown any clear evidence of subsurface origin, although a small white etching crack was observed at the bottom of the main crater. It is not clear to the author whether the microstructural modification which prevented

the etching of the material surrounding the crack was the consequence or a cause of the damage formation, or if it could be related to the presence of a defect or inclusion at locations other than the plane examined by the reported section. As in the previously analysed cases, surface micro-cracks were oriented against the sliding direction.

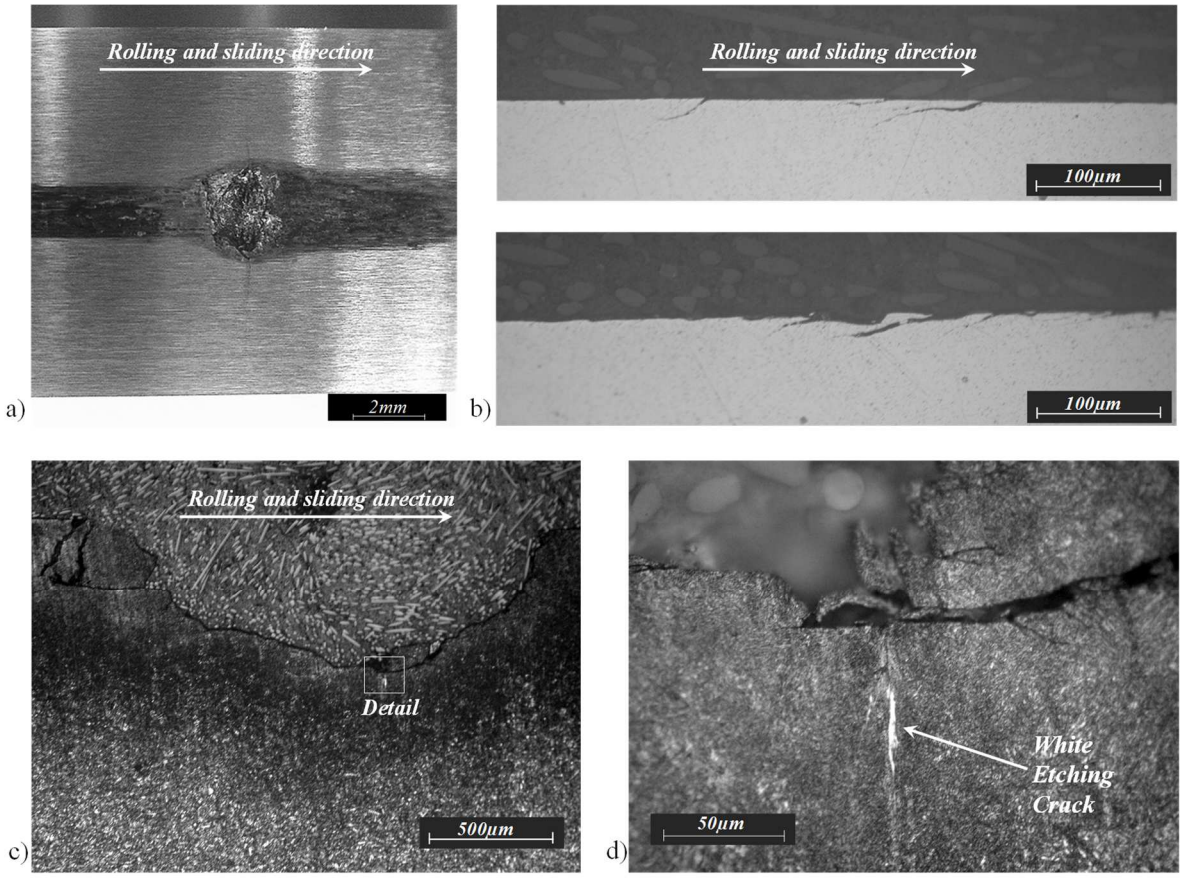

Figure 6.36 a) Crater on the surface of the greater disc in test #5, after $4.69 \cdot 10^6$ cycles at 3000 MPa. b) Cracks on the surface of the specimen. c) Section of the crater. d) White Etching Crack at the bottom of the crater.

To date, the small number of performed tests, together with the restricted range of pressure within which pitting was obtained, make impossible the determination of a fatigue curve with the available data. However, if an inverse slope of 13.22 is imposed for the curve, following the same procedure described in chapter 4, a rough approximation of the endurance limits is possible. Figure 6.37 compares the curves obtained for shot peened and un-peened specimens with such approach with the curve proposed in chapter 4, based on sun gear failures observed during FSTs.

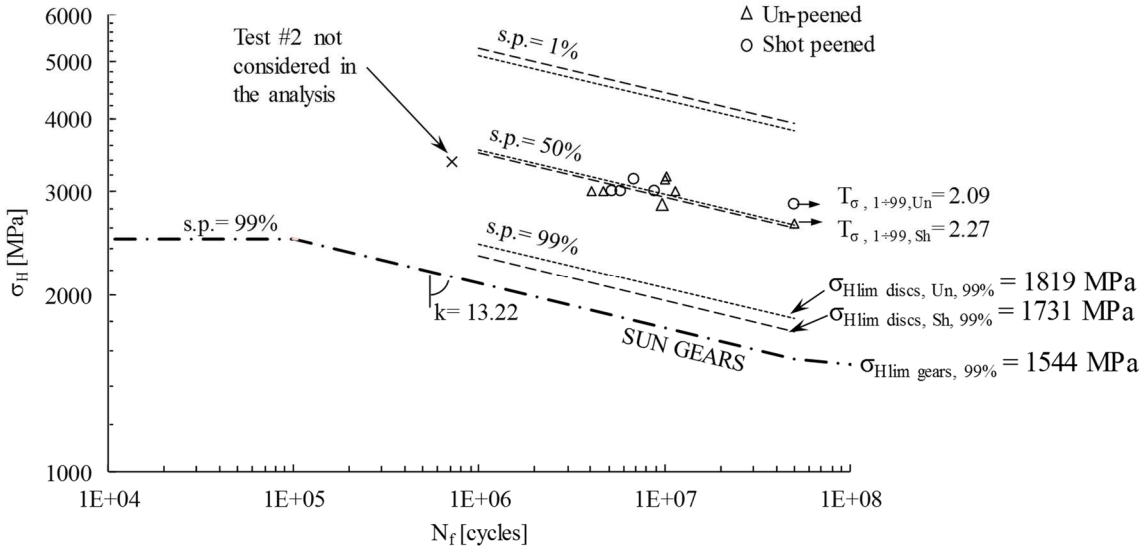

Figure 6.37 Fatigue curves obtained from a statistical analysis of failures on shot peened and un-peened specimens by imposing an inverse slope of 13.22, compared to the curve derived in chapter 4 from sun gear failures during FSTs.

Based on these results, it can be noted that no significant improvement derived from the shot peening treatment, neither from the viewpoint of the limit stress, nor as regarding the statistical scatter of data. If shot peened and un-peened specimens are treated separately, the relevant endurance values for a survival probability of 99% obtained by a statistical analysis carried out following the prescription of the ISO standard 12107 [106], are only 11% and 17% higher than the limit calculated for sun gears respectively. Nevertheless, as mentioned in the previous chapter, the width of the scatter bands depends on the number of experimental data upon which the statistical analysis is based. Therefore, all data of shot peened and un-peened specimens were also analysed together as shown in Figure 6.38. The resulting scatter index diminished up to a value of $T_\sigma = 1.51$, and, hence, the endurance value at 99% of survival probability became $\sigma_{Hlim\ disc,99\%} = 2133$ MPa, that is 38% higher than the value calculated for case hardened sun gears.

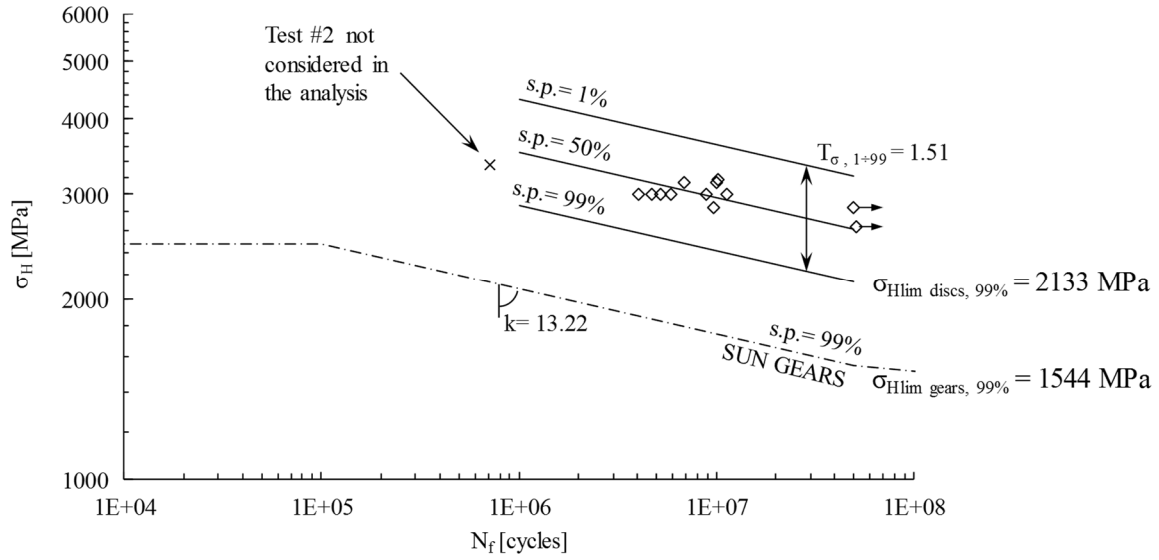

Figure 6.38 Fatigue curves obtained considering all the high SRR discs failures regardless the surface treatment.

On the other hand, it is worth noting that the statistical scatter in this case is substantially identical to the value of $T_{\sigma,1\div99} = 1.52$ derived by the analysis reported in chapter 4. Nevertheless, it is important to remark that, if the same mean values and variance here calculated for the lifetimes of discs were obtained with a higher number of experimental data (as for the un gear analysis) the resulting scatter index relevant to the load carrying capacity of discs could be further reduced.

The higher durability of specimens with respect to gears in these tests, could be attributed to the changes on the surface of the specimens due to micropitting and wear. Figure 6.39 reports a measure of the deviation from the original surface performed on a un-peened specimen of the high SRR series, after $11.36 \cdot 10\text{^}6$ cycles with a load of 2.8 kN, which was intended to generate a contact pressure between the surfaces of 3000 MPa. However, at the end of the test a circumferential groove was formed on the surface of the flat disc, while the surface of the crowned disc was substantially unmodified, despite the surface hardness (see Figure 6.40) and the number of contact cycles were equal for the two discs. An evaluation of the curvature radius in the middle of the groove was possible by considering the width *w* of the groove at 10 µm from the bottom, and finding by equation (6.8) the value of the radius of the arc having a sagitta of 10 µm and a span equal to *w*.

$$R = \frac{w^2}{8 \cdot 0.01} + \frac{0.01}{2} \tag{6.8}$$

In test #4, the final groove had a bottom radius of 18mm which, combined with the 15 mm crown radius of the mating disc, would result in a contact pressure of about 1770 MPa with the load of 2.8 kN imposed at the beginning of the test.

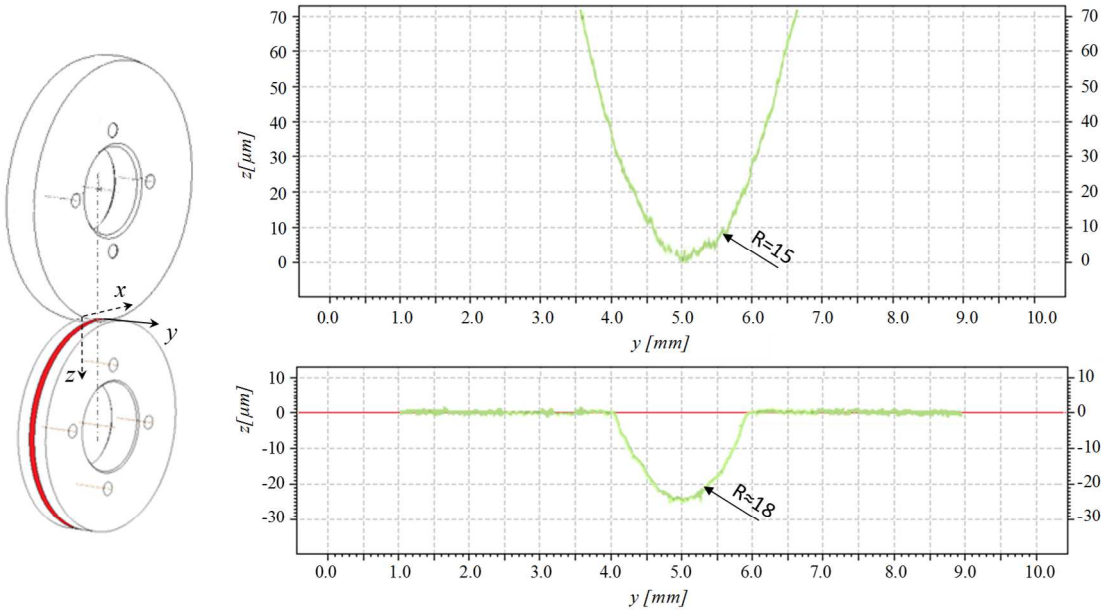

	BEFORE TESTING	*AFTER 11.36·10⁶ CYCLES WITH F =2.8 kN*
Crowned specimen, R_{y1} [mm]	∞	-18
Cylindrical specimen, R_{y2} [mm]	15	15
Pressure [MPa]	3000	1770

Figure 6.39 Measurement of the profile of the discs after test #4.

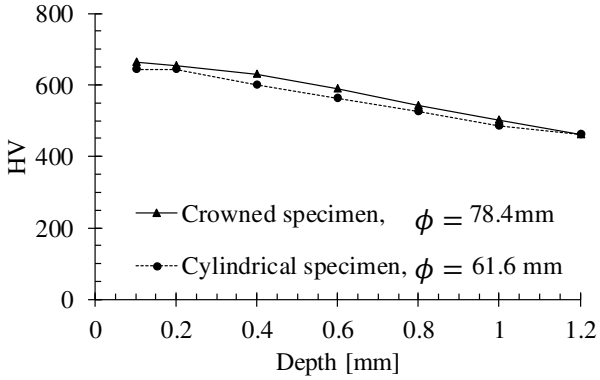

Figure 6.40 Micro-hardness profiles of the discs of test #4.

This phenomenon did not occur in tests with through hardened discs because, in contact between cylinders, the pressure is uniformly distributed in the transverse direction with respect to rolling and therefore each point in the contact strip is subjected to the same load history and wear rate.

The profile measurements performed on the cylindrical disc after the test are reported in Figure 6.41 for the un-peened specimens of tests number 3, 4, 6 and 10, and in Figure 6.42 for the shot peened specimens used in tests number 9, 11, and 12.

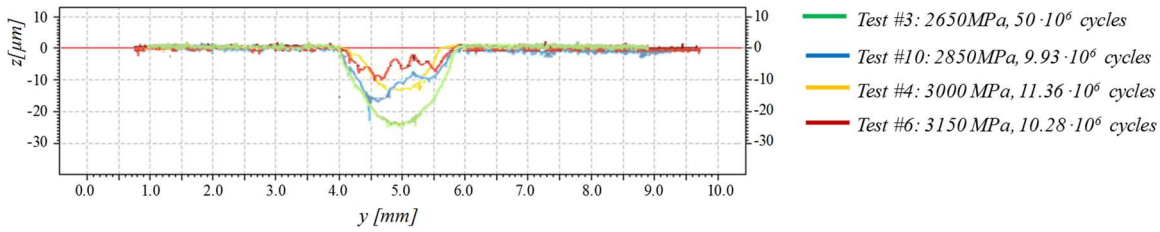

Figure 6.41 Profile measurement performed on the cylindrical discs of tests number 3, 4, 6 and 10.

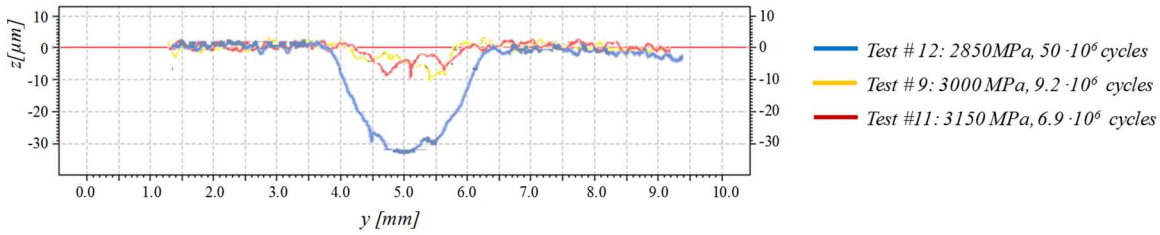

Figure 6.42 Profile measurement performed on the cylindrical discs of tests number 9, 11, and 12.

Tests performed at lower pressure values typically show deeper grooves, especially when the lower load is accompanied by a greater duration. Moreover, the small depth of the groove in specimens of tests 6, 9 and 11 as well as its irregular profile suggests that the lower speed of rotation imposed for these tests due to the increased thermal conditions, could have influenced the wear rate of the discs. In the case of tests number 3, and 12, where the measured groove showed a regular shape and could be represented quite well by a circumference arc, it was possible to estimate the pressure value at the end of the test, as already done in Figure 6.39 for test number 4 (see Table 6.5). Figure 6.43 shows the positions that the relevant experimental points would assume in the pressure-life chart, if it was confirmed that the groove had formed in an early stage of the test and then no further change in the geometry had occurred. Although with this consideration data would be much more consistent with gears results, it should be remarked that the increasing groove depth reported in Figure 6.41 and Figure 6.42 for tests with higher number of cycles suggests that the geometry modification is a continuous process and therefore the final value of pressure cannot be representative of the whole test.

Table 6.5 Estimated values of groove radius and contact pressure at the end of tests number 3, 4 and 12.

Test	Applied load	Initial pressure	Groove radius	Pressure at the end of the test
#	[N]	[Mpa]	[mm]	[Mpa]
3	1940	2650	22	1860
4	2815	3000	18	1770
12	2410	2850	18	1680

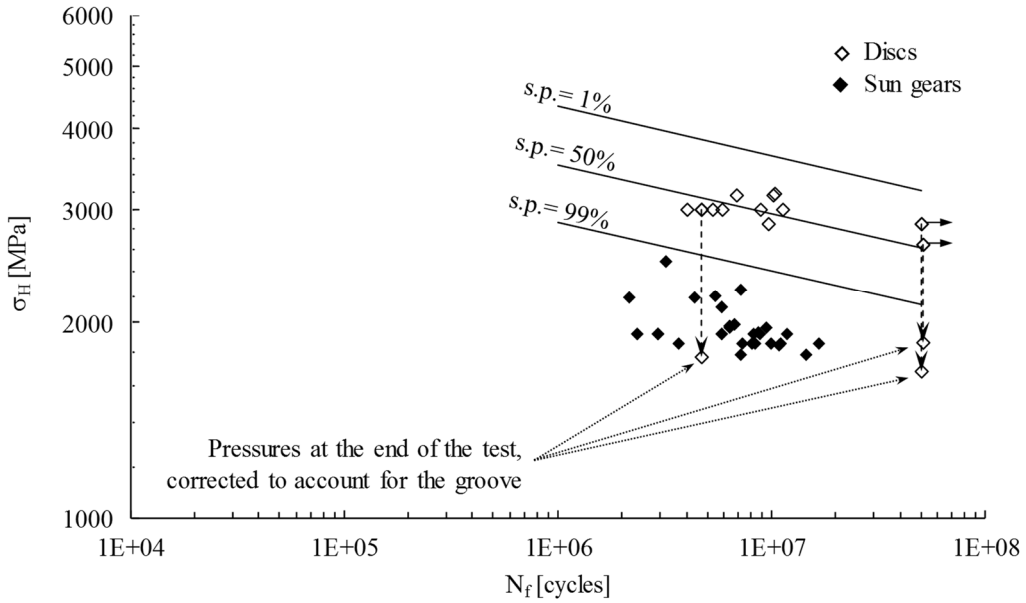

Figure 6.43 Pressure-life data of case hardened disc specimens compared with sun gears failures analysed in chapter 4. Since in this case gears data are directly compared with disc tests performed in various conditions in terms of lubricant, surface finish and speeds, the correction applied in chapter 4 to make data coherent with the curve of ISO 6336 was not applied here.

It is important to remember that the removal of material from the surface due to wear and micropitting is common in sun gears as well. Nevertheless, as shown in Figure 6.44 (see Figure 2.12 for details of the damaged sun gear), in the case of gears the phenomenon occurs almost exclusively in the dedendum where the SRR is negative and therefore a groove form in the orthogonal direction with respect to the direction of relative motion of the surfaces. Thus, the upper edge of the groove, which constitutes a site of stress concentration due to the reduced curvature radius and the probable presence of surface cracks, is repeatedly overpassed by the teeth of the mating gear and often represent the initiation cause of macropits formation.

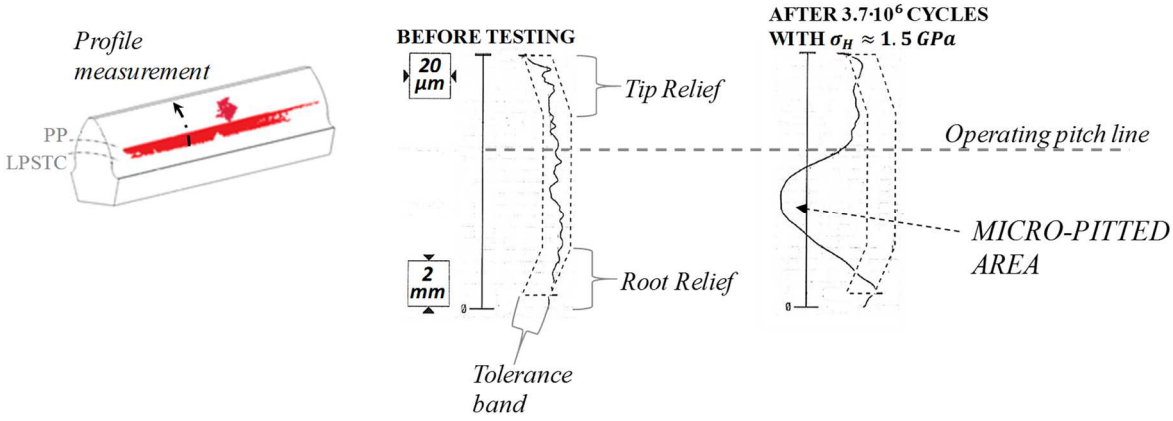

Figure 6.44 profile diagrams showing the deviation of the surface of a sun gear from the nominal profile in the normal direction, before and after the test.

Hence, while in disc specimens the modification of surface topography lead to an increase in the fatigue performances, the same phenomenon could drastically reduce the lifetime of gears.

Moreover the same possible reasons proposed in section 6.3.1 for the higher load carrying capacity of through hardened disc specimens with respect to gears, still holds also for case hardened steels.

6.5 Discussion of the results and conclusions

The problems related to the change in the surface geometry of the specimens make difficult the interpretation of the results of disc tests. Further investigations are necessary to assess whether such modifications develop progressively during the test or occur in an early stage after which the contact conditions remain stationary, although the analysis reported in Figure 6.41 and Figure 6.42 seems to support the former hypothesis. Nevertheless, some consideration may be drawn on the basis of the outcomes of the tests performed to date:

- Good agreement both in terms of craters morphology and crack path beneath the surface was found between macropitting observed in gears and disc specimens. This observation suggests that the same damaging mechanism take place in the two cases and therefore that disc tests could be successfully used to characterize gears materials.
- Surface distress constitute the initial phase of the damaging process, leading to the formation of shallow surface cracks inclined against the sliding direction. In case

hardened specimens this process is followed by the formation of micropits with consequent material removal from the surface. Macropitting may eventually form, preferentially on the surface with negative SRR.

- In disc tests with point contact specimens, performed on the case hardened 17NiCrMo6-4 discs, the formation of a circumferential groove that enhances the conformity between the mating surfaces, considerably improved the durability of discs and made difficult the extrapolation of limit values of pressure suitable to be used in the context of gears design. Nevertheless, if it was confirmed that the groove form in an early stage of the test, at least for certain values of applied pressure, discs data could be corrected accounting for the actual geometries of the surface in the stationary conditions and would result in better agreement with the results of gears tests.
- Better agreement was found between the fatigue curve provided by the ISO standard 6336 for through hardened steels and data relevant to few preliminary discs tests performed within the present work. The relatively good correlation obtained in this case could be deemed to the line-contact type specimens, where the formation of the groove is prevented since the pressure is evenly distributed over the contact width. However, a different behaviour of through hardened and case hardened materials is possible as well.
- Sometimes, although rarely, macropits may form on the disc with positive SRR before than on the one with negative SRR. When this occurred in the present work, the morphology of the crater was slightly different as compared to the ones observed in the smaller disc, since no arrowhead shape was distinctly observable. The same consideration have been reported in the past also by Murakami an co-workers [31] who proposed that the craters in such cases have probably a subsurface origin.
- The slide-to-roll ratio seem to be a more significant parameter with respect to rolling contact fatigue with respect to the absolute sliding speed. Nevertheless, the absolute speed of rotation might possibly influence the wear rate of discs.
- Although the small number of experimental data and the unsolved issue related to changes in the contact geometry do not allow to draw a final judgement about the effectiveness of shot peening in preventing contact fatigue, no significant improvement in the strength of the treated discs was observed.

Conclusions and future developments

The present dissertation mainly focuses on the analysis of pitting failures on case hardened gears of power transmission systems for off-highway vehicles. The damaging mechanisms leading to the formation of pitting craters on the surface of gears teeth were investigated in the early stage of the research project by means of post-failure examination of case hardened sun gears after bench testing of the complete axles, performed by Carraro S.p.A.. Based on a review of the existing literature some hypothesis were drawn to explain the different morphology of craters encountered in the experimental observations.

The analysis of the database of tests of Carraro S.p.A. also allowed to estimate a design curve against pitting for the case-hardened steels used by the suppliers, based on pressure-life data relevant to the failed sun gears. A theoretical model, implemented by the commercial software KISSsoft, allowed the calculation of the contact pressure acting on sun gears teeth during the analysed tests. The model accounted for the actual tooth geometry, including modifications such as crowning and tip and root relieves, and for all the compliances of gears and shafts. Moreover, data were corrected to account for the difference among speed, surface finish and lubricant of the test as compared to those to which the ISO 6336 fatigue curves are referred, in order to allow a direct comparison between the derived material limits and the ISO prescriptions. Since the torques applied in the bench tests were relevant to the axle sizes, the applied contact stresses were all concentrated in a relatively small range and it was not possible to derive a sufficiently accurate estimation about the slope of the fatigue curve and the positions of high- and low-cycle fatigue knees. Therefore, the experimental data were fitted by assuming the same slope of the curve and endurance values corresponding to the knee points according to the ISO standard. Experimental data showed a statistical scatter comparable with results reported in the literature. The derived fatigue curve resulted slightly above the one suggested in ISO 6336 for medium quality steels.

The analysis of the database of tests performed by Carraro S.p.A. on the complete axles allowed to obtain valuable information about the materials used by the company's suppliers, and will be particularly useful since the derived limits are closely representative of the

performances of the materials as related to the most crucial application with respect to pitting failures, which are, indeed sun gears. Nevertheless, in view of the determination of the absolute pitting load carrying capacity relevant to the sole material, the outcomes of the analysis are affected by some major limitations of these kind of tests: first of all inspections are performed only every 100 hours, therefore the determination of the number of cycles elapsed before the failure of the gear was necessarily approximative. Then, experimental measurement of strain at the tooth root of a sun gear during bench testing of the complete axle showed that the actual distribution of pressure on the tooth face may considerably differ from the calculated values in presence of manufacturing inaccuracies. Since a detailed report of quality controls was not available for all the components involved in the examined tests, it is not possible to determine whether manufacturing accuracies may have played a significant role in the failures occurred during some tests, thus affecting the scatter of results. Hence the estimated curve at 99% of survival probability might be too conservative for systems where the manufacturing and assembly process are more easily controllable as compared to the analysed final drives.

Therefore, a different test procedure was adopted to investigate the pitting behaviour of the material, based on the use of pairs of simple disc specimens in contact under stationary pressure and speed conditions. In principle, such method allows relatively fast and inexpensive tests and at the same times reduces the uncertainty in the value of the maximum contact pressure acting on the surface, avoiding the possible causes of local contact stress concentration or dynamic effects related to the complex geometry and operating conditions of gears.

Several improvements were made on a pre-existing test rig, initially designed and manufactured during the master thesis of the candidate. The modifications were aimed to enhance the control capabilities of the bench and allow automatic inspections of the damaging level of the specimens' surfaces.

Preliminary tests on through hardened discs showed quite good correlation with the fatigue curves proposed by the ISO standard 6336, for the calculation of the load carrying capacity of gears, encouraging further tests with the materials commonly adopted in gears manufacturing by the suppliers of Carraro S.p.A..

Thus, a new specimens geometry was proposed, aimed to resemble the operating conditions of sun gears of a medium power planetary gear set considered as the most representative of the range of Carraro's products. Discs were manufactured in case hardened 17NiCrMo6-4 steel, then part of the specimens were shot peened to investigate the possible beneficial effect of the additional compressive residual stresses induced in the surface layers by the treatment.

Tests on discs, allowed to obtain the same craters morphology observed in gears teeth. Cracks grew at shallow angles beneath the surface of the smaller disc (characterized by the opposite directions of load motion and friction force) and lead to the formation of V-shaped pits. However, the endurance limit for disc specimens appeared to be 38% higher than the one derived by the analysis of pitting failures on sun gears. It was proposed that such difference might be the result of changes in the contact geometry due to wear and micropitting, which enhances the conformity of the surfaces reducing the pressure for a given load. No significant difference was found between the durability of shot peened and un-peened specimens.

It is worth remarking how experimental evidence regarding both gear and discs failures pointed out the strong influence of the local contact geometry in the damaging mechanism related to contact fatigue. The contact geometry is in turn affected by compliances of the system, manufacturing accuracies of the mating components and changes in the surface topography due to wear. This latter aspect is of foremost concern, since the modification may have different effects on the fatigue behaviour, depending on the geometrical and functional characteristics of the component. As an example, it has been shown that material removal from the surface of discs tend to improve their durability, while the same phenomenon occurring in the dedendum of gears teeth represents one of the most common cause of macropits formation.

The primary role played by surface cracks and changes in the contact geometry in contact fatigue, particularly on surfaces characterized by negative values of the slide-to-roll ratio (SRR), suggests that a deep understanding of wear mechanisms, occurring already in the very first phases of the damaging process, is essential. Currently further tests are ongoing to analyse the changes in the surface topography within the lifetime of disc specimens.

More extensive experimental observations are also needed to investigate the differences between craters originated on surfaces with equal and opposite directions of rolling and sliding speeds. In fact, it is yet to be clarified how much the greater likelihood of craters formation on surface with negative SRR could be attributed to the role of the lubricant pressure inside the cracks.

Finally, experimental investigations of the strain distribution along the root of sun gears teeth, will be used again in the next future to analyse the influence of various magnitudes of manufacturing errors in planet carriers, and to study the different behaviour of planetary gear sets with three and four planet gears respectively.

Appendix A

FRICTION ON GEARS TEETH

This appendix is focused on the estimation of the friction force acting on a generic point of a driver gear tooth. It should be remembered that in driver gears friction forces friction forces are always directed toward the tooth root in the dedendum, vanish in correspondence of the pitch line and assume the opposite direction within the addendum (see Figure 1.13). Figure A.1 shows the force applied at a generic point P of a driver spur gear tooth, decomposed into its normal and friction components. Since in the figure P is placed above the pitch line, the friction force is directed toward the tip of the tooth. Thus, the equilibrium condition with respect to the pole O_1 is given by

$$T_1 = F_n\left(r_{b,1} + \rho_{P,1} \cdot \mu\right) \tag{7.1}$$

Therefore, the normal force can be calculated as:

$$F_n = \frac{T_1}{\left(r_{b,1} + \rho_{P,1} \cdot \mu\right)} \tag{7.2}$$

And the friction force is given by

$$F_f = F_n \cdot \mu \tag{7.3}$$

Therefore, if the total reaction force F_n is supposed to be generated by a constant driven torque T_2, its will assume lower values when the contact occurs between the addendum of gear 1 and the dedendum of gear 2, since the relevant lever arm with respect to the pole O_2 is greater when the friction force acting on the driver gear is directed toward the tip of the tooth as in Figure A.1. Conversely, during the contact below the pitch circle of the driver gear, the friction force is directed toward the root of the tooth and the lever arm of the total force with respect to the pole O_2 is smaller, resulting in a higher value of the total reaction force.

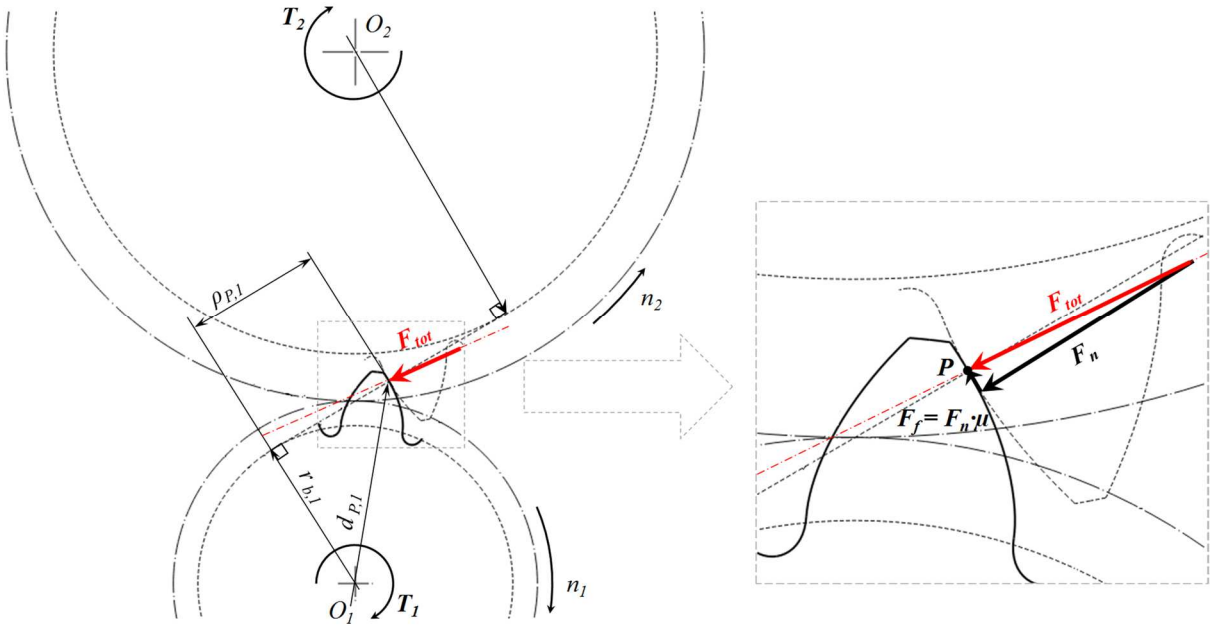

Figure A.1 Normal and friction forces acting on a driver spur gear tooth.

Hence, although the driven torque is constant, the force acting on a gear tooth undergoes to a sudden variation in correspondence of the contact at the pitch circle, which coincides to the passage through a condition of pure rolling, immediately followed by a change in the direction of friction.

Appendix B

CONSIDERATIONS ABOUT GEARS TEST RIGS

It has been shown in this dissertation, the high difficulty to achieve an adequate control on the exact value of contact pressure on the surface gears teeth. For this reason, bench testing on the complete transmission systems are not suitable to allow catching the intrinsic scatter of the phenomenon as related to the sole material, regardless the particular features (geometry, stiffnesses and accuracies) of the rig and gears. This aim can be achieved only with the use of a rig specifically design to minimize the causes of uncertainty in the contact pressure.

The FZG test rig (Figure B.1) is the most diffuse power recirculating device for gear testing. The bench is composed by a couple of shaft connected at one extremity by a slave gearbox, and on the opposite side by the gear pair to be tested. One of the two shaft is provided with a torque transducer, while the second is divided in two parts connected by a clutch. Before the test one of the parts is fixed to the rig frame, while the other is statically preloaded imposing the desired torque by means of a wrench. Then the clutch is closed and the lock to the frame released. The rig is driven by an electric motor.

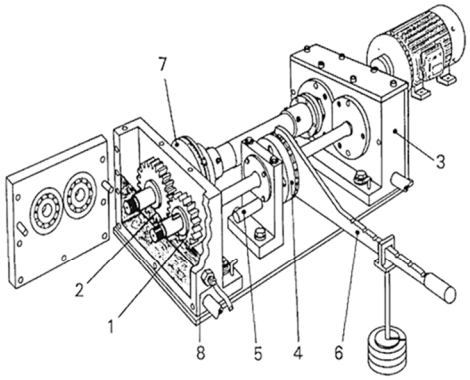

1. Test pinion
2. Test wheel
3. Slave gear box
4. Load clutch
5. Locking pin
6. Load lever
7. Torque measuring device
8. Temperature sensor

C-Type Gears

Centre distance		mm	91.5
Number of teeth	*Pinion*	-	16
	Wheel	-	24
Module		mm	4.5
Pressure angle		°	20
Helix angle		°	0
Face width		mm	14
Profile shift coefficient	*Pinion*	-	0.1817
	Wheel	-	0.1715
Pitch diameter	*Pinion*	mm	73.2
	Wheel	mm	109.8
Tip diameter	*Pinion*	mm	82.5
	Wheel	mm	118.4

Figure B.1 FZG test rig and main features of the Type-C gears [151]

Gears features and test procedures are defined for different purpose of investigation.

An insight of the various specimens features and test parameters suggested by the FVA (Forschungsvereinigung Antriebstechnik – Research Association for Drive Technology) for the micropitting and pitting characterization lubricants, and reported in Table B.1, allowed some useful consideration for the concept of pitting test rigs and procedures:

- Almost all the standard tests are performed under conditions of splash lubrication at 90°C
- Micropitting tests consist in short stages at increasing load levels. Within each stage the load is kept constant and the failure criteria is based on a maximum profile deviation.
- Pitting tests are generally performed with a constant load and the failure criteria is based on the exceeding of a given percentage of damaged area during tests.
- The surface of gears for pitting tests is superfinished to prevent the formation of micropits. Moreover the wheel has a lengthwise crowning and tip and root relieves to ensure a centred distribution of pressure and avoid tip to root interferences.

Nevertheless in the author's opinion the FZG rig is not the most suitable choice to characterize the pitting behaviour of sun gears for off-highway axles, since tests are run with a pitch line speed greater than 8 m/s, which is much higher as compared to the values typically encountered in the application, and results in more favourable lubricating conditions. Using the rig at a lower speeds to resemble the typical operating condition of sun gears in off-highway axles is unfeasible since the test duration would increase excessively. Therefore, the development of a test rig for planetary gear sets seems to be more appropriate and will be one of the foremost future goal of the research project. In fact, a bench test based on a planetary gear unit would allow to perform test in the most representative conditions with a high frequency of load cycles on the sun gear's teeth derived by the simultaneous meshing with at least three planet gears.

Table B.1 Definition of the load stages in the FZG tests

Load Stage	*1*	*2*	*3*	*4*	*5*	*6*	*7*	*8*	*9*	*10*	*11*	*12*
Pinion torque [Nm]	3,3	13,7	35,3	60,8	94,1	135,5	183,4	239,3	302,0	372,6	450,1	534,5
Normal tooth load [N]	99	407	1044	1799	2788	4007	5435	7060	8949	11029	13342	15826
Hertzian stress at pitch point [MPa]	146	295	474	621	773	929	1080	1223	1366	1539	1691	1841

Table B.2 Summary of micropitting and pitting tests for gears lubricants. Refer to Table B.1 for the definition of the load stages (l.s.).

	TEST	REFERENCE STANDARD	APPLICATION	LUBRICATION	ϑ_{oil} [°C]	Ra [µm]	GEARS TYPE*	PITCH-LINE VELOCITY [m/s]	DUTY CYCLE	END OF TEST CRITERIA	OUTPUT
MICROPITTING	GF-C/8,3/90	FVA 54/7	*Standard*	*Spray (2 l/min)*	90	0,5±0,1	GF-C	8,3	*Running-in:* 1 h at l.s. 3 *Short tests:* 16 h at l.s. 5 to 10 if failure occurs at a l.s. ≥ 8 an additional *endurance test* is required: 80 h at l.s. 8 + up to 5 tests for 80 h at l.s. 10	Max. profile deviation >7,5 µm for short tests; Max. profile deviation >20 µm for endurance tests.	Failure load stage SKS.
	GFKT-C/8,3/90	DGMKT 575	*Short test for "screening purposes"*	*Splash*	90	0,5±0,1	GF-C	8,3	*Running-in:* 1 h at l.s. 3 *Short tests:* 16 h at l.s. 7 16 h at l.s. 9	Max. profile deviation > 7,5	Ranking: low, medium, high capacity.
PITTING	PT-C/9:10/90	FVA2/IV	*Standard*	*Splash*	90	0,3±0,1	PT-C	8,3	*Running-in:* 2 h at l.s. 6 *Test until failure* at l.s. 9 for lubricant viscosity ν < VG 100 *Test until failure* at l.s.10 for lubricant viscosity ν ≥ VG 100	4% of damaged area in a flank of the pinion	LC50: life at 50% of survival probability obtained by a Weibull analysis over a minimum of three tests.
	PTX-C/10/90	FVA371/2	*Suggested for lubricant producers*	*Splash*	90	0,1±0,05	PTX-C	8,3	*Single stage test* at l.s. 10 until failure	4% of damaged area in a flank of the pinion	As above
	PTX-C/SNC/90	FVA371/2	*Suggested for gears users and manufacturers*	*Splash*	90	0,1±0,05	PTX-C	8,3	As above plus at least 2 tests at l.s. 9 or 11 depending on whether the duration in l.s.10 has been greater or lower than $15 \cdot 10^6$ cycles respectively	4% of damaged area in a flank of the pinion	As above
	KPTX	FVA/DGMK 16/2006	*Short test for "screening purposes"*	*Splash*	Running - in: 60 Test: 90	0,1±0,05	PTX-C	8,6	*Running-in:* 2 h at l.s. 5 Maximum $12.7 \cdot 10^6$ (or until failure) at l.s. 9 with inspections every $1.8 \cdot 10^6$ cycles If the first stage is passed, $12.7 \cdot 10^6$ (or until failure) at l.s. 10 otherwise the test is repeated on the opposite flank	4% of damaged area in a flank of the pinion	Ranking: low, medium, high capacity.

*Gears of the C-type differ for the following features:
GF-C: gears are manufactured with a specified high surface roughness R_a=0.5 ± 0.1 µm
PT-C: gears are manufactured with a specified low surface roughness R_a=0.3 ± 0.1 µm
PTX-C: Both the gears are superfinished up to R_a=0.5 ± 0.05 µm to suppress micropitting, The wheel has crowning and tip and tooth relief.

To overcome the limits of FSTs, the rig should present the following features:

- The structure must allow fast set-up and dismounting for frequent inspections. The possibility of extracting in few minutes the sun gear from the system and perform profile measurements near the rig will considerably contribute to time and costs saving.
- As far as possible, the operating conditions of gears should be independent from the applied load and the dynamic of the driving system. In other words the coefficients $K_A, K_V, K_{H\beta}$ and $K_{H\alpha}$ calculated according to the ISO standard should be as close as possible to unit, or at least almost constant for a wide range of applied torques.
- The bench should be designed using parts already employed in the products of Carraro, in order to limit the costs of the rig set-up and of the specimens, improve the reliability and allow an easy maintenance.

To limit the problem of compliances of gears and support, an existing sun gear design could be adapted by reducing the face width up to 10÷15 mm. This solution allows to generate a wide range of contact pressures with moderate required torque levels and therefore limited deformations. Adequate crowning and tip and root relieves are still needed to avoid edge loading and tip-to-root interferences.

References

[1] C. Dengo, Fatigue performance evaluation of gears used in off-highway drivelines, Uiversity of Padova, 2015.

[2] K.L. Johnson, One Hundred Years of Hertz Contact, Proc. Inst. Mech. Eng. 196 (1982) 363–378. doi:10.1243/PIME_PROC_1982_196_039_02.

[3] K.L. Johnson, Contact Mechanics, Cambridge University Press, 1987.

[4] A.P. Boresi, R.J. Schmidt, Advanced Mechanics Of Materials, 6TH ED, Wiley India Pvt. Limited, 2009.

[5] H.R. Thomas, V.A. Hoersch, Stresses due to the pressure of one elastic solid upon another with special reference to railroad rails : a report, (1930).

[6] K.L. Johnson, The Strength of Surfaces in Rolling Contact, Proc. Inst. Mech. Eng. Part C Mech. Eng. Sci. 203 (1989) 151–163. doi:10.1243/PIME_PROC_1989_203_100_02.

[7] B.J. Hamrock, D. Dowson, Ball Bearing Lubrication (The Elastohydrodynamics of Elliptical Contacts), J. Lubr. Technol. 104 (1982) 279. doi:10.1115/1.3253193.

[8] E. McEwen, Stresses in elastic cylinders in contact along a generatrix (including the effect of tangential friction), London, Edinburgh, Dublin Philos. Mag. J. Sci. 40 (1949) 454–459. doi:10.1080/14786444908521733.

[9] J.A. Williams, R.S. Dwyer-Joyce, Contact Between Solid Surfaces, in: C. Press (Ed.), Mod. Tribol. Handb., 2001: pp. 121–162.

[10] C. Santus, M. Beghini, I. Bartilotta, M. Facchini, Surface and subsurface rolling contact fatigue characteristic depths and proposal of stress indexes, Int. J. Fatigue. 45 (2012) 71–81. doi:10.1016/j.ijfatigue.2012.06.012.

[11] B. Bhushan, Modern Tribology Handbook, 2001.

[12] R.S. Zhou, H.S. Cheng, T. Mura, Micropitting in Rolling and Sliding Contact Under Mixed Lubrication, J. Tribol. 111 (1989) 605. doi:10.1115/1.3261984.

[13] S.C. Lee, N. Ren, The Subsurface Stress Field Created by Three-Dimensionally Rough Bodies in Contact with Traction, Tribol. Trans. 37 (1994) 615–621. doi:10.1080/10402009408983337.

[14] M.N. Webster, R.S. Sayles, A numerical-model for the elastic frictionless contact of real

rough surfaces, J. Tribol. 108 (1986) 314–320.

[15] K. T.H., A.V. Olver, Stress history in rolling–sliding contact of rough surfaces, Tribol. Int. 31 (1998) 727–736. doi:10.1016/S0301-679X(98)00085-1.

[16] G. Stachowiak, A.W. Batchelor, Engineering Tribology, Butterworth-Heinemann, 2013.

[17] B.O. Jacobson, J.J. Kalker, Rolling contact phenomena, Springer, 2000.

[18] R.W. Bruce, Handbook of lubrication and tribology, Volume !!: Theory and design, 2nd ed., CRC Press, Taylor & Frencis Group, 2012.

[19] B.J. Hamrock, R.T. Lee, L.G. Houpert, Paper VII(i) Parametric study of performance in elastohydrodynamic lubricated line contacts, 11 (1987) 199–206. doi:10.1016/S0167-8922(08)70946-5.

[20] D. Dowson, G.R. Higginson, A. V. Whitaker, Elasto-Hydrodynamic Lubrication: A Survey of Isothermal Solutions, J. Mech. Eng. Sci. 4 (1962) 121–126. doi:10.1243/JMES_JOUR_1962_004_018_02.

[21] B.J. Hamrock, D. Dowson, Isothermal Elastohydrodynamic Lubrication of Point Contacts: Part III—Fully Flooded Results, J. Lubr. Technol. 99 (1977) 264. doi:10.1115/1.3453074.

[22] ISO/TR 15144-1:2014 - Calculation of micropitting load capacity of cylindrical spur and helical gears -- Part 1: Introduction and basic principles.

[23] S. Glodež, J. Flašker, Z. Ren, A NEW MODEL FOR THE NUMERICAL DETERMINATION OF PITTING RESISTANCE OF GEAR TEETH FLANKS, Fatigue Fract. Eng. Mater. Struct. 20 (1997) 71–83. doi:10.1111/j.1460-2695.1997.tb00403.x.

[24] G. Fajdiga, S. Glodež, J. Kramar, Pitting formation due to surface and subsurface initiated fatigue crack growth in contacting mechanical elements, Wear. 262 (2007) 1217–1224. doi:10.1016/j.wear.2006.11.016.

[25] A. V. Olver, The Mechanism of Rolling Contact Fatigue: An Update, Proc. Inst. Mech. Eng. Part J J. Eng. Tribol. 219 (2005) 313–330. doi:10.1243/135065005X9808.

[26] Y. Ding, N.F. Rieger, Spalling formation mechanism for gears, Wear. 254 (2003) 1307–1317. doi:10.1016/S0043-1648(03)00126-1.

[27] J.W. Blake, H.S. Cheng, A Surface Pitting Life Model for Spur Gears: Part II—Failure Probability Prediction, J. Tribol. 113 (1991) 719. doi:10.1115/1.2920684.

[28] S. Way, Pitting due to rolling contact, J. Appl. Mech. 1935 (n.d.) A49–A58.

[29] Y. Murakami, M. Kaneta, H. Yatsuzuka, Analysis of Surface Crack Propagation in

Lubricated Rolling Contact, A S L E Trans. 28 (1985) 60–68. doi:10.1080/05698198508981595.

[30] Y. Murakami, C. Sakae, K. Ichimaru, Three-Dimensional Fracture Mechanics Analysis of Pit ormation Mechanism Under Lubricated Rolling-Sliding Contact Loading, Tribol. Trans. (1994).

[31] Y. Murakami, C. Sakae, K. Ichimaru, T. Morita, Experimental and Fracture Mechanics Study of the Pit Formation Mechanism Under Repeated Lubricated Rolling-Sliding Contact: Effects of Reversal of Rotation and Change of the Driving Roller, J. Tribol. 119 (1997) 788. doi:10.1115/1.2833886.

[32] A.V. Olver, L.K. Tiew, S. Medina, J.W. Choo, Direct observations of a micropit in an elastohydrodynamic contact, Wear. 256 (2004) 168–175. doi:10.1016/S0043-1648(03)00374-0.

[33] E. Bormetti, G. Donzella, A. Mazzù, Surface and Subsurface Cracks in Rolling Contact Fatigue of Hardened Components, Tribol. Trans. 45 (2002) 274–283. doi:10.1080/10402000208982550.

[34] M. Boniardi, F. D'Errico, C. Tagliabue, Influence of carburizing and nitriding on failure of gears – A case study, Eng. Fail. Anal. 13 (2006) 312–339. doi:10.1016/j.engfailanal.2005.02.021.

[35] R.L. Errichello, C. Hewette, R. Eckert, Point-Surface-Origin Macropitting Caused by Geometric Stress Concentration, Gear Technol.

[36] S. Ancellotti, M. Benedetti, M. Dallago, V. Fontanari, Fluid Pressurization and Entrapment Effects on the SIFs of Cracks produced under lubricated Rolling-Sliding Contact Fatigue, Procedia Struct. Integr. 2 (2016) 3098–3108. doi:10.1016/J.PROSTR.2016.06.387.

[37] M. Dallago, M. Benedetti, S. Ancellotti, V. Fontanari, The role of lubricating fluid pressurization and entrapment on the path of inclined edge cracks originated under rolling–sliding contact fatigue: Numerical analyses vs. experimental evidences, Int. J. Fatigue. (2016). doi:10.1016/j.ijfatigue.2016.02.014.

[38] A.F. Bower, Influence of crack face friction and trapped fluid on surface initiated rolling contact fatigue cracks, J. Tribol. 110 (1988) 704–711.

[39] L.M. Keer, M.D. Bryant, A Pitting Model for Rolling Contact Fatigue, J. Lubr. Technol. 105 (1983) 198. doi:10.1115/1.3254565.

[40] F. Sadeghi, B. Jalalahmadi, T.S. Slack, N. Raje, N.K. Arakere, A Review of Rolling

Contact Fatigue, J. Tribol. 131 (2009) 41403. doi:10.1115/1.3209132.

[41] A. Grabulov, R. Petrov, H.W. Zandbergen, EBSD investigation of the crack initiation and TEM/FIB analyses of the microstructural changes around the cracks formed under Rolling Contact Fatigue (RCF), Int. J. Fatigue. 32 (2010) 576–583. doi:10.1016/j.ijfatigue.2009.07.002.

[42] M.-H. Evans, White structure flaking (WSF) in wind turbine gearbox bearings: Effects of “butterflies” and white etching cracks (WECs), Mater. Sci. Technol. 28 (2012) 3–22. doi:10.1179/026708311X13135950699254.

[43] R. Errichello, R. Budny, R. Eckert, Investigations of Bearing Failures Associated with White Etching Areas (WEAs) in Wind Turbine Gearboxes, Tribol. Trans. 56 (2013) 1069–1076. doi:10.1080/10402004.2013.823531.

[44] T. Bruce, E. Rounding, H. Long, R.S. Dwyer-Joice, Characterisation of white etching crack damage in wind turbine gearbox bearings, Wear. 338–339 (2015) 164–177. doi:10.1016/J.WEAR.2015.06.008.

[45] M.-H. Evans, An updated review: white etching cracks (WECs) and axial cracks in wind turbine gearbox bearings, Mater. Sci. Technol. 32 (2016) 1133–1169. doi:10.1080/02670836.2015.1133022.

[46] B.R. Höhn, P. Oster, K. Michaelis, New Test Methods for the Evaluation of Wear, Scuffing and Pitting Capacity of Gear Lubricants, AGMA Tech. Pap. 98FTM8. (1998).

[47] W.E. Littmann, R.L. Widner, Propagation of Contact Fatigue From Surface and Subsurface Origins, J. Basic Eng. 88 (1966) 624. doi:10.1115/1.3645922.

[48] J.R. Davis, Gear Materials, Properties, and Manufacture, (2005).

[49] D. Hannes, B. Alfredsson, Modelling of Surface Initiated Rolling Contact Fatigue Damage, Procedia Eng. 66 (2013) 766–774. doi:10.1016/J.PROENG.2013.12.130.

[50] G. Espejel, A. Gabelli, The progression of surface rolling contact fatigue damage of rolling bearings, Evol. SKF.

[51] L.F. and I. Batista, Dias, Lebrun, Contact fatigue of automotive gears: evolution and effects of residual stresses introduced by surface treatments, Fatigue & Fract. Eng. Mater. Struct. 23 (2000) 217–228. doi:10.1046/j.1460-2695.2000.00268.x.

[52] M. Guagliano, E. Riva, M. Guidetti, Contact fatigue failure analysis of shot-peened gears, Eng. Fail. Anal. 9 (2002) 147–158. doi:10.1016/S1350-6307(01)00002-4.

[53] Y. Gao, Influence of Deep-Nitriding and Shot Peening on Rolling Contact Fatigue Performance of 32Cr3MoVA Steel, J. Mater. Eng. Perform. 17 (2007) 455–459.

doi:10.1007/s11665-007-9155-7.

[54] I. Fernández Pariente, M. Guagliano, Contact fatigue damage analysis of shot peened gears by means of X-ray measurements, Eng. Fail. Anal. 16 (2009) 964–971. doi:10.1016/j.engfailanal.2008.08.020.

[55] M. Benedetti, V. Fontanari, B.R. Hohn, P. Oster, T. Tobie, Influence of shot peening on bending tooth fatigue limit of case hardened gears, Int. J. Fatigue. 24 (2002) 1127–1136. doi:10.1016/S0142-1123(02)00034-8.

[56] G. Olmi, M. Comandini, A. Freddi, Fatigue on Shot-Peened Gears: Experimentation, Simulation and Sensitivity Analyses, Strain. 46 (2010) 382–395. doi:10.1111/j.1475-1305.2009.00685.x.

[57] ISO 6336 Calculation of load carrying capacity of spur and helical gears, (2006).

[58] AGMA 2101 : Fundamental Rating Factors and Calculation Methods for Involute Spur and Helical Gear Teeth.

[59] M. Vrbka, I. Krupka, P. Svoboda, P. Serka, T. Navrat, M. Hartl, et al., Effect of shot peening on rolling contact fatigue and lubricant film thickness within mixed lubricated non-conformal rolling/sliding contacts, Tribol. Int. 44 (2011) 1726–1735. doi:10.1016/J.TRIBOINT.2011.06.019.

[60] A. Terrin, C. Dengo, G. Meneghetti, Experimental analysis of contact fatigue damage in case hardened gears for off-highway axles, Eng. Fail. Anal. 76 (2017) 10–26. doi:10.1016/j.engfailanal.2017.01.019.

[61] T.E. Tallian, Simplified Contact Fatigue Life Prediction Model—Part I: Review of Published Models, J. Tribol. 114 (1992) 207. doi:10.1115/1.2920875.

[62] E. Conrado, Tarantino Gabriella, Un modello per la resistenza a pitting degli ingranaggi, Organi Di Trasm. 152–157.

[63] G. Lundberg, A. Palmgren, Dynamic capacity of rolling bearings, Acta Polytech. Mech. Eng. Ser. 1. (1947).

[64] W. Weibull, A statistical theory of the strength of materials, R. Swedish Acad. Eng. Sci. Proc. No. (1939).

[65] J.J. Coy, D.P. Townsend, E. V Zaretsky, Analysis of dynamic capacity of low contact ratio spur gears using Lundberg-Palmgren theory, NASA Techincal Note D-8029. (1975).

[66] D.P. Townsend, J.J. Coy, E. V. Zaretsky, Experimental and Analytical Load-Life Relation for AISI 9310 Steel Spur Gears, J. Mech. Des. 100 (1978) 54.

doi:10.1115/1.3453893.

[67] AGMA 411.02 - Design Procedure for Aircraft Engine and Power Take-Off Spur and Helical Gears, (1966).

[68] AGMA 210.02:1965 - Surface Durability Of Spur Gear Teeth, (1965).

[69] A. Walvekar, F. Sadeghi, Rolling contact fatigue of case carburized steels, Int. J. Fatigue. 95 (2017) 264–281. doi:10.1016/J.IJFATIGUE.2016.11.003.

[70] S. Li, A. Kahraman, Micro-pitting fatigue lives of lubricated point contacts: Experiments and model validation, Int. J. Fatigue. 48 (2013) 9–18. doi:10.1016/j.ijfatigue.2012.12.003.

[71] E. Melan, Zur Plastizität des räumlichen Kontinuums, Ingenieur-Archiv. 9 (1938) 116–126. doi:10.1007/BF02084409.

[72] K.L. Johnson, A Shakedown Limit in Rolling Contact, Proc. 4th US Natl. Congr. Appl. Mech. Berkeley ASME. (1962) 288.

[73] A.R.S. Ponter, A General Shakedown Theorem for Elastic/Plastic Bodies with Work Hardening, Proc. 3rd Int. Conf. Struct. Mech. Imp. Coll. London. (1975). https://repository.lib.ncsu.edu/handle/1840.20/28450 (accessed September 22, 2017).

[74] A.R.S. Ponter, A.D. Hearl, K.L. Johnson, Application of the kinematical shakedown theorem to rolling and sliding point contacts, J. Mech. Phys. Solids. 33 (1985) 339–362. doi:10.1016/0022-5096(85)90033-X.

[75] J.W. Ringsberg, M. Loo-Morrey, B.L. Josefson, A. Kapoor, J.H. Beynon, Prediction of fatigue crack initiation for rolling contact fatigue, Int. J. Fatigue. 22 (2000) 205–215. doi:10.1016/S0142-1123(99)00125-5.

[76] J.W. Ringsberg, Life prediction of rolling contact fatigue crack initiation, Int. J. Fatigue. 23 (2001) 575–586. doi:10.1016/S0142-1123(01)00024-X.

[77] A.D. Hearle, Deformation, shakedown and fatigue in rolling contact., (1985).

[78] A. Kapoor, K.L. Johnson, Effect of changes in contact geometry on shakedown of surfaces in rolling/sliding contact, Int. J. Mech. Sci. 34 (1992) 223–239. doi:10.1016/0020-7403(92)90073-P.

[79] M. Ciavarella, F. Monno, A comparison of multiaxial fatigue criteria as applied to rolling contact fatigue, Tribol. Int. 43 (2010) 2139–2144. doi:10.1016/j.triboint.2010.06.003.

[80] A. Ekberg, E. Kabo, H. Andersson, An engineering model for prediction of rolling contact fatigue of railway wheels, Fatigue Fract. Eng. Mater. Struct. 25 (2002) 899–909. doi:10.1046/j.1460-2695.2002.00535.x.

[81] Dang Van Ky, Sur la résistance à la fatigue des métaux, Sci. Tech. Armement. 44 (1973).

[82] K. Dang Van, M.H. Maitournam, Rolling contact in railways: modelling, simulation and damage prediction, Fatigue Fract. Eng. Mater. Struct. 26 (2003) 939–948. doi:10.1046/j.1460-2695.2003.00698.x.

[83] M. Ciavarella, F. Monno, G. Demelio, On the Dang Van fatigue limit in rolling contact fatigue, Int. J. Fatigue. 28 (2006) 852–863. doi:10.1016/J.IJFATIGUE.2005.11.002.

[84] H. Desimone, A. Bernasconi, S. Beretta, On the application of Dang Van criterion to rolling contact fatigue, Wear. 260 (2006) 567–572. doi:10.1016/j.wear.2005.03.007.

[85] G. Niemann, H. Winter, B.-R. Höhn, Maschinenelemente/ Band 1, Konstruktion und Berechnung von Verbindungen, Lagern, Wellen., Springer, 2005.

[86] A.R.S. Ponter, H.F. Chen, M. Ciavarella, G. Specchia, Shakedown analyses for rolling and sliding contact problems, Int. J. Solids Struct. 43 (2006) 4201–4219. doi:10.1016/J.IJSOLSTR.2005.05.046.

[87] P. Rycerz, A. Olver, A. Kadiric, Propagation of surface initiated rolling contact fatigue cracks in bearing steel, Int. J. Fatigue. 97 (2017) 29–38. doi:10.1016/J.IJFATIGUE.2016.12.004.

[88] M. Beghini, C. Santus, An application of the weight function technique to inclined surface cracks under rolling contact fatigue, assessment and parametric analysis, Eng. Fract. Mech. 98 (2013) 153–168. doi:10.1016/J.ENGFRACMECH.2012.10.024.

[89] H. NISITANI, The Two-Dimensional Stress Problem Solved Using an Electric Digital Computer, Bull. JSME. 11 (1968) 14–23. doi:10.1299/jsme1958.11.14.

[90] H. Nisitani, Y. Murakami, Stress intensity factors of an elliptical crack or a semi-elliptical crack subject to tension, Int. J. Fract. 10 (1974) 353–368. doi:10.1007/BF00035496.

[91] L.M. Keer, M.D. Bryant, G.K. Haritos, Subsurface and Surface Cracking Due to Hertzian Contact, J. Lubr. Technol. 104 (1982) 347. doi:10.1115/1.3253217.

[92] M.T. Hanson, L.M. Keer, An Analytical Life Prediction Model for the Crack Propagation Occurring in Contact Fatigue Failure, Tribol. Trans. 35 (1992) 451–461. doi:10.1080/10402009208982143.

[93] J. Flasker, G. Fajdiga, S. Glodez, T.K. Hellen, Numerical simulation of surface pitting due to contact loading, Int. J. Fatigue. 23 (2001) 599–605. doi:10.1016/S0142-1123(01)00020-2.

[94] M.F. Frolish, D.I. Fletcher, J.H. Beynon, A quantitative model for predicting the

morphology of surface initiated rolling contact fatigue cracks in back-up roll steels, Fatigue & Fract. Eng. Mater. Struct. 25 (2002) 1073–1086. doi:10.1046/j.1460-2695.2002.00601.x.

[95] J.W. Ringsberg, A. Bergkvist, On propagation of short rolling contact fatigue cracks, Fatigue & Fract. Eng. Mater. Struct. 26 (2003) 969–983. doi:10.1046/j.1460-2695.2003.00657.x.

[96] S. Bogdanski, P. Lewicki, 3D model of liquid entrapment mechanism for rolling contact fatigue cracks in rails, Wear. 265 (2008) 1356–1362. doi:10.1016/J.WEAR.2008.03.014.

[97] G. Fajdiga, M. Sraml, Fatigue crack initiation and propagation under cyclic contact loading, Eng. Fract. Mech. 76 (2009) 1320–1335. doi:10.1016/J.ENGFRACMECH.2009.02.005.

[98] V.V. Panasyuk, O.P. Datsyshyn, Material Damages and Life Time of Solids under a Cyclic Contact, Procedia Mater. Sci. 3 (2014) 1250–1256. doi:10.1016/J.MSPRO.2014.06.203.

[99] DIN 3990, Calculation of load capacity of cylindrical gears, (1987).

[100] AGMA 925-A03 | AGMA - American Gear Manufacturers Association.

[101] FVA Information Sheet No. 243 “Scuffing Test EP-Oils, Method to Assess the Scuffing Load Capacity of Lubricants with High EP Performance Using an FZG Gear Test Rig,”.

[102] R. Errichello, Critique of the ISO 15144-1 Method to Predict the Risk of Micropitting : Gear Technology March/April 2016, Gear Technol. (2016).

[103] B.B. Eng, K. Mahr, I. Ag, U. Kissling, K. Ag, Comparison between different commercial gear tooth contact analysis software packages.

[104] C. Weber, K. Banascheck, Elastische Formänderung der Zähne und der anschliessenden Teile der Radkorper von Zahnradgetrieben, FVA Rep. 129 134. (1955).

[105] ISO 6336-2:2006 - Calculation of load capacity of spur and helical gears -- Part 2: Calculation of surface durability (pitting), (n.d.). [106] ISO 12107:2003 - Metallic materials -- Fatigue testing -- Statistical planning and analysis of data.

[107] G. Niemann, H. Winter, Maschinenelemente: Band 2: Getriebe allgemein, Zahnradgetriebe - Grundlagen, Stirnradgetriebe, Springer-Verlag, 1985.

[108] B.H.-L. Yeh, Dynamic loads on spur gear teeth., University of British Columbia, 1959. doi:10.14288/1.0105974.

[109] M. Utagawa, T. Harada, Dynamic Loads on Spur Gear Teeth at High Speed : Influence of the Pressure Angle Errors and Comparison between the Reduction Gears and the

Speed-up Gears, Bull. JSME. 4 (1961) 706–713. doi:10.1299/jsme1958.4.706.

[110] J.A. Pethick, The construction and use of a test machine to measure dynamic loads on gear teeth., Thesis (M.S. in Mechanical Engineering), United States Naval Academy, 1967.

[111] T. Hidaka, Y. Terauchi, Dynamic Behavior of Planetary Gear : 1st Report Load Distribution in Planetary Gear, Bull. JSME. 19 (1976) 690–698. doi:10.1299/jsme1958.19.690.

[112] F.B. Oswald, Gear Tooth Stress Measurements on the UH-60A Helicopter Transmission, NASA Tech. Pap. 2698 (1987) 17 p.

[113] T.L. Krantz, Gear tooth stress measurements of two helicopter planetary stages, in: Sixth Int. Power Transm. Gearing Conf., Phoenix, Arizona, 1992.

[114] H. Ligata, A. Kahraman, A. Singh, An Experimental Study of the Influence of Manufacturing Errors on the Planetary Gear Stresses and Planet Load Sharing, J. Mech. Des. 130 (2008) 41701. doi:10.1115/1.2885194.

[115] R.F. Handschuh, Recent advances in the analysis of spiral bevel gears, (1997).

[116] M.A. Hotait, A. Kahraman, T. Nishino, An Investigation of Root Stresses of Hypoid Gears with Misalignments, J. Mech. Des. 133 (2011) 71006. doi:10.1115/1.4004224.

[117] S. Baud, P. Velex, Static and Dynamic Tooth Loading in Spur and Helical Geared Systems-Experiments and Model Validation, J. Mech. Des. 124 (2002) 334. doi:10.1115/1.1462044.

[118] C. Zhou, B. Hu, S. Chen, L. Ma, Wireless measurement and dynamic contact analysis on the root stress of a light-load spur gear drive, Aust. J. Mech. Eng. (2016) 1–9. doi:10.1080/14484846.2016.1210999.

[119] A. Singh, Epicyclic Load Sharing Map-Application As a Design Tool, AGMA Pap. 11FTM05. (2011).

[120] M. Weck, A. Kruse, A. Gohritz, Determination of Surface Fatigue of Gear Material by Roller Tests, J. Mech. Des. 100 (1978) 433. doi:10.1115/1.3453947.

[121] L. Flamand, D. Berthe, M. Godet, Simulation of Hertzian Contacts Found in Spur Gears with a High Performance Disk Machine, J. Mech. Des. 103 (1981) 204. doi:10.1115/1.3254866.

[122] C.M.R. Wilkinson, A. V. Olver, The Durability of Gear and Disc Specimens — Part I: The Effect of Some Novel Materials and Surface Treatments, Tribol. Trans. 42 (1999) 503–510. doi:10.1080/10402009908982247.

[123] C.M.R. Wilkinson, A. V. Olver, The Durability of Gear and Disc Specimens—Part II: Post Failure Examination and Gear-Disc Correlation, Tribol. Trans. 42 (1999) 610–618. doi:10.1080/10402009908982260.

[124] H. Rösch, Untersuchungen zur Wälzfestigkeit von Rollen: Einfluss von Werkstoff, Wärmebehandlung und Schlupfe (Investigation on pitting capacity of rollers - Influence of material, heat treatment and slip ratio), (1976).

[125] K. Fujita, A. Yoshida, Effects of Case Depth and Relative Radius of Curvature on Surface Durability of Case-Hardened Chromium Molybdenum Steel Roller, J. Mech. Des. 103 (1981) 474. doi:10.1115/1.3254942.

[126] M. Kobayashi, K. Hasegawa, Effect of shot peening on the pitting fatigue strength of gears, in: ICSP-4, 1990: pp. 465–476.

[127] R.C. Graham, A. Olver, P.B. Macpherson, Graham: An Investigation into the Mechanisms of Pitting... - Google Scholar, in: Century 2 Int. Power Transm. Gearing Conf., Contribution of the American Society of Mechanical Engineers, 1980.

[128] Y. Kimura, M. Sekizawa, A. Nitanai, Wear and fatigue in rolling contact, Wear. 253 (2002) 9–16. doi:10.1016/S0043-1648(02)00077-7.

[129] BS 436-3:1986 - Spur and helical gears. Method for calculation of contact and root bending stress limitations for metallic involute gears.

[130] ISO 6336-5:2016 - Calculation of load capacity of spur and helical gears -- Part 5: Strength and quality of materials.

[131] H.E. Merritt, Worm Gear Performance, Proc. Inst. Mech. Eng. 129 (1935) 127–194. doi:10.1243/PIME_PROC_1935_129_011_02.

[132] FZG: Technical Equipment, (n.d.). https://www.fzg.mw.tum.de/en/research/technical-equipment/ (accessed October 4, 2017).

[133] MPR (Micro Pitting Rig), (n.d.). http://pcs-instruments.com/product/mpr-micro-pitting-rig/ (accessed October 4, 2017).

[134] S. Li, A. Kahraman, A fatigue model for contacts under mixed elastohydrodynamic lubrication condition, Int. J. Fatigue. 33 (2011) 427–436. doi:10.1016/J.IJFATIGUE.2010.09.021.

[135] T. Ahlroos, H. Ronkainen, A. Helle, R. Parikka, J. Virta, S. Varjus, Twin disc micropitting tests, Tribol. Int. 42 (2009) 1460–1466. doi:10.1016/j.triboint.2009.05.023.

[136] C. Gorla, F. Rosa, E. Conrado, H. Albertini, Bending and contact fatigue strength of innovative steels for large gears, J. Mech. Eng. Sci. 228 (2014) 2469–2482.

doi:10.1177/0954406213519614.

[137] G.E. et al. Totten, Bench Testing of Industrial Fluid Lubrication and Wear Properties, ASTM International, 2001. doi:10.1520/STP1404-EB.

[138] M. Simon, Messung von elasto-hidrodynamischen Parameter, und hire Auswirkung auf die Grübchentragfähigkeit vergüteter Scheiben und Zahnräder. (Measurement of EHD parameters and their influence on pitting capacity of through hardened discs and gears), (1984).

[139] B.-R. Hoehn, K. Michaelis, A. Doleschel, Limitations of Bench Testing for Gear Lubricants, in: Bench Test. Ind. Fluid Lubr. Wear Prop. Used Mach. Appl., ASTM International, 100 Barr Harbor Drive, PO Box C700, West Conshohocken, PA 19428-2959, 2001: pp. 15-15–18. doi:10.1520/STP10497S.

[140] J. Kleemola, A. Lehtovaara, Experimental simulation of gear contact along the line of action, Tribol. Int. 42 (2009) 1453–1459. doi:10.1016/j.triboint.2009.06.007.

[141] A. Terrin, Design, manufacturing and testing of a twin-disc test rig for the surface fatigue characterization of materials, Università degli Studi di Padova, 2013.

[142] G. Meneghetti, S. Giacometti, A. Terrin, Twin disc testing apparatus, 2015.

[143] M. Osellame, Analisi del danneggiamento per fatica da contatto e sviluppo di una macchina di prova sperimentale, Università degli Studi di Padova, n.d.

[144] B.R. Höhn, K. Michaelis, H.P. Otto, Pitting load carrying capacity under increased thermal conditions, in: 3rd Int. Conf. Integrity, Reliab. Fail. Porto/Portugal, 2009.

[145] L. Piffer, Sviluppo, calibrazione e primi test di una macchina di tipo twin-disc per prove di resistenza a pitting su acciai, Università degli Studi di Padova, 2016.

[146] G. Meneghetti, A. Terrin, L. Piffer, Rolling contact fatigue characterization of gears materials using twin disc tests., in: Atti Del 45° Convegno Naz. AIAS, 2016.

[147] R. Errichello, Morphology of Micropitting, 11FTM17, Am. Gear Manuf. Assoc. (2011).

[148] S.G. G. Meneghetti, A.Terrin, A twin disc test rig for contact fatigue characterization of gear materials, in: Struct. Integr. Procedia, 2016.

[149] K. Fujita, A. Yoshida, The effect of changing the rolling direction on the rolling contact fatigue lives of annealed and case-hardened steel rollers, Wear. 43 (1977) 315–327.

[150] W.R. Tyfour, J.H. Beynon, The effect of rolling direction reversal on fatigue crack morphology and propagation, Tribol. Int. 27 (1994) 273–282.

[151] B.-R. Hoehn, P. Oster, T. Tobie, K. Michaelis, Test methods for gear lubricants, Fuels Lubr. . 47 (2008).

Ringraziamenti

Oltre al grande valore dato dall'approfondimento di specifiche competenze, questo percorso ha rappresentato per me un'inestimabile occasione per sperimentare un modo nuovo di vedere i problemi, di analizzarli e, per quanto mi è stato possibile, di provare a spiegarli ed a proporre soluzioni, prendendo spunto dalle voci esperte che, di volta in volta, ho avuto modo di ascoltare.
Desidero pertanto ringraziare innanzitutto il professor Giovanni Meneghetti per avermi offerto l'opportunità di intraprendere questo progetto ed avermi guidato sempre con impegno e massima professionalità lungo un percorso che è stato un'occasione di grande crescita sotto svariati punti di vista che vanno ben oltre all'aspetto puramente tecnico.
Grazie a Carraro S.p.A., che ha finanziato il periodo di apprendistato di alta formazione e ricerca. In particolare ringrazio l'ing. Fulvio Lo Conte, correlatore di questa tesi, che da anni sostiene la ricerca e l'innovazione all'interno dell'azienda, per aver sempre creduto nel progetto, dedicando tempo per seguirne l'avanzamento e promuovendo gli investimenti necessari.
Un ringraziamento particolare va a Carlo per il costante supporto durante questi anni, già a partire dallo sviluppo del banco prova durante la mia tesi di laurea. Grazie per i preziosi consigli e l'enorme disponibilità sempre dimostrata.
Grazie a Massimiliano per quello che mi ha insegnato in questi tre anni, e per avermi lasciato l'autonomia necessaria ad assolvere agli obbiettivi più puramente accademici, a costo di un più elevato carico di lavoro da parte sua e degli altri componenti del gruppo.
Un doveroso ringraziamento va inoltre a Stefano che mi ha guidato nel progetto del banco Twin-Disc e ha seguito quasi interamente la realizzazione dei componenti meccanici. A lui va la mia sincera ammirazione per l'indole vulcanica e l'estrema disponibilità e simpatia.
Grazie anche a Gabriele, che ha realizzato la maggior parte dei componenti necessari per le modifiche al banco prova offrendo di volta in volta utili suggerimenti.
Ringrazio inoltre, tutti coloro con cui non ho lavorato sempre a stretto contatto ma hanno offerto un significativo contributo allo svolgimento di questo lavoro. In particolare grazie a Fabio Scarpa per il prezioso supporto nelle prime analisi metallografiche, a Diego Rizzato, Fabrizio

Roncato, Simone Sabbadin, Michele Ceccon, Luca Beccaro per l'aiuto nei test, e a Renzo Niero per la cortesia con cui si è impegnato per soddisfare le richieste di analisi metrologiche anche quando richiedevano operazioni non convenzionali. Grazie inoltre a Davide Zampiva, Federica Masetto, Stefano Griggio, Moreno Maso ed Ermanno Martellozzo per il loro apporto in varie occasioni.

Infine, desidero ringraziare chi mi ha sostenuto e incoraggiato ad intraprendere questa strada, in particolare i miei genitori, a cui spetterebbero infiniti altri ringraziamenti per altrettanti validi motivi.

Grazie a Clelia, per essermi sempre stata vicina, con amorevole comprensione, nei periodi in cui il lavoro ha sottratto parte del nostro tempo.

Grazie ad Ettore, che in un modo o nell'altro sa sempre come distrarci dai pensieri apparentemente più importanti, riordinando la nostra scala delle priorità.

Padova, 29/12/2017